Interaction of Degradation, Deformation and Transport Processes in Municipal Solid Waste Landfills

Von der
Fakultät Architektur, Bauingenieurwesen und Umweltwissenschaften
der Technischen Universität Carolo-Wilhelmina
zu Braunschweig

zur Erlangung des Grades einer
Doktoringenieurin (Dr.-Ing.)
genehmigte

Dissertation

von
Sonja Bente
geboren am 08.04.1976
aus Diepholz

Eingereicht am: 29.03.2010
Mündliche Prüfung am: 27.10.2010

Berichter: Prof. Dr.-Ing. Dieter Dinkler
Prof. Dr.-Ing. Rainer Helmig
Prüfer: Prof. Dr.-Ing. Andreas Haarstrick

Braunschweig 2011

ISBN 978-3926031-11-2

Herausgeber: Prof. Dr.-Ing. Dieter Dinkler

Kurzfassung

In dieser Arbeit wird ein Modell für die simultane Kopplung des Spannungsverformungsverhaltens, der Abbauprozesse und der Transportprozesse in Deponien vorgestellt. Das Modell ist im Rahmen der Theorie Poröser Medien entwickelt. Die Interaktionen sind mit der Kopplung der physikalischen Felder über ein repräsentatives Elementarvolumen berücksichtigt. Ein zweistufiges Abbaumodell beschreibt den anaeroben Abbau der Organik und die Wärmeentwicklung infolge exothermer Reaktionen. Mehrphasentransport und physikalische Austauschprozesse sind beschrieben. In Kooperation mit der Edinburgh Napier University werden Versuche zum Wasserrückhaltevermögen von Abfall durchgeführt. Ein Kompaktionsmodell wird vorgestellt, bei dem die Kompaktionsrate nicht nur von der Spannung, sondern auch von der Dichte der festen Substanz abhängt. Dies ermöglicht die direkte Kopplung an das Reaktionsmodell und damit die Beschreibung abbauinduzierter Setzungen. Der Einfluss der Verformung auf die Porosität und die Permeabilität sind berücksichtigt. Das Konzept der effektiven Spannungen erlaubt zusammen mit dem Kompaktionsmodell die getrennnte Beschreibung von Setzungsmechanismen. Für die räumliche Diskretisierung der Bilanzgleichungen wird eine Kombination der Finite-Elemente Methode und des Box-Verfahrens verwendet. Das Modell wird anhand von Laborversuchen validiert. Anwendungen auf Deponiestrukturen beinhalten die Langzeit-Prognose von Setzungen, die Untersuchung eines Gasfassungssystems und die Modellierung der aktiven Bewässerung auf Deponien zur Beschleunigung der Abbauprozesse.

Abstract

In this thesis a model for the complex interactions between deformation, degradation and transport processe in municipal solid waste landfills is presented. Key aspects of the model are a joint continuum mechanical framework and a monolithic solution of the governing equations within the Theory of Porous Media. Interactions are considered by coupling the governing physical fields over the domain of a representative elementary volume via selected state variables. A simplified two-stage degradation model describes anaerobic biological processes. Heat generation from exothermic reactions is considered. Transport of the leachate and the landfill gas are described by means of a generalised Darcy law and the influence of deformation on the hydraulic properties is considered. In cooperation with Edinburgh Napier University experiments on the moisture retention properties of waste are performed. The model for stress-deformation behaviour includes a novel creep model which combines stress-dependency of creep rate with density-dependency. Via the solid dry bulk density, the creep rate is coupled to degradation which enables description of degradation-induced settlements. The concept of effective stress is included in the mechanical equilibrium and thus a separate description of separate settlement phenomena is enabled. A combination of the Finite-Element method and the Box method in an ALE formulation is applied for spatial discretisation of the governing physical fields. The model is verified and validated against a benchmark for multiphase flow and a waste lysimeter experiment. Analyses of a landfill structure show the capabilities of the model in the estimation of long-term settlements, in the description of a gas extraction system and in modelling of an infiltration layer.

Contents

1 Introduction 1

1.1 Background . . . 1
1.2 Motivation and Objective . . . 2
1.3 State of the Art . . . 4
1.4 Outline of the Thesis . . . 9

2 Continuum Mechanical Fundamentals 11

2.1 Theory of Porous Media . . . 11
2.2 Fundamentals of large strain continuum mechanics . . . 13
  2.2.1 Description of motion . . . 13
  2.2.2 Strain measures . . . 15
  2.2.3 Stress tensors . . . 17
2.3 Balance equations for a three-phase model . . . 18
  2.3.1 Principle of Virtual Work for the mixture . . . 18
  2.3.2 Mass balance for solid components in Total Lagrangian description 19
  2.3.3 Integral form of mass balance for fluid components in ALE description 19
    2.3.3.1 Time derivative of a volume integral over a moving volume 20
    2.3.3.2 Mass conservation for a moving reference frame . . . 22
  2.3.4 Balance of angular momentum . . . 23
  2.3.5 Balance of energy . . . 23
2.4 Discretisation of model equations in time and space . . . 24

3 Model for Degradation and Heat Generation 27

3.1 Phenomenology of Biogological Degradation in MSW Landfills . . . 27
3.2 Models for Degradation Processes in MSW . . . 29
3.3 Constitutive Model for Biological Degradation Including Heat Generation and Transfer . . . 35
  3.3.1 Stoichiometry . . . 35
  3.3.2 Reaction Kinetics . . . 37
  3.3.3 Influence of Milieu Conditions . . . 38
3.4 Simulation of a Lysimeter Experiment . . . 43
3.5 Heat Generation . . . 47
  3.5.1 Reaction Enthalpies . . . 47
  3.5.2 Heat Capacity . . . 49
  3.5.3 Heat Conductivity of the Porous Mixture . . . 50
  3.5.4 Heat Conductivity of the Solid Phase . . . 50

4 Constitutive Model for Multiphase, Multicomponent Transport in Waste 55

4.1 Models for Transport Processes in Waste . . . 55
4.2 Moisture Storage in Waste . . . 58
  4.2.1 Porosity and Pore Structure . . . 58
  4.2.2 Moisture Retention and Matric Suction . . . 61

4.3 Flow of Liquid and Gas Phase . . . 68
  4.3.1 Darcy's Law . . . 68
  4.3.2 Saturated Hydraulic Conductivity of Waste and Deformation Dependent Permeability . . . 69
  4.3.3 Unsaturated Hydraulic Conductivity . . . 71
  4.3.4 Temperature Dependence of Viscosity . . . 72
4.4 Transport by Diffusion . . . 74
4.5 Physical Exchange Processes . . . 75
  4.5.1 Saturated Vapour Pressure . . . 75
  4.5.2 Vapour Pressure Reduction . . . 76
  4.5.3 Gas Mixture . . . 76
  4.5.4 Dissolution of Carbon Dioxide . . . 77
  4.5.5 Liquid Mixture . . . 78
4.6 Effective Stress . . . 78

5 Stress-Deformation Behaviour of MSW 85
5.1 Phenomenology . . . 85
  5.1.1 Classification and Unit Weight . . . 85
  5.1.2 Shear Strength and Tensile Strength . . . 85
  5.1.3 Settlements . . . 87
5.2 Constitutive Model for Stress Deformation Behaviour of Municipal Solid Waste . . . 91
  5.2.1 Small Elastic Strains . . . 93
  5.2.2 Unit Weight of Solid Mixture . . . 94
  5.2.3 Constitutive Model for the Basic Matrix . . . 94
  5.2.4 Constitutive Model for the Fibres . . . 100
5.3 Influence of Water Content on Shear Strength . . . 102

6 Solution of the Coupled Initial Boundary Value Problem 105
6.1 Assembly of Final Balance Equations in Integral Form . . . 106
6.2 Iterative Solution and Linearisation . . . 111
6.3 Structure of the Algorithm . . . 115

7 Analysis of Coupled Processes 119
7.1 Validation of Coupled Transport and Deformation with the ALERT Liakopoulos Benchmark . . . 119
7.2 Validation Based on Experiments with two Consolidating Anaerobic Reactors (CAR) . . . 124
  7.2.1 Simulation of CAR 1 . . . 126
  7.2.2 Simulation of CAR 2 . . . 135
  7.2.3 Comparative Simulations without Degradation . . . 138
7.3 Coupled Analyses of a Landfill Structure . . . 140
  7.3.1 Influence of Organic Matter Content on Settlements . . . 141
  7.3.2 Simulation of a Gas Extraction System . . . 151
  7.3.3 Modelling of an Infiltration Layer . . . 155
  7.3.4 Landfill with Inhomogeneous Density Distribution . . . 161
7.4 Discussion and Outlook . . . 165

8 Summary 171

Notations

Mathematical Symbols

d	differential
∂	partial derivative
$(\;)\cdot(\;)$	inner product
	$\mathbf{A}\cdot\mathbf{B} = \mathbf{A}_{ij}\mathbf{B}_{kl}\mathbf{g}_i \otimes \mathbf{g}_j \cdot \mathbf{g}_k \otimes \mathbf{g}_l = \mathbf{A}_{ij}\mathbf{B}_{kl}\mathbf{g}_j \cdot \mathbf{g}_k \mathbf{g}_i \otimes \mathbf{g}_l$
$(\;):(\;)$	inner product
	$\mathbf{A}:\mathbf{B} = \mathbf{A}_{ij}\mathbf{B}_{kl}\mathbf{g}_i \otimes \mathbf{g}_j \cdot \mathbf{g}_k \otimes \mathbf{g}_l = \mathbf{A}_{ij}\mathbf{B}_{kl}\mathbf{g}_i \cdot \mathbf{g}_k \mathbf{g}_j \cdot \mathbf{g}_l$
$(\;)\otimes(\;)$	dyadic product
δ	prefix for virtual quantities
$(\;)^T$	transposed tensor of 2^{nd} order
$(\;)^{-1}$	inverse of second order tensor
$(\;)^{-T}$	transposed, inverse second order tensor
$(\;)^{T_{ij}}$	transposition for tensor $\mathbf{A}$ with basis $\mathbf{g}$, where $\mathbf{A}$ is of more than 2^{nd} order
	$(\mathbf{g_1} \otimes \mathbf{g_2} \otimes \mathbf{g_3} \otimes \mathbf{g_4})^{T_{13}} = (\mathbf{g_3} \otimes \mathbf{g_2} \otimes \mathbf{g_1} \otimes \mathbf{g_4})$
$\dot{(\;)}$	material time derivative
grad ( )	gradient operator w.r.t. current configuration
Grad ( )	gradient operator w.r.t. reference configuration
div( )	divergence operator, w.r.t. current configuration
tr( )	trace of a second order tensor
log	decadic logarithm

Scalar quantities

Latin letters

a, A	surface area
a_M	parameter in description of vapour pressure
a_v	volumetric strain
$a_{v,in}$	inelastic, volumetric strain
A_{cr}	parameter creep model
A_S	parameter for temperature dependency of gas viscosity
b_M	parameter in description of vapour pressure
c'	effective cohesion
c_M	parameter in description of vapour pressure
c_p	heat capacity
C_S	parameter for temperature dependency of gas viscosity
D'	diffusion coefficient
D	effective diffusion coefficient
e	volume-specific energy
g	gravitational constant

H	mean radius of meniscus curvature $H = \frac{1}{2}\left(\frac{1}{r_1} + \frac{1}{r_2}\right)$
I_1	1^{st} invariant of a second order tensor $\mathbf{A}$ $I_{1,\mathbf{A}} = \text{tr } \mathbf{A}$
I_2	2^{nd} invariant of a second order tensor $\mathbf{A}$ $I_{2,\mathbf{A}} = \frac{1}{2}(\mathbf{A}^T : \mathbf{A} - \text{tr}(\mathbf{A})^2)$
I_3	3^{rd} invariant of a second order tensor $\mathbf{A}$ $I_{3,\mathbf{A}} = \det \mathbf{A}$
$J_{2,D}$	2^{nd} invariant of deviator
$J_{3,D}$	3^{rd} invariant of deviator
k_H	Henry constant
$k_{\pi,f}$	hydraulic conductivity of phase π
$k_{\pi,rel}$	relative permeability of phase π
K	permeability
m	molar fraction
M	molar mass
m_{VG}	parameter of van Genuchten SWCC representation
n_M	mol number
n^α	volume fraction of constituent α
n_{cr}	parameter in creep model
$n_{l,res}$	residual volumetric moisture content
n_{VG}	parameter of van Genuchten SWCC representation
p_{atm}	atmospheric pressure
p_c	capillary pressure
p_{cr}	parameter in creep model
p_{bub}	bubbling pressure, air entry pressure
p_π	pressure of fluid phase π
p_{sat}	saturated vapour pressure
p_{vap}	vapour pressure
R	universal gas constant
S_e	effective saturation
S_π	saturation of phase π
$S_{\pi,res}$	residual saturation of phase π
t	time
v, V	volume
w_π^β	mass fraction of component β in phase π
Y	yield coefficient
$\tilde{Y}$	modified yield coefficient

Greek letters

α_P	parameter in effective stress formulation for weighting of pore pressure
α_{VG}	parameter of van Genuchten SWCC representation
χ	parameter in effective stress formulation
ΔH_f^0	reaction enthalpy
ΔH_s	dissolution enthalpy
ΔH_{vap}	evaporation enthalpy
$\dot{\gamma}_{pl}$	plastic multiplier
$\dot{\gamma}_{cr}$	multiplier creep model
η_π	dynamic viscosity of phase π
η_λ	parameter for effective heat conductivity
κ_ϕ	parameter in relation for compaction dependence of permeability
λ_{BC}	parameter of Brooks and Corey SWCC representation
λ_{eff}	effective heat conductivity
λ_L	lower Wiener bound (of macroscopic heat conductivity)
λ_π	mobility of phase π
λ_U	upper Wiener bound (of macroscopic heat conductivity)
ν	kinematic viscosity
ν_P	Poisson's ratio
$\nu_{S,0}$	kinematic viscosity of gas phase at reference temperature $\Theta_{S,0}$
ϕ	porosity
ϕ'	effective angle of internal friction
ψ	angle of dilatancy
$\tilde{\rho}^\alpha$	intrinsic, real density of constituent α
ρ^α	partial density of constituent α w.r.t. current configuration
ρ^α_{ref}	partial density of constituent α w.r.t. reference configuration
$\tilde{\rho}_\pi$	intrinsic, real density of phase π
ρ_π	partial density of phase π
σ_w	surface tension of water
τ	tortuosity
Θ	temperature
$\Theta_{S,0}$	reference temperature in description of gas viscosity

Vector quantities

$\mathbf{n}$	normal vector
$\mathbf{x}$	spatial coordinates
$\mathbf{X}$	material coordinates
$\mathbf{u}$	displacement
$\mathbf{v}$	velocity
$\mathbf{v}_{\pi D}$	Darcy velocity of fluid phase π
$\mathbf{v}_{\pi s}$	relative velocity between phase π and solid
$\mathbf{v}_{\pi}^{\beta}$	diffusive velocity
$\mathbf{g}$	gravitation
$\mathbf{t}$	surface traction

Tensors of second order

$\mathbf{A}$	Almansi strain tensor
$\mathbf{b}$	left Cauchy-Green tensor
$\mathbf{C}$	right Cauchy-Green tensor
$\mathbf{D}$	strain rate tensor
$\mathbf{E}$	Green strain tensor
$\mathbf{F}$	deformation gradient
$\mathbf{H}$	displacement gradient
$\mathbf{K}$	permeability tensor
$\mathbf{L}$	spatial velocity gradient
$\mathbf{P}$	1^{st} Piola-Kirchhoff stress tensor
$\mathbf{R}$	rotational tensor
$\mathbf{S}$	2^{nd} Piola-Kirchhoff stress tensor
$\mathbf{T}$	Cauchy stress tensor
$\overset{\vee}{\mathbf{T}}{}^{\alpha}$	Partial stress tensor with respect to total cross section of a mixture
$\tilde{\mathbf{T}}$	Kirchhoff stress tensor

Tensors of fourth order

$\mathbb{C}$	Elasticity tensor
$\mathbb{S}$	Flexibility tensor

Matrices

$\mathbf{K}_T$	tangent (stiffness) matrix
$\mathbf{K}_{uu}$	submatrix of tangent (stiffness) matrix
$\mathbf{r}$	residual vector

Subscripts and Superscripts

Latin letters

(aq)	aqueous solution
B	basic matrix
cr	creep
DO	degradable organic matter
el	elastic
F	fibres
g	gaseous phase
(g)	gaseous aggregate state
i	current state
IM	inert matter
in	inelastic
l	liquid phase
(l)	liquid aggregate state
pl	spontaneous-plastic
ref	reference configuration
s	solid phase
X	biomass (herein equiv. to bacteria genera)

Greek letters

α	constituent, with $\alpha \in \{s, l, g, \mathrm{CO_2}, \mathrm{CH_4}, \mathrm{H_2O}, Ac, F, B, IM, DO, X\}$
β	component (of a phase), with $\beta \in \{\mathrm{CO_2}, \mathrm{CH_4}, \mathrm{H_2O}, Ac, F, B, IM, DO, X\}$
π	phase, with $\pi \in \{s, l, g\}$

Substances, chemical species

Ac	acetic acid
B	basic matrix
DO	degradable organic matter
$C_5H_7NO_2$	biomass
$C_6H_{12}O_6$	glucose
$C_{30}H_{53.4}O_{14}N_{0.7}$	organic matter
CH_3COOH	acetic acid
CH_4	methane
CO_2	carbon dioxide
F	fibres
H_2	hydrogen
H_2O	water
IM	inert matter
NH_3	ammonia
VFA	volatile fatty acids
X	biomass

Abbreviations and Acronyms

ALERT	Alliance of Laboratories in Europe for Research and Technology (ALERT) "Geomaterials"
AWG	AbfallWirtschaftsGesellschaft mbH (engl. Waste Management Corporation; Waste mangement authority of the administrative district Diepholz, Germany)
BGBl.	Bundesgesetzblatt (engl. Federal Law Gazette)
BMP	Biochemical Methane Potential
BTC	Breakthrough Curve, of a tracer experiment
CAR	Consolidating anaerobic reactor
CDM	Clean Development Mechanism
CT	Computer tomograph
DFG	Deutsche Forschungsgemeinschaft (engl. German Research Foundation)
GTZ	Deutsche Gesellschaft für Technische Zusammenarbeit mbH (engl. German Technical Cooperation)
IPCC	Intergovernmental Panel on Climate Change
IWWG	International Waste Working Group
LMTG	Landfill Modelling Task Group (of IWWG)
MSW	Municipal Solid Waste
NIST	National Institute of Standards and Technology
SFB	Sonderforschungsbereich, (engl. Collaborative Research Center)
SWCC	Soil Water Characteristic Curve
UBA	Umweltbundesamt, (engl. The Federal Environment Agency; Germany)
UNFCCC	United Nations Framework Convention on Climate Change
US EPA	Unites States Environmental Protection Agency

Further variables and abbreviations are defined throughout the text at first appearance.

1 Introduction

1.1 Background

Initiation of modern sanitary landfilling in Germany can be considered to go back to the 1950s when the economic miracle (Wirtschaftswunder) is under way. Waste amounts heavily increase at that time and, thus, a more systematically organised waste collection system is established. Joint waste management authorities are founded and the former disposal sites, mainly open, community-based dumps, are replaced by the first sanitary landfills in the late 1960s/early 1970s, e.g. AWG [7]. Currently, an opposite trend is observable. One aim of German resource management policy is to stop landfilling of municipal solid waste (MSW) totally until the year 2020. Disposal quota of MSW drops already from almost 40 % in 1997 to less than 1 % in 2006, UBA [230], which is partly the consequence of an obligation to pre-treatment since June 2005. Also, other countries undertake efforts to increase pre-treatment. Sustainable waste mangement policy according to Agenda 21 places waste minimisation ahead of recycling and treatment or disposal. The idea of urban mining comes up in order to utilise the resource potential of landfills. Thus, it is sometimes argued, that in a short term, there is no more object of application for landfill models. Furthermore, it is often regarded impossible to develop a model for such heterogeneous and complex systems like MSW landfills. So, in response to the question whether there is still the need for research on landfill modelling it may be considered that, despite all efforts, landfilling remains a major way of waste treatment, especially in developing and industrialising countries. According to GTZ website [94], waste composition is becoming more and more complex and waste amounts are increasing. In its guidelines on waste management, GTZ [93] considers landfills to be an indispensable part of each waste management system. For foreseeable future, the disposal of a non-recycable waste fraction will be necessary. Especially in low-income countries, disposal is often the best available technology for waste treatment.

Furthermore, in the industrialised countries, the landfills that had been built previously are still present. By now, it remains unknown for how long those landfills have to be monitored as existing landfill sites are still in aftercare period, Heyer [105]. With respect to monitoring and structural health, landfill operators are especially interested in quantification of gaseous emissions and settlements, in the assessment of landfill body stability and in leachate volume and composition, as visualised in figure 1.1.

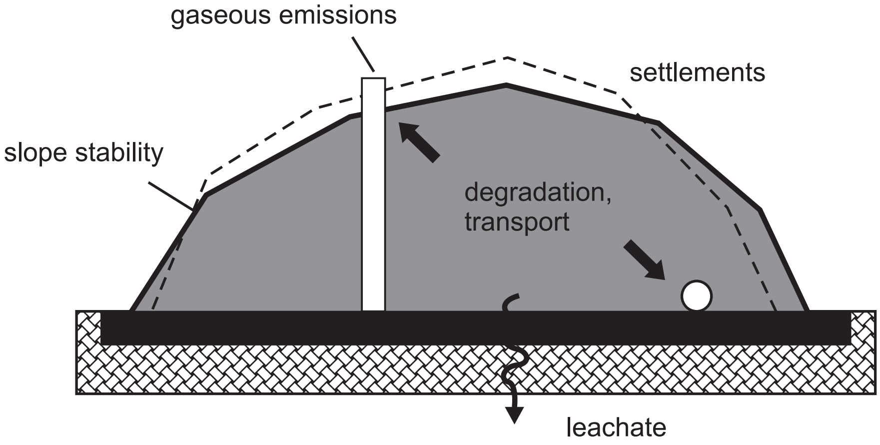

Figure 1.1: Major phenomena in landfills

The monitoring issue is addressed by the collaborative research centre *SFB 477 - Life Cycle Assessment of Structures via Innovative Monitoring* which starts at the Technische Universität Braunschweig in 1998. The aim is to develop new methods for structural health assessment. The damage potential of landfill structures is ranked high, and so landfill engineering becomes, besides classical structural engineering, one major branch of SFB 477. Within project B6 of SFB 477, models for long-term landfill behaviour are developed at the Institute of Structural Analysis in cooperation with the Institute of Biochemical Engineering and the Leichtweiß-Institute. Development starts with models for both time-dependent mechanical behaviour and reactive transport processes. Based on the findings from modelling single and less coupled phenomena, a fully coupled model is developed which is the topic of this thesis.

1.2 Motivation and Objective

As discussed above, municipal solid waste (MSW) landfills are civil engineering structures requiring appropriate methods for design and monitoring. According to recent regulations, cf. the new German landfill act (Verordnung zur Vereinfachung des Deponierechts, 27. April 2009, BGBl. 2009 I, S. 900, operative since 16th July 2009), the required detailedness of measurements and data acquisition is increased, including also a waste cadastre. To accompany the regulatory demand by simulations, methods have to be applied which can process spatially varying information. In that sense, waste heterogeneity is not necessarily an obstacle to modelling, but clearly promotes development of models that allow for consideration of spatially distributed data.
The transient behaviour of landfills is very complex as major phenomena may be coupled in different ways. As shown in figure 1.2, the observable phenomena can be split up into three major parts: mechanical, hydraulical and biochemical processes. If they influence each other directly or indirectly, models for single phenomena might give inaccurate prognoses. In a landfill, organic matter is usually decomposed under anaerobic conditions.

Landfill gas, which contains mainly methane and carbon dioxide, is generated. Reaction rates are influenced by environmental conditions like water content, temperature and pH. If deformation changes the hydraulic properties, reactions are affected indirectly by transport processes. If solid matter is degraded, the material becomes more loose which increases its compressibility. Thus, long-term settlements might occur due to biological decomposition as shown in laboratory tests and site measurements, see section 5.1.3. Furthermore, slope stability might be influenced by infiltrating liquid or degradation-induced change of the waste's structure. The proposed coupled model covers the major phenomena depicted in figure 1.2 including main interactions. Thereby, the governing equations are coupled strongly by a simultaneous solution procedure within a joint mechanical framework. Compared to a partitioned strategy, simultaneous solution may exhibit better convergence properties in case of strong interactions. The developed model serves, together with information on landfill site data, as a basis for recommendations on monitoring of landfills.

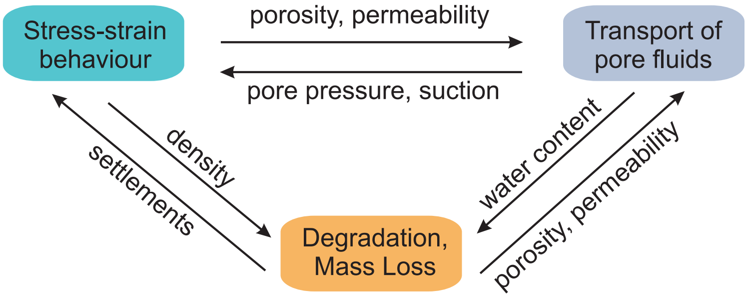

Figure 1.2: Interactions of major coupled phenomena in landfills

The complexity of the processes is not necessarily an obstacle to modelling but in turn it may be regarded as an argument *for* modelling. The process of model development helps identifying lacks in knowledge and experimental evidence. Modelling may define experimental demand and helps to improve and optimise experimental design. Although models will not replace experiments totally, models which are calibrated against experiments can assist in planning of experimental routes. Considering that some experiments, like oedometric tests or tensile tests, can be very time consuming, effective experimental planning is of high importance.

Many of the existing models are based on a partitioned solution of the coupled problem. Often empirical functions are used to consider aspects of coupling. For instance, hydraulic conductivity is sometimes related to landfill depths. If the model does not include the evolution of density due to overburden pressure, changes in compaction and conductivity cannot be directly considered. If settlements are related to a constant degradation rate of biological matter, a change in environmental conditions has to be taken into account. Thus, it is the objective of this thesis to develop a coupled model whithin a unified continuum mechanical framework with the application of a simultaneous solution procedure.

1.3 State of the Art

The development of mathematical models for landfill behaviour starts in the 1970s with more or less empirical models for single processes. Areas of interest are especially the gas production of landfills, surface settlements and water balance. More advanced models concentrate both on a refinement of the description of single processes itself, for example a more detailed reaction scheme, and on coupling of different processes that are considered isolated before. Models for single phenomena may be classified according to the three major phenomena into models for

1) the mechanical behaviour,
2) transport processes of different fluid phases,
3) and biodegradation.

Models for single processes are explained in conjunction with description of constitutive modelling, i.e. in chapters 3, 4 and 5. The term *coupled model* refers to models that couple at least two of the major processes as itemised above.

Models for multifield and multiphysics problems are of high importance for description of various materials, like soil, living tissue, concrete or metal foams. Many approaches from those fields can be adopted for landfill modelling, whereas the focus is ususally laid on geomaterials because of their similarities to MSW. Coupled processes in geomaterials are described, for example, in the fields of reservoir engineering, site remediation, assessment of radioactive waste repositories or geotechnical engineering for unsaturated soils. The increasing interest on thermal and chemical effects gives rise to development of so-called THMC models that describe coupled thermal, hydraulical, mechanical and chemical processes. The latter is addressed by the project DECOVALEX, an international joint research center on the DEvelopment of COupled models and their VALidation against EXperiments in nuclear waste isolation. The research group focuses on development of models for geotechnical and geological barriers and fractured rocks, Birkholzer et al. [23]. For recent developments in unsaturated soil mechanics, the reader may be referred to the publications by the members of the research group *Mechanics of Unsaturated Soils*, Schanz [208], or on the publications of the network ALERT Geomaterials, e.g. Laloui et al. [137], and references herein.

Whereas most models are based on a macroscopic description within the *Theory of Porous Media* or the *Theory of Mixtures*, e.g. the models by Collin et al. [41], Ricken and de Boer [198], Ehlers et al. [61], Graf [91], Schrefler [211], Francois and Laloui [81], Chen et al. [39] or Francois et al. [82], there are also approaches on microscopic level. As such, Papafotiou et al. [191] simulate the drainage of heterogeneous porous media by the Lattice-Boltzmann method. The results are validated against a drainage experiment using X-rays of the used sand to enable a discrete modelling of the pore space. Similarly, Narsilio et al. [181] utilise CT scans for comparing Darcy flow with the solution obtained from solving the Navier-

Stokes equations. In general, such approaches are also conceivable for waste, CT scans of waste samples are presented by Watson et al. [240]. In practice, however, the exact pore structure is not known.

When reviewing coupled models for waste, certain main interactions of interest can be identified, the

- coupling of flow processes with degradation,
- coupling of deformation and degradation,
- and coupling of all three major processes, i.e. deformation, transport and degradation

Considerably less models exist which cover coupling of deformation and transport only. The following paragraphs review some of the coupled models developed for an application on municipal solid waste.

Models for Reactive Transport One of the first publications on coupling of transport and degradation is published by Straub and Lynch [221]. Both aerobic and anaerobic processes are described using Monod kinetics. Moisture movement is assumed to follow Darcy's law, whereas the gas phase remains passive. The solubilisation of gaseous components is considered by means of Henry's law. Similarly, Demetracopoulos et al. [49] describe both moisture movement and leachate production including organic contaminant concentrations. El-Fadel et al. [65] couple degradation with convective gas transport according to Darcy and diffusive gas flow. Also, seven carbon sources are considered in their degradation model. Several models for reactive gas transport in waste are reviewed by El-Fadel et al. [68]. Oldenburg [187] and Oldenburg et al. [186] consider coupled reactions and transport in the model TOUGH2. Compaction is described by a simple uncoupled model. Heat generation, due to both aerobic and anaerobic processes, is described, whereas again Monod kinetics are used for determination of degradation rates considering temperature dependency. The pH is estimated using charge balances, but its influence on reactions is neglected.

Islam and Singhal [117] present a model for one-dimensional reactive transport of leachate containing different components. They consider the interactions between microbial redox reactions and inorganic geochemical reactions. Change of porosity and permeability due to biomass growth and minerals are described. A bioclogging module for existing multiphase flow codes is presented by Brovelli et al. [32]. Clogging is also the driving force for development of the model BioClog by Cooke et al. [42], in which clogging, driven by microbial growth, is coupled with solute transport. Detachment of biofilm due to shear stress and adsorption of suspended particles is described as well. The porosity is directly determined from the biofilm thickness and a model for grain package. Recently, Gholamifard et al. [90] present a model for anaerobic degradation in landfills coupled with multiphase flow based on Darcy's law. The degradation model consists of a hydrolysis step and a gas

generation step, whereas generation of heat is considered. The model is validated against measurements in a pilot bioreactor landfill.
Within SFB 477, a model for coupled degradation and transport is developed by Hanel [99] which includes a comparison of a detailed and a reduced two stage reaction scheme. Based on Hanel's work, growth of biofilm and its influence on porosity and permeability is investigated by Kindlein et al. [125].

Coupling Mechanical Behaviour and Degradation Several attempts are made to analyse the influence of degradation, especially on settlements. A basic approach is to assume that secondary settlement follows the kinetics of biological degradation. Thus, formulations for the secondary settlement are often derived from first order kinetics, as for example in the models by Park and Lee [193], Oweis [190] or Hettiarachchi et al. [104]. The coupling of settlement and degradation, thus, starts with implementing simple degradation models into empirical settlement models or vice versa. Another widely used assumption is that secondary settlement is linear with respect to logarithm of time, e.g. in the approach by Wall and Zeiss [237] who investigate the relation of degradation and settlement in lysimeters. Secondary compression may then be defined by a secondary compression ratio. For a recent overview on settlement models with special focus on degradation induced settlements the reader may be referred to Elagroudy et al. [70]. Machado et al. [152] adopt an idea by McDougall [157] and use a void change parameter to model secondary compression. Mass loss is described by a first order decay model. A novel aspect is to take into account the influence of changes in the fibrous fraction on the mechanical strength properties of municipal solid waste.

Interaction of Transport and Deformation Bleiker et al. [26] adopt the Gibson-Lo model to evaluate settlements and consider that a refuse column is made up of a series of layers by which they include landfill construction history into their calculations. Strain, which is dependent on depth, is used to update densities and to consider changes in hydraulic conductivity. Demirekler et al. [50] present a model of water balance type with consideration of the time dependent construction of a landfill. Each cell is divided into layers, whereas each layer represents a single-mixed reactor. Vertical stresses, which depend on the density of waste mass, influence the saturated hydraulic conductivity. Koerner and Soong [131] describe scenarios of leachate distribution in landfills and analyse their effect on landfill stability by means of a two dimensional modified Bishop method. A basic coupling between deformation and transport is presented by De Velásquez et al. [48] who implement the variation of field capacity with depth in a water balance model. Within SFB 477, the coupling of transport and deformation is included by Bente et al. [21] and Krase [135].

Coupling Mechanical Behaviour, Transport and Degradation One of the earliest, very comprehensive coupled model, is presented by Young and Davies [246]. Their work is based on the conviction that single processes should not be considered isolated from each other because of significant interactions. The developed model describes moisture and gas transport, heat flow and extraction of gas by means of a system of wells. The transfer between gas and liquid phase is described using Henry's law. In the degradation module, eight basic reactions are considered. The influence of pH and temperature on degradation rates is described. Three-dimensional analyses are conducted using the Finite-Element method. The model is validated against measurements on-site and recommendations on monitoring are given. In addition, a one-dimensional double-porosity model is tested, whereas the authors conclude that, at least for applications on capped landfills, a single-porosity model can sufficiently describe water movement.

In general, increasing interest of researchers on coupled phenomena in waste and their modelling is observable. This is, for example, proven by the response to a modelling challenge organised by the University of Southampton, Beaven [14]. MODUELO is a three-dimensional model developed at the University of Cantabria. The first version consists of a hydrological module, see Garcia de Cortazar et al. [86], and a model for degradation, Garcia de Cortazar et al. [87]. The model is able to reproduce the filling history of a landfill site. Besides moisture storage and transport, the water balance of each cell includes precipitation, surface runoff and evaporation. Horizontal and vertical moisture flow are modelled separately and are based on Darcy's law. It is supposed that anaerobic degradation of organic matter can be described by two steps, hydrolysis and gasification. For both steps, first order kinetics are applied. The model is calibrated using data on leachate characteristics from a Spanish landfill. Later, MODUELO is modified and extended by Garcia de Cortazar and Monzon [85] and published under the name MODUELO2. The extended version includes a relation of hydraulic conductivity to landfill depth. The methods for taking into account evapotranspiration and surface runoff are modified and waste components can be described in a more detailed manner. Reaction processes and stoichometry are extended to a scheme of three stages and seven processes. The influence of moisture content on hydrolysis rate is considered. A settlement model, which accounts for the influence of degradation, is included and is considered as being a part of future MODUELO3, see Lobo et al. [145].

Hashemi et al. [100] present a three-dimensional model for gas generation and transport of four components, CH_4, CO_2, N_2 and O_2, whereas they assume steady state conditions. Convective and diffusive flow of gas is described. The model accounts for different horizontal and vertical permeabilities. Degradation of three types of waste, readily, moderately and least degradable, is described by means of Monod kinetics, in which a constant biomass concentration is assumed. The balance equation for gas flow is discretised by means of a Finite-Volumes scheme. For solving the nonlinearities, a conjugate gradient method is used. Several parameter settings and boundary conditions are investigated within an application of the model on a landfill site. The model is extended to transient conditions by Sanchez et al. [206]. Furthermore, the effect of mechanical dispersion is analysed. In a subsequent paper, Sanchez et al. [207], genetic algoritms are used to find optimal parameters for gas production.

A two-dimensional model is presented by White et al. [243] that is later known under the acronym LDAT. The stoichiometry follows the model by Young and Davies, whereas Monod kinetics are used. The growth rate of methanogenic biomass is limited dependent on pH. An empirical dependency of dry density and permeability on effective stress is implemented. The effective stress is evaluated based on total stress and pore pressure. Transport of liquid and gas is considered, whereas it is assumed that gas is at atmospheric pressure due to instantaneous ventilation; capillary effects are not described. Extensions of the model are published by White et al. [242]. The modified version considers three dimensions and the evaluation of pH by an ion balance. Additional pathways are added to describe aeration including aerobic degradation, Nayagum et al. [182]. Settlements are linked to degradation by solid mass loss.

Liu et al. [144] apply unsaturated consolidation theory in one dimension. They assume that no excess pore pressures are generated within the landfill. They formulate a differential equation for the gas pressure and provide an analytical solution. The change of gas volume is related to volumetric strain. Model simulations are compared within two field cases. They note that two- or three-dimensional models are necessary and that there is a need for more geotechnical data.

The model HBM presented by McDougall and Hay [158] and McDougall [157] couples hydraulical processes, degradation and mechanical behaviour within a staggered solution procedure. The Cam clay model is used to describe plastic deformations. To investigate how solid mass loss caused by biodegradation is transferred into settlements, a void change parameter is introduced. It describes the loosening or densification during degradation and the influence on combined isotropic and kinematic hardening. Another essential part of the model is the consideration of a landfill's construction history.

Machado et al. [152] pick up the work by McDougall and consider the effect of degradation on settlements in a similar manner by applying a void change parameter. The parameter α is assumed to be proportional to degraded solid waste mass, which is described by a first order decay model. Influence of degradation on deviatoric stresses of the fibres is modelled as well. Furthermore, the effect of mass loss on the volume fractions of fibres and paste as well as the effect of degradation on maximum deviatoric stress and Young's modulus is described. Machado et al. use data from triaxial tests for model validation.

One of the first approaches on coupling the major phenomena in a strong, simultaneous procedure is presented by Ricken and Ustohalova [199] and Ustohalova et al. [233]. A modified version of the model is later published under the name DepSim. The tri-phase model is developed within the Theory of Porous Media, whereas its thermodynamic consistency is proven by fulfilling the entropy inequality. Applications of the model are presented by Ustohalova [232] and Ricken et al. [200].

Durmusoglu et al. [55] present a multiphase model which couples gas production with liquid and gas flow according to Darcys law considering capillary effects. Time-dependent deformation is modelled using Maxwell's rheology. A Bishop-type effective stress is used. To the author's knowledge, this is, besides the model developed in the SFB 477, the only model which includes an effective stress concept for unsaturated conditions. The balance equations are solved by means of the Finite-Element Method for one dimension. The model is applied on a hypothetical landfill, whereas results for deformable and rigid solid skeleton are compared. The authors conclude that coupling of gas generation and deformation is important for obtaining realistic simulation results. Later, settlements for unsaturated and saturated conditions are compared by Durmusoglu et al. [56].

Yu et al. [247] develop a model for analysing the gas flow to a gas extraction well in a deformable landfill. Mechanical behaviour is described by a series connection of a Hooke and a Kelvin element. The rheological element enables description of primary and secondary settlements. The authors consider the waste to have a mean moisture content of 55 % dry mass and conclude that the effect of suction on compression is negligible in that range referring to the data by Kazimoglu [122]. The constitutive law for compression is coupled with the gas balance. They assume isothermal conditions, constant porosity and saturation. Also, degradation rates and gas conductivity of the waste are assumed to be constant. They compare numerical results with an analytical solution and with field measurements of gas flux and settlement. Recommendations according to the design of the gas extraction system are given based on parameter studies according to the effect of operational vacuum, anisotropy of permeability and cover properties.

Berger and Krause [22] present a model for self-ignition of disposals which covers self-heating, ignition and fire propagation. The model is implemented into the multiphysics software COMSOL.

1.4 Outline of the Thesis

The model developed within SFB 477 is extended to a full coupling of mechanical, hydraulical and biological processes based on the work by Hanel [99], Kindlein et al. [125], Ebers-Ernst [58] and Krase [135]. An important aspect is to describe the interaction of degradation and mechanics by a density-dependent creep model and the description of deformation-dependent hydraulic parameters.

The explanation of the developed model starts with an introduction into the continuum mechanical framework in chapter 2, in which also the methods for discretisation in space and time are discussed. The next three chapters describe the phenomenological behaviour of waste and its constitutive modelling starting with the local degradation model in chapter 3. The aspects of moisture storage and movement in waste are discussed in chapter 4. The third major part of the constitutive model is the mechanical behaviour described in chapter 5. An essential part is the development of a novel creep model to cover degradation induced settlements. Based on the constitutive approach, the balance equations, which are derived in a general form in chapter 2, are formulated in detail in chapter 6. The iterative solution procedure is explained as well. In chapter 7, laboratory tests are used for validation of the model. The simulations are supplemented by analyses of a landfill structure. Based on the experiences gained in literature review, development and application, some aspects of landfill modelling are critically discussed. The chapter closes with recommendations on monitoring and an outlook on possible model extensions.

2 Continuum Mechanical Fundamentals

The proposed model treats municipal solid waste as a continuum within the *Theory of Porous Media*. Finite strains are considered in the description of deformation and stresses. The chapter closes with a derivation of general balance equations for a triphasic model. Thereby, a Lagrangian description of the solid skeleton is combined with an Arbitrary Lagrangian-Eulerian description of the fluid phases and their components. For an overview of the Theory of Mixtures the reader is referred to Bowen [30], recent developments in the Theory of Porous Media are for example explained by de Boer [47].

2.1 Theory of Porous Media

As already indicated in chapter 1, municipal solid waste is a porous material consisting of a solid skeleton and a pore space. The microscopic view in figure 2.1 visualises that the solid phase consists of several components. According to the shape of the solid particles, granular, soil-like particles can be distinguished from elongate, fibrous particles. Furthermore, the solid matter may be divided with respect to biological degradability, so that inert matter, organic matter and biomass are distinguished. In general, two fluid phases, leachate and landfill gas, fill the pore space. Both fluid phases are formed by several chemical substances, whereas the composition changes due to ongoing degradation and physical exchange processes.

The objective of avoiding a discrete description of all constituents requires a method which enables a virtual homogenisation of the material. Municipal solid waste then can be described adopting the continuum mechanical framework for single constituent materials. In this thesis, the *Theory of Porous Media* is applied. It is based on the *Theory of Mixtures* whereas the portions of the mixture's constituents are restricted by the *Concept of Volume Fractions*. The constituents are homogenised over a control volume, which is termed *Representative Elementary Volume*, REV. The size of the REV depends on the spatial variation of properties or the waste's composition. Uguccioni and Zeiss [231] recommend averaging of flow parameters over the area of one to ten m^2 with respect to waste. The REV determines the scale of uniform properties and does in general not coincide with any numerical discretisation. At a spatial point $\mathbf{x}$, all constituents exist simultaneously with their volume fraction. This approach is also termed *superimposed continua*. A prerequisite is that the homogenisation process is possible and valid for description of the selected phenomena.

The constituents α of the waste mixture are divided both into *components* β and *phases* π.

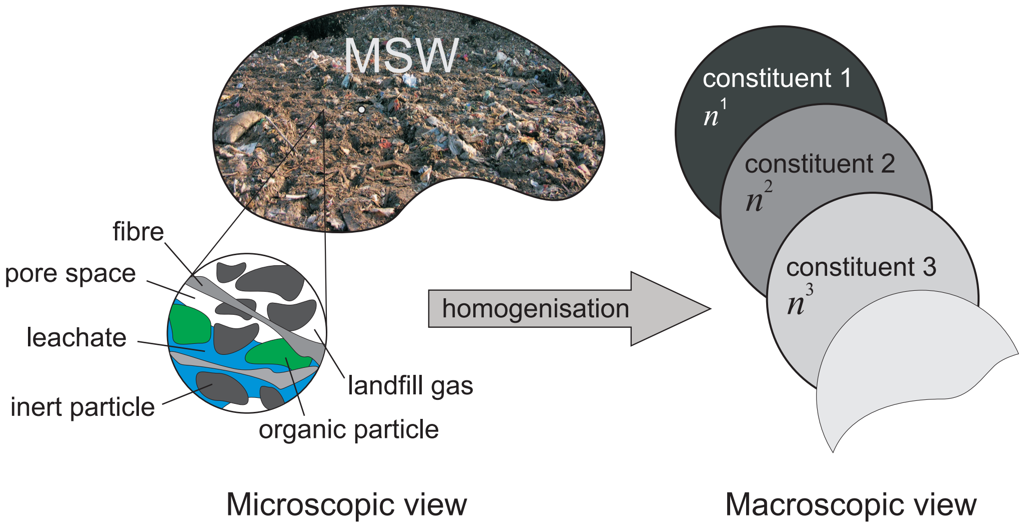

Figure 2.1: Microscopic view and homogenisation

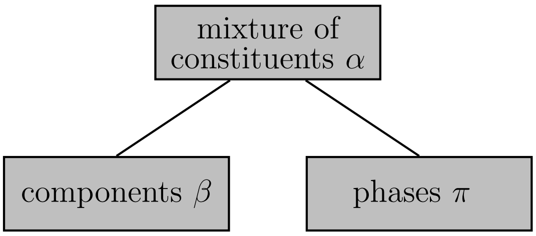

Figure 2.2: Breakdown of mixture into constituents, phases and components

The term phase is related to the aggregate state, components are the substances which form the phases. The components themselves thus belong to distinct phases whereas also phase changes are possible.

Due to the homogenisation, the exact discrete distribution of all constituents may remain unknown, each of them is considered only by its volume fraction n^α, see figure 2.1, macroscopic view.

As indicated, the developed model considers three phases: one solid (s) and two fluid phases, namely liquid (l) and gas (g). The components of each phase are defined by the detailedness of the constitutive model and are discussed in chapters 3 to 5. Each constituent α, each phase π and each component β occupy a certain volume dv^α, dv^π and dv^β. The particular volume fractions n^α, n^π and n^β are defined by

$$n^\alpha = \frac{dv^\alpha}{dv} \ , \ n^\beta = \frac{dv^\beta}{dv} \text{ and } n^\pi = \frac{dv^\pi}{dv} \ . \tag{2.1}$$

The saturation constraint demands that the sum of all volume fractions is equal to unity

$$\sum_\alpha n^\alpha = 1 \text{ and } \sum_\beta n^\beta = 1 \text{ and } \sum_\pi n^\pi = 1 \ . \tag{2.2}$$

The sum of the volume fractions of the fluid phases is related to the porosity ϕ which is the fraction of the pore volume dv^p and defined by

$$\phi = \frac{dv^l + dv^g}{dv} = \frac{dv^p}{dv} = n^l + n^g = 1 - n^s \ . \tag{2.3}$$

The volume fractions of the fluid phases are often expressed in terms of the saturation, which is described by

$$S^l = \frac{dv^l}{dv^p} = \frac{n^l}{n^p} \text{ and } S^g = \frac{dv^g}{dv^p} = \frac{n^g}{n^p} \ , \text{ whereas } S^l + S^g = 1 \ . \tag{2.4}$$

For $S_l = 1$ the porous medium is fully saturated, for $S_l = 0$ the material is dry. Intermediate states are called *unsaturated* or *partially saturated*. If the constituents are immiscible, they occupy their own partial volume and different densities can be defined. The *intrinsic density* or *real density* $\tilde{\rho}^\alpha$ relates the mass of a constituent α to the volume occupied by the constituent. The *partial density* ρ^α relates the mass to the total volume, whereas both density measures can be transformed into each other by the volume fraction

$$\tilde{\rho}^\alpha = \frac{m^\alpha}{dv^\alpha} \text{ and } \rho^\alpha = \frac{m^\alpha}{dv} \ , \text{ whith } \rho^\alpha = n^\alpha \tilde{\rho}^\alpha \ . \tag{2.5}$$

The partial density corresponds to the *bulk density*. If the constituent α is incompressible, the intrinsic density is constant, whereas the partial density may still change due to a change in volume fraction. Like for the volume fractions, the partial densities of all constitutents add up to 1.

2.2 Fundamentals of large strain continuum mechanics

Municipal solid waste is, in general, exposed to large deformations. This requires to develop the model within continuum mechanics for finite deformations including large strains. The present section briefly explains important quantities of this theory. For more detailed information on large strain continuum mechanics as well as proofs of the relations used herein the reader is referred to Haupt [101], Bonet and Wood [29], Holzapfel [107] or Parisch [192]. Subscripts are used if kinematic quantities are described, other quantities are identified by superscripts.

2.2.1 Description of motion

In the most general case, each of the constituents may follow its own motion χ_α, as shown in figure 2.3, left. For the description of motion, *material* points $\mathbf{X}_\alpha$, which refer to a material particle, and points defined by *spatial* coordinates $\mathbf{x}$ are distinguished. The motion of the continuum may, on the one hand, be described by a mapping of a material

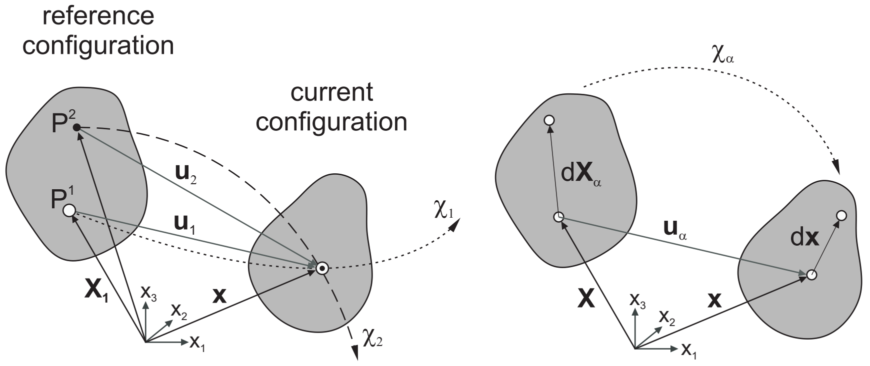

Figure 2.3: Motion functions and configurations (left) and change of a vector described by the deformation gradient (right)

point, identified by $\mathbf{X}_\alpha$, to a spatial point $\mathbf{x}$

$$\mathbf{x} = \chi_\alpha(\mathbf{X}_\alpha, t) \ , \tag{2.6}$$

which is known as *material* or *Lagrangian* description of motion. In other words, an observer is fixed to a material particle and moves with this particle. On the other hand, the mapping

$$\mathbf{X}_\alpha = \chi_\alpha^{-1}(\mathbf{x}, t) \tag{2.7}$$

identifies the material points which pass the spatial point $\mathbf{x}$ at time t by their position in the reference configuration $\mathbf{X}_\alpha$. Any observer is thus fixed to a particular point in space, which is known as *Eulerian* description. Correspondingly, physical quantities ψ of the form $\psi = \psi(\mathbf{X}_\alpha, t)$ are termed Lagrangian, and quantities of the form $\psi = \psi(\mathbf{x}, t)$ are termed Eulerian. It is also possible to consider a method in between those two cases. Such a method is the Arbitrary Lagrangian-Eulerian method, which is used to derive the balance equations for the fluid phases in section 2.3.3.

The displacement vector $\mathbf{u}_\alpha$ is defined by

$$\mathbf{u}_\alpha = \mathbf{x} - \mathbf{X}_\alpha \ . \tag{2.8}$$

The gradient of the displacement vector with respect to the reference configuration can be used to determine the *deformation gradient* $\mathbf{F}$. This quantity describes the change of the relative spatial position of two particles before and after deformation, i.e. in reference and current configuration. Independent motion functions result in independent velocity fields and deformation gradients. $\mathbf{F}_\alpha$ is defined by

$$\mathbf{F}_\alpha = \frac{\partial \mathbf{x}}{\partial \mathbf{X}_\alpha} = \mathbf{1} + \text{Grad}_{\,\alpha}\mathbf{u}_\alpha = \text{Grad}_{\,\alpha}\mathbf{x} \ . \tag{2.9}$$

The deformation gradient enables transformation of volume elements dV_α and surface elements dA_α between the configurations

$$dv = \det \mathbf{F}_\alpha dV_\alpha \;\text{ and }\; \mathbf{n}\, da = \det \mathbf{F}_\alpha (\mathbf{F}_\alpha)^{-T} \mathbf{N}\, dA_\alpha \;, \tag{2.10}$$

where $\mathbf{n}$ and $\mathbf{N}$ are normal vectors to the surface element in its material and spatial configuration respectively. The latter equation is known as Nanson's formula.
The velocity of phase π is given by the time derivative of the spatial position vector

$$\mathbf{v}_\pi = \frac{d\mathbf{x}}{dt} = \frac{d}{dt}\chi_\pi(\mathbf{X}_\pi, t) \;. \tag{2.11}$$

In general, the velocity of a component β may not coincide with the velocity of a phase π, for example for diffusive and dispersive transport processes. Then, relative velocities are defined by

$$\mathbf{v}_{\beta\pi} = \mathbf{v}_\beta - \mathbf{v}_\pi \;. \tag{2.12}$$

Lagrangian and Eulerian representations of a quantity lead to different time derivatives. The *material time derivative* of a material quantity ψ^β coincides with the local time derivative

$$\frac{d\psi^\beta}{dt} = \frac{\partial \psi^\beta}{\partial t} = \dot{\psi}^\beta \;, \tag{2.13}$$

whereas the time derivative of the corresponding spatial quantity for an observer moving with the π phase consists of the local variation plus a convective term, which accounts for the change in ψ^β due to motion in space with the velocity $\mathbf{v}_\pi$

$$\left.\frac{d\psi^\beta}{dt}\right|_\pi = \frac{\partial \psi^\beta}{\partial t} + \operatorname{grad} \psi^\beta \cdot \mathbf{v}_\pi \;. \tag{2.14}$$

2.2.2 Strain measures

The scalar products of two vectorial line elements $d\mathbf{x}$ and $d\mathbf{X}_\alpha$ are used to define the *right Cauchy-Green tensor* $\mathbf{C}_\alpha$

$$\mathbf{C}_\alpha = (\mathbf{F}_\alpha)^T \mathbf{F}_\alpha \;\text{ where }\; \mathrm{d}\mathbf{x}\, \mathrm{d}\mathbf{x} = \mathrm{d}\mathbf{X}_\alpha\, \mathbf{C}_\alpha\, \mathrm{d}\mathbf{X}_\alpha \;, \tag{2.15}$$

and the *left Cauchy-Green tensor* $\mathbf{b}_\alpha$

$$\mathbf{b}_\alpha = \mathbf{F}_\alpha (\mathbf{F}_\alpha)^T \;\text{ where }\; \mathrm{d}\mathbf{X}_\alpha\, \mathrm{d}\mathbf{X}_\alpha = \mathrm{d}\mathbf{x}\, (\mathbf{b}_\alpha)^{-1}\, \mathrm{d}\mathbf{x} \;, \tag{2.16}$$

which serve as measures of strain. The difference of the scalar products of the vectorial line elements is used to define the *Lagrangian* or *Green strain tensor* $\mathbf{E}_\alpha$

$$\mathbf{E}_\alpha = \frac{1}{2}(\mathbf{C}_\alpha - \mathbf{1}) \text{ such that } \frac{1}{2}(\mathrm{d}\mathbf{x}\,\mathrm{d}\mathbf{x} - \mathrm{d}\mathbf{X}_\alpha\,\mathrm{d}\mathbf{X}_\alpha) = \mathrm{d}\mathbf{X}_\alpha\,\mathbf{E}_\alpha\,\mathrm{d}\mathbf{X}_\alpha\,, \tag{2.17}$$

and the *Eulerian* or *Almansi strain tensor* $\mathbf{A}_\alpha$

$$\mathbf{A}_\alpha = \frac{1}{2}(\mathbf{1} - (\mathbf{b}_\alpha)^{-1}) \text{ such that } \frac{1}{2}(\mathrm{d}\mathbf{x}\,\mathrm{d}\mathbf{x} - \mathrm{d}\mathbf{X}_\alpha\,\mathrm{d}\mathbf{X}_\alpha) = \mathrm{d}\mathbf{x}\,\mathbf{A}_\alpha\,\mathrm{d}\mathbf{x}\,. \tag{2.18}$$

The well-known engineering strain is a special case of the large strain quantities and can be derived for small strains neglecting terms of higher order.

Constitutive modelling of time-dependent deformation requires definition of time derivatives of deformation and strain tensors. The *spatial velocity gradient* $\mathbf{L}_\alpha = \operatorname{grad}\mathbf{v}_\alpha$ describes the change in length and orientation of a vectorial line element $d\mathbf{x}$ with time

$$d\dot{\mathbf{x}} = \frac{\partial \mathbf{F}_\alpha}{\partial t}\cdot d\mathbf{X}_\alpha = \frac{\partial \mathbf{F}_\alpha}{\partial t}\cdot(\mathbf{F}_\alpha)^{-1}d\mathbf{x} = \mathbf{L}_\alpha\cdot d\mathbf{x}\,. \tag{2.19}$$

The tensor $\mathbf{L}_\alpha$ can be split up into the symmetric tensor $\mathbf{D}_\alpha$, which is the *spatial stretching tensor* describing the change in length, and the skew-symmetric tensor $\mathbf{W}_\alpha$, which describes the rotational change and is termed *vorticity tensor*. The spatial stretching tensor can also be expressed using the material time derivative of the Green strain tensor $\dot{\mathbf{E}}_\alpha$, with

$$\dot{\mathbf{E}}_\alpha = \frac{1}{2}((\dot{\mathbf{F}}_\alpha)^T\mathbf{F}_\alpha + (\mathbf{F}_\alpha)^T\dot{\mathbf{F}}_\alpha)\,, \tag{2.20}$$

so that

$$\mathbf{D}_\alpha = (\mathbf{F}_\alpha)^{-T}\cdot\dot{\mathbf{E}}_\alpha\cdot(\mathbf{F}_\alpha)^{-1}\,. \tag{2.21}$$

To describe the time-dependent deformation in a way which is not dependent on the relative motion of any observer, *objective* tensor quantities are required. Objective time derivatives of tensorial fields are obtained applying the *Lie time derivative*. For the Almansi strain tensor this is

$$\overset{\triangle}{\mathbf{A}}_\alpha = \mathbf{A}_\alpha\Big|_\alpha + \mathbf{A}_\alpha\cdot\mathbf{L}_\alpha + (\mathbf{L}_\alpha)^T\cdot\mathbf{A}_\alpha\,, \tag{2.22}$$

whereas $\overset{\triangle}{\mathbf{A}}_\alpha$ coincides with the covariant *Oldroyd rate* of the Almansi strain tensor.

2.2.3 Stress tensors

Analogously to the strain measures, stress tensors are defined both on the material and on the spatial configuration. The partial *Cauchy-stress* $\overset{\vee}{\mathbf{T}}{}^{\alpha}$, determines the stress state in a spatial point and refers to the surface element da in the current configuration as shown in figure 2.4. Thus, the traction vector $\mathbf{t}^{\alpha}$, which acts on the element da, can be evaluated by

$$\mathbf{t}^{\alpha}\mathrm{da} = \overset{\vee}{\mathbf{T}}{}^{\alpha}\ \mathbf{n}\ \mathrm{da} = \mathbf{P}^{\alpha}\ \mathbf{N}\ \mathrm{dA}\ . \tag{2.23}$$

Cauchy stresses are often termed *true stresses* as they act on the deformed surface element. The *partial* Cauchy stress $\overset{\vee}{\mathbf{T}}{}^{\alpha}$ acts on the area of the mixture whereas $\mathbf{T}^{\alpha}$ is defined as the partial stress acting on the area of the constitutent α. The two tensors are related by

$$\overset{\vee}{\mathbf{T}}{}^{\alpha} = \mathbf{T}^{\alpha} \cdot n^{\alpha}\ . \tag{2.24}$$

The *first Piola-Kirchhoff stress tensor* $\mathbf{P}^{\alpha}$, given by

$$\mathbf{P}^{\alpha} = \det\mathbf{F}_{\alpha} \cdot \mathbf{T}^{\alpha}\ \cdot \mathbf{F}_{\alpha}^{-T}\ , \tag{2.25}$$

measures with the undeformed surface element, but the corresponding traction vector, see (2.23), acts on the current configuration as well. The tensor $\mathbf{P}^{\alpha}$ is a two-field stress tensor and has a non-symmetric coefficient matrix. With a *pull-back*, a transformation of a spatial quantity to a material quantity, the symmetric *second Piola-Kirchhoff stress tensor* $\mathbf{S}^{\alpha}$ is given by

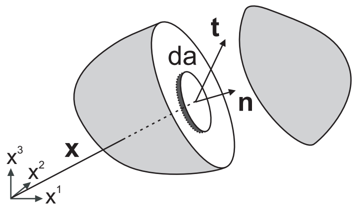

Figure 2.4: Stress state and traction vector

$$\mathbf{S}^{\alpha} = \det\mathbf{F}_{\alpha} \cdot \mathbf{F}_{\alpha}^{-1} \cdot \mathbf{T}^{\alpha}\ \cdot \mathbf{F}_{\alpha}^{-T}\ . \tag{2.26}$$

Another important quantity is the *Kirchhoff stress tensor* $\tilde{\mathbf{T}}^{\alpha}$, also termed weighted Cauchy stress tensor, which is

$$\tilde{\mathbf{T}}^{\alpha} = \det\mathbf{F}_{\alpha} \cdot \mathbf{T}^{\alpha}\ . \tag{2.27}$$

The sum of the partial stresses $\overset{\vee}{\mathbf{T}}^\alpha$ equals the total stress of the mixture $\mathbf{T}$

$$\sum_\alpha \overset{\vee}{\mathbf{T}}^\alpha = \mathbf{T} \; . \tag{2.28}$$

2.3 Balance equations for a three-phase model

The *Principle of Virtual Work* is formulated for a triphasic model together with equations of conservation of mass, momentum and energy considering a solid, a liquid and a gas phase. The balance equations refer to different reference systems. For general derivation of balance laws for mixtures the reader is referred to de Boer [47] or Lewis and Schrefler [142].

The macroscopic approach of the Theory of Porous Media with its superimposed continua implies a *volume-coupled* approach. Thereby, overlying physical fields are coupled by joint state variables. Another strategy is a discrete description of the constituents with a coupling over the interfaces, i.e. the boundaries of the phases.

In this thesis, a Lagrangian description of the solid skeleton is combined with an ALE description of the fluid phases, whereas the reference configuration is the current configuration of the solid phase.

The description of boundary conditions is explained in section 6.1 after constitutive relations are included in the approach.

2.3.1 Principle of Virtual Work for the mixture

The Principle of Virtual Work is equivalent to the equilibrium of forces. Its Total Lagrangian representation (2.29) is applied here to desribe the balance of internal and external forces considering the mixture as a whole. Due to consideration of large strains and nonlinear material behaviour the virtual work is nonlinear with respect to both the kinematics and the material. A derivation of the Principle of Virtual Work from the balance of momentum can be found in Bathe [10] or Parisch [192]

$$\begin{aligned} \underbrace{\int_{V_0} \delta\mathbf{E} : \mathbf{S} \, dV}_{\text{virtual internal work}} + \underbrace{\int_{V_0} \delta\mathbf{u} \, \rho_{ref} \, \delta\ddot{\mathbf{u}} \, dV}_{\text{work of inertia forces}} &= \underbrace{\int_{\Gamma_0} \delta\mathbf{u} \, \mathbf{t_0} \, dS}_{\text{work of surface pressures}} \\ &+ \underbrace{\int_{V_0} \delta\mathbf{u} \, \rho_{ref} \, \mathbf{g} \, dV}_{\text{work of volume forces}} \; . \end{aligned} \tag{2.29}$$

Inertia forces are not further considered in this thesis.

2.3.2 Mass balance for solid components in Total Lagrangian description

The Principle of Virtual Work is used in its Total Lagrangian description, i.e. with respect to the reference configuration. Thereby, it is assumed that the motion of the solid phase acts as the reference system. In this case, the mass balance for the constituents which move with the reference system is quite simple to describe. The partial density on the reference configuration, ρ^{α}_{ref}, and the partial density on the current configuration, ρ^{α}, are defined by

$$\rho^{\alpha}_{ref} = \frac{m^{\alpha}}{dV_{\alpha}} \text{ and } \rho^{\alpha} = \frac{m^{\alpha}}{dv} \ . \tag{2.30}$$

Thereby, the volume dV_{α} refers to the volume in reference configuration and dv to the volume in the deformed configuration. Together with (2.10) the densities are related by the deformation gradient by

$$\rho^{\alpha} = \frac{m^{\alpha}}{dv} = \frac{m^{\alpha}}{\det \mathbf{F}_{\alpha} \cdot dV_{\alpha}} \Longrightarrow \rho^{\alpha} = \rho^{\alpha}_{ref} \cdot (\det \mathbf{F}_{\alpha})^{-1} \ . \tag{2.31}$$

In other words, the densities are transformed analogously to volume elements, since the material points are fixed to the volume (no relative movement). One has to keep in mind that reference and current configuration do not necessarily refer to points in time. The density with respect to the reference configuration ρ^{α}_{ref} is time dependent in the proposed model due to degradation processes.

2.3.3 Integral form of mass balance for fluid components in ALE description

The fluid phases and their components, are formulated in Eulerian description. The reference frame is however not fixed, but connected to the solid phase. Thus, the Eulerian spatial frame moves with the velocity of the solid phase. This represents a special case of an Arbitrary Lagrangian-Eulerian description, see for example Donea [53] and Donea et al. [54], whereas here the movement of the reference frame coincides with the movement of one of the constituents, i.e. the solid skeleton.

The basic idea of the ALE method is to combine both the advantages of the classical Lagrangian and the Eulerian description. The purely Lagrangian description is widely used in solid mechanics. Thereby the nodes of the mesh coincide with the material points of the solid and are fixed to them during deformation, see figure 2.5, top. If the deformations are small, this approach does not lead to strong distortions of the mesh. Contrary, a Lagrangian description in fluid mechanics might quickly lead to strong deformations of the mesh making a remeshing necessary. A discussion on that can be found in Bathe [10]. The Eulerian description is applied very often in fluid mechanics. Thereby, an observer is fixed to a spatial point and views material points passing the corresponding control volume, which remaines fixed, see figure 2.5, middle.

In the ALE description, the nodes of the control volume may move arbitrarily, figure 2.5, bottom. Neither the material configuration (Lagrangian) nor the spatial configuration (Eulerian) are considered as a reference. Rather, an additional domain is needed which serves then as the reference frame. Thus, high distortions of the continuum can be handled better with the ALE method than with a purely Lagrangian approach. For more detailed information on the ALE method the reader is referred to Donea et al. [54]. Note that the Eulerian view has to be distinguished from what is termed Updated Lagrangian description, which is still based on a Lagrangian viewpoint, but the balance equations are integrated on the current, spatial configuration, see for example Holzapfel [107]. For derivation of balance equations in Eulerian description on a moving domain it is first necessary to derive the time derivative of a volume integral, which is shown in the following section. Next, the balance equations are derived following Rossow [202].

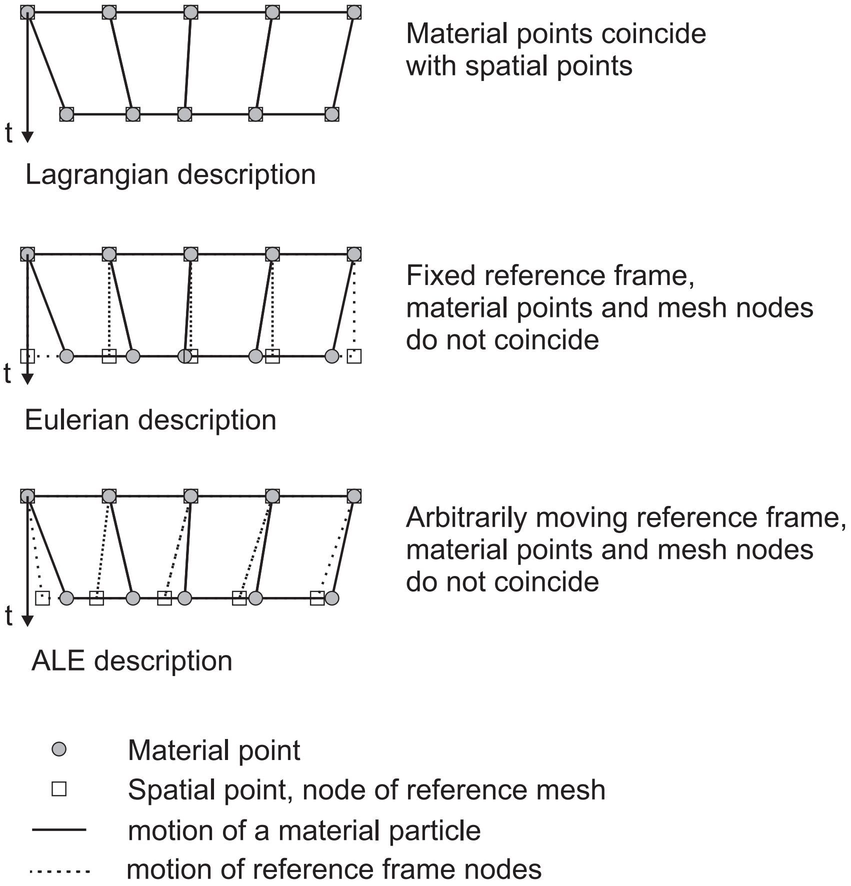

Figure 2.5: Comparison of particle and mesh motion for Lagrangian, Eulerian and ALE description, redrawn from Donea et al. [54]

2.3.3.1 Time derivative of a volume integral over a moving volume

The amount of an intensive quantity ϕ in a control volume equals the corresponding volume integral ψ, which is an extensive quantity. The detailed derivation is shown for a scalar quantity but the procedure is straightforward for any vector quantity. For better

readability any indices for identification of a particular component are skipped.
Let ϕ be a scalar volume-specific field function $\phi = \phi(x, y, z, t)$, as for example density, then the content ψ in a general time-dependent volume is

$$\psi(t) = \int \phi \, dV \; . \tag{2.32}$$

The time derivative of ψ may be expressed by the chain rule

$$\frac{d\psi}{dt} = \frac{d}{dt} \int \phi \, dV = \int\limits_V \frac{\partial \phi}{\partial t} \, dV + \int\limits_V \phi \, \frac{dV}{dt} \; . \tag{2.33}$$

Equation (2.33) shows that the time derivative of the integral depends both on the time-dependent change of the function ϕ itself and on the change of the control volume V, see also figure 2.6. The volume dV as shown in figure 2.7 equals

$$dV = \mathbf{n} \cdot \mathbf{v}_s \cdot dt \cdot dS \; . \tag{2.34}$$

assuming that the length of the boundary dS is constant. Using (2.34) the volume integral

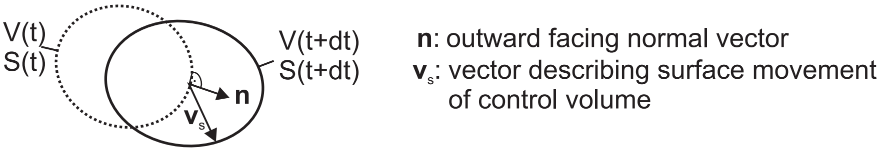

Figure 2.6: Change of a control volume $V(t)$ with time

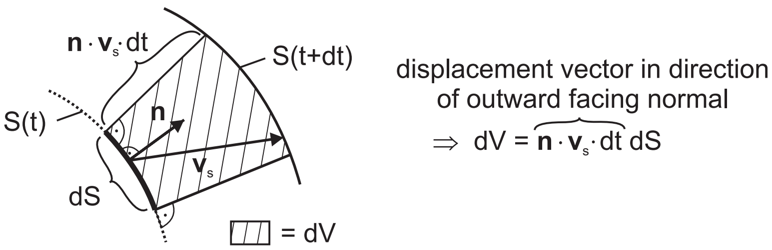

Figure 2.7: Change of an infinite volume element dV with time

is transformed into a surface integral so that the time derivative of ϕ is

$$\frac{d\psi}{dt} = \frac{d}{dt} \int\limits_{V(t)} \phi dV = \int\limits_{V(t)} \frac{\partial \phi}{\partial t} dV + \int\limits_{S(t)} \phi \mathbf{n} \cdot \mathbf{v}_s \, dS \; . \tag{2.35}$$

Equation (2.35) is often referred to as *Reynolds Transport Theorem.* The first term of the right hand side describes the local rate of change in the fixed control volume. The second term represents the influence of the changing boundaries of the control volume. For a time-*in*dependent volume the time derivative of the volume integral ψ thus equals the integral of the time derivative of the intensive quantity ϕ as the second term vanishes due to $v_s = 0$.

2.3.3.2 Mass conservation for a moving reference frame

The discussion in the previous section is used to derive the mass balance equation for a constituent α which is moving with phase π. In the model, the surface velocity coincides with the velocity of the solid phase, as the solid phase movement serves as a reference. The mass of component α in a control volume is

$$m^\alpha = \int\limits_{V(t)} \rho^\alpha dV \ , \tag{2.36}$$

and, using (2.35), its time derivative equals

$$\frac{dm^\alpha}{dt} = \frac{d}{dt}\int\limits_{V(t)} \rho^\alpha dV = \int\limits_{V(t)} \frac{\partial \rho^\alpha}{\partial t} dV + \int\limits_{S(t)} \rho^\alpha \mathbf{n}\mathbf{v}_s dS \ . \tag{2.37}$$

In a domain which is free of sources and sinks any change in mass of component α is caused by a flux over the moving boundary of the control volume, see figure 2.8. Therefore, the rate of change in mass is balanced by the surface fluxes

$$\frac{dm^\alpha}{dt} = -\int\limits_{S(t)} \rho^\alpha (\mathbf{v}_\pi - \mathbf{v}_s)\mathbf{n}\, dS \ , \tag{2.38}$$

whereas $\mathbf{v}_\pi$ equals the component's velocity $\mathbf{v}^\alpha$ considering convective fluxes only.

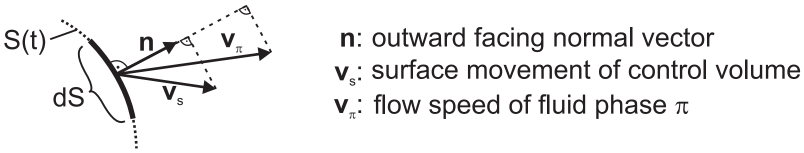

Figure 2.8: Surface velocity and flow speed

Using the first part of (2.37) the mass balance in its integral and conservative form yields

$$\frac{d}{dt}\int\limits_{V(t)} \rho^\alpha dV + \int\limits_{S(t)} \rho^\alpha (\mathbf{v}_\pi - \mathbf{v}_s)\mathbf{n}\, dS = 0 \ . \tag{2.39}$$

In that way, directly the integral form of the equation of mass conservation is derived. A derivation of (2.39) starting from the differential balance equations is for example shown by Donea et al. [54].

If the second part of (2.37) is used to further simplify the mass balance, the *Geometric*

Conservation Law is obtained

$$\int\limits_{V(t)} \frac{\partial \rho^\alpha}{\partial t} dV + \int\limits_{S(t)} \rho \mathbf{v}_\pi \cdot \mathbf{n}\, dS = 0 \;, \tag{2.40}$$

which is termed *non-conservative* as no flux balances are formulated any more, in other words, the surface fluxes are no more separated from the local rate of change in the control volume.

In case of the proposed model for waste also sources and sinks due to reactions or physical exchange have to be considered so that the right hand side of (2.39) is not equal to zero and thus has to be extended by an additional term r^α, which describes a local rate of change in density due to reactions

$$\frac{d}{dt} \int\limits_{V(t)} \rho^\alpha dV + \int\limits_{S(t)} \rho^\alpha (\mathbf{v}_\pi - \mathbf{v}_s) \cdot \mathbf{n}\, dS = \int r^\alpha\, dV. \tag{2.41}$$

If the surface velocity $\mathbf{v}_s = 0$, the Eulerian representation of the equation for conservation of mass is obtained, for $\mathbf{v}_s = \mathbf{v}_\pi$ the Lagrangian one.

Adding the mass balance equations of the single components yields the mass balance for the whole mixture.

The derivation of the mass balance for the gas phase is straightforward. The mass balances are shown in detail after explanation of the constitutive model.

2.3.4 Balance of angular momentum

The balance of angular momentum yields a symmetric Cauchy stress tensor. A derivation is for example shown in Parisch [192]. It may be remarked, that also theories exist which consider conservation of angular momentum not by a priori fulfillment of the symmetry of the Cauchy stress tensor, but by an additional conservative quantity. For a recent overview see for example Münch [174].

2.3.5 Balance of energy

As shown in chapter 1 landfills might exhibit high variations in temperature which in turn influences degradation and transport. The proposed model thus considers a transient temperature. Analogously to the mass balance, the equation for conservation of energy is considered for the whole mixture. It is assumed that all constituents have the same temperature. The energy converted in the different processes has to be balanced. Due to the degradation processes and physical exchange processes the equation for conservation of energy is very complex. The general form is analogous to the mass balance equation. Storage terms and convective terms are balanced by sources and sinks due to degradation. The general balance of energy for the whole mixture with the volume-specific energy e

yields

$$\frac{d}{dt}\int\limits_{V(t)} e\,dV + \sum_{\alpha}\int\limits_{S(t)} e_{\alpha}(\mathbf{v}^{\alpha} - \mathbf{v}^{s})\mathbf{n}\,dS = \sum\int r_{e,\alpha}dV. \tag{2.42}$$

with a term r_e accounting for sources and sinks. The individual terms are explained in detail after description of the constitutive model.

2.4 Discretisation of model equations in time and space

As no analytical solution for the coupled problem is known, the system of coupled field equations is solved numerically. For discretisation in time, an implicit finite difference scheme, the Backward Euler method, is used. Thereby the differential quotient describes the derivation at the end of the time interval. The implicit Euler method requires an iterative solution of the discrete equations, but offers advantages regarding stability and time step size, if compared for example with the explicit, Forward Euler method.

For discretisation of the governing balance equations (2.29), (2.41) and (2.42) in space, a combination of the Finite-Element method and the Box method, proposed by Helmig [103], is applied. Thereby, the Box method is applied on a moving reference frame, as already used in Bente et al. [21] and Krase [135].

The Principle of Virtual Work in its Total Lagrangian form, as given by (2.29), is discretised by a Bubnov-Galerkin Finite-Element approximation. Thereby, the same set of ansatz functions $\mathbf{N}$ is used both for displacements $\mathbf{u}$ and virtual displacements $\delta\mathbf{u}$

$$\mathbf{u} = \sum_{i}(\hat{u}_i \cdot N_i) \text{ and } \delta\mathbf{u} = \sum_{i}(\delta\hat{u}_i \cdot N_i)\ , \tag{2.43}$$

with i as counters over finite element nodes. Discrete quantities are denoted by $\hat{(\ )}$. In this thesis, an isoparametric finite element concept with 9 nodes is used. Correspondingly, quadratic ansatz functions describe both the displacement field and the element geometry. The integrals in (2.29) are evaluated by the Gaussian quadrature formula. For an introduction into the Finite-Element method the reader may be referred to Bathe [10] or Dinkler and Ahrens [51].

The discrete integral form of the mass balance is obtained by the Box method as described by Helmig [103]. The method is also termed *subdomain collocation finite volume method* or *node centered finite volume method.* The approach may be derived from a weighted residual approximation whereas linear ansatz functions are used. The constant test functions are equal to unity over the domain of a box. The box grid is derived from the finite element mesh, whereas the corner nodes of the finite element mesh are the centers of the boxes. The corner nodes of a box are formed by the centers of adjacent finite elements and by the midpoints of their edges. The element concept is shown in figure 2.9. The derivation

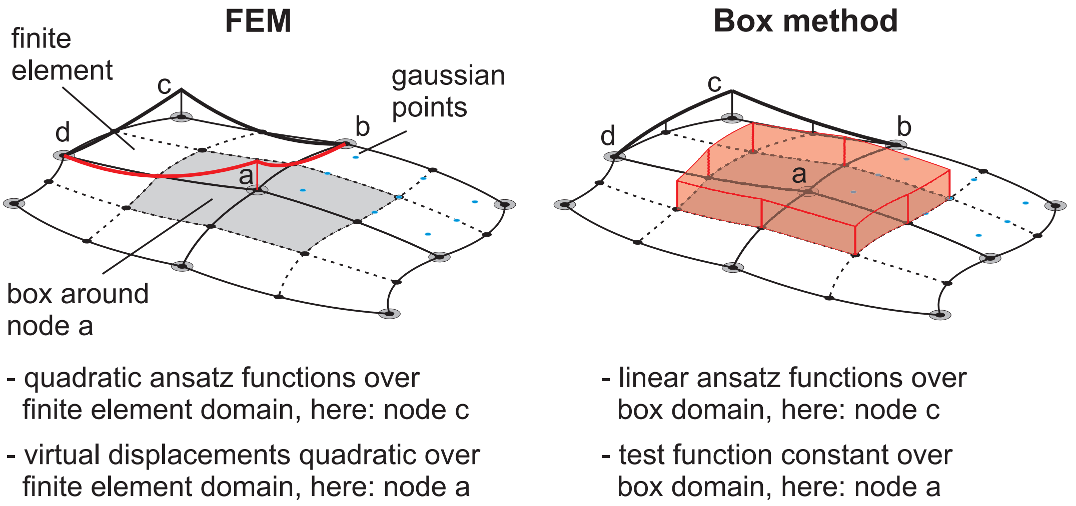

Figure 2.9: Ansatz functions and test functions for FEM and BOX method

of the discrete form is explained in detail by Helmig [103] and extended straightforward to a moving reference frame. Together with a mass lumping of the storage terms the discrete form of equation (2.41) for box i yields

$$\frac{\hat{\rho}_i^{\alpha,t+1}\cdot \mathrm{d}V_i^{t+1} - \hat{\rho}_i^{\alpha,t}\cdot \mathrm{d}V_i^{t}}{\Delta t} + \int_S (\hat{\rho}_U^{\alpha}(\hat{\mathbf{v}}_\pi - \hat{\mathbf{v}}_s)\cdot \mathbf{n})\Big|^{t+1} dS = \hat{r}_i^{\alpha,t+1}\cdot \mathrm{d}V_i^{t+1}\,. \tag{2.44}$$

The discrete formulation of the storage term reveals, that the rate of change comprises both the change of the conservative variable itself and of the box volume dV_i. The density $\hat{\rho}_i^{\alpha,t+1}$ is the partial density of α at the center node of box i. By means of the linear ansatz functions used in the Box method, values at Gaussian points are evaluated if required for coupling terms. The density $\hat{\rho}_U^{\alpha}$ is the upstream density at the surface of box i. For stabilisation of the convective terms, a fully upwinding is used, not only of the density but also of mobility. The upwinding reveals the hyperbolic character of the differential equation in space. The procedure is analogous to *Godunov's scheme.*

The Box method is a conservative scheme, as the rate of change of a conservative variable is balanced by fluxes over the boundaries of a control volume. Due to the mass lumping, the discretisation takes the form of a finite volumes method. It reduces non-physical oscillations of the solution. The integration may be formulated easily and a clear implementation of stabilisation is possible. The upwinding induces, however, numerical diffusion, especially for course meshes. In the coupling with the Bubnov-Galerkin discretisation the transfer of nodal values and gauss point values, as well as elemental and box quantities requires additional computational effort.

A detailed comparison of the Box method with other discretisation methods for multiphase flow in porous media is not within the scope of this thesis and the reader may be referred to Huber and Helmig, [109] and [110].

3 Model for Degradation and Heat Generation

The chapter gives an overview of the degradation processes occuring in MSW landfills and describes the selected modelling approach. The model is based on the previous work within SFB 477, especially Hanel [99], Haarstrick et al. [95] and Kindlein et al. [125]. The influence of parameters is investigated on local level. Furthermore, heat generation and local parameters of heat transport are discussed.

3.1 Phenomenology of Biogological Degradation in MSW Landfills

Depending on the present oxygen supply, two general mechanisms of biological degradation of organic matter are distinguished. In the presence of oxygen, organic matter is decomposed *aerobically* to carbon dioxide and water. In case of lacking oxygen, degradation proceeds under *anaerobic* conditions with the production of carbon dioxide and methane. Different by-products arise from these two pathways. Due to the water content at emplacement, subsequent compaction and infiltrating precipitation, degradation proceeds mainly under anaerobic conditions in landfills.

The entire process of anaerobic degradation passes several steps, whereas usually four main steps are considered as visualised in figure 3.1. The steps of the process are related to the activity of different bacteria populations, herein termed *biomass*. Often, three major groups are distinguished. During the first step, *hydrolysis*, the long-chain substances are transferred to short-chain molecules. Then, within the *acidogenesis*, the hydrolytic-fermentative bacteria convert the hydrolised particles to organic acids along with the production of hydrogen and carbon dioxide. In the third step, the *acetogenesis*, organic acids are decomposed to acetic acid by acetogenetic bacteria. During the fourth stage, *methanogenesis*, the methanogenic bacteria produce methane from acetic acid or carbon dioxide and hydrogen.

In general, the anaerobic process is more likely to become unstable compared to aerobic degradation. It proceeds efficiently at a nearly neutral pH. Environmental conditions influence the process and some substances might inhibit certain reactions steps of the process. Several models are developed to describe the complex degradation process in landfills, an overview is given in section 3.2. The products of the different reaction steps determine the composition of the landfill gas and the leachate. As a landfill is built up over many years, different parts of it may be within different phases of decomposition, leading to spatially varying leachate and gas compositions.

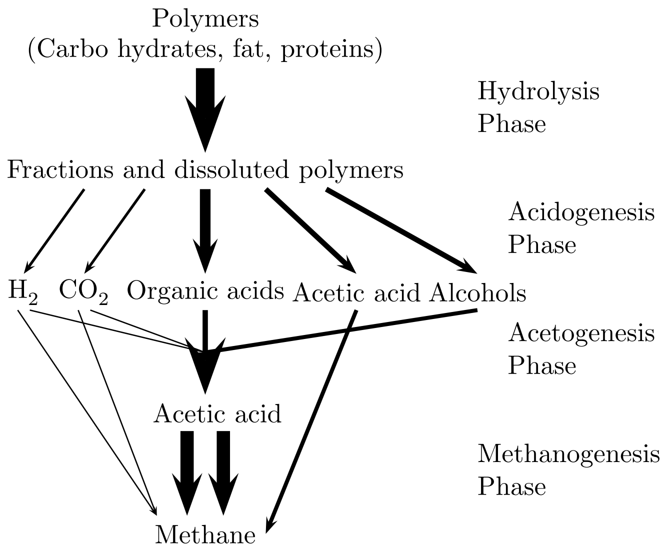

Figure 3.1: Main steps of anaerobic degradation, after Mudrack and Kunst [173]

Farquhar and Rovers [78] are among the first to structure the landfill gas evolution by developing a typical pattern, see figure 3.2.

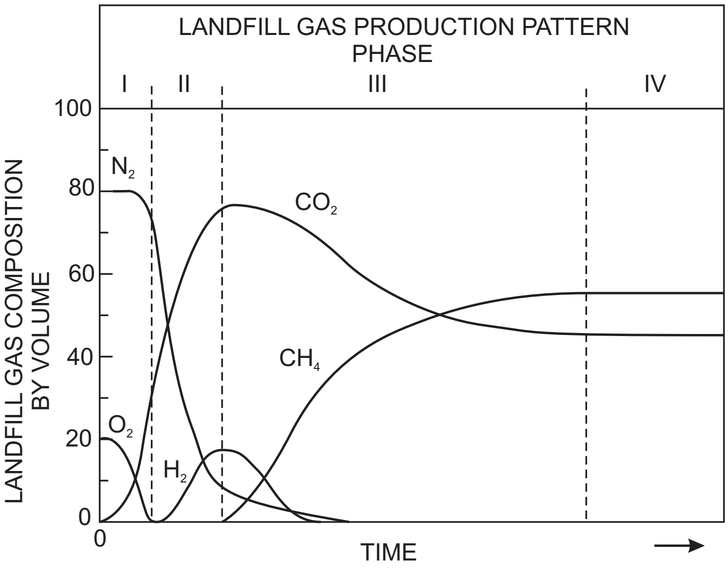

Figure 3.2: Gaseous emissions from landfills, redrawn after Farquhar and Rovers [78]

In a short period after emplacement, phase I, aerobic conditions might dominate the process until the present oxygen is consumed. Then the process enters the anaerobic phase, II, whereas no methane is produced initially. A peak in CO_2 develops and the hydrogen concentration is increasing. Phase III is termed unsteady methanogenic phase during which the production of methane establishes. In phase IV, the steady methanogenic phase, the fractions of the original landfill gas components, i.e. carbon dioxide and methane, reach a steady value. Variations from the pattern may, of course, occur due to changes in environmental conditions.

Similarly as for landfill gas, a typical pattern of leachate composition is derived by Kjeldsen et al. [127] based on their review of leachate data, see figure 3.3. It is related to an extended landfill gas pattern. As discussed in chapter 1, predictions beyond the stable methanogenic phase are subject to speculation because most landfills still are in this phase or an earlier phase, so long-term data is not available.

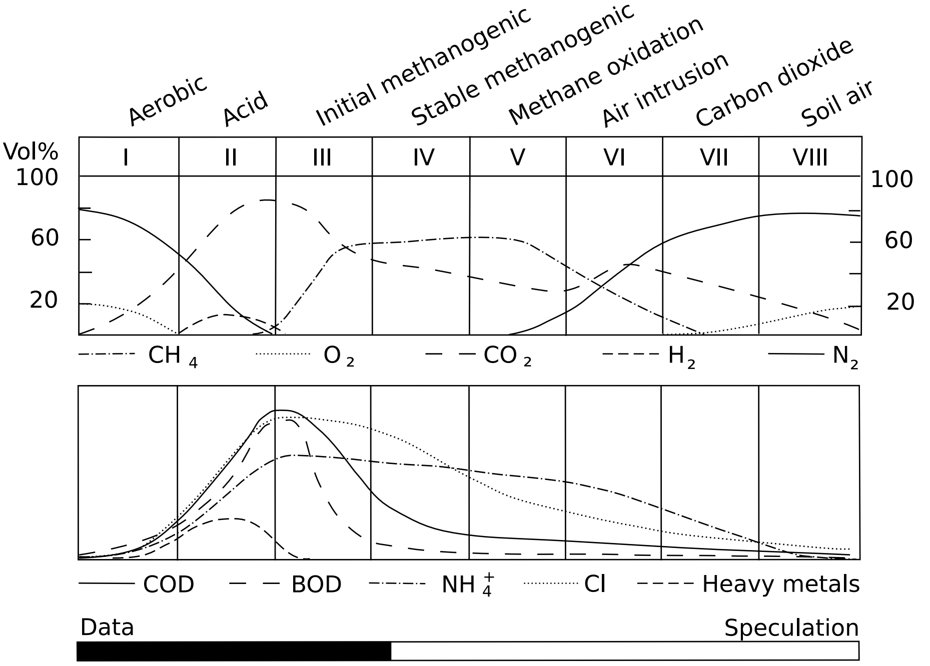

Figure 3.3: Leachate composition in landfills, after Kjeldsen et al. [127]

The production of acids in the acidogenic phase results in a pH decrease. Hence, the highest BOD and COD, parameters representing the biological and chemical oxygen demand respectively, are measured at the end of the acid phase. The onset of the methanogenic phase is accompanied by an increase in pH, as the methanogenesis step is usually much quicker than hydrolysis, therefore acids do not accumulate. With the decomposition of carboxyclic acids, COD and BOD decrease, whereas also the BOD:COD ratio decreaseas. In general, the aerobic process is accompanied by much higher temperatures than the anaerobic process. Zeccos [248] reports about in-situ tests at a MSW landfill in the US where temperatures up to 45 °C are measured in waste samples obtained by drilling. An increase of temperature with depth is observable. Figure 3.4 shows temperature profiles measured in boreholes by Mora-Naranjo et al. [169], temperature is up to 60 °C, similar values are measured in other landfills.

3.2 Models for Degradation Processes in MSW

This section concentrates on models for degradation of organic matter under mainly anaerobic conditions. Models which focus on aerobic processes are for example reviewed by Mason [155] and Hamelers [98]. With regard to the variety of models developed so far, this section does not claim to be self-contained. Instead, the aim is to show the historical

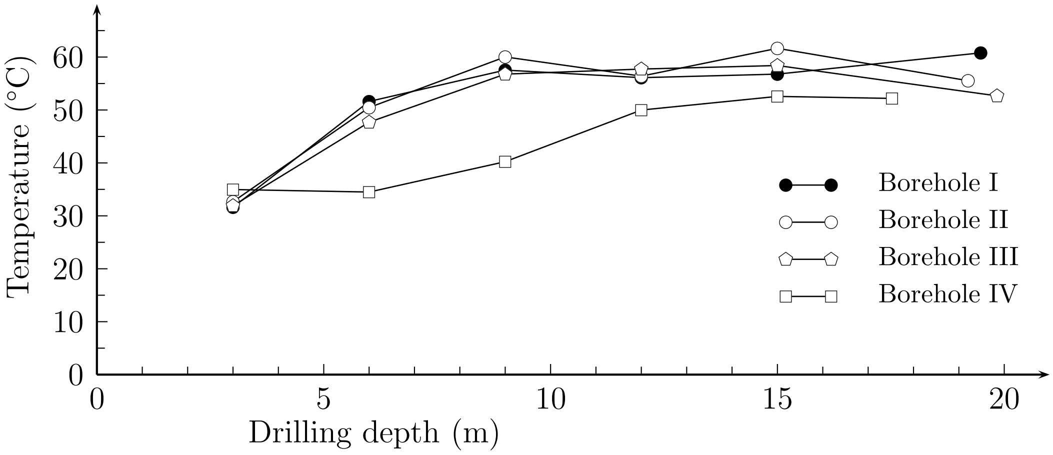

Figure 3.4: Landfill temperature profile from Mora-Naranjo et al. [169]

development and to point out important steps and key issues. Thereby, the review's focus are reaction models applied to waste, whereas many models exist in the field of waste water or manure treatment. General, comprehensive overviews on anaerobic degradation models are recently given by Gavala et al. [88] or Lyberatos and Skiadas [149].

One major aim of the first reaction models for landfills is to estimate gas production, which is of high importance for the design of gas extraction systems and for the evaluation of their effectiveness. With the concerns about global climate change, another field of interest comes up, as there is an interest to quantify (reductions of) greenhouse gas emissions from waste deposits. Nowadays also the active treatment of solid waste in mechanical biological treatment plants is becoming an established technology. For the process engineering of those plants, phenomenology of degradation has to be understood and described as well. Landfill reaction modelling starts with empirical based relations, sometimes called black box models, from which the models are more and more modified and extended. Major steps of advancement are

a) extension of reaction scheme: from one step to multistage sequential, increasing number of components,
b) refinement of kinetics description,
c) consideration of milieu influences,
d) more detailed description of waste composition,
e) new methods for parameter determination,
f) and model validation, from lab scale to application on landfill sites.

The first landfill gas production models estimate the anaerobic gas production based on the theoretical methane potential of the waste, which depends on its composition. Organic matter content and the kinetic reaction constants are among the main parameters of those models. A common assumption is often that landfill gas is composed of methane and carbon dioxide. One of the first models is presented by Tabasaran [224] who compares the gas production in a landfill with that in an anaerobic digestor and reduces the theoretical gas potential, depending on the temperature, by an assimilated carbon fraction. Thereby, Tabasaran assumes a linear relationship of a gasifiable carbon fraction and temperature. Time dependency of degradable matter is expressed by first order kinetics. The model by Tabasaran and Rettenberger, [224], [225], is well established in the European waste management society and is still widely used by landfill operators for gas prognoses. Hoeks [106] applies first order kinetics as well. Being aware that gas production rates are high in the early years after landfilling, due to readily degradable material, he splits the organic matter into several fractions dependent on their degradability.

Ehrig [62] investigates the gas production in a lysimeter and compares the models by Tabasaran, Rettenberger and Hoeks for the description of experimental measurements. He adopts the approach by Tabasaran and relates gas production and leachate composition to estimate model parameters. Based on own investigations and published experimental data, he concludes that the influence of pH and water content on gas production is relatively small. The author points out uncertainties with regard to determination of the theoretical gas potential, which is an important parameter in the models, and indicates that biomass production, as assumed by Tabasaran, seems to be relatively high. With respect to the analysed waste, he concludes that splitting organic matter into several fractions does not seem necessary.

Weber [241] adopts the approach by Tabasaran as well, but introduces additional influencing factors which account for waste composition and landfill operation. His model is also quite well established in engineering practice.

Although models like those by Tabasaran and Weber do not explicitly consider different types of organic matter, like that by Hoeks, it is possible and implemented in engineering practice to evaluate gas production within a staggered scheme having the possibility to adjust parameters with respect to waste composition and landfill operation.

One of the early models which include environmental influence in a more detailed manner is the model for gas generation by Kleinstreuer and Poweigha [128]. Microbial growth of two genera of bacteria, methanogenic and acidogenic, and their sensitivity to environmental factors and inihibitory effects are considered.

One of the first model including both microbial growth and a quite detailed sequential reaction scheme is presented by Lee and Donaldson [139]. Their aim is to describe anaerobic celluose digestion with the application on low-level radioactive waste treatment. They include three major conversion steps, namely hydrolysis, acetogenesis and methanogenesis. Monod type kinetics are applied to every step including both limitating and inhibitory effects of substrates.

Direct pH modelling by means of an ion balance is explained by Angelidaki et al. [4]. A detailed description of acidogenesis considers acetic acid as well as butyric and propionic acid. Monod kinetics and non-competitive inhibition are considered as well. Another very detailed model is developed by Vavilin et al. [235]. Their model includes substrate limitation and inhibition, evaluation of pH by an ion balance, temperature and pH effect on rates as well as seven types of microorganisms.

El-Fadel et al. [67] model methane production from waste by means of a (simplified) sequential scheme. They investigate the effect of initial biomass concentrations on degradation, whereas microbial growth is directly included by applying Monod kinetics to the acidogenesis and methanogenesis steps. Hydrolysis is modelled by first order kinetics. Total biomass is split up into acidogenic biomass and methanogenic biomass, and the modelling of pH is discussed.

By now, the review shows that model development in the early years covers already most aspects as listed above. From the very beginning, researchers consider the influence of environmental conditions on anaerobic degradation, especially temperature and pH. Also, they are aware of difficulties in parameter estimation. Most models are validated at lab scale using results from lysimeter testing. In general, not sufficient experimental data as well as field data are available at that time, as highlighted by El-Fadel et al. [68] in their review of gas production models published between 1976 and 1993. Furthermore, El-Fadel et al. identify the need for coupled models that treat landfills as a multiphase porous medium.

Lyberatos and Skiadas [149] identify four key issues that should be addressed in future modelling work: a general framework as a standard for hydrolysis and acidogenesis, description of environmental conditions, inhibitory effects and modelling of heterogeneous systems. The first task is addressed by the International Anaerobic Modelling Task Group, founded in 1997, in order to provide a common platform for model development. An outcome of their work is the Anaerobic Digestion Model No. 1 presented in 2001.

Within the field of international climate protection, the IPCC (Intergovernmental Panel on Climate Change) describes in [115] three approaches for estimating methane emissions from disposal sites: the first one (theoretical gas yield methodology) is based on the assumption that the theoretical methane potential is released in the year of disposal, the second (default methodology) considers the degradable carbon fraction, and the third (theoretical first order kinetics method) is quite similar to the approach by Weber and recommended in [114] and [116]. If a CDM (Clean Development Mechanism) has to be approved, methods are necessary for estimating methane generation from a particular landfill in the absence of the project activity (baseline scenario). As such, the FOD (first order decay) method is later approved within the baseline method AM0025 by the UNFCCC CDM Executive Board [37]. For the European Pollutant and Transfer Register E-PRTR , formerly EPER, diffuse emissions from landfills have to be reported. Initially the default method of IPCC is recommended by the Federal Environment Agency, UBA [229], for the German country report. For all reports from the year 2007 on, the first order decay method is chosen, Butz [35]. Contrary to EPER, the E-PRTR includes also landfills in aftercare phase, thus, the approach is modified by Butz [36]. In a supporting document, EPA [71], Ireland's Environmental Protection Agency lists seven models for determining diffuse emissions from landfills for EPER, most of them are simple first order decay models. Prognoses of methane emission rates with the different models are both compared among each other and with data from a landfill site. One prognosis is close to the measured emission rate with a deviation less than 10 %. However, the maximum predicted value differs by a factor of nine from the measured one; the minimum predicted value is about 40 % of the measured rate. It is suggested to gain more reliable results by analysing more landfill data. A similar analysis is done by Ogor and Guerbois [185] who compare five of the same models using data from 4 landfill sites. Deviations are different for landfill cells, whereas, deviations of CH_4 emissions are higher than total gas production. When discussing the results, it needs to be considered that, in fact, the compared models are quite similar. Another comparative study is published very recently by Thompson et al. [227].

The Landfill Gas Emissions Model LandGEM (for latest version see EPA [72]) is developed by the EPA Office of Research and Development and the Clean Air Technology Center. Its objective is to estimate total landfill gas and methane generation, as well as emissions of carbon dioxide, nonmethane organic compounds and individual air pollutants from landfills. On behalf of US EPA other country specific models are published and are based on simple first order kinetics, [73], [74], [75], [76].

The development of landfill modelling within the area of climate protection shows that mainly simple models are applied. For many applications this is appropriate, because usually not the emission of an individual landfill is considered. Rather, an estimation of country specific emissions is made, as indicated by Scharff and Jacobs [209]. However, for approval of CDM methods, emissions have to be estimated for a particular landfill to quantify the baseline scenario, so that both licensing organisations and landfill operators might benefit from more advanced models.

Many models developed by the waste management reasarch community in the current century adopt the efforts made so far, like detailed waste description, detailed sequential reaction scheme, Monod kinetics including inhibitory effects, pH modelling, heat generation, and environmental influences. In 2001, the first version of the model developed within the SFB 477 is published by Haarstrick et al. [95]. The model is extended by two additional biomass cultures and an aerobic step by Haarstrick et al. [96]. Mora-Naranjo et al. [169] as well as Reichel and Haarstrick [197] add a function for the influence of water content. Additionally, Monod kinetics are modified using the approach by Mankad and Bungay, see Reichel [196], to avoid excess reduction of degradation rate if several limiting substrates are present.

Another very detailed scheme is published by Siegrist et al. [215], who consider 19 processes and 23 components including six types of biomass. Dissociation equilibrium of 4 components is considered directly. Degradation kinetics include microbial growth, except for the rate of hydrolysis. Biogas stripping is included as well.

The model GasSim is developed on behalf of the Environment Agency of England and Wales by Attenborough et al., [6] and Attenborough et al. [5]. To cover parameter uncertainty, GasSim includes a Monte-Carlo Simulation of input parameters. The different modules of the model are validated against production and emission data from several landfills. The source term for gas generation is based on first order kinetics. Four major gas components are considered, whereas other trace gases can be estimated implicitly by predefining trace gas fractions. In an overall balance, gas utilisation and flaring is considered, thus, being more close to landfill engineering and operation than other models. GasSim is among the few models that are distributed commercially, see www.gassim.co.uk.

Another recent issue is to describe the biofilm more explicitly on the microscale, like presented by Rotter et al. [203] with their model CHAMP for hydrolysis of cellulose. They distinguish explicitly between free-floating acidogens and acidogens bounded to the substrate. The latter control the rate of hydrolysis. Attachment of floating bacteria is described by a diffusion process of particles. Sloughing of biofilm is supposed to occur due to excess biomass growth and shrinkage of cellulose particles. The process depends on the surface area of the particles. The model assumes fully saturated conditions. They validate their model by comparison with an existing verified model because experimental data on bacterial colonisation and biofilm transfer is not available. An analogue issue is addressed by Heinke et al. [102] who describe the transfer of solid organic material to solute matter, and vice versa, by a sorption process. The approach is implemented by Reichel [196] in the model POSE.

The review clarifies that there is not a stringent chronological order from simple to advanced models. Rather, both are developed and applied at the same time. In many engineering applications, quite simple models of the type developed in the 1970s are still used. Many researchers concentrate on more detailed models, simultaneously introducing more input parameters that are often hardly measurable in experiments. Thus, some work also focuses on new methods for parameter determination. One of the first work on Monte-Carlo methods and neural networks applied on waste is done by Dach et al. [44]. Reichel [196] applies genetic algorithms and neural networks. Other models like GasSim, include a method for covering parameter uncertainty by probabilistic approaches. Hosser et al. [108] conduct sensitivity investigations by reliability theory to identify important parameters. Comparative applications of models show sinificant deviations in results. A few more critical issues on modelling are addressed in section 7.4.

3.3 Constitutive Model for Biological Degradation Including Heat Generation and Transfer

In this thesis, the complex biological degradation process is described by means of a two-stage reaction scheme which is derived from the more detailed models by Haarstrick et al. [95], Hanel [99] and Reichel and Haarstrick [197]. A first step is to identify important reactions and components, which allows to merge the complex mechanisms in a more or less simplified reaction scheme. The reduced model is already briefly described in Hanel [99] and Kindlein et al. [126]. However, an explanation is necessary, as latest findings according to parameters and reaction stoichiometry following Reichel and Haarstrick [197] are considered so that modifications to the previous version are made. Including reaction kinetics, the selected reactions determine the components that have to be balanced in the overall model.

3.3.1 Stoichiometry

The biological decomposition is related to the growth of biomass. The *yield coefficient* describes a change in concentration of biomass dX corresponding to a change in concentration of a substrate dS and is defined by

$$Y_{X/S} = dX/dS \,. \tag{3.1}$$

Simultaneously, it describes the relation of the rate of change of the components, i.e. $Y_{X/S} = \frac{dX/dt}{dS/dt}$. For instance, a yield coefficient of $Y_{X/s} = 0.1\ g/g$ implies that 0.1 g biomass are produced from the degradation of 1 g of main substrate. By means of the yield coefficient, equations for decomposition r and for microbial growth b can be summarised to a total reaction R by

$$R = (1 - \tilde{Y}) \cdot (r) + \tilde{Y} \cdot (b) \ \ (\text{mol}) \,. \tag{3.2}$$

Yield coefficients may be given both in terms of mol, $\tilde{Y}$, and mass, Y. The two representations are related by

$$\tilde{Y} = Y \cdot \frac{1}{\alpha_b^X} \cdot \frac{m^{ms}}{m^X} \,, \tag{3.3}$$

whereas α_b^X is the stoichiometric coefficient of biomass in reaction b. m_{ms} and m_X are the molar mass of the main substrate of the reaction (stoichiometric coefficient=1) and biomass, respectively. For the reduced model, stoichiometry derivation starts with the basic reactions for hydrolysis, acidogenesis, acetogenesis and methanogenesis and is summarised in table 3.1. The argumentation follows Hanel [99] and Kindlein et al. [126]. For organic matter, an average molecular composition of $1\,C_{30}H_{53.4}O_{14}N_{0.7}$ is assumed follow-

Table 3.1: Derivation of reaction stoichiometry for simplified scheme, final equations R1, R2 and L are highlighted in grey

Degradation reactions (mol)	
r1	$1\,C_{30}H_{53.4}O_{14}N_{0.7} + 16\,H_2O \longrightarrow 5\,C_6H_{12}O_6 + 11.65\,H_2 + 0.7\,NH_3$
r2	$1\,C_6H_{12}O_6 + 2\,H_2O \longrightarrow 2\,C_2H_4O_2 + 2\,CO_2 + 4\,H_2$
r3	$C_2H_4O_2 \longrightarrow CH_4 + CO_2$
r4	$CO_2 + 4\,H_2 \longrightarrow CH_4 + 2\,H_2O$
Biomass growth (mol)	
b1	$1\,C_6H_{12}O_6 + 1.2\,NH_3 \longrightarrow 1.2\ C_5H_7NO_2 + 3.6\ H_2O$
b2	$C_2H_4O_2 + 0.4\,NH_3 \longrightarrow 0.4\,C_5H_7NO_2 + 1.2\,H_2O$
b3	$CO_2 + 2\,H_2 + 0.2NH_3 \longrightarrow 0.2\,C_5H_7NO_2 + 1.6\,H_2O$
Combined reactions (mol)	
r1,r2/b1	$1\,C_{30}H_{53.4}O_{14}N_{0.7} + 24.514\ H_2O \longrightarrow 9.469C_2H_4O_2 + 9.469CO_2 + 30.588\,H_2 + 0.382\,NH_3 + 0.319\,C_5H_7NO_2$
r3/b2,r4/b3	$1\,C_2H_4O_2 + 3.230H_2 + 0.040NH_3 \longrightarrow 1.736H_2O + 1.707CH_4 + 0.092CO_2 + 0.040C_5H_7NO_2$
Total reaction after combination (mol)	
R'	$1\,C_{30}H_{53.4}O_{14}N_{0.7} + 8.074H_2O \longrightarrow 10.337CO_2 + 16.162CH_4 + 0.700C_5H_7NO_2$
Final reaction steps (g)	
R1	$1\,C_{30}H_{53.4}O_{14}N_{0.7} + 0.76H_2O \longrightarrow 0.98C_2H_4O_2 + 0.72CO_2 + 0.06C_5H_7NO_2$
R2	$1\,C_2H_4O_2 \longrightarrow 0.43CH_4 + 0.06CO_2 + 0.49H_2O + 0.02C_5H_7NO_2$
Final total reaction (g)	
R	$1\,C_{30}H_{53.4}O_{14}N_{0.7} + 0.28H_2O \longrightarrow 0.42CH_4 + 0.78CO_2 + 0.08C_5H_7NO_2$
Lysis of Biomass (g)	
L	$1\ C_5H_7NO_2 \longrightarrow\ 1\,C_{30}H_{53.4}O_{14}N_{0.7}$

ing Reichel and Haarstrick [197]. Acetic acid is considered as surrogate for all organic acids when summarising acidogenesis and acetogenesis steps. First, the reactions of organic matter reacting to glucose, r1, glucose to acetic acid, r2, and glucose to biomass, b1, are combined. The choice of the yield coefficients is given in table 3.2 and based on the work by Reichel and Haarstrick [197], whereas slight modifications are made to adjust final gas composition with respect to model experiments in section 3.4. The result is the combined reaction r1,r2/b1. Next, the methanogenesis steps r3 and r4 are combined with the corresponding biomass reactions b2 and b3 with the yield coefficients according to table 3.2. The resulting two reactions are combined with such a ratio that all hydrogen produced in r1,r2/b1 is consumed and that the volume ratio of methane and carbon dioxide in the final reaction matches a desired value of 60 to 40 % in view of the simulations in

Table 3.2: Yield coefficients

r_i	Y (g/g)	Main substrate	Coefficient of biomass in reactions $b_i^{1)}$	$\tilde{Y}$ (mol/mol)
r1	0	-	-	0
r2	0.0400	Glucose	1.2	0.0531
r3	0.0440	Acetic Acid	0.4	0.0584
r4	0.0513	Carbon dioxide	0.2	0.0998

$^{1)}$ see table 3.1

section 3.4. This procedure leads to the summarised reaction r3/b2,r4/b3 and to the total reaction R'. Hydrogen and Ammonia are not balanced in the model which is supposed to be sufficient for describing the stable methanogenic phase. Their mass is attributed to biomass to obtain finally equations R1 and R2 which are consistent in terms of mass.

Thus, the final scheme consists of two stages. During the first stage, organic matter and water are decomposed to acetic acid, carbon dioxide and biomass. In the next step, acetic acid reacts to methane, carbon dioxide, water and biomass. Consequently, the model considers that the landfill gas consists mainly of methane and carbon dioxide (and vapour), making it herewith applicable to anaerobic conditions. The generated biomass is subjected to lysis, whereas it is assumed that it is converted to organic matter in step L ensuring conservation of mass. The resulting final, total reaction is denoted by R. The reaction scheme implies a gas yield of 44 mol/kg organic matter. Since any aerobic step is not considered yet, initial aerobic activity or a final aerobic phase as indicated in figure 3.3 cannot be described. For long-term analysis, this is regarded unimportant, as confirmed by Straub and Lynch [222] with respect to long-term quality of leachate.

The procedure described above is a phenomenological approach and covers important steps for long-term analysis of the anaerobic stages. Alternatively, systematical approaches like the ILDM method (Intrinsic Low-Dimensional Manifolds in Composition Space) represent a very interesting methodology for the simplification of detailed reaction chemistry, especially if coupling with transport processes is required. The general idea of the ILDM is to analyse how a system reacts to perturbations at a certain state by means of modal analysis of the Jacobian, see Maas and Pope [150].

3.3.2 Reaction Kinetics

Decomposition is catalysed by microbiological growth, which is influenced by growth-limiting substrates. Furthermore, environmental conditions, especially temperature, water content and pH, are supposed to influence the activity of bacteria, see figure 3.5.

Monod [168] shows that the growth of bacterial cultures may be described by a hyperbolic

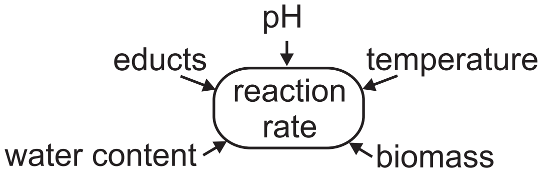

Figure 3.5: Factors influencing degradation rate

function so that the rate of change of a substrate S is - in terms of partial density -

$$\dot{\rho}^S = \mu_{max} \frac{\rho^S}{K^S + \rho^S} \cdot \rho^X \ , \tag{3.4}$$

whereas μ_{max} is the maximum degradation rate, ρ^S is the density of a limiting substrate S and ρ^X is the partial density of biomass. The Monod constant K^S with $[K_S] = \mathrm{kg/m^3}$ correponds to the partial density of the limiting substrate at which the actual degradation rate is half the maximum rate (therefore also termed *half-saturation constant*). The lower the value of K^S, the lower the concentration of substrate to obtain a particular reaction rate is. The order of the kinetic's description according to Monod depends on substrate and on biomass concentration, hence, the evolution of the concentrations causes a change of the kinetic's order. For substrate concentrations $\rho^S \ll K^S$, the reaction is of second order as the rate depends both on the concentration of the biomass and the concentration of the substrate. If $\rho^S \gg K^S$, the reaction is of first order with respect to the concentration of the biomass. A stage of substrate saturation is reached and the rate cannot be increased further by adding substrate.

The original Monod kinetic considers the limiting effect of one substrate, whereas further extension is possible by a multiplicative connection of corresponding terms. It is assumed that no substrate excess inhibition occurs, i.e. high substrate concentrations do not deccelerate the process. For the lysis of biomass, a rate law of first order is assumed. Hence, in detail the rates of the reactions R1, R2 and L are

$$R1: \quad \dot{\rho}^{DO} = \mu_{max,R1} \, \frac{\rho^{DO}}{K^{DO} + \rho^{DO}} \cdot \rho^X \cdot f_\Theta \cdot f_{S_l} \cdot f_{pH} \ , \tag{3.5}$$

$$R2: \quad \dot{\rho}^{Ac} = \mu_{max,R2} \, \frac{\rho^{Ac}}{K^{Ac} + \rho^{Ac}} \cdot \rho^X \cdot f_\Theta \cdot f_{S_l} \cdot f_{pH} \ , \tag{3.6}$$

$$L: \quad \dot{\rho}^{X} = \mu_{max,L} \, \rho^X \cdot f_{\Theta,L} \ . \tag{3.7}$$

The factors f_Θ, f_{S_l} and f_{pH} describe the influence of temperature, water content and pH, respectively, and are explained in section 3.3.3.

3.3.3 Influence of Milieu Conditions

Several experimental data prove the influence of environmental conditions on biological decomposition and mathematical formulations are developed to describe the effects. An overview is given by Meima et al. [162] and others. Often, water content w, temperature Θ and pH are considered to be limiting to microbial growth. Their influence is implemented in the proposed model by multiplying the rate under optimum conditions with factors f_w, f_Θ and f_{pH} varying between zero and one, compare equations (3.5), (3.6) and (3.7). One should note that the multiplicative connection might result in an underestimation of the specific growth rate.

More experimental evidence is needed to give an in-depth understanding of the evolution of milieu conditions. For example, Staley et al. [219] find that methanogenesis is initiated in experiments also at pH values that had been previously considered to be too low. Two explanations for this effect are given, acid-tolerant methanogens that are initiating the process and the pH-neutral niche theory.

Temperature Each group of bacteria has an optimum temperature range which are usually determined under laboratory conditions. Experimental data and functions describing the dependency reviewed by Meima et al. [162] are depicted in figure 3.6.

The bell-shaped temperature function f_Θ used in this thesis for reactions R1 and R2 is a product of two functions, $f_{\Theta,1}$ and $f_{\Theta,2}$. The first function equals the approach shown by Haarstrick et al. [95]. The second function enables an overall non-symmetric pattern by reducing the values of the first function for high temperatures, so that

$$f_\Theta = f_{\Theta,1} \cdot f_{\Theta,2} \tag{3.8}$$

$$f_{\Theta,1} = e^{-\left[(k_\Theta(\Theta-\Theta_{opt}))^2\right]} \tag{3.9}$$

$$f_{\Theta,2} = \begin{cases} 1, & \text{for } \Theta < \Theta_l \\ \frac{1}{2}(1+\cos\frac{(\Theta-\Theta_l)\pi}{\Theta_h-\Theta_l}), & \text{for } \Theta_l \leq \Theta \leq \Theta_h \\ 0 & \text{for } \Theta > \Theta_h \; . \end{cases} \tag{3.10}$$

The quantities k_Θ, Θ_{opt}, Θ_l and Θ_h are parameters to fit the relation to experimental data. Table 3.3 lists the corresponding parameters which are referred to in the simulations and for which the function is plotted in figure 3.6 together with data as reviewed by Meima et al. [162]. In set 1, one parameter choice is used for both reactions, whereas, in set 2 separate parameters are used assuming a lower optimum temperature. For the lysis of

Table 3.3: Parameters for temperature functions $f_{\Theta,1}$ and $f_{\Theta,2}$

	k_Θ (1/°C)	Θ_{opt} (°C)	Θ_l (°C)	Θ_h (°C)
		set 1		
0.030	57	70	80	
		set 2		
R1	0.030	20	50	70
R2	0.045	30	42	80

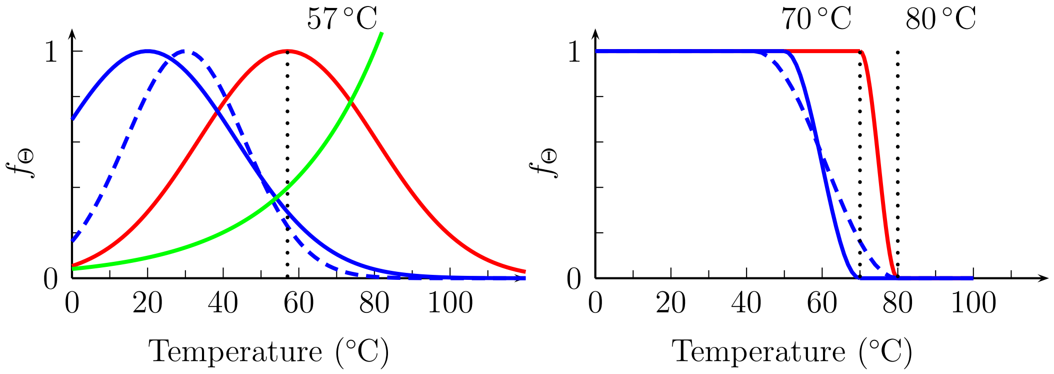

a) function f_1 with θ_{opt}=57 °C

b) function f_2 with θ_h =70 °C, θ_l =80 °C

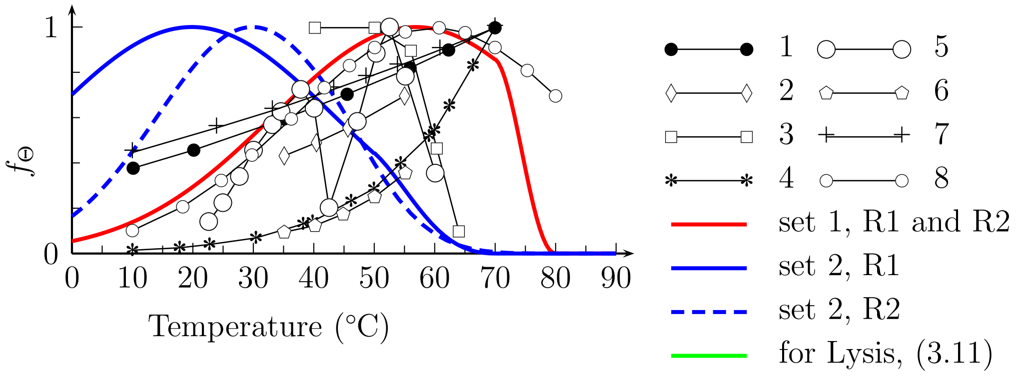

c) function $f_1 \cdot f_2$ with θ_{opt}=57 °C, θ_h =70 °C, θ_l =80 °C

Figure 3.6: Functions for considering influence of temperature on degradation rates. Curves 1 - 8 are taken from the review by Meima et al. [162]. Curves 2, 5 and 6 represent measured data, the remaining curves are plots of functions used by different researchers. Sets 1 and 2 are used in own simulations.

biomass, reaction L, a functional relation proposed by Haarstrick et al. [96] is used for $f_{\theta,L}$ with

$$f_{\Theta,L} = e^{k_{\Theta,L}(\Theta - \Theta_{opt,L})} , \tag{3.11}$$

whereas $k_{\Theta,L} = 0.04$ and $\Theta_{opt,L} = 80$ °C. Contrary to the other relations, the function's values exceed $f_\Theta = 1.0$ at high temperatures, considering that death of biomass proceeds faster. The relation is plotted in figure 3.6.

pH The review by Meima et al. shows that the optimum pH range of methanogenic bacteria, figure 3.7, is slightly lower than that of acidogenic bacteria, figure 3.8. In the coupled model, the evolution of pH is described by means of an ion balance which is already described in detail by Haarstrick et al. [95]. Due to the reduced number of components in the simplified reaction scheme, the pH value can be evaluated realistically for limited conditions only. The work by Reichel and Haarstrick [197] shows, however, that even with a detailed model, a correct description of pH throughout all stages of degradation is difficult. Some effects, like buffer capacity of the waste, are not completely clarified yet. For the influence of pH on degradation rate f_{pH} the relation

$$f_{pH} = \frac{K_{pH}}{K_{pH} + \frac{(10^{pH} - 10^{pH_{opt}})^2}{10^{(pH + pH_{opt})}}} \tag{3.12}$$

is applied according to Haarstrick et al. [95] with the parameters K_{pH} and pH_{opt}. Figure 3.9 shows the bell-shaped pattern of the pH function for different parameter sets. In general, the pattern is equal to the approach used by Reichel [196]. The parameter pH_{opt} determines the location of the symmetry axis of the bell-shaped curve and K_{pH} determines the width of the curve. Reichel assumes values of 7.35 and 220 for general anaerobic bacteria and 7 and 50 for methanogenic bacteria. Within this contribution, the latter set of parameters is used.

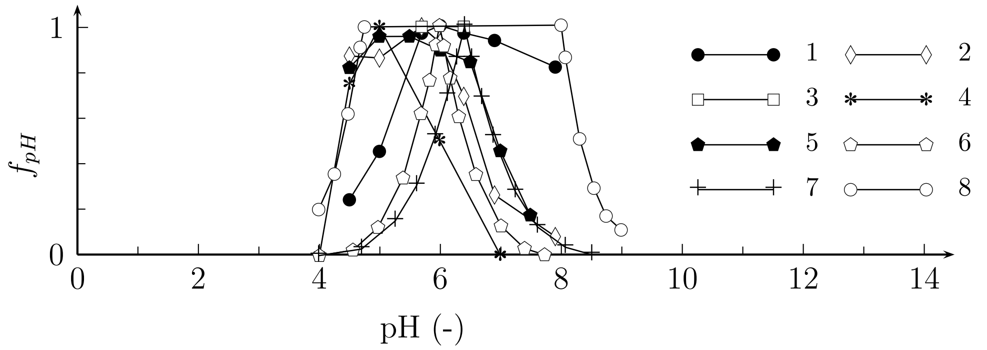

Figure 3.7: Influence of pH on degradation for anaerobic bacteria. Data 1-7 reviewed by Meima et al. [162], curve 8 used by Meima.

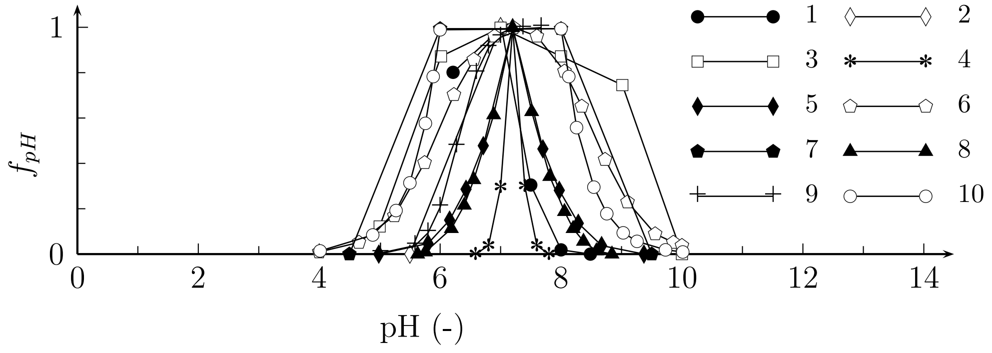

Figure 3.8: Influence of pH on degradation for methanogenic bacteria. Data 1-9 reviewed by Meima et al. [162], curve 10 used by Meima.

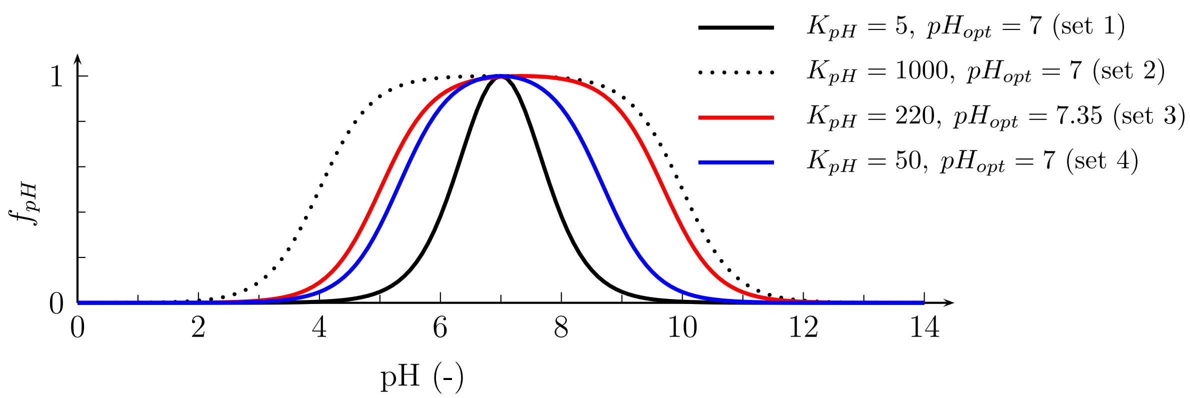

Figure 3.9: Plot of function f_{pH} used in this thesis for different parameter sets

Moisture Content Moisture content influences degradation rate via nutrient supply. Meima et al. [162] apply a linear function based on experimental data. Within this thesis, the following function is used

$$f_w = 1/2 + \frac{1}{\pi} \arctan\left[(w - w_{opt})\ F_W\right] \ . \tag{3.13}$$

The function f_w is plotted for different parameter sets in figure 3.10 in terms of mass on a wet mass basis together with the data shown by Meima. The parameter w_{opt} determines the water content at the inflexion point, whereas Fw determines the steepest slope. Wet moisture content is related to porosity and liquid saturation by

$$w_{wet} = \frac{S_l \phi \tilde{\rho}_l}{\rho_s + S_l \phi \tilde{\rho}_l} \ . \tag{3.14}$$

Thus, if porosity is increased due to loss of solid matter, the saturation decreases leading to a decrease of the rate. Contrary to the saturation, the water content does not change upon deformation (assuming no boundary flux, just due to geometry update). Therefore, by this formulation the magnitude of f_w is dependent on the contained mass of liquid and does not change upon geometry change.

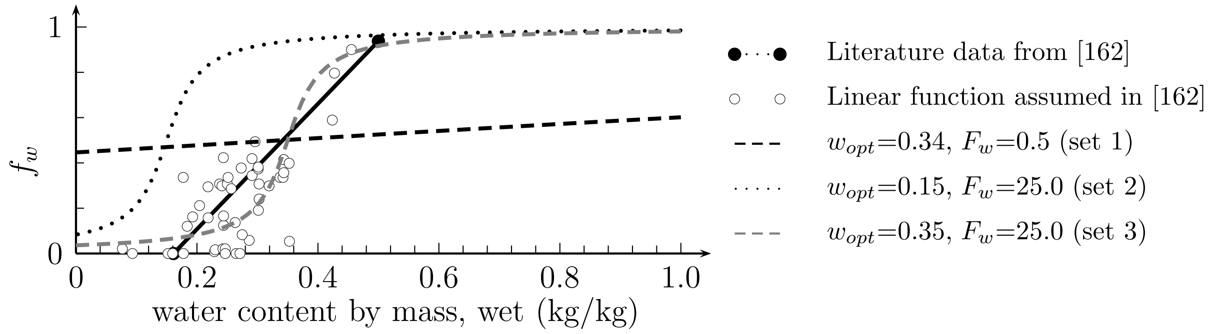

Figure 3.10: Influence function f_w for water content on degradation rate, different parameter sets compared with data from Meima et al. [162]

3.4 Simulation of a Lysimeter Experiment

The properties and applicability of the degradation model, as well as the influence of parameter choice, are investigated by a simulation of a lysimeter experiment. Comprehensive data about two consolidating anaerobic reactors, CAR, are presented by Beaven et al. [16]. Over a period of three years, fresh MSW samples are vertically loaded while degradation occurs simultaneously. During the test period, several quantities, e.g. settlement, gas and leachate composition, are measured on a regular basis. A detailed description of the set-up is given in section 7.2, in which the fully coupled analysis, including settlements and transport, is discussed.

The conditions in the lysimeter sample are regarded as being homogeneous allowing a local analysis of degradation. Using reactions R1, R2 and L from table 3.1 a system of coupled differential equations is formulated as follows

$$
\begin{array}{rcrlrlrl}
\dfrac{\partial \rho^{DO}}{\partial t} & = & - & 1.00\, r_1 & & & + & 1.00\, r_3 \\
\dfrac{\partial \rho^{\mathrm{H_2O}}}{\partial t} & = & - & 0.76\, r_1 & + & 0.49\, r_2 & & \\
\dfrac{\partial \rho^{Ac}}{\partial t} & = & + & 0.98\, r_1 & - & 1.00\, r_2 & & \\
\dfrac{\partial \rho^{\mathrm{CO_2}}}{\partial t} & = & + & 0.72\, r_1 & - & 0.06\, r_2 & & \\
\dfrac{\partial \rho^{\mathrm{CH_4}}}{\partial t} & = & & & + & 0.43\, r_2 & & \\
\dfrac{\partial \rho^{X}}{\partial t} & = & + & 0.06\, r_1 & + & 0.02\, r_2 & - & 1.00\, r_3\,.
\end{array}
$$

The system of ODEs is solved by means of the classical Runge-Kutta method. The parameters r_1, r_2 and r_3 represent the reaction rates determined by equations (3.5), (3.6) and (3.7), respectively. The rates are not constant but dependent on the concentration of the substrates. Different parameter sets are compared as listed in table 3.4.

For comparing experimental measurements of lysimeter CAR 1 with the simulation, the partial density of acetic acid (representing VFA) and the partial densities of the gas components are transferred to concentration (mg/l) and gas volume (l) respectively. This is possible since both sample size and liquid volume in the sample are known. The waste sample is regarded as being fully saturated over the entire duration of the test. The gas volume is computed from the mass of the components for a temperature of $\Theta = 30\,^\circ\mathrm{C}$.

Sets of four different parameter combinations are investigated. The initial conditions are based on the data from Beaven et al. [16] and listed in table 3.4 together with the kinetic parameters. The temperature is kept at constant 30°C. The pH is most times around pH=7 except in the early acidification stage and the column is completely saturated all times. Hence, environmental conditions remain nearly constant and the degradation rate

Table 3.4: Parameter sets for Simulation of CAR1

set	parameters, initial conditions	graph
set 1	$K^{DO,R1}$=80 kg/m^3; $K^{Ac,R2}$=4 kg/m^3; $\mu_{max,R1} = 1\,\mathrm{d}^{-1}$; $\mu_{max,R2} = 4\,\mathrm{d}^{-1}$; $\mu_{max,L} = 0.002\,\mathrm{d}^{-1}$; $\rho^{DO} = 51.3\,\mathrm{kg/m}^3$; $\rho^{\mathrm{H_2O}} = 621.6\,\mathrm{kg/m}^3$; $\rho^{Ac} = 1.5\,\mathrm{kg/m}^3 \cong 6000\,\mathrm{mg/l}$; $\rho^{\mathrm{CO_2}} = 0\,\mathrm{kg/m}^3$; $\rho^{\mathrm{CH_4}} = 120\,\mathrm{kg/m}^3$; $\rho^{X} = 0.01\,\mathrm{kg/m}^3$	⬛
set 2	like set 1, but $K_{S,R1}$=250 kg/m^3	🟦
set 3	like set 1, but $\mu_{max,R1} = 0.3\,\mathrm{d}^{-1}$	🟥
set 4	like set 1, but $\mu_{max,L} = 0.02\,\mathrm{d}^{-1}$	🟩

is not further reduced. The simulation with the basic set, set 1, shows that both acetic acid concentration and cumulative gas production can be described satisfactorily, see figure 3.11 (c) and (d). However, the peaks in the VFA concentration cannot be reproduced. In general, hydrolysis step is faster then methanogenesis step and, thus, acids may not accumulate. The approximation of gas production rate is satisfying in the beginning, approximately until the inflection point in the gas volume curve. Beyond this point, the gas production rate is overestimated by the model until ca. 200 days.

The single gas volumes of methane and carbon dioxide increase very quickly until the organic matter is almost completely decomposed after 200 days while a ratio of 60 % methane to 40 % per volume is maintained, figure 3.11 (e). Water volume decreases in correspondance to degradation in steps R1 and R2, see figure 3.11 (b).

Examining the simulations with set 2, set 3 and set 4, an overall perfect approximation seems unobtainable using the simplified model. On account of only one type of organic matter with a unique decomposition rate and of a single biomass, degradation rate is too high in the later stages. In fact, the used waste is supposed to consist of different organic fractions which are more or less readily degradable. Thus, the reaction rate $\mu_{max,R1}$ is not a constant material quantity. Instead, it may be assumed that the readily degradable fractions are decomposed very quickly in the lysimeter while the microorganisms need more time to process the moderate or least degradable fractions. Furthermore, different biomass populations exist, as explained in section 3.1.

From the evolution of mass of organic matter, figure 3.11 (a), it is observed that the rate, as given with the Monod kinetic, is increased further depending on the parameter set. This increase is due to the accelerating effect of biomass. The evolution of biomass, figure 3.11 (f), shows that its concentration is increasing during the process, which accelerates the three reaction steps. As a single biomass is considered in the model, the process is to some extent self-accelerating. If, for example, biomass is produced in step R1, the rates of all other steps are increased as well. After all organic matter is decomposed, the biomass is not growing any more but dies with a decreasing rate, eq. (3.7) and figure 3.11 (f).

The change of the maximum reaction rate of reaction R1 in set 3 influences the overall process in two ways. Firstly, as the rate of R1 is less in set 3 compared to set 1, the production of the corresponding educts is slowed down. Secondly, as both less acetic acid and biomass are produced in a certain time interval, also the rate of the processes R2 and L are influenced via the kinetic description, although the reaction rates $\mu_{max,R2}$ and $\mu_{max,L}$ are not changed. The magnitude of the influence of biomass is also dependent on the yield coefficient as it determines how much biomass is produced during the steps. A constant biomass is used by Hanel [99] in the reduced model.

The influence of the magnitude of the Monod constant is analysed by comparing the results for set 1 and set 2. The increase in Monod constant leads to a decrease of decomposition rate, both of R1 and R2, via the coupling over the biomass.

A very interesting effect can be observed by comparing set 1 and set 4. An increase of the lysis rate leads to a faster decay of the microorganisms. Thus, cumulative gas production and decay of organic matter is slowlier in the beginning compared to the basic case set 1. After a maximum at about 300 days, the biomass decays totally, so that all other degradation processes stop as well. This indicates that the biomass decay rate exceeds its growth rate for the particular parameter set.

A further effect is observable in the simulations for sets 1-3. Beyond the time, when all organic matter is degraded, still gas is produced. The explanation for that is the formulation of lysis stoichiometry, reaction L, in table 3.1. The biomass decays to organic matter and in that way increases the stock of substrate which is then further decomposed in steps R1 and R2. The analyses show that the reactions and their corresponding kinetic laws are coupled in several ways making the correct choice of parameters a challenging task.

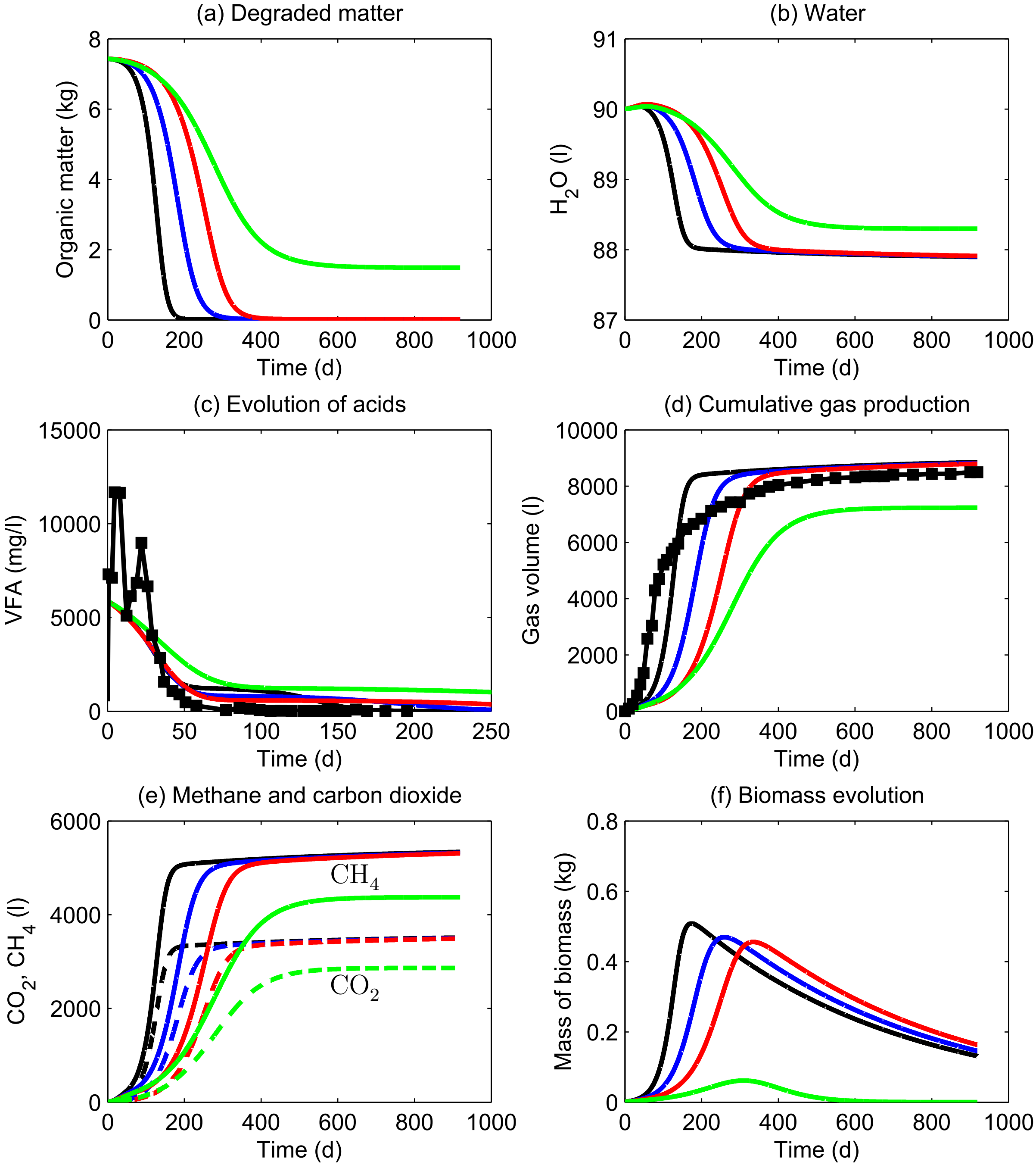

Figure 3.11: Comparison of different parameter sets for simulation of the CAR experiment, legend included in table 3.4

3.5 Heat Generation

Both reactions are supposed to be exothermic. In general less heat arises from anaerobic than from aerobic processes. Generated heat is transported convectively and by thermal conduction. Heat conduction due to a gradient in temperature is described by means of Fourier's law which defines the heat flux q (W/m^2) dependent on the thermal conductivity λ_s by

$$q = -\lambda_s \cdot \text{grad } \Theta \; . \tag{3.15}$$

Dach et al. [44] summarise all mechanisms of heat transport, i.e. diffusion, radiation and conduction, by an equivalent heat conductivity. In this thesis, the mechanisms are treated separately, whereas conduction, convection and diffusion are considered yet, see also (6.9).

3.5.1 Reaction Enthalpies

The energy, which is released in chemical reactions, is called reaction energy and can be split up into volume work and reaction enthalpy, which is released in form of heat. The reaction enthalpy under standard conditions $\Delta \mathrm{H}^0_R$ is the sum of the standard formation enthalpies $\Delta \mathrm{H}^0_f$ of the products minus the corresponding sum of the educts

$$\Delta \mathrm{H}^0_R = \Sigma \Delta \mathrm{H}^0_f \text{ (products)} - \Sigma \Delta \mathrm{H}^0_f \text{ (educts)} \; . \tag{3.16}$$

The standard formation enthalpies are dependent on the aggregate state and tabulated for many components. Table 3.5 lists standard formation enthalpies for the components of the reaction scheme with respect to the derivation in table 3.1. Tabulated values for the formation enthalpy of organic matter are not found in the literature. Hanel [99] assumes reaction enthalpies of −37 075 kJ per kg organic matter and −23 300 kJ per kg acetic acid for steps R1 and R2, respectively, which seems quite high compared to a reaction energy of −686 kcal/mol, equivalent to −15 932 kJ/kg, for aerobic degradation of glucose.
In general, heat generation may vary as it depends on the elemental composition of organic matter. In this thesis, published values on heat generation as reviewed by Yesiller et al. [245] are used to derive the standard formation enthalpy of organic matter for the selected molecular formula $C_{30}H_{53.4}O_{14}N_{0.7}$.
Based on organic matter composition, first the stoichiometry for the complete conversion reaction, excluding any biomass growth, is derived, see table 3.6. The corresponding enthalpies for each component, including the stoichiometric coefficients, are given as well. Only the enthalpy of organic matter, $\Delta \mathrm{H}^0_{f,DO}$ is unknown. It is back calculated for several values of heat generation, a)-g) in table 3.7. The back calculation suggests values for the formation enthalpy between −4961.24 kJ/kg and 6636.88 kJ/kg. Next, those values are inserted in the reaction scheme used herein, as shown in table 3.8.

Table 3.5: Standard formation enthalpies of components

component	state	molar mass (g/mol)	ΔH_f^0 (kJ/mol)	ΔH_f^0 (kJ/kg)	Source
H_2O	(l)	18.0152	−285.9	−15 869.932 06	[171]
$C_6H_{12}O_6$	(s)	180.1572	−1268.3	−7038.297 66	NIST
NH_3	(g)	17.0304	−46.19	−2712.208 76	[171]
H_2	(g)	2.0158	element in its most stable form, value=0		
CO_2	(g)	44.0098	−393.5	−8941.190 37	[171]
$C_2H_4O_2$	(l)	60.0520	−484	−8059.681 61	NIST
CH_4	(g)	16.0425	−74.6	−4650.148 04	NIST
$C_5H_7NO_2$	(s)	113.1158	−500	−4420.25	estimated[1)]
$C_{30}H_{53.4}O_{14}N_{0.7}$	(s)	647.948	derived in tables 3.6 to 3.8		

NIST: National Institute of Standards and Technology, Chemistry WebBook, http://webbook.nist.gov/chemistry/, access in December 2009

[1)] estimated from formation enthalpies from NIST for solid components with same molecular formula

Table 3.6: Stoichiometry for total reaction of anaerobic degradation and corresponding formation enthalpies

Stoichiometry of complete reaction in terms of mol and kg					
1.0 $C_{30}H_{53.4}O_{14}N_{0.7}$ +	10.175 H_2O →	12.087 CO_2 +	17.913 CH_4 +	0.700 NH_3	(mol)
1.0	0.283	0.820	+ 0.443	+ 0.018	(kg)
Enthalpies for stoichiometry in terms of mol and kg					
$\Delta H_{f,organic}^0$	−2909.03	−4756.23	−1336.31	−32.33	(kJ,mol)
$\Delta H_{f,organic}^0$	−4484.29	−7331.76	−2059.93	−49.84	(kJ,kg)

Table 3.7: Derived standard formation enthalpies for organic matter based on data published in Yesiller et al. [245]

	Source	heat generation	reaction enthalpy (kJ/mol OM)	formation enthalpy $\Delta H_{f,DO}^0$ (kJ/mol)	formation enthalpy $\Delta H_{f,DO}^0$ (kJ/kg)
a)	Pirt (1978)	-68 J/mol CH_4	-1.22	-3214.63	-4961.24
b)	Tschobanoglous (1993)	-5450 kJ/kg OM	-3531.32	315.47	486.88
c)	El-Fadel (1996)	-3163 kJ/kg OM	-2049.46	-1166.38	-1800.12
d)	El-Fadel (1996)	-265 kJ/mol CH_4	-4746.95	1531.1	2363.00
e)	El-Fadel (1996)	-109 kJ/mol CH_4	-1952.52	-1263.33	-1949.74
f)	Yoshida and Rowe (2003)	-43.5 kJ/mol CH_4	-779.22	-2436.63	-3760.53
g)	Tschobanoglous (1993)	-11600 kJ/kg OM	-7516.20	4300.35	6636.88

OM = organic matter

Table 3.8: Application of derived enthalpies on stoichiometry of simplified scheme

Stoichiometry (kg) and enthalpies (kJ) for step R1						
1 $C_{30}H_{53.4}O_{14}N_{0.7}$	+ 0.76 H_2O	→ 0.72 CO_2	+ 0.98 $C_2H_4O_2$	+ 0.06 $C_5H_7NO_2$		
-4,961.24					2,443.1	a)
-486.88					-3,005.02	b)
-1,800.12					-718.02	c)
2363	-12,087.80	-6,426.6	-7904.64	-274.7	-4,881.14	d)
-1,949.74					-568.41	e)
-3,760.53					1,242.39	f)
6,636.88					-9,155.02	g)
Stoichiometry [kg] and enthalpies [kJ] for step R2						
1 $C_2H_4O_2$	→ 0.49 H_2O	+ 0.06 CO_2	+ 0.43 CH_4	+ 0.02 $C_5H_7NO_2$		
-8,059.63	-7,798.08	-566.34	-2,000.34	-66.81	-2,371.94	
Stoichiometry [kg] and enthalpies [kJ] for total reaction R						
1 $C_{30}H_{53.4}O_{14}N_{0.7}$	+ 0.28 H_2O	→ 0.78 CO_2	+ 0.42 CH_4	+ 0.08 $C_5H_7NO_2$		
-4,961.24					116.77	a)
-486.88					-5331.35	b)
-1,800.12					-3044.35	c)
2363	-4,439.68	-6,982.05	-1,961.87	-340.23	-7207.47	d)
-1,949.74					-2894.74	e)
-3,760.53					-1083.94	f)
6,636.88					-11,481.35	g)

Table 3.9: Heat capacities $c_{p,\pi}^{\beta}$ of solid, liquid and gaseous components (kJ/(kg · K))

$c_{p,g}^{H_2O} = 1.80$	$c_{p,l}^{H_2O} = 4.18$	$c_{p,s}^{DO} = 0.8$
$c_{p,g}^{CO_2} = 0.82$	$c_{p,l}^{CO_2} = 4.18$	$c_{p,s}^{IM} = 0.8$
$c_{p,g}^{CH_4} = 2.19$	$c_{p,l}^{Ac} = 2.05$	$c_{p,s}^{X} = 0.8$

Data for fluid components taken from NIST,
National Institute of Standards and Technology, Chemistry WebBook,
http://webbook.nist.gov/chemistry/, access in December 2009.

The application whithin the proposed reaction scheme provides much lower values than those used by Hanel [99]. For R1 the highest heat release is −9155 kJ/kg, for the total reaction R it is −11 481.35 kJ/kg. Some sets, a) and f), result in endothermic conditions. Finally, set c) is chosen for all further analyses.

3.5.2 Heat Capacity

Heat capacities are required for determination of stored energy and are listed for the single components in table 3.9. The heat capacity of the solid components is chosen similar to soil. A detailed derivation analog to the heat conductivity would be possible as well.

3.5.3 Heat Conductivity of the Porous Mixture

For evaluation of the heat flux according to (3.15), knowledge of heat conductivity λ_s is essential. Hence, a macroscopic quantity describing the heat conductivity of the waste mixture, λ_{eff}, has to be determined. A discussion on heat conductivity in porous media is given for example by Kaviany [121]. The heat conductivity of a porous material is dependent on the conductivity of the constituents and on their volume fractions n^α. The conductivity of the solid phase of the waste itself is dependent on the solid components and derived in section 3.5.4. Additionally, the overall effective conductivity is influenced by porosity and liquid saturation. Often, the lower and upper Wiener bounds, λ^L and λ^U, are used to assess the limits of macroscopic heat conductivity. They are based on the assumption of a parallel or serial connection of the constituents respectively, so that

$$\lambda^L = \left(\sum_{\alpha=1}^{n} \frac{n^\alpha}{\lambda^\alpha} \right)^{-1} \text{ (in series) } \quad \text{and} \quad \lambda^U = \sum_{\alpha=1}^{n} n^\alpha \lambda^\alpha \text{ (in parallel)} \,. \tag{3.17}$$

The conductivity takes its lowest value for a serial connection of all materials, figure 3.12 a), and its highest value for a parallel alignment, figure 3.12 b). The Wiener bounds are independent of the pore structure and thus applicable on any porous medium, Tong et al. [228]. The final, effective conductivity is interpolated between λ^L and λ^U using the parameter η_λ. This represents again an interpolation between a serial and a parallel connection of the alignments corresponding to the Wiener bounds, see figure 3.12 c) and d).

$$c) \;\; \lambda_{eff.} = (1-\eta)\lambda^L + \eta_\lambda \lambda^U \quad \text{or} \quad d) \;\; \lambda_{eff.} = \left(\frac{(1-\eta)}{\lambda^L} + \frac{\eta_\lambda}{\lambda^U} \right)^{-1} \,. \tag{3.18}$$

More detailed combinations can be defined straightforward. In this thesis, the first formulation of (3.18) is applied, whereas the parameter η_λ is chosen to $\eta_\lambda = 0.75$. Dach et al. [44] apply the second approach in his model for waste. A detailed comparison of the approaches may be the subject of further investigations, but is not within the scope of this thesis. The conductivities of the fluid phases are assumed to be $\lambda_l = 6.15 \times 10^{-04}\,\mathrm{kW/(m \cdot K)}$ and $\lambda_g = 2.77 \times 10^{-05}\,\mathrm{kW/(m \cdot K)}$. Additionally, a heat-transmission resistance coefficient of $\alpha_t = 0.05\,(\mathrm{m^2 \cdot K)/W}$ at outer heat flux boundaries is assumed.

3.5.4 Heat Conductivity of the Solid Phase

The derivation of solid phase heat conductivity is based on the composition of the waste used in the CAR experiments and on data for waste from the city of Neumünster shown by Sigel [216] (NMS waste), see charts 3.13 and 3.14. Thermal conductivities and densities of different (waste) materials are given in Miller and Clesceri [164] and are listed in tables 3.10 and 3.11 for the corresponding fractions. The conductivity of the solid phase is derived at

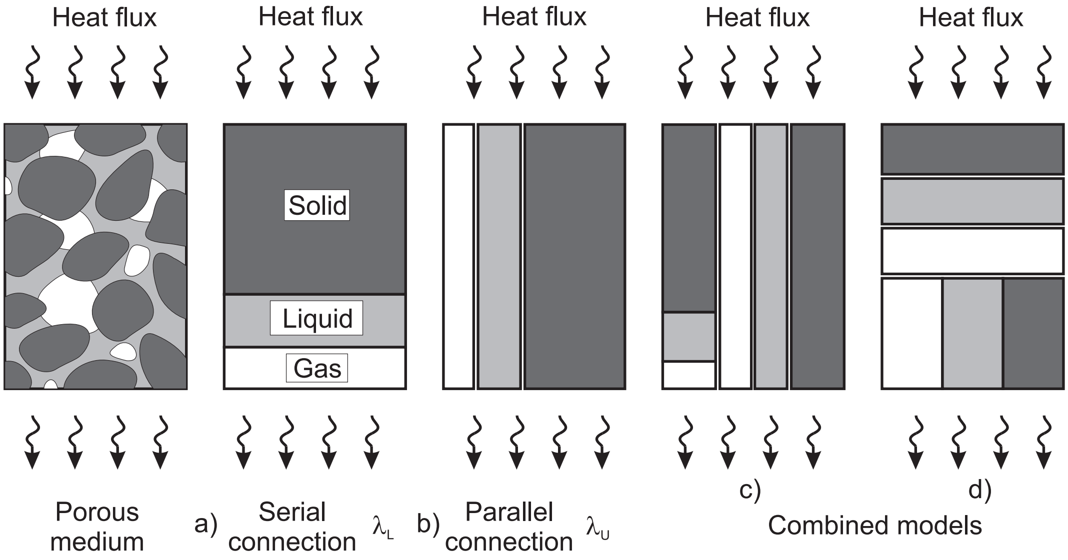

Figure 3.12: Heat conductivity models for porous media, after Tong et al. [228]

the lower and upper Wiener bounds, λ_s^L and λ_s^U, according to (3.17). Simultaneously, the intrinsic solid density is derived. As the solid particles are assumed to be incompressible, their conductivity is not a function of stress. An additional dependence on temperature is not considered as well.

For the CAR waste, an intrinsic density of $\tilde{\rho}_s = 870\,\mathrm{kg/m^3}$ is obtained, whereas, for the Neumünster waste (NMS) the density is $\tilde{\rho}_s = 1042\,\mathrm{kg/m^3}$. The effective solid thermal conductivity is between $0.104\,\mathrm{W/(m\cdot K)}$ and $3.264\,\mathrm{W/(m\cdot K)}$ for the CAR and between $0.103\,\mathrm{W/(m\cdot K)}$ and $0.265\,\mathrm{W/(m\cdot K)}$ for the Neumünster waste. The range for the NMS waste is considerably low mainly due to the lower fraction of metals. For the CAR waste, it is assumed that the metal fraction is contributed by a value of 5 % to Aluminium. The plastic fraction of the NMS waste is attributed to light and heavy plastic one half each. It has to be emphasised that the intrinsic density and the conductivity are, of course, dependent on the intrinsic densities of the components which are partly difficult to estimate, e.g. for food. The obtained data is thus recognised to be within an realistic range. For the computations later on, a heat conductivity of $\lambda_s = 0.150\,\mathrm{W/(m\cdot K)}$ is assumed if not stated elsewise.

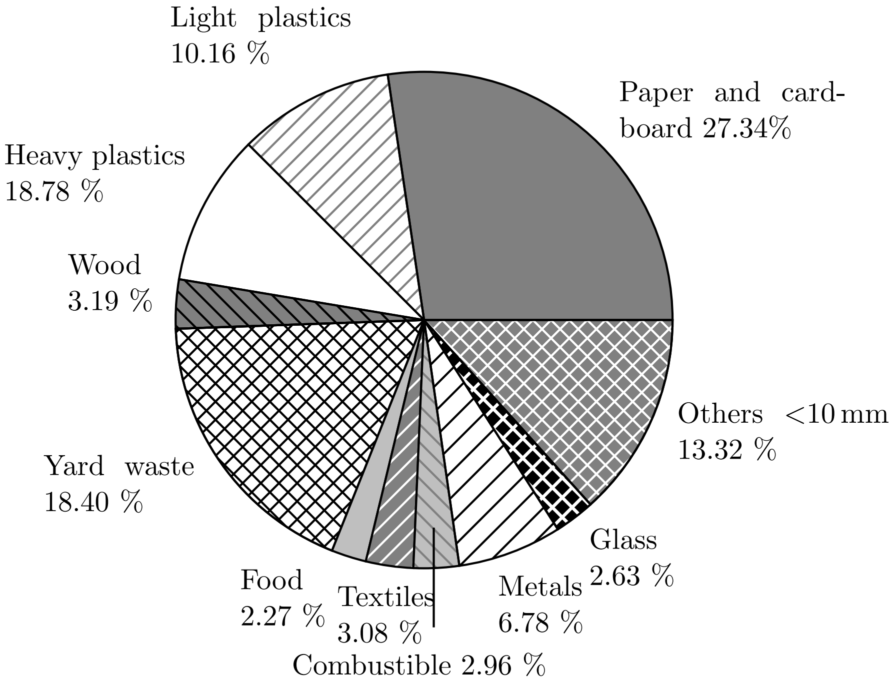

Figure 3.13: Composition of waste used in CAR experiments, mass fractions by dry weight, Ivanova [118]

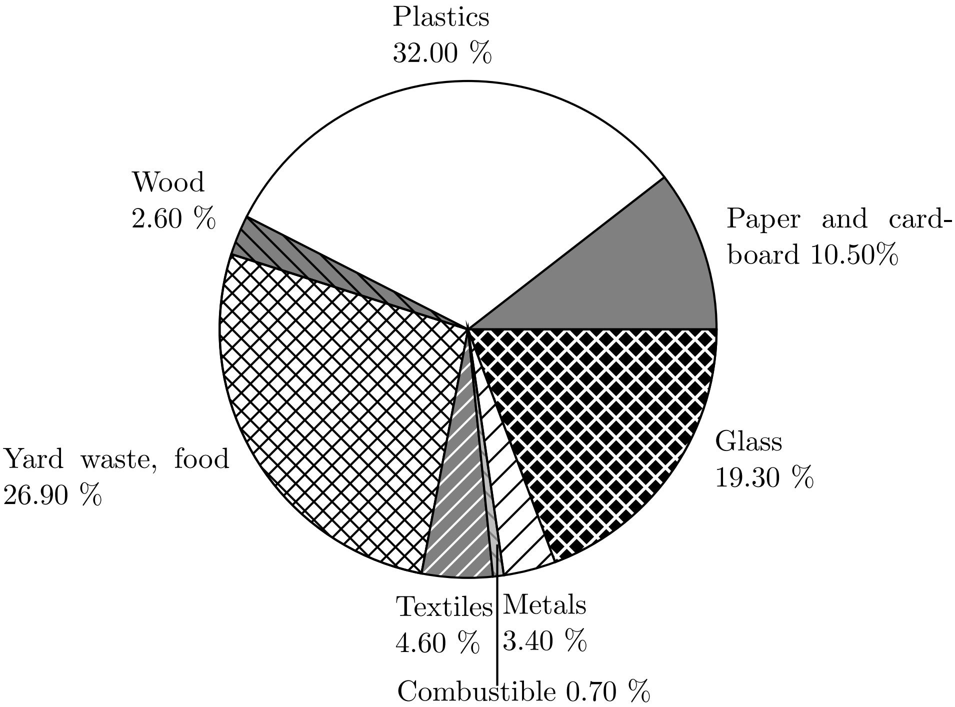

Figure 3.14: Composition of waste from Neumünster, mass fractions by dry weight, Sigel [216]

Table 3.10: Mass fractions in CAR test, for determination of $\tilde{\rho}_s$ and λ

					λ_s^L	λ_s^U
MSW fraction	Conductivity λ (W/(m · K))	Intrinsic density $\tilde{\rho}$ (kg/m^3)	Mass fraction (%)	Volume (m^3)	volume fraction times lambda (W/(m · K))	volume fraction div. by lambda ((m · K)/W)
Food	0.05	1100	2.27	0.002	0.001	0.359
Paper, cardboard	0.14	920	27.34	0.030	0.036	1.846
Heavy plastics	0.16	920	9.87	0.011	0.015	0.583
Light plastics	0.16	600	10.16	0.017	0.024	0.920
Textiles	0.33	1300	3.08	0.002	0.007	0.062
Yard waste	0.05	700	18.40	0.026	0.011	4.572
Wood	0.15	800	3.19	0.004	0.005	0.231
Glass	0.77	2500	2.63	0.001	0.007	0.012
Metals	16.00	7000	1.78	2.54e-4	0.035	1.38e-4
Aluminium	192.17	2700	5.00	0.002	3.095	8.38e-5
Fine fraction others	0.16	900	13.32	0.015	0.021	0.805
Combustibles	0.16	600	2.96	0.005	0.007	0.268
Sum			**100.00**	**0.115**	**3.264**	9.660
reciprocal						**0.104**

Table 3.11: Mass fractions in NMS waste, for determination of $\tilde{\rho}_s$ and λ

					λ_s^L	λ_s^U
MSW fraction	Conductivity λ (W/(m·K))	Intrinsic density $\tilde{\rho}$ (kg/m^3)	Mass fraction (%)	Volume (m^3)	volume fraction times lambda (W/(m·K))	volume fraction div lambda ((m·K)/W)
Food	0.05	1100	20.00	0.018	0.009	3.648
Paper, cardboard	0.14	920	10.50	0.011	0.017	0.818
Heavy plastics	0.16	920	16.00	0.017	0.029	1.091
Light plastics	0.16	600	16.00	0.027	0.044	1.672
Textiles	0.33	1300	4.60	0.004	0.012	0.108
Yard waste	0.05	700	6.90	0.010	0.005	1.978
Wood	0.15	800	2.60	0.003	0.005	0.217
Glass	0.77	2500	19.30	0.008	0.062	0.101
Metals	16.00	7000	3.40	4.86e-04	0.081	0.0003
Aluminium	192.17	2700				
Fine fraction, others	0.16	900				
Combustibles	0.16	600	0.700	0.001	0.002	0.076
Sum			**100**	**0.096**	**0.265**	9.706
reciprocal						**0.103**

4 Constitutive Model for Multiphase, Multicomponent Transport in Waste

As described by figure 2.1, waste is a porous medium with two phases filling the pore space: a gas phase (the landfill gas) and a liquid phase (the leachate). In general, states between full saturation and dry conditions are possible, compare also (2.4). However, if a landfill is equipped with a working drainage system, the waste is likely to be unsaturated at most times. Local saturated conditions may occur due to intermediate layers with low hydraulic conductivity.

Products of the degradation processes influence the composition of both the liquid and the gas phase, cf. figure 3.3. The components of the phases are transported with the phase velocity which is termed convective transport. Several effects may cause a deviation of purely convective transport. Triggered by Brown's molecular movement, components are also transported by diffusive processes if gradients in concentration are present. Additionally, transport relative to the phase velocity may be caused by dispersion, whereby components are diverted around the solid particles. Longitudinal and Lateral dispersion are distinguished. Retardation describes the retention of components, for example due to sorption.

Considering that the fluid phases of MSW are composed of several components, multiphasic, multicomponent transport has to be modelled including description of phase changes. As in description of mechanical phenomena, approaches from soil mechanics are often applied on waste. The following sections show the hydraulic properties of municipal solid waste in detail and explain the selected modelling approach after a brief review of existing models in section 4.1. Section 4.2.2 includes a description and discussion of own experiments on the moisture retention behaviour of MBT waste performed in cooperation with Edinburgh Napier University.

4.1 Models for Transport Processes in Waste

Key issues of developed models are the description of water balance, leachate chemistry, moisture movement and gas transport. A basic difference between many leachate models is the treatment of the landfill body itself. Some models focus on the water balance of the entire landfill only. The moisture distribution within the waste body itself is not described but only the balance of fluxes into and out of the waste body. This approach is often called *water balance method*. Other models additionally describe the transport process within the waste by a spatial discretisation of the landfill body. Those models are sometimes termed *distributed models.*

Both types of models are developed and analysed by Straub and Lynch [221]. The authors compare a model, that treats a waste volume as a single well-mixed reactor with a one-dimensional model based on solution of Richards' equation by means of a finite difference scheme and explicit time integration. For describing unsaturated conductivity data obtained for a fine grained soil is used, as sufficient data for MSW is not available at that time. The model is validated using data from a lysimeter experiment and later extended to include influence of degradation processes, see [222].

Similarly, the model by Korfiatis et al. [134] for flow processes in refuse solves Richards' equation. The difficulties with an explicit time discretisation scheme, like also used by Straub and Lynch, are discussed and an implicit scheme is chosen. Korfiatis et al. also face a lack of data on water retention behaviour of waste, and so an experimental leaching column is set up for validation of their model. Rainfall events are simulated by controlled moisture input. The column is equipped with tensiometers to monitor suction over refuse depth. With the same material, one of the first moisture retention curve for waste is determined in separate experiments. From tensiometer readings, the occurence of channeling is concluded. Later, a sensitivity analysis is conducted by Demetracopoulos et al. [49] to analyse the influence of grid size and time stepping as well as permeability and diffusivity on the results.

One of the most popular water balance models is presented in the early 1980s under the name *Hydrologic Evaluation of Landfill Performance Program* HELP, cf. Schroeder et al. [212]. HELP is widely used in engineering practice. It describes the two dimensional water flow through a landfill and considers various effects on the water balance like surface storage, snowmelt, surface runoff, infiltration, evapotranspiration and leachate recirculation. Various combinations of vegetation, cover soils, waste cells and liner systems may be modelled. Different layer types account for vertical gravity driven percolation and lateral drainage. Thereby, unsaturated hydraulic conductivity is considered.

Noble and Arnold [183] present the one dimensional finite difference model FULFILL which solves Richards' equation in one dimension. For validation of the model, a vertical infiltration experiment and a capillary rise experiment are conducted in a laboratory column. Shredded paper serves as a substitute for MSW. Both a power law and an exponential relationship are used to describe the dependency of permeability and suction on saturation. The authors correlate their results to the Washburn equation for capillary flow. The experiments show the significance of capillary effects on moisture flux.

In their model FILL, Khanbilvardi et al. [124] solve Richards' equation for two dimensions including surface runoff, snowmelt and evaporation. FILL is used to simulate leachate flow in a landfill site, and the results are compared with those obtained by HELP and a model by US EPA. Their results show that the correct description of surface runoff and evaporation are of high importance. Similar issues are discussed by Murphy and Garwell [178] who review water balance models developed between 1980 and 1994. They analyse a laboratory scale model of a final cover system considering surface runoff, infiltration and leakage.

McDougall et al. [159] solve Richards' equation in two dimensions by means of the finite element method. The authors apply a soil moisture characteristic curve and a relative permeability function derived from tests on a mixture of partially humified peat and cocoa shells. The model is verified using literature data on column tests. One novel aspect of their model is that it allows for description of the infilling process of a landfill by a successive activation of finite elements. In a series of tests, the model is used to simulate moisture distribution in an idealised landfill site geometry using rainfall statistics. A discussion of their contribution, see [160], indicates the need for a fully coupled model, so that variation of hydraulic conductivity dependent on stress and degradation state can be modelled. Whereas many researchers apply numerical methods, in some cases also analytical solutions are available for certain initial and boundary conditions are applied. For instance, Shackelford and Glade [213] describe mass leaching in contaminated soil laboratory columns. They consider advection, dispersion and retardation of components with the aim of modelling solute breakthrough curves (BTC) in column testing.

Breakthrough curves obtained in column testing may indicate the occurence of preferential flow in waste, like observable in structured soils. A general review on channeling flow is for example given by Brusseau and Rao [33]. Motivated by previous observations by researchers, Uguccioni and Zeiss [231] are among the first to model moisture movement in MSW including preferential flow. They compare the HELP model and PREFLO, a two-domain model for unsaturated flow in fractured porous media. Based on their findings, the authors recommend development of a novel approach for leachate prediction in MSW considering two-domain flow.

Similarly, Bendz et al. [18] assume that the flow pattern in landfills consists of mainly convective flow of mobile water in a channel domain and transport within a matrix domain where capillary forces and diffusion are dominant. Vertical flow in the matrix domain is neglected. A mass transfer between the two domains is included. Bendz and Singh [17] calibrate the previously developed model using breakthrough curves of tracer experiments in a waste column.

McCreanor and Reinhart [156] apply the SUTRA model developed by United States Geological Survey to describe recirculation. Heterogeneous properties of the waste are described by a statistical distribution of hydraulic conductivity. Cases with isotropic and anisotropic conductivity are compared. The authors verify their approach using data from landfill sites with a recirculation system. They point out that channeled flow is a major mechanisms for which not much knowledge exists yet.

Preferential pathways in MSW are addressed by Rosqvist and Destouni [201] in a study on lithium transport through both a biodegraded solid waste sample and a pilot-scale landfill. Tracer tests with lithium are conducted and the resultant breakthrough curves (BTCs) are analysed using a probabilistic approach. BTC patterns indicate a rapid flow through preferential paths followed by slow flow in domains with less mobile water. Additionally, exchange between the domains by diffusion is likely to occur. The site tests show that quite a high amount of tracer is displaced laterally, indicating an anisotropic permeability of the waste. It is concluded that models which treat waste as a homogeneous porous medium are not sufficiently appropriate.

Extending the dual-domain approach , also triple porosity models may be developed as shown by Bai and Roegiers [9].

Oonk and Woelders [188] point out the impact of preferential flow in landfills as well. Furthermore they state that integrated models are needed and that research on hydrologic properties of waste has to be increased.

The review shows that the significance of preferential flow in waste is widely recognised, whereas in practice Darcy type models are often used. For description of multiphase flow, knowledge on moisture retention behaviour of waste is needed. Still, there are only a few data sets available, partly because experiments are in general difficult with waste material. By solving Richards' equation, liquid flow in the unsaturated zone is described by a flow of the liquid phase only, whereas the influence of air movement is not directly considered. The procedure implies that no gas pressure gradients occur as the gas phase is free to move in any case. Schrefler et al. [210] pick up the findings of other researchers, that this assumption is not appropriate in every case and develop a model for unsaturated consolidation including multiphase flow. The explicit consideration of the gas phase in landfills is important if gas pressure rise due to degradation is considered and if it cannot be assumed in any case that gas leaves the waste instantaneously.

For a more comprehensive overview of transport models the reader may be referred to the reviews by El-Fadel et al. [66], [67], and [68], or Kazimoglu [122].

4.2 Moisture Storage in Waste

The moisture storage properties of waste are very important for modelling and discussed here in a special section as they are different to those of most soils or other porous media. For an overview of soil hydraulic properties the reader may be referred to Fredlund [84], Durner and Flühler [57] and others.

4.2.1 Porosity and Pore Structure

The observation of preferential flow in experiments on waste indicates special characteristics of the waste's pore structure. Whereas soil particles represent a pure solid itself, so that the pore space is mainly the volume between the particles, sometimes termed *inter-*

particle pore volume, the individual particles of waste may exhibit an *intraparticle* pore space as well, which is formed by very small or even closed pores within the visible solid particles. In that sense, also *micropores* and *macropores* are often distinguished, which is however not a unique definition, if no distinct pore size limits are given.

Correspondingly, the fluid phases in MSW may exist in a free form and in a bounded form, being trapped in closed pores and isolated from the fast convective transport in the larger macropores. The liquid can then also be regarded as being part of the solid material, see figure 4.1. Correspondingly, different quantities describing porosity may be distinguished, such as *total porosity*, *drainable porosity* or *effective porosity*. The moisture retention properties of waste cause that often a waste sample visibly appears more dry as a soil sample of same water content.

The existance of a micropore system is proven by measurements of *field capacity*. This quantity is of high importance for engineering practice to estimate the amount of leachate retained by the waste, although a clear definition is often lacking, see De Velásquez et al. [48]. McDougall et al. [161] observe that gravimetric moisture content remains unaffected from overburden pressure at low stresses as the water is stored in the micropores and mainly the macropore systems is compressed first. Similarly, the measurements by Blight et al. [27] show only small changes in field capacity for unit weights from $2.5\,\mathrm{kN/m^3}$ to $12.6\,\mathrm{kN/m^3}$. As described in section 4.1, the tailing of breakthrough curves in tracer experiments is often attributed to a micro-/macropore regime, e.g. by Rosqvist and Destouni [201]. Total porosity is not constant but dependent on the compaction state of the material.

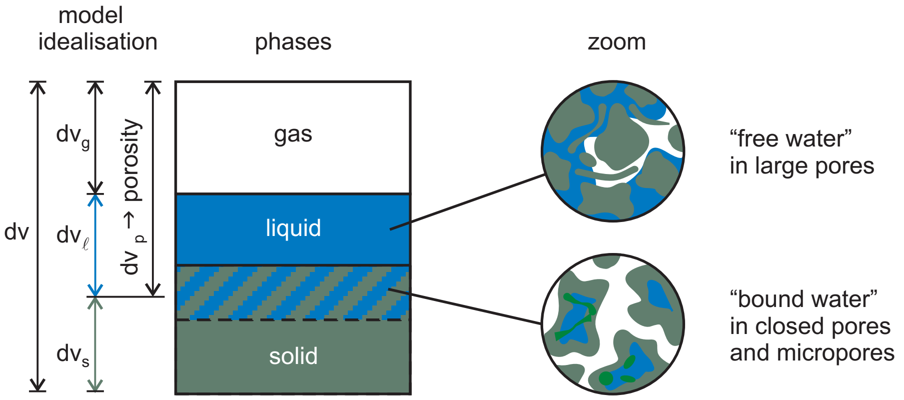

Figure 4.1: Model of moisture storage in MSW, [167]

If degradation processes are neglected, compaction may be caused by the compressibility of the granular skeleton and by the compressibility of the solid particles. At this point, it is very important to clarify the *definition of a solid waste particle*. Within this contribution, a solid particle refers to the solid phase itself. The intraparticle pore space is attributed to the total pore space, and it is assumed that the solid grains are incompressible. Thus, for the case that no mass exchange with the solid phase occurs, the porosity on the current configuration is dependent on the deformation only. The whole volume change $\Delta v = dv - dV_0$ of a control volume of the mixture results in a corresponding

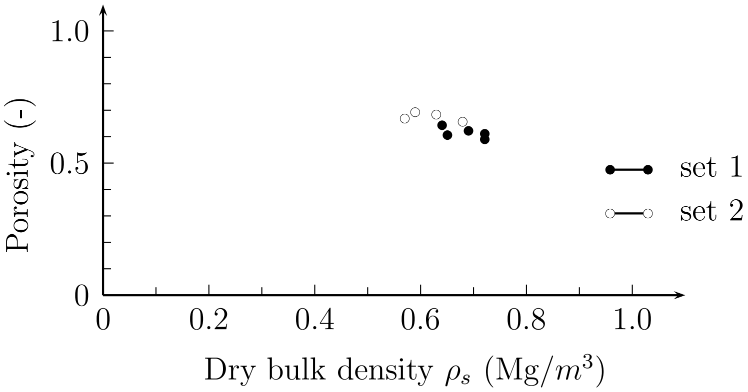

Figure 4.2: Porosity values measured by Bente and McDougall [20]

volume change of the pore space. The current porosity ϕ can then be derived from the initial porosity ϕ_0 using (2.3) and (2.10) to

$$\phi = \frac{dV_0^p + \Delta v}{dV_0 + \Delta v} = \frac{dV_0\phi_0 + dv - dV_0}{dv} = 1 + (\phi_0 - 1)\frac{dV_0}{dv} = 1 + \frac{(\phi_0 - 1)}{\det \mathbf{F}_s} \ , \qquad (4.1)$$

where dV_0 and dV_0^p represent initial volume and initial pore volume, respectively, and where dv is the current volume of a REV. When the volume change equals the initial pore volume, the porosity becomes zero. This state is related to the intrinsic density $\tilde{\rho}_s$. Alternatively, approaches may be applied that separate compressibility of the grains and of the solid skeleton by a multiplicative split of the deformation gradient, see de Boer [47]. If solid mass loss due to degradation of organic matter is considered as well, the porosity is not directly linked to deformation only. Rather, it is related to partial solid density ρ_s and intrinsic density $\tilde{\rho}_s$ by

$$\phi = \frac{dv - dv_s}{dv} = \frac{dv - \frac{\rho_s dv}{\tilde{\rho}_s}}{dv} = \frac{\tilde{\rho}_s - \rho_s}{\tilde{\rho}_s} = 1 - \frac{\rho_s}{\tilde{\rho}_s} \ . \qquad (4.2)$$

A crucial point is the knowledge of the intrinsic density $\tilde{\rho}_s$, which is – like porosity – difficult to measure. It may vary considerably dependent on the contained materials. Very light plastics might be contained together with very heavy metals or stones. For instance, figure 4.2 shows experimental data on relation of dry density and porosity of MBT waste from Bente and McDougall [20]. The porosity is estimated from the water content at full saturation. Thereby, one has to keep in mind that this represents a lower limit only, as still air pockets might exist due to insufficient saturation of the intraparticle pore space. The variation in density is however not accompanied by a corresponding change in porosity. Additional experiments may identify the influence of sample size on the results. For the analyses later on, intrinsic density of waste materials is estimated from a composition analysis and intrinsic densities of the components as shown in section 3.5.3.

4.2.2 Moisture Retention and Matric Suction

The retention of the wetting, liquid phase in open pores is caused by capillary effects. The *capillary pressure*, or *matric suction*, p_c is the difference between the pressure of the gas phase, representing the non-wetting phase here, and the liquid pressure

$$p_c = p_g - p_l \; . \tag{4.3}$$

Its magnitude depends on the pore size, on the surface tension of the liquid and on the texture of the surface of the pores. For engineering practice and modelling, suction is usually related to moisture content or saturation, based on the idea that pores of different diameter are filled at different stages of moisture content, starting with infiltration of the smallest pores at low saturations. The mathematical representation of this relation is termed *Soil Water Characteristic Curve*[1]. Thereby, the saturation S_l is often expressed in terms of the dimensionless effective saturation S_e which is defined by

$$S_e = \frac{S_l - S_{l,res}}{1 - S_{l,res}} = \frac{n_l - n_{l,res}}{\phi - n_{l,res}} \; , \tag{4.4}$$

where $S_{l,res}$ is the *residual water content*. This quantity is often supposed to reflect an irreducible water content, e.g. by Mitchell and Santamarina [166]. In contrast, some researchers note that a solely physical interpretation is impossible, Helmig [103], and that its meaning depends at least on its experimental determination, so that a treatment of $S_{l,res}$ as a curve fitting parameter is considered to be sensible as well, e.g. Corey [43]. The latter interpretations are followed in this contribution, too.

The SWCC is a very essential relation in the modelling of unsaturated conditions. It influences seepage velocities, pressure fields and, dependent on the formulation, the effective stress. A change in the SWCC may thus affect simulation results remarkably. In general, total suction is the sum of matric suction and osmotic suction, which is triggered by solutes in the pore fluid. The effect of osmotic suction is neglected in this thesis.

Two approaches for a SWCC are applied in this thesis, whereas no hysteresis is considered. According to Brooks and Corey [31] the capillary pressure is

$$p_c = \frac{p_b}{S_e^{(1/\lambda_{BC})}} \tag{4.5}$$

with the *air entry pressure* or *bubbling pressure* p_b and a parameter λ_{BC}. The soil water characteristic curve according to Brooks and Corey exhibits a discontinuity at $S_e = 1.0$. Motivated by the advantages of a continuous closed form equation for numerical applica-

---

[1] Several names are used in the literature for the SWCC, including *moisture retention curve*, *soil-water retention curve*, *specific retention curve* and *moisture characteristic curve*.

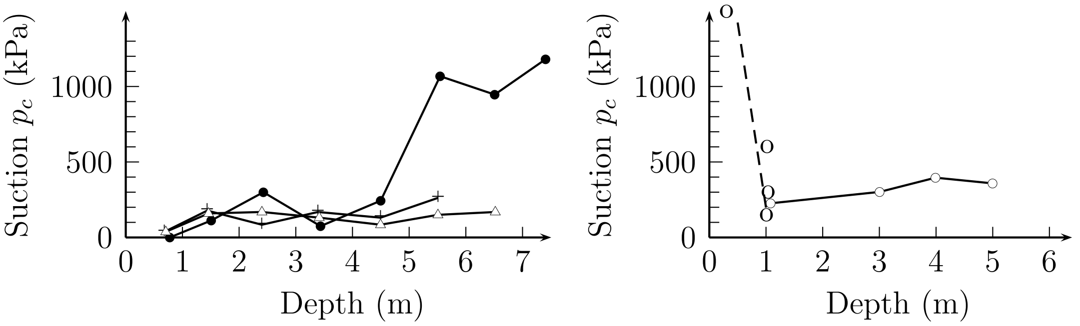

Figure 4.3: Site measurement of suction profiles at end of dry season by Blight et al.. Measurement in three boreholes at Coastal Park landfill (left) and two boreholes at Linbro Park landfill (right).

tions van Genuchten [234] develops the relation

$$p_c = \frac{1}{\alpha_{VG}}((S_e)^{-1/m_{VG}} - 1)^{1/n_{VG}} \text{ where } m_{VG} - 1 + \frac{1}{n_{VG}} = k \text{ and } k \in \mathbb{N} , \qquad (4.6)$$

with the parameters α_{VG}, m_{VG} and n_{VG}. A relation between m_{VG} and n_{VG} enables integration of the equation presented by Mualem [172]. Often $k = 0$ is chosen, so that $m_{VG} = 1 - 1/n_{VG}$.

Korfiatis et al. [134] are among the first to determine a moisture retention curve for waste, in particular for a six months old refuse from a local landfill, see figures 4.6 and 4.7. McDougall et al. [159] determine a SWCC for a mixture of peat and cocoa shells as a surrogate for MSW. The material has a very high water content at saturation and so the obtained curve is shifted to a saturated water content of about 35 % which is assumed be more likely for waste. Kazimoglu [122] presents measurements of suction in an artificial waste sample using a pressure plate apparatus. The data is plotted together with own data in figures 4.6 and 4.7. Site measurements of suction by Blight et al. [27] at two African landfills are shown in figure 4.3. At the end of dry season, suction is measured in boreholes by means of psychrometers. At most borehole depths, suction is below 300 kPa, wheras the values are not given in direct relation to water content. Relatively high suctions are observed at Linbro Park landfill in the upper layer of 1 m, which can be explained by a higher evaporation near to the surface. It is interesting that in one borehole at Coastal Park landfill suction suddenly increases at a depth of 5 m indicating an area of lower moisture content than above. From the measured values, Blight et al. conclude that the waste contains sufficient moisture to maintain biological activity. Although experimental evidence concerning suction in waste has considerably increased the last years, it seems that the mechanisms of moisture retention are still not completely understood and that experimental evidence is still lacking. This is confirmed by the outcomes of the first workshop on moisture retention of waste MMW 1, [167].

The importance of moisture retention data for multiphase flow modelling motivates the performance of own experiments. In cooperation with Dr. John McDougall, Edinburgh Napier University, the water retention behaviour of mechanically biologically pretreated (MBT) waste is investigated combining pressure plate tests and tensiometer measurements, the latter of which are not discussed herein.

The MBT material, shown in figure 4.4 (a), is provided by a treatment plant in Hannover, Germany. After a mechanical treatment, which includes removal of large objects, shredding, sieving and scanning for metals, the residual fine fraction is treated first anaerobically and then aerobically. The particle size distribution as obtained from a small 600 g sample, is shown in figure 4.4 (b). The pressure plate extractor is a laboratory equipment for the determination of moisture retention properties of porous media like soils. It is especially suited to small soil samples that can be removed from the apparatus and weighed to determine moisture content. Figure 4.5 shows the experimental setup including a cross section of the pressure plate extractor in (c). It consists of a pressure vessel within which there is a high air entry ceramic disc. The used plate has an air entry pressure of 3 bar, corresponding to approximately 300 kPa. The pressure vessel is connected to a compressed air supply. Initially, the ceramic disc is saturated with water. By a tube through the wall of the vessel the disc is connected to a water filled burette outside the pressure vessel,

(a) Material, 2 £ coin for comparison

(b) Results of sieve analysis

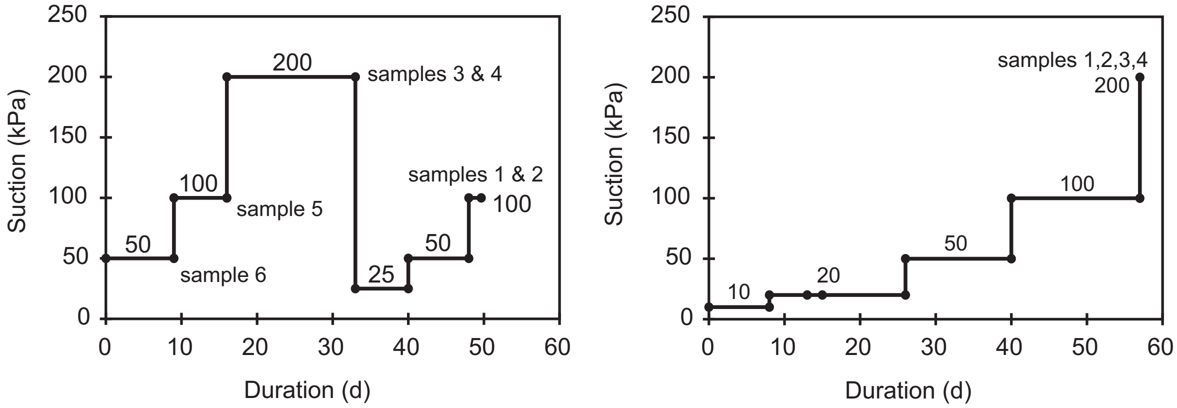

(c) Pressure sequence set 1

(d) Pressure sequence set 2

Figure 4.4: Pressure plate tests at Edinburgh Napier University, May 2009, material and pressure sequences

which is open to the atmosphere. Hence, the water in the ceramic disc is at atmospheric pressure. The difference between the air pressure in the vessel and the pressure of the water in the ceramic disc equals–if in equilibrium with the pressure of the water in the sample–the suction acting on the soil sample. The burette readings are used as an indicator for equilibrium at a certain suction level. The first test regime (set 1) comprises 6

(a) Samples on ceramic disc

(b) Pressure plate extractor

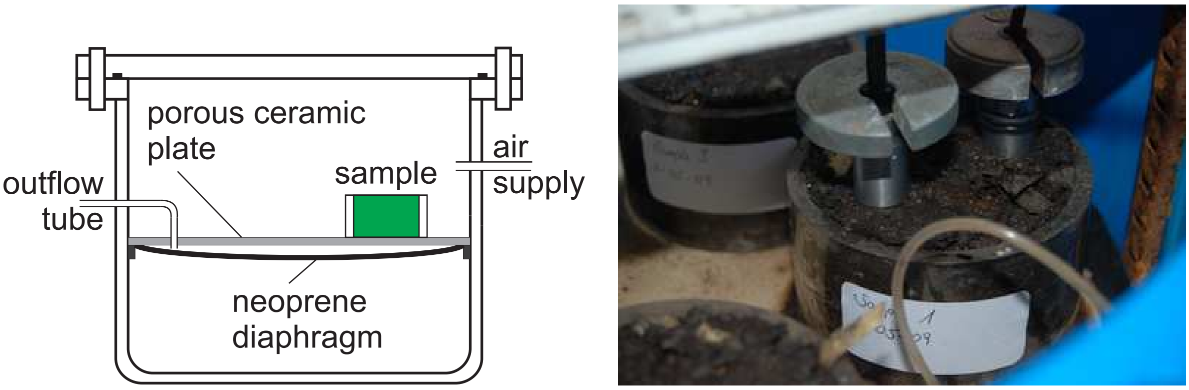

(c) Cross section of pressure plate extractor

(d) Close-up of sample

Figure 4.5: Pressure plate tests at Edinburgh Napier University, May 2009, experimental setup

MBT samples whereas the imposed pressure is first increased and then decreased, representing a sequence of drying and wetting, see figure 4.4 (c). Some samples are removed from the test programme for drying at a specific imposed suction (samples 3, 4, 5 and 6) whereas others are weighed at a specific suction and then returned to the pressure plate for equilibration at a new suction (samples 1 and 2). Moisture content for samples 1 and 2 is back calculated from weighing before and after oven drying at the end of the test. In set 2, four samples of MBT are investigated analogously. The pressure sequence includes drying only and all samples go through the complete pressure sequence, see figure 4.4 (d). On removal from the suction loading phase all samples, with the exception of sample 6 from set 1, are saturated in the perspex rings for 48 h to establish the saturated volumetric moisture content that is assumed to equal porosity.

Imposed suctions and corresponding moisture contents are shown in figures 4.6 and 4.7 for

both sets. A mathematical interpretation of the water retention curve using both Brooks and Corey and van Genuchten is plotted as well. The obtained parameter sets are listed in tables 4.1 and 4.2. The data points are scaled with porosity to plot the results in terms of both n_l and S_l.[1] For comparison, the data or SWCCs published by other researchers are plotted as well (note that the data from Stoltz and Gourc shows suctions up to 8 kPa, so the data points are within a very low range in the used scale.)
The highest imposed suction of 200 kPa leads to a volumetric moisture content of 43 % for set 1 and 30 % for set 2. Using the porosities according to figure 4.2 this refers to saturations of about 70 % and 45 %. It is remarkable that even for the same material at nearly the same density the capillary pressure relations do not coincide. This can be seen for example from the samples at 0.69 and 0.68 Mg/m^3 or 0.63 and 0.64 Mg/m^3. Any conclusions on density dependency have thus to be drawn very carefully. It is assumed that the variation is mainly due to the different intrinsic density of particles contained in the individual samples.
The resulting curve is thus more a product of the entire data set and does not allow for any distinction between retention properties at different densities. Such a distinction may indeed not be possible since the densities at which the test can be performed in this way is limited. Samples subjected to greater compaction are very slow to absorb added water whereas more lightly compacted material tends to drop out of the perspex ring. Hence the data obtained here is presented as an interpretation of moisture retention of the particular MBT waste with a dry density of approximately 0.7 Mg/m^3.
Although a formulation of the SWCC dependent on density or porosity seems to be reasonable, it is important to note that any relation may be only valid for a particular material at a certain composition and cannot neccessarily be transferred to other waste materials. Suggestions for a relation are made by Krase et al. [136]. Following the discussion above, a SWCC, which is independent of compaction, is assumed for further analyses.

Table 4.1: Parameters for describing different experimental results by the relation according to Brooks and Corey

	parameters Brooks Corey				
	ϕ	λ_{BC}	p_{bub} (kPa)	$n_{l,res}$	$S_{l,res}$
Stoltz and Gourc [220], 0.54 Mg/m^3	0.63	0.86	2.95	0.260	0.41
Stoltz and Gourc [220], 0.77 Mg/m^3	0.46	0.21	7.98	0.190	0.41
Bente and McDougall [20]^1, set 2 (0.57 to 0.68)Mg/m^3	0.70	0.24	8.00	0.140	0.20
Bente and McDougall [20]^1, set 1 (0.64 to 0.75)Mg/m^3	0.62	0.45	8.00	0.403	0.65

^{1} MBT waste

Still it may be subject to discussion whether the whole concept of capillary action can be transferred to laboratory and site conditions of waste and landfills. Engineering practice often does not prove strong capillary rise. A great moisture retention capacity is, however,

---

[1] For the description with the relations of Brooks and Corey and Van Genuchten one average porosity for each parameter set is used. Thus, the fittings differ slightly in the two representations.

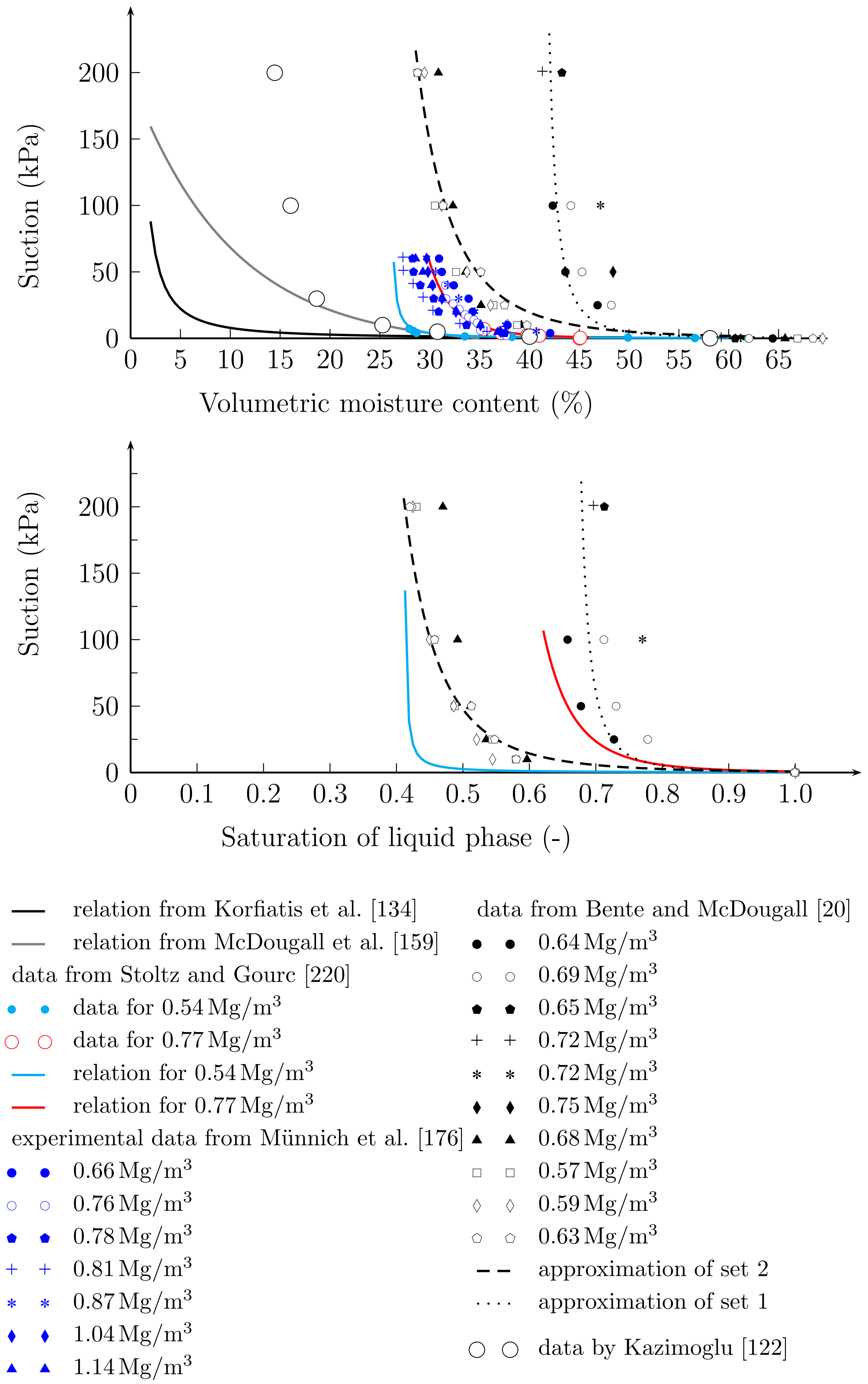

Figure 4.6: Measured suction and its mathematical representations according to Brooks and Corey in comparison with literature data on waste materials with different dry densities. Data from [20] and [220] is shown both in terms of volumetric moisture content and liquid saturation.

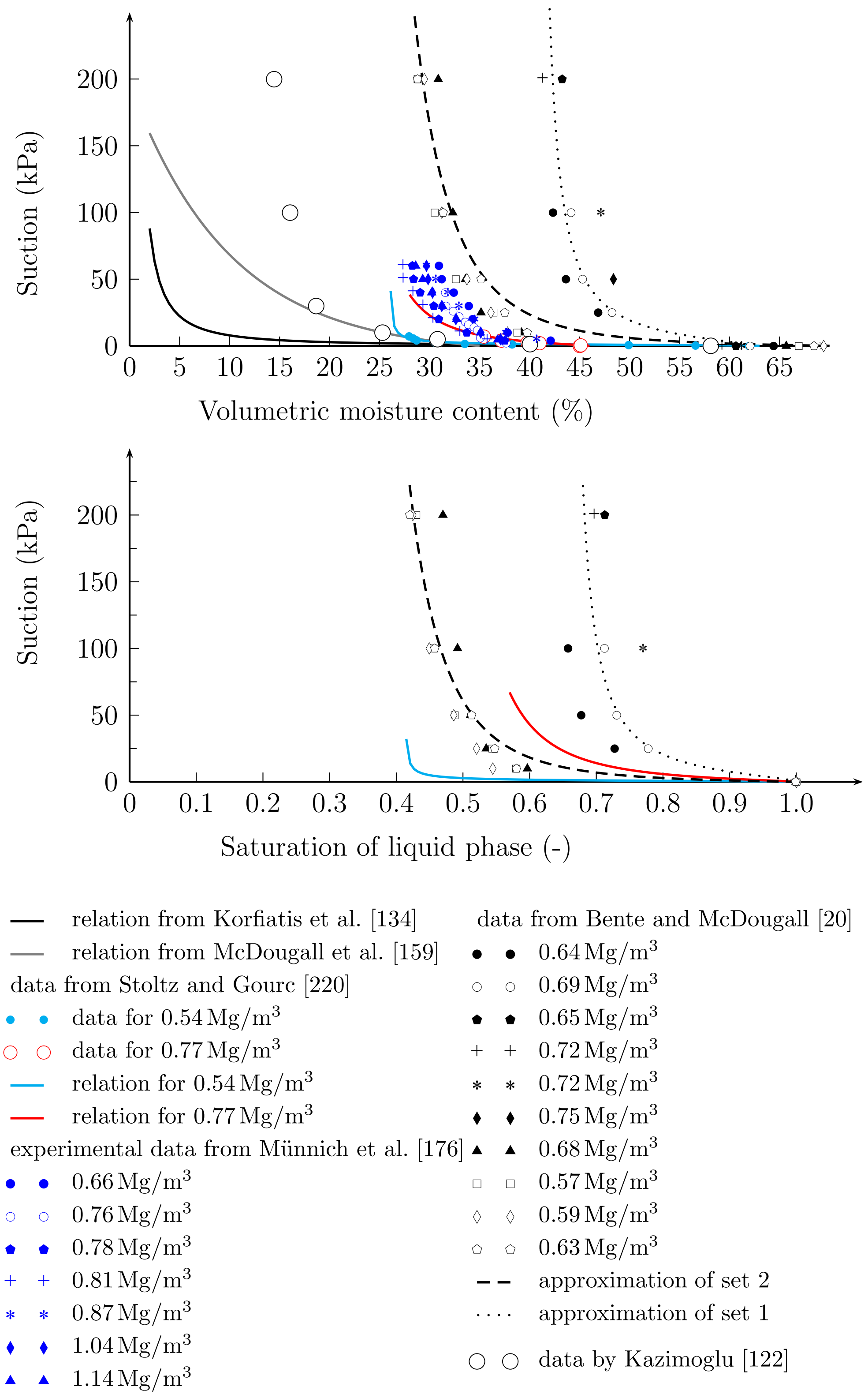

Figure 4.7: Measured suction and its mathematical representation according to van Genuchten in comparison with literature data on waste materials with different dry densities. Data from [20] and [220] is shown both in terms of volumetric moisture content and liquid saturation.

Table 4.2: Parameters for describing different experimental results by the relation according to van Genuchten

	parameters Van Genuchten					
	ϕ	α_{VG} ($\mathrm{kPa^{-1}}$)	m_{VG}	n_{VG}	$n_{l,res}$	$S_{l,res}$
Stoltz and Gourc [220], 0.54 $\mathrm{Mg/m^3}$	0.63	1.250	0.60	2.50	0.260	0.41
Stoltz and Gourc [220], 0.77 $\mathrm{Mg/m^3}$	0.46	0.400	0.29	1.40	0.190	0.41
Bente and McDougall [20][1] set 2 (0.57 to 0.68) $\mathrm{Mg/m^3}$	0.70	0.900	0.20	1.25	0.140	0.21
Bente and McDougall [20][1] set 1 (0.64 to 0.75) $\mathrm{Mg/m^3}$	0.62	0.150	0.41	1.70	0.403	0.65
cited in Rüth et al. [204][1,3]	0.50	0.015	0.20	1.25	0	0
cited in Rüth et al. [204][2,3]	0.65	0.040	0.31	1.45	0.07	0.11

[1] MBT waste, [2] compost,[3] own additional assumption: $\phi = S^l$

usually observed, but this may be attributable to an intraparticle pore space as well. A hydrophobic surface of the waste particles might interfer wetting, which is for example observed if the material is very dry. Another explanation for less capillary rise than expected from laboratory experiments may be capillary barrier effects. More experimental data is needed for an in-depths understanding of moisture storage in waste. Based on the experience gained in the experiments on MBT waste, it seems interesting to compare suction measurements of different sieving sizes and to combine suction measurements with outflow experiments. The effect of sample size is very interesting as well, but testing larger samples would increase time for equilibration in the pressure plate extractor considerably.

4.3 Flow of Liquid and Gas Phase

Either fluid phase simultaneously flows through the pore space, whereas the two phases interact with each other. Following the macroscopic approach described in chapter 2, the Darcy velocity is used to describe convective transport. Convective gas flow is considered in addition to liquid flow mainly to describe gas pressure rise from chemical reactions. Any influence of preferential flow or channeling is not considered yet, but represents an interesting future extension of the model.

4.3.1 Darcy's Law

Darcy's law is empirically derived for saturated, one-dimensional flow and states a linear relationship of macroscopic velocity and pressure gradient. It is important to notice that the Darcy velocity does not represent the real, average relative velocity between fluid and solid $v_{\pi s}$, as it is an averaged quantity, also termed *filter velocity* or *seepage velocity*. It equals the volume flux through a sample divided by its total cross section. The Darcy law can be generalised to cover unsaturated flow by introducing relative permeabilities $k_{\pi,rel}$. For a liquid and a gas phase, the Darcy velocities $\mathbf{v}_{l,D}$ and $\mathbf{v}_{g,D}$ within a three-dimensional framework are

$$\mathbf{v}_{l,D} = n_l \mathbf{v}_{ls} = n_l(\mathbf{v}_l - \mathbf{v}_s) = -\frac{k_{l,rel}}{\eta_l}\mathbf{K}(\operatorname{grad} p_l - \tilde{\rho}_l \mathbf{g}) \text{ , and} \tag{4.7}$$

$$\mathbf{v}_{g,D} = n_g \mathbf{v}_{gs} = n_g(\mathbf{v}_g - \mathbf{v}_s) = -\frac{k_{g,rel}}{\eta_g}\mathbf{K}(\operatorname{grad} p_g - \tilde{\rho}_g \mathbf{g}) \text{ .} \tag{4.8}$$

In general, the permeability $\mathbf{K}$ (m^2) may be anisotropic and represents a tensor quantity. Permeability is related to the hydraulic conductivity $\mathbf{k}_f$ (m/s) by

$$\mathbf{k}_{\pi,f} = \mathbf{K}\frac{\rho_\pi}{\eta_\pi}g = \mathbf{K}\frac{1}{\nu_\pi}\,g \quad \Longrightarrow \text{e.g. for liquid at } 20\,^\circ\mathrm{C} \;\; \mathbf{k}_{l,f}(\mathrm{m/s}) = \mathbf{K}\cdot 1\times 10^{7}\,(\mathrm{m}^2)\text{ .} \tag{4.9}$$

The permeability is a property of the pore space only. In contrast, the hydraulic conductivity depends on the fluid properties and, via the dynamic viscosity η_π or the kinematic viscosity ν_π, also on the temperature. The relation of relative permeability and dynamic viscosity $\lambda_\pi = \frac{k_{\pi,rel}}{\eta_\pi}$ is termed *mobility* of phase π.

The term $(\operatorname{grad} p_\pi - \tilde{\rho}_\pi \mathbf{g})$ shows that the Darcy velocity is zero if the pressure gradient coincides with the pressure gradient at hydrostatic conditions. The Darcy law is valid for a certain range of flow velocities, w.r.t. waste this issue is addressed by Hanel [99]. By applying Darcy's law, nonlinearities due to inertia effects or turbulences are assumed not to be relevant in the considered flow regime. An overview of non-Darcian models, like the Forchheimer equation, is for example given by Hamdan [97].

4.3.2 Saturated Hydraulic Conductivity of Waste and Deformation Dependent Permeability

In experiments usually the hydraulic conductivity is measured and the permeability then back calculated considering temperature and fluid density. Dixon and Jones [52] report about engineering properties of municipal solid waste and stress the variation of hydraulic conductivity. An overview of published conductivity data is for example given in Durmusoglu et al. [56] and Beaven [13]. The published hydraulic conductivity varies over several orders of magnitude from $3\times10^{-8}\,\mathrm{m/s}$ to $2\times10^{-2}\,\mathrm{m/s}$. For a temperature of $10\,^\circ\mathrm{C}$ and a density of $1000\,\mathrm{kg/m^3}$ this corresponds to a permeability variation of $4.0\times10^{-15}\,\mathrm{m}^2$ to $2.7\times10^{-9}\,\mathrm{m}^2$.

A comprehensive overview on factors influencing hydraulic conductivity is recently given by Hudson [112]. Among the several factors, the proposed coupled model considers the influence of compaction on permeability and the influence of temperature on the fluid viscosity.

Several experiments, e.g. by Chen and Chynoweth [38], Durmusoglu et al. [56] and Powrie et al. [194], prove that hydraulic conductivity, and therefore also the permeability, decreases with densification. Figure 4.8 shows data from Powrie et al. [194]. On a semi-

logarithmic scale the relation of hydraulic conductivity and wet density is nearly linear, whereas the slope is almost equal for the four tested materials.
With respect to permeability change, the state of densification is expressed by the porosity in this thesis. Thereby, the effect of compaction on permeability is taken into account by a power law (4.10) between porosity and permeability, as for example used by [63],

$$\mathbf{K} = \mathbf{K}_0 \cdot \left(\frac{\phi_t}{\phi_0}\right)^{\kappa_\phi} \quad \Longrightarrow \quad \mathbf{K} = \left(\frac{\tilde{\rho}_s - \rho_{s,i}}{\tilde{\rho}_s - \rho_{s,0}}\right)^{\kappa_\phi} \cdot \mathbf{K}_0 \;\text{ with }\; (4.2)\;. \tag{4.10}$$

ϕ_0 and $\mathbf{K}_0$ refer to initial porosity and permeability respectively. The parameter κ enables a weighting of the deformation dependence. For $\kappa_\phi = 0$ the permeability remains constant, if $\kappa_\phi = 1$ a linear relationship is obtained. It is assumed that the change of permeability is isotropic, i.e. a unique value of κ_ϕ is used for all principal directions. Additionally, experiments like those by Münnich et al. [175] show a difference between horizontal and vertical conductivity. The way of emplacement in thin layers with subsequent compaction causes an orientation of the particles in horizontal direction leading to an anisotropic permeability. In this thesis, it is assumed that the principal directions of permeability coincide with the orientation of the fibres in the local frame, so that the tensor $\mathbf{K}_{loc}$ has a diagonal coefficient matrix

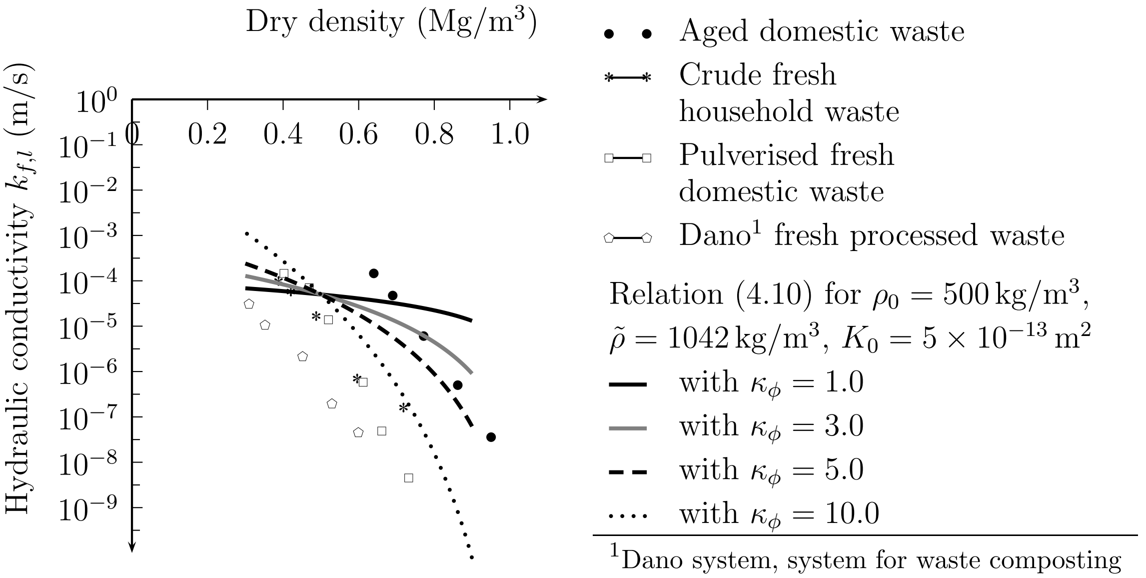

Figure 4.8: Saturated hydraulic conductivity of the liquid phase vs. dry density, from Powrie et al. [194], compared with modelling approach

$$\mathbf{K}_{loc} = \begin{pmatrix} K_{11} & 0 & 0 \\ 0 & K_{22} & 0 \\ 0 & 0 & K_{33} \end{pmatrix} . \tag{4.11}$$

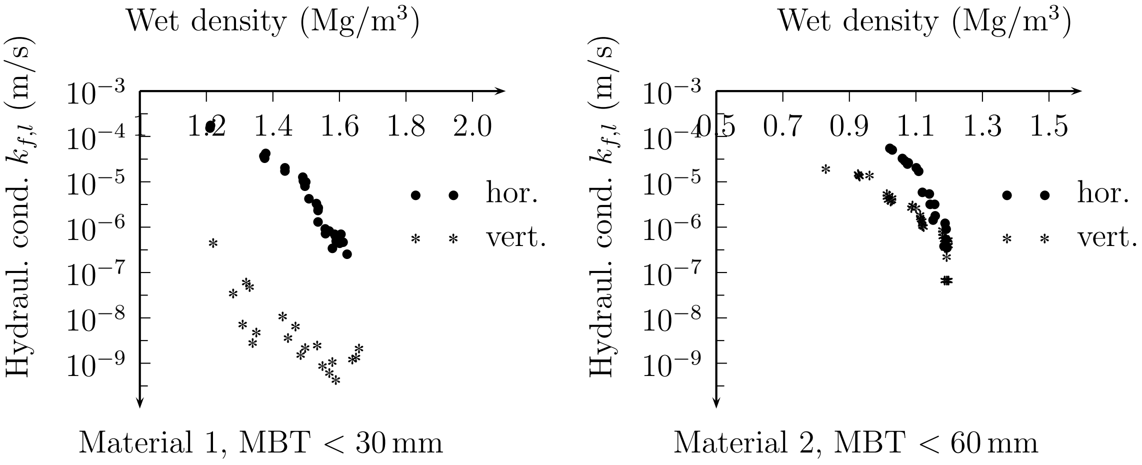

Figure 4.9: Tests by Münnich et al. [175] on relation of vertical and horizontal conductivity of mechanically and biologically pretreated waste

Figure 4.9 shows horizontal and vertical hydraulic conductivities for different wet densities as measured by Münnich et al. [175]. Two materials are compared in the experimental investigation. Material 1 ist treated aerobically and sieved to obtain a fraction with particle sizes smaller than 30 mm. Material 2 is treated anaerobically and aerobically and then sieved to particle sizes smaller than 60 mm.Throughout this thesis, a relation of vertical to horizontal permeability of $K_V : K_H = 1 : 10$ is assumed.

During deformation, two cases are conceivable. First, the planes of high permeability might rotate according to the deflection of a control volume, or, the initial orientation might be retained. In the model, the influence of rotation may be described by a transformation of local permeability to the global frame with the tensor $\mathbf{R}$

$$\mathbf{K}_{glob} = \mathbf{R} \cdot \mathbf{K}_{loc} \cdot \mathbf{R}^T \ . \tag{4.12}$$

The same tensor is used in to determine the orientation of fibrous particles. The rotation tensor $\mathbf{R}$ is formed by the vectors describing the initial principal directions of permeability which are rotated using the deformation gradient. If the rotational deformations are small, the tensor $\mathbf{R}$ is set equal to $\mathbf{1}$ in (4.12).

4.3.3 Unsaturated Hydraulic Conductivity

The direct experimental determination of unsaturated hydraulic conductivity is difficult, so researchers develop approaches to calculate unsaturated hydraulic conductivity from the soil water retention curve, which can be obtained more easily. Thereby, the conductivity at full saturation is scaled with the relative permeability $k_{\pi,rel}$. Among the most popular models are the approaches by Brooks and Corey [31] together with Burdine [34] with

$$k_{l,rel} = S_e^{\frac{2+3\lambda_{BC}}{\lambda_{BC}}} \quad \text{and} \quad k_{g,rel} = (1-S_e)^2 \left(1 - S_e^{\frac{2+\lambda_{BC}}{\lambda_{BC}}}\right) , \tag{4.13}$$

and van Genuchten [234] together with Mualem [172] where

$$k_{l,rel} = S_e^{\frac{1}{2}} \left(1 - \left(1 - S_e^{\frac{1}{m_{VG}}}\right)^{m_{VG}}\right)^2 \quad \text{and} \quad k_{g,rel} = (1-S_e)^{\frac{1}{3}} \left(1 - S_e^{\frac{1}{m_{VG}}}\right)^{2m_{VG}} . \tag{4.14}$$

Figure 4.10 shows the relative permeabilities using both (4.13) and (4.14) in terms of volumetric moisture content for the data from [20] as well as Stoltz and Gourc [220], as shown in section 4.2.2.

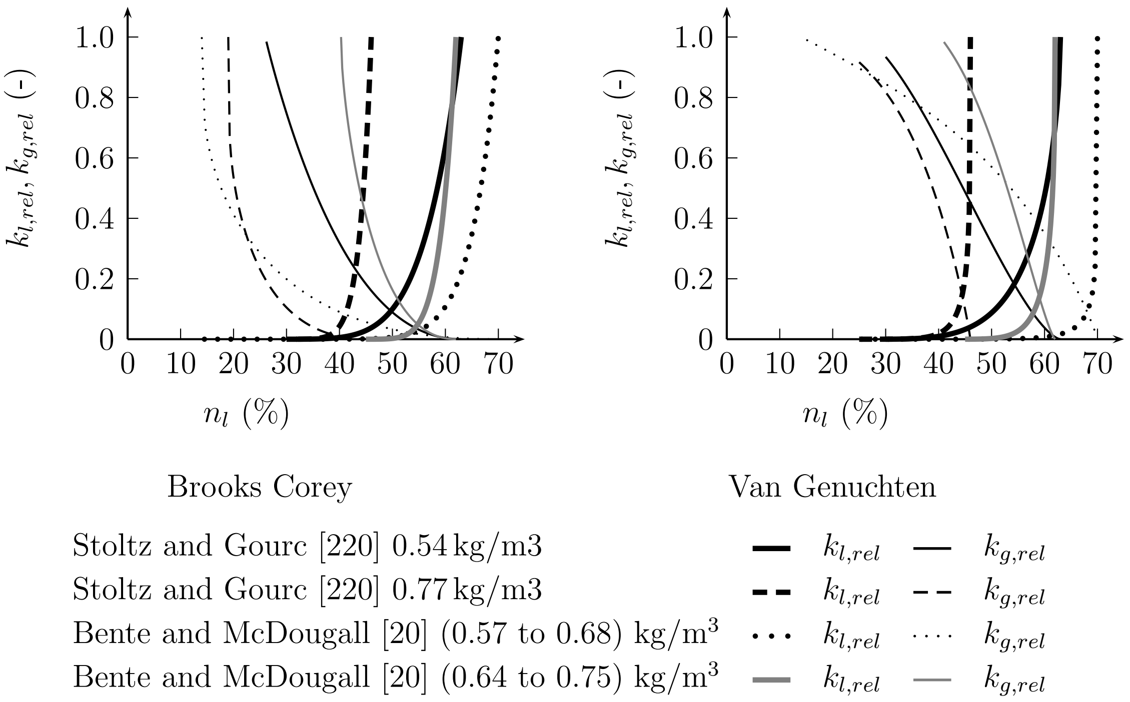

Brooks Corey

Van Genuchten

Figure 4.10: Relative permeabilities after Brooks Corey (left) and Van Genuchten (right) for the data from [20] and [220] in terms of volumetric moisture content

4.3.4 Temperature Dependence of Viscosity

As seen before, the fluid viscosity influences the hydraulic conductivity. The density variations due to the composition of the liquid phase are very small, so only the temperature effect is considered here. The viscosity of the liquid phase is supposed to equal that of water. For its temperature dependence the following relation, proposed by Poiseuille, is given in Oumeraci [189]

$$\nu_l = \frac{1.78 \times 10^{-6}}{1.0 + 0.0337\,\Theta + 0.000221\,\Theta^2} , \tag{4.15}$$

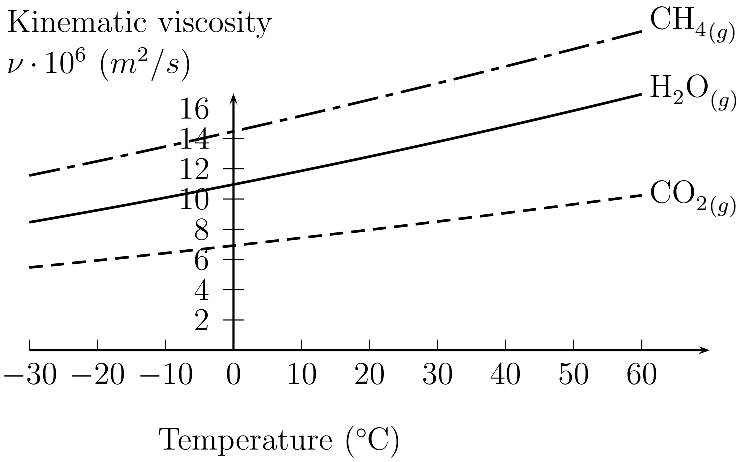

Figure 4.11: Temperature dependence of gas component viscosities

whereas the kinematic viscosity ν_l is obtained in $(\mathrm{m}^2/\mathrm{s})$ if the temperature Θ is given in (°C).

The viscosity of the gas mixture is determined after Helmig [103] using the temperature dependent viscosities of the gas components weighted by the mass fractions respectively

$$\nu_g \approx \sum w_g^\alpha \cdot \nu_g^\alpha \ . \tag{4.16}$$

The temperature dependency of the component's kinematic viscosity is described using the relation proposed by Sutherland [223]

$$\nu = \nu_0 \sqrt{\left(\frac{\Theta}{\Theta_0}\right)^3} \frac{1+\frac{C_S}{\Theta_0}}{1+\frac{C_S}{\Theta}} = A_S \frac{\sqrt{\Theta^3}}{1+\frac{C_S}{\Theta}} \ . \tag{4.17}$$

Sutherland's constant A_S and C_S, are given in table 4.3 for the three components. Relation (4.17) is plotted for the three constituents in figure 4.11.

Table 4.3: Sutherland constants for temperature dependency of viscosity of gaseous components, taken from D'Ans and Lax [46]. ν_0 and η_0 are the viscosities at the reference temperature Θ_0

component	Θ_0	$\tilde{\rho}^\beta$	$\eta_0 \cdot 10^9$	C_S	$\nu_0 10^4$	$A_S \cdot 10^{11}$	range
	(°C)	(kg/m^3)	(Pa $\cdot$ s)	(K)	(m^2/s)	$\left(\frac{m^2}{s \cdot K^{3/2}}\right)$	
$CO_{2\,(g)}$	0	1.977	1366	274	0.0692	307	0-100
$CH_{4\,(g)}$	17	0.675	1094	198	0.1620	553	0-100
$H_2O_{(g)}$	99	0.579	1255	673	0.2170	841	100-350

Table 4.4: Effective diffusion coefficients in multicomponent liquid and gas mixture

component	D'^{β}_{π} (m/s^2)
$H_2O_{(g)}$	2.50×10^{-5}
$CO_{2\,(g)}$	1.54×10^{-5}
$CH_{4\,(g)}$	1.58×10^{-5}
$CO_{2\,(aq)}$	2.00×10^{-9}
$CH_3COOH_{(l)}$	1.20×10^{-9}

4.4 Transport by Diffusion

Diffusion leads to an equalisation of concentration gradients caused by Brown's molecular movement. According to Fick's law and using the macroscopic approach applied by Hanel [99] the diffusive mass I_D flux is given by

$$I_D = -D^{\beta}_{\pi}\,\phi\,S_{\pi}\,\mathrm{grad}\,c^{\beta}\ , \tag{4.18}$$

with the coefficient of diffusion D^{β}_{π}. For the multicomponent gas mixture, effective diffusion coefficients are derived from molecular diffusion coefficients after the approach by Fairbanks and Wilke [77]. Thereby, a mass ratio of CO_2:CH_4:H_2O=0.59:0.39:0.02 is assumed for the gas phase. The diffusion coefficients of the liquid phase's components are derived using the approach by Wilke and Chang [244] for diffusion in water at a temperature of $\Theta \sim 20\,°C$. The coefficients are assumed to be constant and listed in table 4.4. Furthermore, diffusion in a porous medium is less than in free water, due to tortuosity of the pores. Several approaches exist to transfer the diffusion coefficients, for a recent review see for example Shen and Chen [214]. Following [99], the approach shown in Warrick [239], which is based on the work by Millington and Quirk [165], is applied. It considers the influence of phase saturation and porosity on tortuosity τ_{π}

$$\tau_l = \frac{n_l^{7/3}}{\phi^2} = S_l^{7/3}\cdot\phi^{1/3} \ \text{ and } \ \tau_g = \frac{n_g^{7/3}}{\phi^2} = S_g^{7/3}\cdot\phi^{1/3}\ , \tag{4.19}$$

and the diffusion coefficients become

$$D^{\beta}_{l} = \tau_l \cdot D'^{\beta}_{l} \ \text{ and } \ D^{\beta}_{g} = \tau_g \cdot D'^{\beta}_{g}\ . \tag{4.20}$$

It is thus assumed that diffusion is affected by tortuosity similarly in both the liquid and the gas phase. In experiments, it is difficult to separate the effects of diffusion and dispersion. So it is common practice to summarise the two mechanisms in a coefficient of *hydrodynamic dispersion*. Its consideration within the model as well as detailed investigations on the effects of diffusion and dispersion represent a possible future extension of the work.

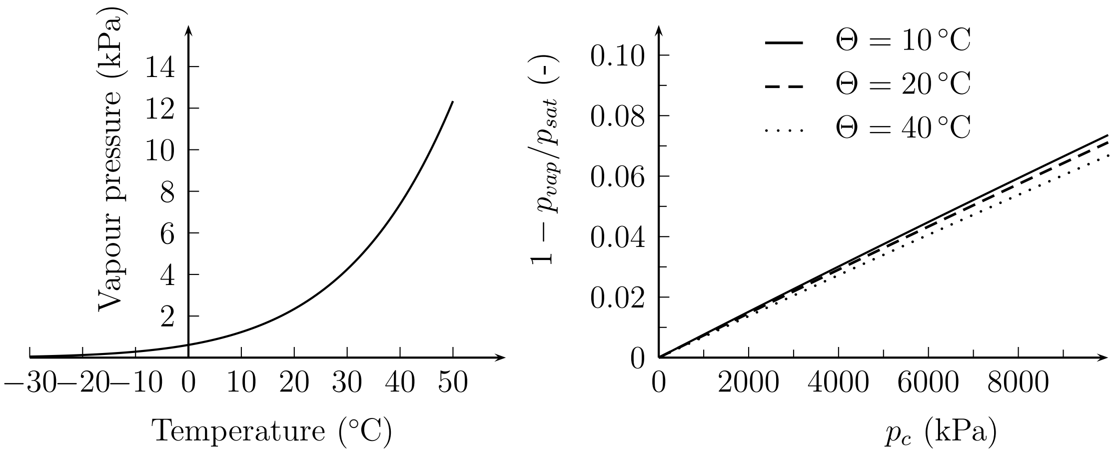

Figure 4.12: Magnus approximation of saturated vapour pressure using the coefficients of Tetens [226] (left) and deviation of vapour pressure and saturated vapour pressure-dependent on suction for Θ = 10 °C, 20 °C and 40 °C (right)

4.5 Physical Exchange Processes

Some components are considered to exist both in gaseous and in liquid state. The proposed model describes evaporation and condensation of water as well as dissolution of carbon dioxide. Required relations are explained in the following subsections.

4.5.1 Saturated Vapour Pressure

Evaporation occurs from the surface of a liquid. The saturated vapour pressure represents the pressure of a gas phase, saturated with vapour, in case of evaporation in a closed container at equilibrium state. The Clausius-Clapeyron equation describes the temperature dependence of saturated vapour pressure. Several approximations to this relation of various complexity are developed, an overview is for example given by Alduchov and Eskridge [2]. One simple form is suggested by Magnus [153]

$$p_{sat}(\Theta) = c_M \; exp(\frac{a_M \Theta}{b_M + \Theta}) \; , \tag{4.21}$$

whereas a_M,b_M and c_M are parameters. Their choice is discussed in several publications. In this contribution, the estimation of Tetens [226] is used, so that

$$p_{sat}(\Theta) = 611 \times 10^{\frac{7.5\Theta(^\circ\mathrm{C})}{237.3+\Theta(^\circ\mathrm{C})}} = 611 \times 10^{\frac{7.5\Theta(K)-2048.625}{\Theta(K)-35.85}} \; (\mathrm{Pa}) \; . \tag{4.22}$$

The relation is plotted in figure 4.12, left. With an increase of temperature, the vapour pressure increases exponentially.

4.5.2 Vapour Pressure Reduction

The saturated vapour pressure as explained in section 4.5.1 refers to evaporation above a plane of water. Due to capillarity, a liquid surface is curved within a porous medium. As described by the Kelvin equation, the vapour pressure decreases as the mean radius of curvature H decreases

$$2H\sigma_w = (p_{vap} - p_{sat}) - \frac{R\Theta}{V_{l,M}} \ln \frac{p_{vap}}{p_{sat,0}} \;, \tag{4.23}$$

with the universal gas constant $R = 8.314\,472\,\mathrm{J/mol\cdot K}$ and the molar volume of water $v_l = 1.8 \times 10^{-5}\,\mathrm{m^3/mol}$. The term $p_{vap} - p_{sat}$ is usually negligible, Kaviany [121]. Surface tension σ_w and curvature of the surface between two fluid phases are related to pressure difference, i.e. to capillary pressure, as described by Laplace's equation

$$p_g - p_l = 2H\sigma_w \;. \tag{4.24}$$

Combination of (4.23) and (4.24) leads to following relation for the vapour pressure

$$p_{vap} = exp(\frac{-p_c \cdot V_{l,M}}{R \cdot \Theta}) \cdot p_{sat} \;. \tag{4.25}$$

Using relation (4.25), the difference of p_{vap}/p_{sat} to 1 is plotted in figure 4.12, right, for different temperatures. It shows that the vapor pressure is reduced about less than 1 % within suction ranges up to 1 MPa.

The model formulation does not allow complete drying, as then the corresponding mass balance would vanish. Thus, total evaporation is avoided by a regularisation, whereas the vapour pressure is set to zero for very low saturations.

The evaporation enthalpy ΔH_{vap} is considered in the balance of energy, whereas it is formulated temperature-dependent by

$$\Delta H_{vap} = 2.783 \times 10^{+03} - 5.166 \times 10^{-02}\Theta - 3.622 \times 10^{-03}\Theta^2 \;. \tag{4.26}$$

4.5.3 Gas Mixture

The gas phase is considered to be an ideal gas mixture. The partial pressure of a component is equal to the pressure as if the gas volume V_g was filled only by this component. According to the ideal gas law, the partial pressure p_g^β is

$$p_g^\beta = n_g^\beta \frac{R\Theta}{V_g} = m^\beta \frac{R^\beta \Theta}{V_g} \;, \tag{4.27}$$

where the specific gas constant R^β ist defined by

$$R^\beta = \frac{R}{M^\beta} \; . \tag{4.28}$$

In equations (4.27) and (4.28) n^β is the mol number of β, M^β is the molar mass and m^β the mass. The pressure of the gas mixture is equal to the sum of the partial pressures according to Dalton's law, (4.29). The sum of the mass fractions equals 1 (4.30) and the partial densities sum up to the total density of the gas phase, (4.31)

$$p^g = \sum_\beta p_g^\beta \; = p_g^{\mathrm{CH}_4} + p_g^{\mathrm{CO}_2} + p_g^{\mathrm{H}_2\mathrm{O}} \; , \tag{4.29}$$

$$1 = \sum_\beta w_g^\beta = w_g^{\mathrm{CH}_4} + w_g^{\mathrm{CO}_2} + w_g^{\mathrm{H}_2\mathrm{O}} \; \text{, and} \tag{4.30}$$

$$\tilde{\rho}^g = \sum_\beta \rho_g^\beta \; = \rho_g^{\mathrm{CH}_4} + \rho_g^{\mathrm{CO}_2} + \rho_g^{\mathrm{H}_2\mathrm{O}} \; . \tag{4.31}$$

Using (4.27) to (4.31) the following expression for the partial density of methane can be derived

$$\rho_g^{\mathrm{CH}_4} = \left(\frac{p_g - p_g^{\mathrm{H}_2\mathrm{O}}}{R\Theta} + \frac{\rho_g^{\mathrm{H}_2\mathrm{O}}}{M^{\mathrm{CO}_2}} \right) \frac{1}{\frac{1}{M^{\mathrm{CH}_4}} + \frac{1}{M^{\mathrm{CO}_2}} \frac{1}{w_g^{\mathrm{CH}_4} - 1}} \; . \tag{4.32}$$

A regularisation is included to avoid division by zero, as such that the partial density of methane is set to zero for very low mass fractions of methane below 1×10^{-10}. The partial pressure of methane is determinable by ideal gas law and subsequently partial density of CO_2, partial pressure and total density can be evaluated. The mass fraction of $\mathrm{H}_2\mathrm{O}$ and CO_2 are given by

$$w_g^{\mathrm{H}_2\mathrm{O}} = \rho_g^{\mathrm{H}_2\mathrm{O}} \tilde{\rho}_g \text{ and } w_g^{\mathrm{CO}_2} = \rho_g^{\mathrm{CO}_2} \tilde{\rho}_g \; . \tag{4.33}$$

4.5.4 Dissolution of Carbon Dioxide

The dissolution of methane is neglected as its portion is very small. The dissolution of carbon dioxide is described by Henry's law. The kinetics of dissolution are not considered, rather, it is assumed that the fraction in the gas phase and the fraction in the liquid phase are in equilibrium. The relation of the two concentrations then equals the Henry coefficient. Different formulations exist and thus also slightly different definitions of Henry's coefficient $k_H^{\mathrm{CO}_2}$. Here, the mol fraction $\kappa_l^{\mathrm{CO}_2}$ of CO_2 in liquid is determined by

$$\kappa_l^{CO2} = p_g^{\mathrm{CO}_2} \cdot k_H^{\mathrm{CO}_2} \quad \text{with} \quad \kappa_l^{CO2} = \frac{n^{\mathrm{CO}_{2\,(\mathrm{aq})}}}{n^{\mathrm{CO}_{2\,(\mathrm{aq})}} + n^{\mathrm{H}_2\mathrm{O}_{(\mathrm{l})}}} \; . \tag{4.34}$$

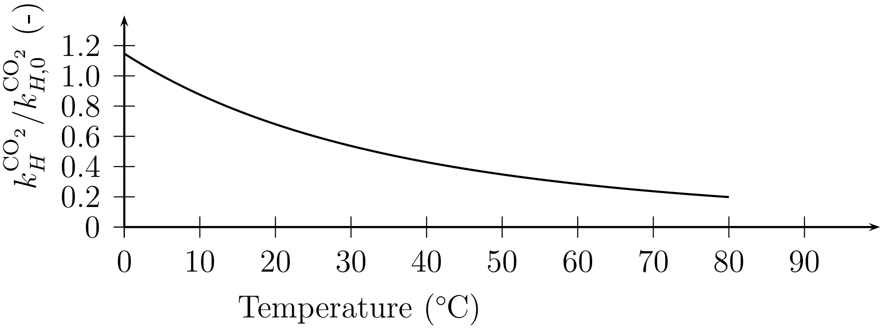

Figure 4.13: Temperature dependency of Henry's coefficient

The temperature dependency of Henry's coefficient is described by the following relation

$$k_H^{\mathrm{CO}_2} = k_{H,0}^{\mathrm{CO}_2} \cdot exp\left(\frac{\Delta H_s}{R}\left(\frac{1}{\Theta} - \frac{1}{\Theta_0}\right)\right) \,, \tag{4.35}$$

whereas $k_{H,0}^{\mathrm{CO}_2}$ is the Henry coefficient at a reference temperature Θ_0, and ΔH_s is the solution enthalpy under standard conditions. Relation (4.35) is plotted in figure 4.13 for $k_{H,0}^{\mathrm{CO}_2} = 0.034\,\mathrm{mol/(kg \cdot bar)} = 6.04 \times 10^{-09}\,\mathrm{mol_{CO2}/(mol_{H2O} \cdot Pa)}$, $\Theta_0 = 298.15\,\mathrm{K}$ and $\frac{\Delta_s H0}{R}$=2400 K according to NIST[2]. The complete dissolution, which would lead to a vanishing mass balance of gaseous carbon dioxide is prevented by means of a regularisation at low saturations.

4.5.5 Liquid Mixture

The mass fractions $w_l^{\mathrm{CO}_2}$ and $w_l^{\mathrm{H}_2\mathrm{O}}$ can be determined from the mass fraction of acetic acid w_l^{Ac} which is selected as a primary variable. The mass fraction of carbon dioxide in the liquid phase $w_l^{\mathrm{CO}_2}$ is

$$w_l^{\mathrm{CO}_2} = \frac{\left(1 - w_l^{Ac.}\right) \kappa_l^{\mathrm{CO}_2} M^{\mathrm{CO}_2}}{\kappa_l^{\mathrm{CO}_2} M^{\mathrm{CO}_2} + (1 - \kappa_l^{\mathrm{CO}_2}) M^{\mathrm{H}_2\mathrm{O}}} \,, \tag{4.36}$$

and the mass fraction of water and intrinsic density of the liquid phase can be determined by 4.30 and 4.29 as well as the partial densities of the components.

4.6 Effective Stress

For unsaturated conditions, the effective stress is very much related to the constitutive model for moisture retention, motivating its discussion in the present chapter.

The mechanisms of slope failure events motivate the application of the effective stress concept within modelling of landfills. Especially landfills without an operating leachate collection system may exhibit local saturated areas, cf. Koerner and Soong [130]. If ex-

---

[2] NIST Chemistry WebBook, http://webbook.nist.gov/chemistry/, last access 12-2009

cess pore pressures are created, the effective stress is reduced which increases the risk of shear failure of the waste body. In engineering practice, at present the liquid pore pressure is considered in the calculation of slope stability using classical engineering methods, e.g. Bishop's method of slices, see for example Kölsch [133]. However, not many models for landfills are developed so far, which consider the effective stress in an overall coupled model for transport processes and degradation. This may represent one step forward to investigate the conditions, under which excess pore pressures might develop. A model which takes the effective stress into account is presented by Durmusoglu et al. [55], who use a Bishop-type effective stress with $\chi = S_l$ as well. Contrary to soil, there is no experimental evidence for waste known to the author yet, which would justify the use of a particular effective stress formulation. As such, Gharabaghi et al. [89] highlight the fact that some fundamental geotechnical principles, like the applicability of the Mohr-Coulomb failure criterion or the validity of Terzaghi's effective stress concept with respect to MSW, are not finally approved yet.

Not only the liquid pressure but also the gas pressure may be taken into account. Merry et al. [163] investigate the effect of degradation induced gas pressure raise and its influence on liquid pressure and effective stress. A model to estimate excess pore pressure due to gas formation is presented, whereas the effect of suction on effective stress is neglected.

The *concept of effective stress* goes back to the work of Terzaghi who describes the phenomenon of consolidation, i.e. settlements due to dissipation of excess pore pressure, in saturated soils. Considering a small strain notation for better readability, the effective stress $\boldsymbol{\sigma'}$ after Terzaghi is defined by

$$\boldsymbol{\sigma}' = \boldsymbol{\sigma} + \alpha_p p_l \mathbf{1} \quad \text{with } \alpha_p = 1.0 \; , \tag{4.37}$$

and includes the assumption of an incompressible fluid and incompressible solid grains. Extended approaches with $\alpha_p \neq 1.0$ are developed to consider grain compressibility. In (4.37), compressive stresses $\boldsymbol{\sigma}$ are negative, and the fluid pressure p_l is positive. The effective stress is a macroscopic quantity and is not equal to the real, local stress between the solid particles. It enables to describe a multiconstituent porous medium with a single stress quantity. Figure 4.14 gives an interpretation of effective stress for saturated conditions. In a saturated medium, the pressure of the liquid phase p_l acts as hydrostatic pressure on the solid grains, see figure 4.14. Thus, the stress within the solid grains is composed of a fraction due to liquid pressure, and an additional part due to stresses which are beared via the solid grains only, in figure 4.14 denoted by σ_s. Equilibrium of forces in vertical direction and comparison with Terzaghi's equation shows that the effective stress can be interpreted as the mean stress in the solid grains exceeding the liquid pressure related to the total cross section A. σ_s itself is a mean stress, because on microscopic level every grain may exhibit an individual stress state. The stress in the solid grains due to liquid pressure is also termed *neutral stress*.

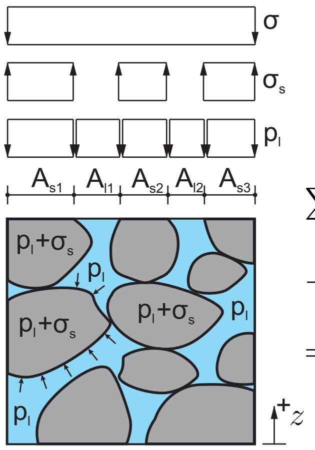

$$\textstyle\sum_i A_{si} = A_s,\ \sum_i A_{li} = A_l$$

$$-\sigma A + \sigma_s A_s - p_l A = 0$$

$$\Rightarrow \sigma = \underbrace{\sigma_s \tfrac{A_s}{A}}_{\text{effective stress } \sigma'} - p_l$$

Figure 4.14: Interpretation of effective stress in saturated conditions

The effective stress is often referred to as being the stress, which controls the mechanical properties, particularly shear strength and volume change. Thus, the constitutive relations for material behaviour are usually formulated in terms of effective stress.

Extending Terzaghi's work, several other formulations for the effective stress in soils are developed. A comprehensive overview is recently given by Nuth and Laloui [184]. For saturated conditions, most models differ mainly in the formulation of the pore pressure by modifying α_p in (4.37).

The extension of the effective stress to unsaturated conditions starts with the work of Bishop [24] who describes the effective stress by

$$\boldsymbol{\sigma}' = \boldsymbol{\sigma} + (p_g - \chi(p_g - p_l))\mathbf{1} \ , \tag{4.38}$$

and recommends its use mainly for fine grain soils at low degrees of saturation, as for other cases the effective stress after Terzaghi remains a good approximation. Again compressive stresses are negative and fluid pressures are positive. Equation (4.38) shows that the effective stress is dependent on suction. If the soil is unsaturated, the suction causes additional compressive stress of the solid phase. The increase in cohesion of the particles with increasing suction is termed *apparent cohesion*.

Similarly as for the parameter α_p, several approaches for the Bishop parameter χ or for effective stress are developed. Thereby, χ is often defined in a way which includes (4.37) and the net stress $(\sigma + p_g)$ as limits at full saturation and dry conditions respectively. Table 4.5 gives an overview of some approaches. The developments within the Theory of Mixtures permit derivations of effective stress formulations and verification of many concepts, that were originally concluded from experimental results. Those discussions are helpful to clarify the meaning of empirically derived parameters. Hutter et al. [113] show that the Bishop parameter χ equals the saturation of the wetting phase if the solid grains and the liquid are assumed to be incompressible and if the gas is compressible.

Table 4.5: Overview of selected approaches for *single effective stress* for unsaturated soils, small strain representations with stress σ

author(s)	effective stress or Bishop parameter χ
Bishop [24]	$\sigma' = \sigma + p_g - \chi(p_g - p_l)$
Aitchison [1]	$\sigma' = \sigma + (0.3 \text{ to } 0.35)\, p_c$
Skempton [218]	$\sigma' = \sigma - (1 - \frac{Cs}{C})S_\chi p_l$ for volume change $\sigma' = \sigma - (1 - \frac{\text{a tan}\psi}{\text{tan}\phi'})S_\chi p_l$ for shear strength $S_\chi = 1 + (1 - \chi)\frac{p_g - p_l}{p_l}$, a is related to contact area between grains, ϕ' = angle of internal friction, ψ = angle of intrinsic shearing resistance of the solid substance itself
Bluhm and de Boer [28]	$\sigma' = \sigma - \frac{1}{n_l}\left[p_g - (n_s + n_l)\left(\left(\frac{n_s+n_g}{n_s+n_l}\right)p_g - p_l\right)\right]$
Khalili and Kabbaz [123]	$\chi = \left(\frac{p_c}{p_b}\right)^{-0.55}$ for $p_c > p_b$ and $\chi = 1$ for $p_c < p_b$
Lewis and Schrefler [142]	$\chi = S_l$
cited in Lu and Likos [147]	$\chi = S_e$
cited in Lu and Likos [147]	$\chi = \left(\frac{n_l}{n_{ls}}\right)^\kappa$ n_{ls} = volumetric water content at saturation
de Boer [47]	$\sigma' = \sigma + p_g - (n_s + n_l)(p_g - p_l) - n_s\frac{K_{SN}}{K_{SR}+K_{SN}}p_l$ where K_{SN} and K_{SR} are the compression moduli of the solid skeleton and the material
Gudehus, citet in Von Wolffersdorff [236]	$\chi = S_l(2 - S_l)$

More recently, Gray and Schrefler [92] prove that Bishop's parameter corresponds to the fraction of the solid surface in contact with the liquid phase.

In contrast to the single effective stress, Fredlund and Morgenstern [83] suggest the use of independent stress variables, whereas different combinations are possible. Net stress $(\sigma + p_g)$ and suction $(p_g - p_l)$ are widely used in that context. Following the discussion of shortcomings and advantages of the different approaches by Nuth and Laloui [184], in this thesis the Bishop type effective stress is used, whereas the Bishop parameter χ is assumed to equal the saturation of the liquid phase $\chi = S_l$. The weighted pore pressure p

is substracted from the effective stress so that the 2^{nd} Piola Kirchhoff Stress tensor, which is defined in (2.26) and represents total stress can be split up by

$$\mathbf{S} = \mathbf{F}^{-1}(\tilde{\mathbf{T}}_e - \det \mathbf{F}_s(p_g + S_l(p_l - p_g))\mathbf{1}))\mathbf{F}_s^{-T} \, . \tag{4.39}$$

Therefore, an increase in suction induces an additional compressive stress. Figure 4.15 compares the product $(\chi \cdot p_c)$ for two different formulations of the Bishop parameter χ using the van Genuchten approximations of the data by Bente and McDougall [20]. If p_g equals atmospheric pressure, the term $\chi \cdot p_c$ coincides with the increase in effective stress due to suction. The very high slope of the SWCC at low saturations is retained in the plot of $(\chi \cdot p_c)$ leading to a strong increase in effective stress at dry states. For instance, a pore pressure of 200 kPa is equivalent to overburden pressure of $\sim$ 20 m of waste, leading to a corresponding volume change dependent on the compaction state of the waste, cf. the formulation of the creep model in section 5.2.3. Both due to evaporation and degradation processes that consume water, states with high suction might occur in the present model. This gives rise to the discussion how suction affects the effective stress for saturations near or below the residual saturation. Fredlund [84] discusses this issue for soil and indicates that the effect of matric suction on the mechanical behaviour may become negligible for dry conditions. Experiments show that suction approaches a limiting value of 620 - 980 MPa as the water content decreases to 0 %. Thus, it may be suggested here for waste, to decouple the effective stress from the SWCC that is used to describe multiphase flow. In the current modelling approach, suction is limited to 20 kPa.

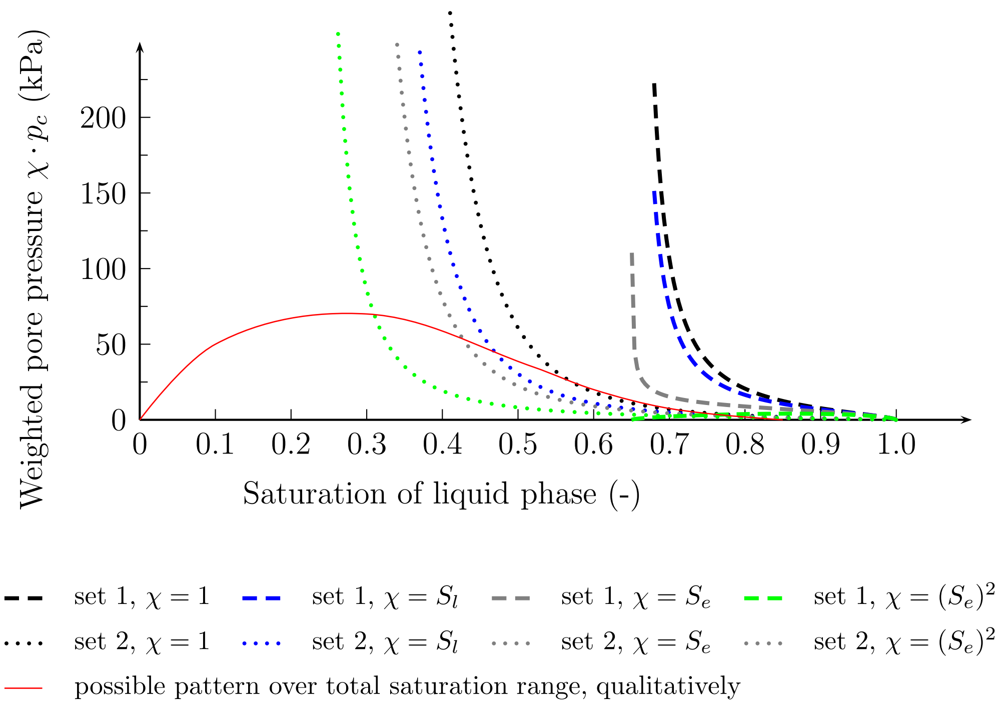

Figure 4.15: Suction weighted by different variants of Bishop parameter χ

Further research is necessary to develop a unified framework for effective stress in waste, which may include advanced experimental testing as done already for unsaturated soils. Thereby, the special properties of waste like the existance of a macropore domain and a micropore domain may be taken into account. For instance, Bagherieh et al. [8] investigate suction and effective stress by experiments on kaolin samples with a double porosity structure. If decrease in saturation due to evaporation or chemical reactions is considered, a closed-form relation for effective stress over the total saturation range from $S_l = 0$ to $S_l = 1$ should be developed, a possible qualitatively pattern is shown in figure 4.15. Any other effects of the influence of moisture content on mechanical properties, for instance change in effective shear parameters, are discussed in chapter 5.

5 Stress-Deformation Behaviour of MSW

The stress-deformation behaviour of the waste's solid skeleton is described based on the models by Ebers-Ernst [58] and Krase [135]. The applied constitutive model is explained in section 5.2 after an introduction into the mechanical properties of MSW in section 5.1. The last section 5.3 discusses aspects of the influence of moisture content on mechanical strength.

5.1 Phenomenology

Stress-deformation behaviour of waste is often compared to that of soils, whereas major differences occur due to the waste's composition and due to its content of degradable particles. In this section, special focus is laid on degradation induced settlements, which motivates development of a novel creep model to cover those effects. For an in-depth description of shear strength and stability, the reader is referred to Kockel [129], Kölsch [132], Ebers-Ernst [58] and Krase [135].

5.1.1 Classification and Unit Weight

The appropriate classification of municipal solid waste is a research issue itself and important for comparison of experimental results, see Dixon and Jones [52]. Waste can be classified in several ways on different levels. A rough classification is usually made by grouping waste under terms like household waste or commercial waste. Often fractions are assessed with respect to their degradability as well. A sorting analysis may provide a more detailed informative basis on waste composition. A particle size distribution may give similar informations, if waste fractions and particle size are correlated. Not only the maximum dimension of particles, but also their shape, e.g. if round or elongate, is important for assessment of mechanical strength.

The unit weight of municipal solid waste is dependent on the contained materials, on the compaction state and on the water content. An overview of densities and unit weight is given by Zeccos [248] or Dixon and Jones [52]. Unit weight determined from in-situ measurements or estimated varies between $3\,\mathrm{kN/m^3}$ and $17.5\,\mathrm{kN/m^3}$.

5.1.2 Shear Strength and Tensile Strength

Like for general frictional materials, overburden pressure increases the frictional resistance against shearing in the waste's porous skeleton. However, an additional effect in waste is

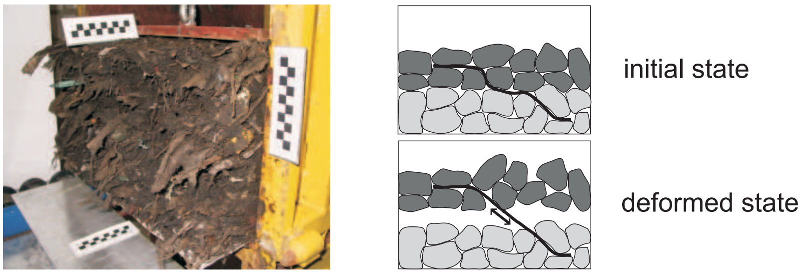

Figure 5.1: Influence of fibrous particles in waste on strength. Left: Waste sample in small scale tensile test (source: Jan Bauer, Leichtweiß- Institut für Wasserbau, TU Braunschweig). Right: Visualisation of reinforcement effect, from Kölsch [132]

found to be significant in experiments. Kockel [129] performs triaxial tests and does partly not observe any point of failure within the maximum possible displacement of the experimental device. Instead, a hardening effect is observed with ongoing deformation. The effective friction angle tends to increase at high strains. The lack of any point of failure is attributed to the reinforcing effect of fibrous particles in the waste. Figure 5.1 (left) shows a photo of a waste sample in an apparatus for small scale tensile tests. The fibrous particles, e.g. elongate pieces of plastic foils, are clearly noticeable. As shown in figure 5.1, right, the fibres are anchored in the more rounded particles and bear tensile stresses upon deformation. The mechanism is analysed in detail by Kölsch [132] with the performance of large scale tensile tests. Kölsch [132] observes an increase of tensile stress with increase of overburden vertical pressure and terms the effect *fibrous cohesion* in analogy to reinforced earth.

If the fibrous particles are biologically degradable, shear strength may change upon decomposition. Based on his experimental findings, Kockel [129] is among the first to suggest that waste may be described like a composite consisting of a basic matrix and a fibre matrix. For analysis of landfill slope stability often classical geotechnical methods like methods of slices are applied. Thereby, parameters are often estimated very conservatively, shear parameters of organic soft soils like peat are used and the influence of the fibres is neglected.

The experimental findings on fibrous cohesion give rise to a new type of models, which focus more explicitely on the special properties of waste extending the geotechnical methods used before. The model developed by Kölsch [132] is implemented into the methods after Krey and Bishop. Ebers-Ernst [58] develops a constitutive model for MSW in the framework of large strain kinematics, whereas small elastic strains are assumed. The solid material is divided into basic matrix and embedded fibres based on the experimental work by Kockel [129]. An elastoplastic model is applied in order to describe the shear failure mechanism of the basic matrix using the Drucker-Prager criterion. Time-dependent settlements are described by an isotropic creep model. To cover the effect of orientation of the fibres due to the type of emplacement a model for anisotropic elasticity is applied. Tensile strength and spontaneous-plastic deformations of the fibres are described by incorporating the model proposed by Kölsch [132]. Ebers-Ernst's model is later refined and extended by Krase [135]. Thereby, anisotropic creep is considered and a single surface yield function similar to the Mohr-Coulomb criterion is applied.

Lüke [148] also adopts Kockel's idea of splitting the material into two fractions. Thereby, an elasto-viscoplastic model is developed for the basic matrix within linear kinematics. Lüke applies Hooke's law for the elastic domain, which is limited by a yield surface of Cam clay type. A micromechanically based approach is used for the fibres to model the behaviour of the single elements by elasto-viscoplasticity. The interaction of the fibres with the surrounding basic matrix as well as the anisotropic orientation is included in the approach, too.

Like Lüke and Ebers-Ernst, Machado et al. [151] consider waste as a mixture of fibrous elements consisting of plastics mainly and of a paste composed of non-fibrous particles. The behaviour of the fibres is modelled by ideal plasticity applying the von Mises yield criterion. The elastic strains are connected with elastic strains of the paste by an activation function. Plastic deformations of the paste are described by Cam clay plasticity. Young's modulus is formulated stress dependent. The total stresses of the mixture of the two components are equal to the sum of the partial stresses weighted by their volume ratios. A hyperbolic function with two parameters is applied in order to describe time-dependent deformations.

Contrary to the smeared approaches by Ebers-Ernst, Krase and Machado, Singh et al. [217] discretise the reinforcing elements directly by linear elastic bar elements. It is assumed that the material can be split up into 4 major constituents: (1) rigid, (2) soil-like, (3) degradable and compressible, and (4) reinforcing and tensile elements. Elastic deformations of the waste are described by nonlinear, hyperbolic elasticity. Shear strength parameters are derived from experiments and from stochastic modelling.

5.1.3 Settlements

An in-depth understanding of settlement mechanisms is important not only during operation but also for landfill aftercare. Settlement predictions are necessary for decision making on whether a surface liner system can be placed on the landfill and to ensure a safe subsequent utilisation of a landfill site. Settlements are dependent on the type of emplacement and initial compaction. Additionally, they may be influenced by water content and degradation. The solid mass loss due to biological decomposition may lead to creation of additional pore space. The resulting loosening increases the compressibility which accelerates settlements.

In general, settlements are often distinguished

a) dependent on the *phenomena* and *mechanisms* which cause the settlements, or,
b) with respect to development in time by dividing the time-settlement curve into different *phases*.

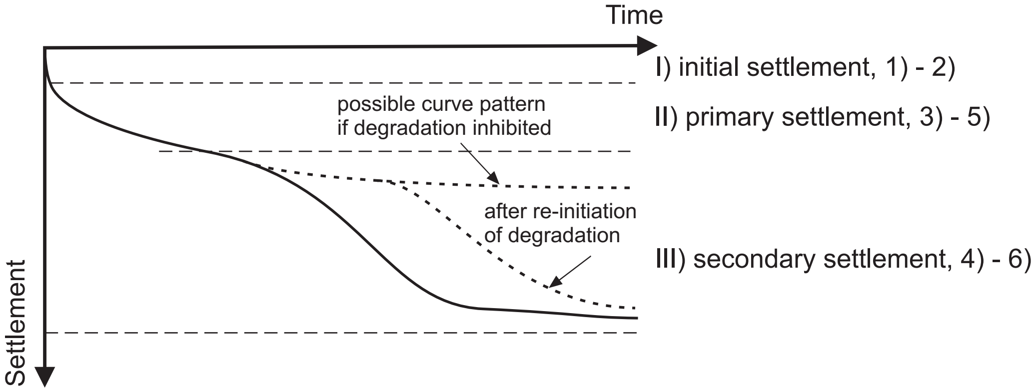

Figure 5.2: Settlement pattern of landfills or waste samples under constant loading

Murphy and Gilbert [179] and Edil et al. [59] are among the first to discuss different mechanisms of settlement. The categorisation by Edil et al. is adopted here and supplemented by the phenomena 3) and 4). Hence, major phenomena are:

1) mechanical effects (distortion, bending, crushing, compression of interparticle and intraparticle voids, reorientation),
2) ravelling (movement of fine particles into large voids),
3) consolidation (dissipation of excess pore pressures),
4) creep of waste materials,
5) physical-chemical effects (corrosion, oxidation and combustion),
6) and bio-chemical decomposition.

Usually, the number of phases is less than the number of processes, i.e. the phases do not correspond to a unique single phenomenon. Often the following three phases are distinguished

I) initial settlement,
II) primary settlement,
III) and secondary settlement.

Sometimes other terms are used, e.g. primary consolidation and secondary compression or primary and secondary creep. The distinction of phases is often related to inflexion points of the time-settlement curve. Different classifications can be found in the literature like recently highlighted by Powrie et al. [195]. Sometimes terms are even used in different sense. Especially the term consolidation might in some publications refer to time dependent compression in general, whereas throughout this thesis, consolidation refers to time dependent deformation due to expulsion of pore water and dissipation of pore pressure under loading only.

Phases and mechanisms can be allocated as shown in figure 5.2. Several one-dimensional approaches exist to describe the time-settlement behaviour of waste. Some are based on a mathematical description of successive phases but not of the mechanisms itselfes. Time-dependent functions are applied and their parameters are determined by fitting numerical results to experimental measurements. Models often assume a linear relationship between settlement and log time. Primary and secondary settlements can then be described by two compression coefficients which correspond to two slopes of a bilinear time-settlement curve in semi-logarithmic scale. For an overview of settlement models applied on MSW landfills the reader is referred to El-Fadel and Khoury [64], Ivanova [118] or Elagroudy et al. [69].

Elagroudy et al. [69] compare settlement predictions based on measured site data as obtained by different settlement models. Site data and predicted results are shown for the sites A and N in figure 5.3. Although the site data is approximated quite sufficiently by all models, predicted settlements differ remarkably in the long term. Whereas some models, like the hyperbolic function or the Gibson-Lo model, predict a declining creep rate, others assume an increasing rate on log t scale, for example the biological model and the power-creep law. The authors conclude that models which include the assumption that settlement strain is linear with respect to logarithm of time do not have the ability to react on changing waste properties and should not be applied on landfills with a high organic matter content.

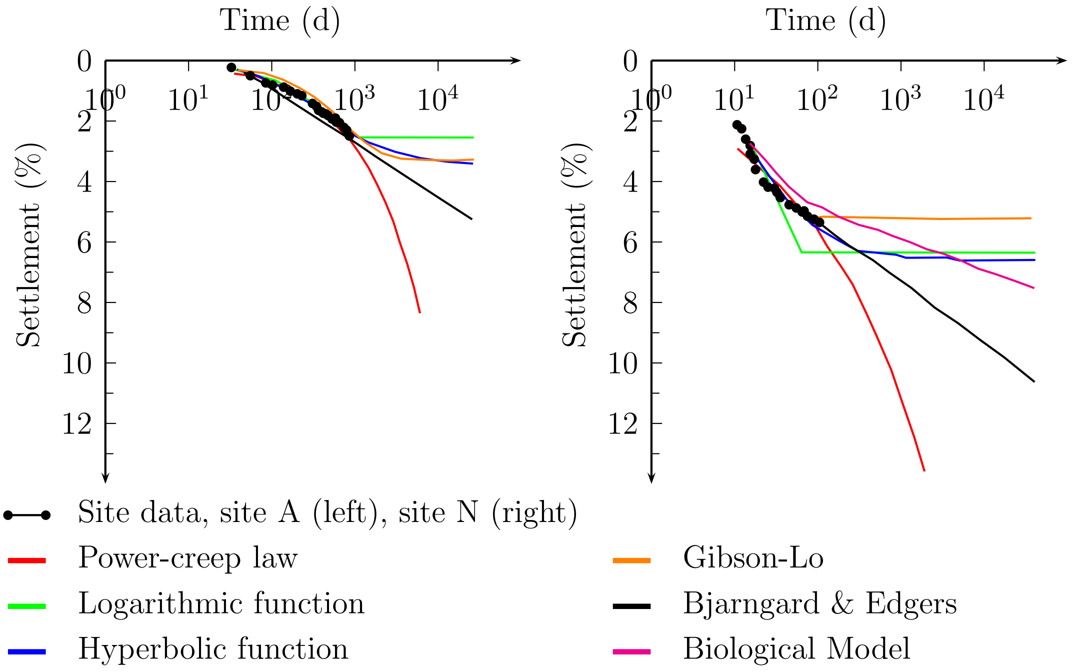

Figure 5.3: Comparison of different settlement models with respect to prediction of site data from two landfill sites, taken from Elagroudy et al. [69]

Bjarngard and Edgers [25] evaluate settlement data from 24 landfills. Settlements are compared in a strain vs. log time plot, selected data are plotted in figure 5.4. Settlements up to 30 % of initial height are measured. At some landfills an increase of settlement rate is observed, which may be explained by solid mass loss during biological degradation.

Wardwell and Nelson [238] present results of oedometric tests on artificial mixtures of kaolin clay and cellulose fibres. Duplicate samples with varying content of fibres are tested.

After a pre-consolidation phase at 24 kN/m^2 the samples are loaded over 190 days with 48 kN/m^2. One sample of each pair is seeded with nutrients to enhance decomposition, the other is left deficient in nutrients. Figure 5.5 shows the measured settlements for fibres' contents of 40 %, 55 % and 70 %.

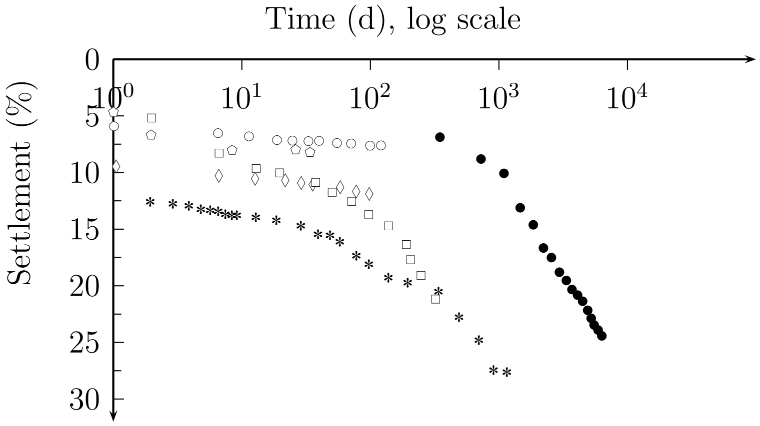

Figure 5.4: Settlements measured at different landfill sites, selected data from Bjarngard and Edgers [25]. Detailed attribution to sites not provided

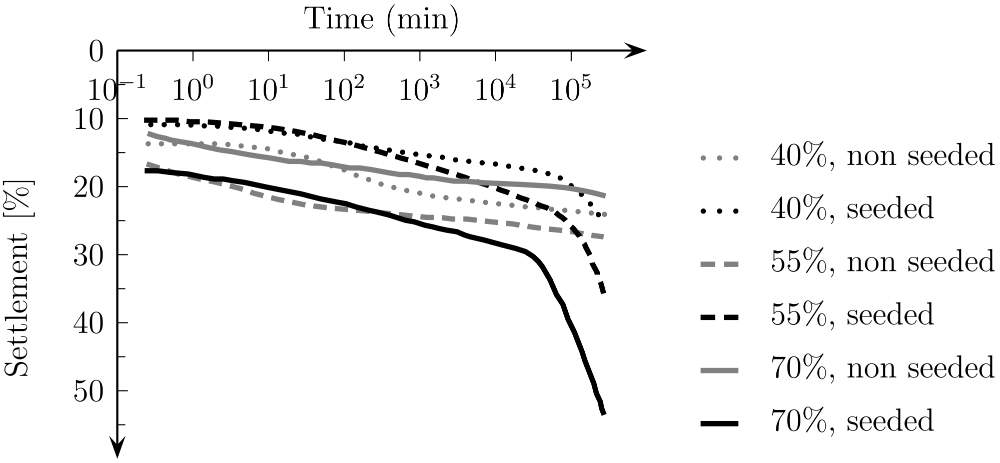

Figure 5.5: Time-settlement curves obtained from oedometric tests on artificial kaolin/cellulose mixtures for varying cellulose content, data from Wardwell and Nelson [238]

Similarly to the landfill data published by Bjarngard and Edgers, a change in settlement rate of the seeded samples is observed in such a way that the time-settlement curve exhibits two distinct slopes on semi-logarithmic scale. This pattern is not observed in the non-seeded samples which behave initially similar to the others. Furthermore, the results show that the magnitude of final settlement during the test period increases with the content of fibres. The experiments confirm the phenomenon of degradation-induced settlements.

The enhancement of biodegradation as performed in the experiments by Wardwell and

Nelson is also used in practical landfill operation. Landfill operators apply techniques to increase biodegradation by adding moisture, e.g. from recirculation of leachate, or by providing aerobic conditions from active aeration. Benson et al. [19] compare settlement measurements at a landfill with both conventionally operated cells and cells with leachate recirculation at elsewise similar conditions. The amount of recirculated leachate is very low and the amount of collected leachate is even slighty lower for the bioreactor cell, probably since the waste is below its moisture retention capacity. Nevertheless, measurements at the gas collection system show that the gas flow rate per unit length of well screen is 69 % higher in the bioreactor cell indicating a faster decomposition. In figure 5.6, settlements are plotted with respect to time. After approximately 2.7 years the settlement in the conventional cell is less than 5 % of the initial height. Surface displacement is up to 25 % in the bioreactor cell, whereas settlement rates vary with time. The authors conclude that settlements may be faster in bioreactor landfills and may also reach a higher magnitude. However, recalling the low leachate volume recirculated, it is likely that faster degradation and settlements are triggered by other effects as well.

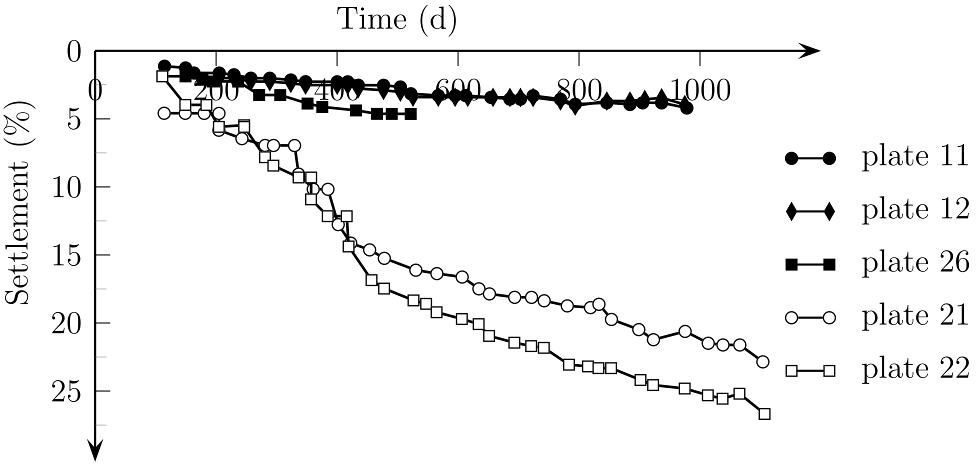

Figure 5.6: Data from Benson et al. [19]. Plates 11, 12 and 26 are from a conventional operated cell, plates 21 and 22 are from a bioreactor cell. Initial waste height is 24.3 m

The data shown in this section clearly motivates the coupling of degradation processes and settlements, especially for long-term modelling of MSW landfills.

5.2 Constitutive Model for Stress Deformation Behaviour of Municipal Solid Waste

As suggested by Kockel [129] and picked up by Ebers-Ernst [58] and Krase [135], the constitutive model treats MSW like a composite in this thesis. The solid phase is supposed to consist of a soil-like basic matrix and embedded fibres as shown in figure 5.7. The basic matrix is made up of the solid, more granular, particles including the pores. The

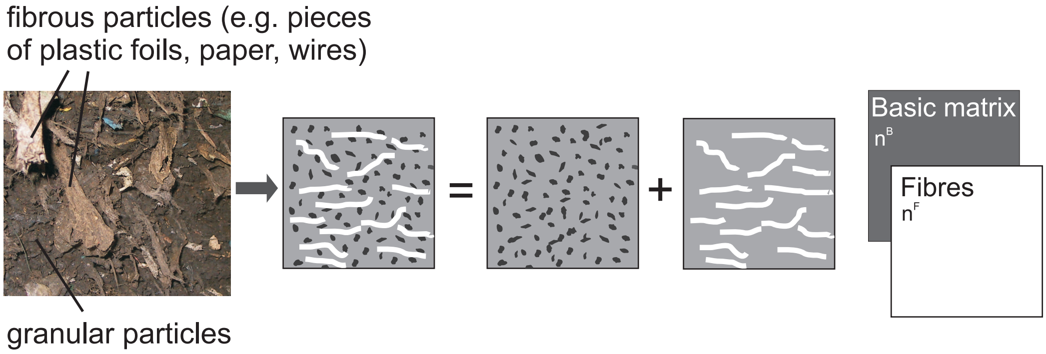

Figure 5.7: Consideration of fibres' reinforcement in model for MSW strength, split into soil-like basic matrix and fibres

fibres represent the elongate, reinforcing particles like pieces of plastic foils. The material models for both fractions are formulated separately, whereas equal displacement fields are assumed. Thus, it is sufficient to consider a single displacement field $\mathbf{u}_s$ for the solid phase only

$$\mathbf{u}^B = \mathbf{u}^F = \mathbf{u}_s \ , \tag{5.1}$$

with indices B denoting the basic matrix and F denoting the fibres. Since a relative movement of the constituents has not to be considered, the strains of basic matrix and fibres coincide as well. The total solid stress is evaluated by the macroscopic stresses of the components multiplied by the volume fractions respectively according to equations (2.23) and (2.24). Using the partial traction vectors the total traction vector is defined by

$$\mathbf{t}^B \cdot da_B + \mathbf{t}^F \cdot da_F = \mathbf{t} \cdot da \Longrightarrow \mathbf{t}^B \cdot \frac{da_B}{da} + \mathbf{t}_F \cdot \frac{da_F}{da} = \mathbf{t} \ . \tag{5.2}$$

If the constituents are statistically distributed in the REV, the Delesscian law states that surface fractions coincide with volume fractions, see Fillunger [79], and one obtains

$$\mathbf{t} = \mathbf{t}^B \cdot n^B + \mathbf{t}^F \cdot n^F \ \text{ and } \ \mathbf{T}^s_e = n^B \cdot \mathbf{T}^B + n^F \cdot \mathbf{T}^F \ . \tag{5.3}$$

The stresses of the two components are evaluated from a given strain. The procedure is visualised in figure 5.8 in a one-dimensional representation. The approach is equivalent to the parallel alignment of two elements describing the constitutive material behaviour of the two components dependent on internal variables. The different elements of the material description are explained in sections 5.2.3 and 5.2.4. An implication from assuming equal displacement fields is that the volume fractions of fibres and basic matrix do not change during deformation and degradation. Equal displacement fields imply equal deformation gradients, and thus the two components undergo the same volumetric strain. Hence, the volume fractions may not change. If degradation processes are considered,

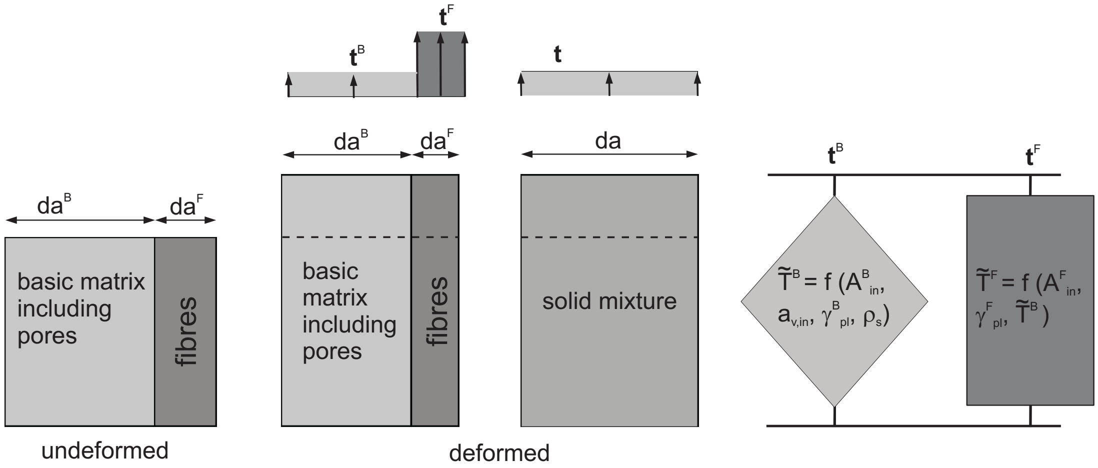

Figure 5.8: Split of stress tensor for a mixture of basic matrix and fibres for one-dimensional case

the total mass loss is attributed by equal parts to the two constituents, i.e. the volume fractions n^B and n^F do not change through decomposition, too. In further extensions of the model this assumption may be abandoned to describe decrease in shear strength with decomposition. Prerequisite are sufficient experimental data.

5.2.1 Small Elastic Strains

Experiments show that waste undergoes in general large deformations. Those deformations may be elastic or inelastic, which may include time-dependent deformation as well. In description of small strain plasticity the linearised Green strain tensor $\boldsymbol{\varepsilon}$ is split up into elastic and inelastic strains $\boldsymbol{\varepsilon}_{el}$ and $\boldsymbol{\varepsilon}_{in}$

$$\boldsymbol{\varepsilon}_s = \frac{1}{2}\left(\text{grad}\,\mathbf{u_s} + \text{grad}\,^T\mathbf{u_s}\right) = \boldsymbol{\varepsilon}_{s,el} + \boldsymbol{\varepsilon}_{s,in}\ . \tag{5.4}$$

This additive split is not applicable when describing large inelastic strains, rather the deformation gradient is split multiplicatively representing a series of mappings

$$\mathbf{F_s} = \mathbf{F}_{s,el} \cdot \mathbf{F}_{s,in}\ . \tag{5.5}$$

The first mapping by $\mathbf{F}_{s,in}$ leads to a stress-free, intermediate configuration with incompatible adjacent particles. On the intermediate configuration, a strain tensor $\boldsymbol{\Gamma}$ can be defined by corresponding mappings of the Green or Almansi strain tensor. The strain $\boldsymbol{\Gamma}$ is decomposable additively similar to the linearised Green strain tensor in (5.4), see for example Haupt [101], so that

$$\boldsymbol{\Gamma} = \boldsymbol{\Gamma}_{el} + \boldsymbol{\Gamma}_{in}\ . \tag{5.6}$$

Regarding waste, the elastic part of deformation is usually small compared to the inelastic part. This enables further simplification of the kinematic relations. The mapping of intermediate and current configuration then is a rotation only, so that the constitutive relations can be expressed by stress and strain measures acting on the current configuration. In this case, the Almansi strain tensor $\mathbf{A}_s$ is additively decomposable into elastic and inelastic parts as well, cf. Krase [135]

$$\mathbf{A}_s = \mathbf{A}_{s,el} + \mathbf{A}_{s,in} \; . \tag{5.7}$$

5.2.2 Unit Weight of Solid Mixture

For evaluation of external virtual work of the self-weight in Total Lagrangian description, cf. (2.29), the density ρ_{ref} with respect to the undeformed domain is required, which is related to the current density ρ by

$$\rho \cdot \det \mathbf{F}_s = \rho_{ref} \; . \tag{5.8}$$

Neglecting the unit weight of the gaseous components the current density with respect to the reference configuration is

$$(\rho_s^{IM} + \rho_s^{DO} + \rho_s^{X} + \rho_l) \cdot \det \mathbf{F}_s = \rho_{ref} \; . \tag{5.9}$$

With ongoing degradation, the density is reduced and correspondingly stresses from overburden pressure decrease.

5.2.3 Constitutive Model for the Basic Matrix

The basic matrix is assumed to be a cohesive, frictional material with properties similar to those of soils. Additionally to elastic and spontaneous plastic deformations, also time-dependent deformations are described. Firstly, time dependent settlements are caused from a change in effective stress. They are considered by splitting the total stress of the mixture into effective stress and pore pressure in the formulation of internal virtual work, compare equation 4.39. Secondly, time-dependent settlements may occur due to creep of the solid skeleton itself or due to the influence of degradation. Correspondingly, the total inelastic strain rate $\mathbf{D}_{s,in}$ is split into a part attributed to spontaneous deformation $\mathbf{D}_{pl}$ and a part due to creep, i.e. compaction, of the solid phase $\mathbf{D}_{cr}$

$$\mathbf{D}_{s,in} = \mathbf{D}_{s,pl} + \mathbf{D}_{s,cr} \; . \tag{5.10}$$

The inelastic strain rate coincides with the covariant Oldroyd rate of the Almansi strain, which equals its material time derivative if the spatial velocity gradient vanishes

$$\mathbf{D}_{s,in} = \overset{\triangle}{\mathbf{A}}_{s,in}, \quad \text{if } \mathbf{L}_s = \mathbf{0} \;\; \overset{\triangle}{\mathbf{A}}_{s,in} = \dot{\mathbf{A}}_{s,in} \; . \tag{5.11}$$

Elasticity For description of reversibel deformations of a compressible material the Neo-Hooke model is applied, see for example Bonet and Wood [29] or Parisch [192]. The Kirchhoff stress tensor is defined by

$$\tilde{\mathbf{T}}^B = \lambda \, ln \, (\det \mathbf{F}_{s,el}) \, \mathbf{1} + \mu \, (\mathbf{B}_{s,el} - \mathbf{1}) \;\; , \tag{5.12}$$

with Lame's constants λ and μ, which are related to Young's modulus E and Poisson's ratio ν by

$$E = \frac{\mu(2\mu + 3\lambda)}{\lambda + \mu} \;\; \text{and} \;\; \nu_P = \frac{\lambda}{2\lambda + 2\mu} \; . \tag{5.13}$$

The assumption of incompressible solid particles remains valid, as the material law describes the behaviour of the whole solid skeleton including the pores. If not stated elsewise the parameters given in table 5.1 are used within the simulations. They are based on a parameter identification using genetic algorithms by Krase [135].

Spontaneous Plastic Deformation Time-independent irreversibel deformations are supposed to occur if a deviatoric yield stress is reached. Irreversible deformation due to hydrostatic stress states are attributed to compaction. Since the basic matrix is supposed to be soil-like, yield criteria developed for soils may be applied. The maximum shear stress is dependent on the hydrostatic stress state if overall compression increases internal resistance against shearing. This leads to cone-shaped yield surfaces. Whereas Ebers-Ernst [58] uses the compression cone of Drucker-Prager, Krase [135] implements a yield surface presented by Ehlers [60] in a version, which is similar to the Mohr-Coulomb criterion and which includes other well-known yield criteria as a special case. A cap may be included as well, but is not applied here. With the invariants of the stress tensor $\tilde{\mathbf{T}}^B$ the yield condition is given by

$$f = \sqrt{J_{2D} \left(1 + \gamma_F \frac{J_{3D}}{J_{2D}^{3/2}} \right)^{m_F} + \frac{1}{2} \delta_F \, I_1^2} + \alpha_F \, I_1 - \kappa_F \leq 0 \; . \tag{5.14}$$

The parameters m_F and δ_F control the shape in the deviatoric plane. When choosing the parameters $\alpha_F, \gamma_F, \delta_F, \kappa_f$ and m_F the convexity of the yield surface has to be ensured. The parameters α_F, κ_f and γ_f are related to the shear parameters, namely effective angle of internal friction ϕ' and effective cohesion c', by

$$\alpha_F = \frac{\sin\phi'}{3} \ , \ \ \kappa_F = c'\cos\phi' \ , \ \ \text{and} \ \ \gamma_F = \frac{\sqrt{27}}{2}\frac{1-\left(\frac{3-\sin\phi'}{3+\sin\phi'}\right)^{2/m}}{1+\left(\frac{3-\sin\phi'}{3+\sin\phi'}\right)^{2/m}} \ . \tag{5.15}$$

As such, the yield surface touches the yield surface after Mohr-Coulomb in the hydrostatic plane for simple shear. The parameter δ_F enables a rounding of the tip of the cone in the tensile region. The shear parameters ϕ', c' and the angle of dilatancy ψ are not constant, but dependent on the compaction state expressed by the inelastic volume strain

$$\phi' = a_{\phi'}\left(\frac{1-\tanh(b_{\phi'}\,a_{v,in})}{2}\right)^{c_{\phi'}} \ , \tag{5.16}$$

$$c' = a_{c'}\left(\frac{1-\tanh(b_{c'}\,a_{v,in})}{2}\right)^{c_{c'}} \ , \ \ \text{and} \tag{5.17}$$

$$\psi = a_{\psi}\left(\frac{1-\tanh(b_{\psi}\,a_{v,in})}{2}\right)^{c_{\psi}} \ . \tag{5.18}$$

where a_j, b_j and c_j with $j \in \phi', c', \psi$ are parameters. The total volumetric strain is nearly equal to the inelastic volume strain and given by

$$\begin{aligned} a_v \approx a_{v,in} &= 1 - \frac{1-a_{v,0}}{\det\mathbf{F}_{s,in}} \\ &= 1-(1-a_{v,0})\sqrt{1-2I_{1,\mathbf{A}_{s,in}}+4\,I_{2,\mathbf{A}_{s,in}}-8\,I_{3,\mathbf{A}_{s,in}}} \ . \end{aligned} \tag{5.19}$$

By setting an initial volumetric strain $a_{v,in,0} \neq 0$ an initial compaction due to a preconsolidation pressure can be considered. Table 5.1 lists the basic parameter set used herein and figure 5.9 shows plots of the yield surface. In a model for the mechanical behaviour, relations (5.16), (5.17) and (5.18) are extended to density dependence by Krase et al. [136], which allows a coupling of shear parameters to degradation in a future extension of the model.

The application of an associated flow rule would lead to unrealistic volumetric strains during yielding. Thus, a non-associated flow rule is applied here based on a plastic potential q^F using the angle of dilatancy ψ

$$q^F = \sqrt{J_2 + \frac{\delta_q}{2}I_1^2} + \alpha_q I_1 \ , \ \ \text{with} \ \ \alpha_q = \frac{\sin\psi}{3} \ , \tag{5.20}$$

wherein J and I are again the invariants of the Kirchhoff stress tensor of the basic matrix[1]. The plastic strain rate is given by

$$\mathbf{D}_{pl} = \dot{\lambda}^B_{pl}\frac{\partial q}{\partial\tilde{\mathbf{T}}^{\mathbf{B}}} \tag{5.21}$$

---

[1] see section on notation for definition

with the plastic multiplier $\dot{\lambda}_{pl}^B$, which describes the magnitude of plastic strains.

Table 5.1: Parameters for elasticity and plasticity in the material desription of the basic matrix

elasticity		
$\lambda = 2885\,\text{kPa}$	$E = 5000\,\text{kPa}$	
$\mu = 1923\,\text{kPa}$	$\nu = 0.3$	
shear parameters		
$a_\phi = 35.0$	$b_\phi = 2.0$	$c_\phi = 1.0$
$a_c = 20.0$	$b_c = 0.0$	$c_c = 0.0$
$\psi = 0$		
yield surface		
$m_F = 0.5$	$\delta_F = 0.01$	$\gamma_F = 1.52$

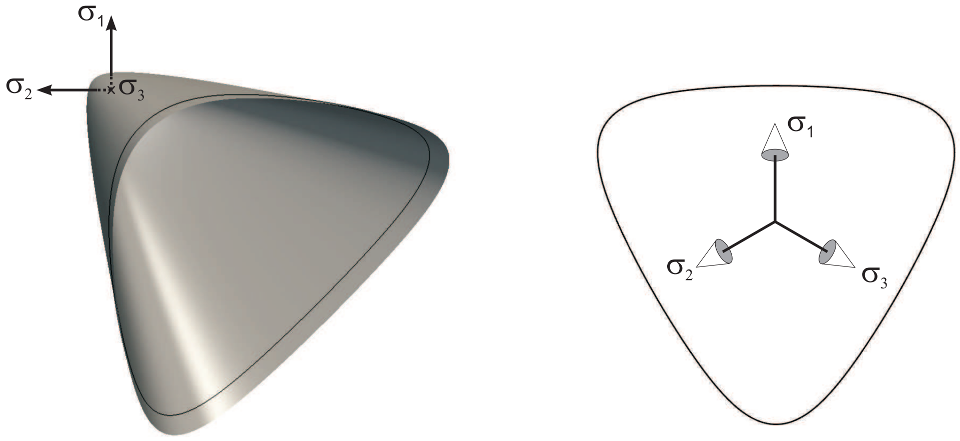

Figure 5.9: Yield surface after eq. (5.14) with parameters from table 5.1 at $a_{v,0} = -0.55$. Three-dimensional view on yield-surface cone and deviatoric plane

Time-Dependent Compaction The origin of the compaction model is a creep model developed by Zhang et al. [249] for describing the compaction behaviour of crushed rock salt. Their model is adopted by Ebers-Ernst [58] for the compaction behaviour of waste and extended to threedimensional stress states. Krase [135] further extends the model to cover anisotropic creep.

The creep rate $\mathbf{D}_{cr}^B$ is defined by the sum of the dyads of the eigenvectors of the effective Kirchhoff stress tensor multiplied by the corresponding creep rate $\gamma_{cr,\alpha}$ in direction of α

$$\mathbf{D}_{cr}^B = \sum_{\alpha=1}^{3} \dot{\gamma}_{cr,\alpha}^B \left(\mathbf{n}_{\tilde{T}_\alpha^B} \otimes \mathbf{n}_{\tilde{T}_\alpha^B} \right) . \tag{5.22}$$

To cover the influence of degradation on settlements in the fully coupled model, the approach by Krase [135] is modified and extended to allow for a direct coupling with decomposition. The creep model is then able to describe two phenomena. Firstly, compaction may be caused by load induced distortion of the solid particles themselves as well as due to compression and structural change of the pore space, of which the first one is assumed to be significant more in the long-term. Secondly, the compaction rate is related to density so that its change due to degradation triggers an increase in settlements. Compaction is thus triggered by change in density or change in effective stress.

The compaction rate is described by the product of two functions, see also Krase et al. [136]. The creep rate in the direction α, which is the direction of the principal stresses, depends on the Kirchhoff stresses of the basic matrix $\tilde{\mathbf{T}}^{e,B}$ and on the dry density ρ_i

$$\dot{\gamma}^{B}_{cr,\alpha} = f_1\left(\tilde{\mathbf{T}}^{e,B}\right) f_2\left(\rho_i, \tilde{\mathbf{T}}^{e,B}\right) \tag{5.23}$$

whereas f_1 is a Norton creep law. The McAuley-brackets ensure that compaction occurs under compressive stress only. The parameter σ_0 serves for a normalisation of the stress $\tilde{\mathbf{T}}^{B}_{\alpha\alpha}$. The parameters A_{cr} and n_{cr} control the stress dependency. The second term f_2 ensures a decreasing creep rate with ongoing compaction and is both dependent on stress and density

$$f_1\left(\tilde{\mathbf{T}}^{e,B}\right) = -A_{cr}\left(\frac{\left\langle -\tilde{\mathbf{T}}^{e,B}_{\alpha\alpha}\right\rangle}{\sigma_0}\right)^{n}_{cr}\,, \tag{5.24}$$

$$f_2\left(\rho_i, \tilde{\mathbf{T}}^{e,B}\right) = \left[\ln\left(\frac{\rho_\infty}{\rho_\infty - \rho_i}\right)\right]^{-p} \cdot \ln\left(\frac{\rho_{max}}{\rho_i}\right)^{p}\,, \tag{5.25}$$

$$\rho_\infty = \frac{b_{cr}\rho_{min} + \left|\sum_{\alpha=1}^{3}\left\langle -\tilde{\mathbf{T}}^{e,B}_{\alpha\alpha}\right\rangle\right|^{a_{cr}}\rho_{max}}{b_{cr} + \left|\sum_{\alpha=1}^{3}\left\langle -\tilde{\mathbf{T}}^{e,B}_{\alpha\alpha}\right\rangle\right|^{a_{cr}}}\,. \tag{5.26}$$

The density ρ_∞ is the maximum density under a certain stress level. It is interpolated between the minimum density ρ_{min} and the maximum density ρ_{max} depending on stress. The parameters a_{cr} and b_{cr} can be determined by means of compression tests under different loadings. The different densities are explained in figure 5.10. If the density ρ_i is reduced due to decomposition, the term f_2 exhibits higher values leading to an increasing creep rate. The creep rate is dependent on effective stress and hence change in effective stress due to drying and wetting influences the magnitude of the creep rate. Alternatively to dry bulk density, the porosity could be used as an indicator of compaction state, but the density is supposed to be easier to measure, which facilitates fitting to experimental results. It may be discussed to formulate the compaction model in terms of total stress, so that suction has no effect on creep. The parameters a_{cr} and b_{cr} are estimated for the CAR experiments performed by Ivanova [118] from the deformations at the end of the tests, see figure 5.11. Thereby, it is assumed that the density obtained at this stage nearly coincides with ρ_∞.

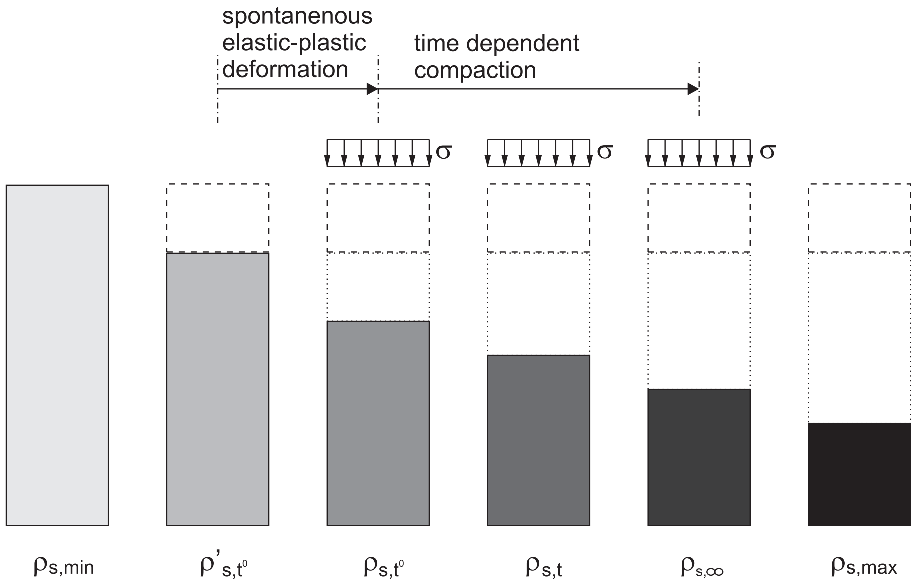

$\rho_{s,min}$	minimum density, loosest possible state, may be chosen equal to initial density
ρ'_{s,t^0}	initial state, density after some preloading at time $t^0 - \Delta t$
ρ_{s,t^0}	density at time t^0 directly after loading with σ
$\rho_{s,t}$	density at time t with $t^0 < t < t_\infty$
$\rho_{s,\infty}$	density after loading with σ at t_∞
$\rho_{s,max}$	maximum density $\rho_{s,max} = \tilde{\rho}_s$, $\phi = 0$

Figure 5.10: Definition of dry densities

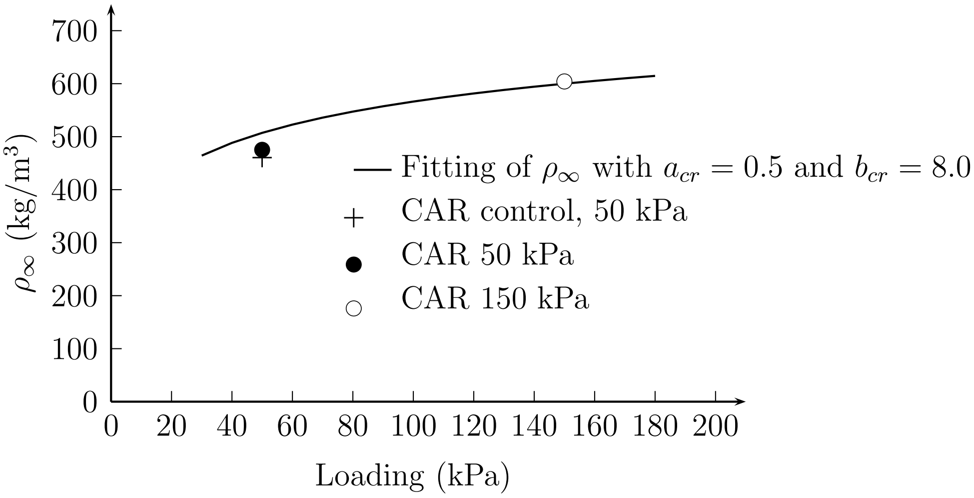

Figure 5.11: Estimation of parameters of the creep model for determination of ρ_∞ in the CAR experiments

5.2.4 Constitutive Model for the Fibres

The material model for the fibres includes both elastic and spontaneous plastic deformations.

Elasticity Due to the way of emplacement in landfills the fibrous particles are oriented in horizontal direction. This leads to anisotropic material behaviour considered by a transversely isotropic stress strain relation

$$\mathbf{T}^F = \left(\mathbf{R}_F^T \otimes \mathbf{R}_F^T\right)^{T_{23}} : \mathbb{C} : \left(\mathbf{R}_F \otimes \mathbf{R}_F\right)^{T_{23}} : \mathbf{A}_{el}^F \,. \tag{5.27}$$

The rotation tensor $\mathbf{R}_F$ considers the orientation of the fibres plane and is used to transform strains and stresses between local and global frame. The flexibility tensor $\mathbb{S}$ with $\mathbb{S} = \mathbb{C}^{-1}$ is taken from Altenbach et al. [3] and given in figure 5.12 with definition of symmetry.

$$\mathbf{S} = \begin{bmatrix} \frac{1}{E_1} & \frac{-\nu_{12}}{E_1} & \frac{-\nu_{23}}{E_3} & 0 & 0 & 0 \\ \frac{-\nu_{12}}{E_1} & \frac{1}{E_1} & \frac{-\nu_{23}}{E_3} & 0 & 0 & 0 \\ \frac{-\nu_{23}}{E_3} & \frac{-\nu_{23}}{E_3} & \frac{1}{E_3} & 0 & 0 & 0 \\ 0 & 0 & 0 & \frac{2(1+\nu_{12})}{E_1} & 0 & 0 \\ 0 & 0 & 0 & 0 & \frac{1}{2G_{13}} & 0 \\ 0 & 0 & 0 & 0 & 0 & \frac{1}{2G_{13}} \end{bmatrix}$$

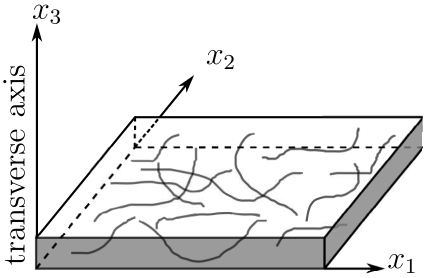

$E_1,\ \nu_{12}$ in fibres plane $(x_1 - x_2)$

$E_3,\ \nu_{23},\ G_{13}$ $\perp$ fibres plane

Figure 5.12: Transversely isotropic flexibility matrix $\mathbb{S} = \mathbb{C}^{-1}$ for defined fibres' orientation in $(x_1 - x_2)$-plane

Plasticity From the performance of large scale tensile tests, Kölsch [132] finds that the tensile strength of the fibrous waste is governed by two mechanisms: the bonding of the fibres in the granular matrix and the rupture of the fibres. The bonding depends on the loading perpendicular to the fibres plane. Both mechanisms are considered by a yield criterion of *Rankine* type

$$f_{t,\alpha} = \tilde{T}_\alpha - \tilde{T}_{t,\alpha} \leq 0 \quad \text{and} \quad f_{c,\alpha} = \tilde{T}_\alpha - \tilde{T}_{c,\alpha} \geq 0 \,, \tag{5.28}$$

with the yield stress in the tensile zone $\tilde{T}_{t,\alpha}$ and the compressive yield stress $\tilde{T}_{c,\alpha}$. The compressive yield stress is set to a very low value of 0.5 kPa in the applications. The tensile yield stress is determined dependent on the compressive stress of the basic matrix perpendicular to the fibres plane, $\tilde{T}_\perp^B$, and on the Almansi strain in principal direction,

$A_{in,\alpha\alpha}$. The approach is shown in figure 5.14. The tensile yield stress is given by

$$\tilde{T}_{t,\alpha} = \tilde{T}_{t,0} + \tilde{T}_m h_1 - (\tilde{T}_{t,0} + \tilde{T}_m) h_2 \tag{5.29}$$

whereas function h_1 controls hardening and function h_2 softening from rupturing of weak fibres or ongoing bonding loss. The two functions are plotted in figure 5.13. $\tilde{T}_m$ includes the limiting of yield stress by maximum bonding or fibre tensile stress as shown in figure 5.14 and is dependent on the stress of the basic matrix as follows

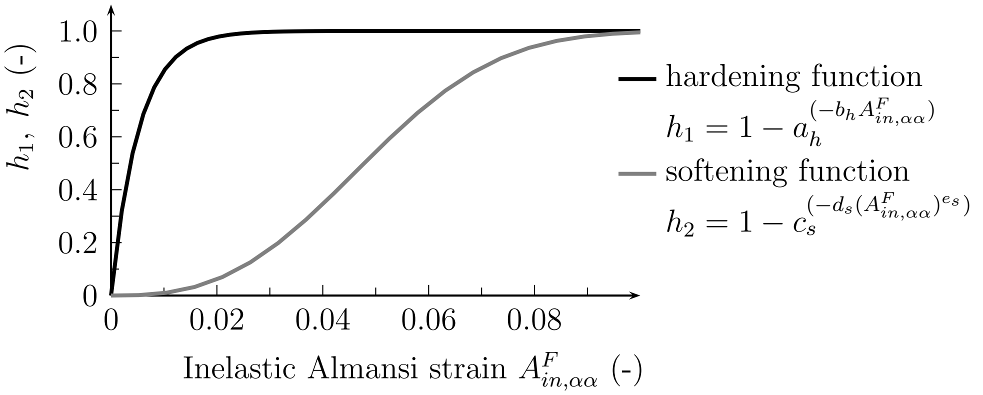

Figure 5.13: Hardening and softening functions h_1 and h_2 in the plasticity model for the fibres

$$\tilde{T}_{m,\alpha} = \begin{cases} \tilde{T}_{min} & \text{for } \tilde{T}^B_\perp > 0 \\ \tilde{T}_{min} + \frac{\tilde{T}_{max} - \tilde{T}_{min}}{\tilde{T}_{crit}} \tilde{T}^B_\perp & \text{for } 0 \geq \tilde{T}^B_\perp > T_{crit} \\ \tilde{T}_{max} & \text{for } \tilde{T}_{crit} > \tilde{T}^B_\perp \ . \end{cases} \tag{5.30}$$

In case that no loading perpendicular to the fibres plane is applied and no hardening is considered, the tensile strength equals a load independent strength $\tilde{T}_{t,0}$. Under vertical loading, the tensile strength is increased due to stronger bonding analogous to a linear friction law dependent on the magnitude of the load. If the tensile strength of the fibres themselves is reached, the fibres rupture and further loading beyond $\tilde{T}_{crit}$ cannot increase tensile strength.

In principal stress state the Rankine criterion is a cuboid as shown in figure 5.14, right. It is assumed that the fibres carry only very low tensile stress perpendicular to the fibres plane.

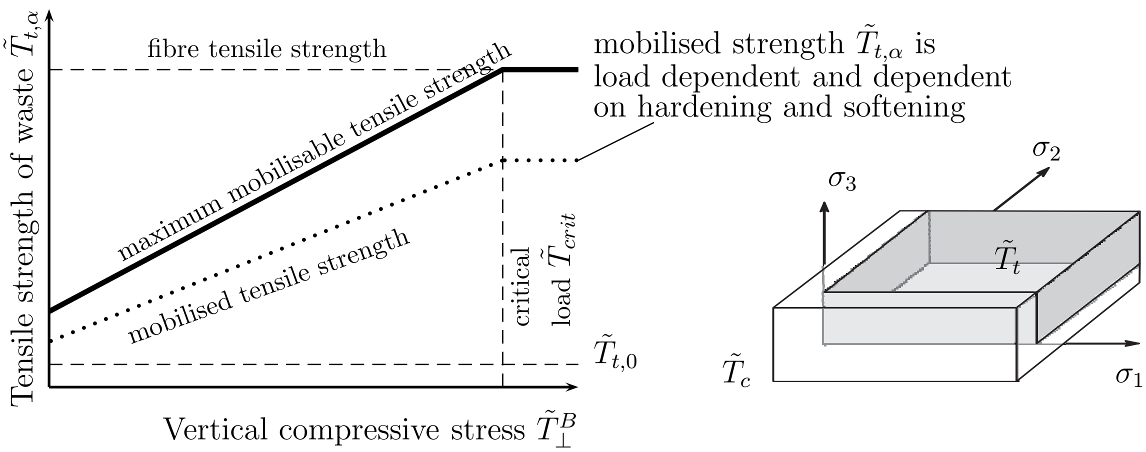

Figure 5.14: Model for dependence of fibres' yield stress on overburden pressure (left) and yield surface form of Rankine yield criterion (right)

Table 5.2 lists the parameters used in the simulations, which are based on the parameter determination by Krase [135]. The flow rule is formulated associatively requiring the determination of six plastic multipliers, which corresponds to the six surfaces of the yield surface in figure 5.14 right.

Table 5.2: Parameters for elasticity and plasticity of the fibres

elasticity					
E_1	$= 87\,506\,\mathrm{kPa}$	E_3	$= 1.0\,\mathrm{kPa}$	ν_{12}	$= 0.333$
ν_{23}	$= 0.0$	G_{13}	$= 1.0\,\mathrm{kPa}$		
tensile strength					
T_0	$= 50\,\mathrm{kPa}$	T_{min}	$= 50\,\mathrm{kPa}$	T_{max}	$= 1338.4\,\mathrm{kPa}$
T_{crit}	$= 400.0$	$T_{c,\alpha}$	$= 0.5\,\mathrm{kPa}$		
hardening and softening					
a_h	$= 2.887$	b_h	$= 178.6$		
c_s	$= 1.49$	d_s	$= 7364.0$	e_s	$= 2.75$

5.3 Influence of Water Content on Shear Strength

Limited effort has yet been made in transferring the approaches from unsaturated soil modelling to constitutive, mechanical modelling of waste, cf. also the discussion on effective stress in section 4.6. Much less experimental data is available for waste than for soils in that context. Experiments, e.g. Münnich et al. [177], Bauer et al. [12] and Bauer et al. [11] show that water content may reduce total shear strength. On the one hand, excess pore pressures reduce effective stress, which reduces maximum shear stress due to the cone-shaped yield surface. This effect is already included in the model by implementation of the effective stress concept in (4.39). Furthermore, it is conceivable that additional effects play a significant role. Even if no excess pore pressures are present, it is likely that water content influences material strength. For example, it might decrease the friction between the granular particles due to increasing sliding contact. Also it might reduce the strength of contained fibrous particles, e.g. paper. To clearly identify the mechanisms, separate tests on the basic matrix and on the total waste mixture are necesesary. Then it can be investigated if any shear strength reduction has to be attributed to the basic matrix or to the fibres. If the reduction is caused by weakening of fibrous cohesion, it would be sensible to use the softening functions of the fibres' model to consider the influence of water content. If the governing mechanisms of shear strength reduction are within the basic matrix, the effective shear parameters may be modified like proposed by Krase [135], who suggests to reduce the shear parameters by factors determined by an arctan-function dependent on water content. The functions cannot be applied, as no experimental evidence supporting parameter choice is available.

Nuth and Laloui [184] find in investigations of critical state lines of kaolin that shear parameters determined at saturated conditions may describe also shear strength under unsaturated conditions. In effective stress representation, neither the angle of friction nor the cohesion show variations, which would require a suction dependent formulation.

The influence of moisture content on shear parameters is a very interesting aspect for future extension of the model, if accompanied by an appropriate experimental programme. Yet, in this thesis a simple linear relationship for angle of internal friction dependent on saturation is implemented. Investigation of slope failure coupled with transport and degradation would, however, require the additional implementation of other numerical algorithms, for example the arc-length-method as used by Krase [135] for stability analysis of the dry solid skeleton. Such analyses are not within the scope of this thesis.

6 Solution of the Coupled Initial Boundary Value Problem

Based on the constitutive model, the balance equations, which are introduced in chapter 2 in their general form, are formulated in detail in equations (6.1) to (6.9). Figure 6.1 gives an overview of the components that have to be balanced, and how they are related by reactions and physical exchange processes. R1, R2 and L refer to the reactions of anaerobic degradation as shown in section 3.3.1. Evaporation/Condensation and dissolution are denoted by P1 and P2, respectively. The consideration of all components in figure 6.1 requires the solution of six mass balance equations. Additionally, the balance of energy is formulated in order to describe instationary temperature fields.

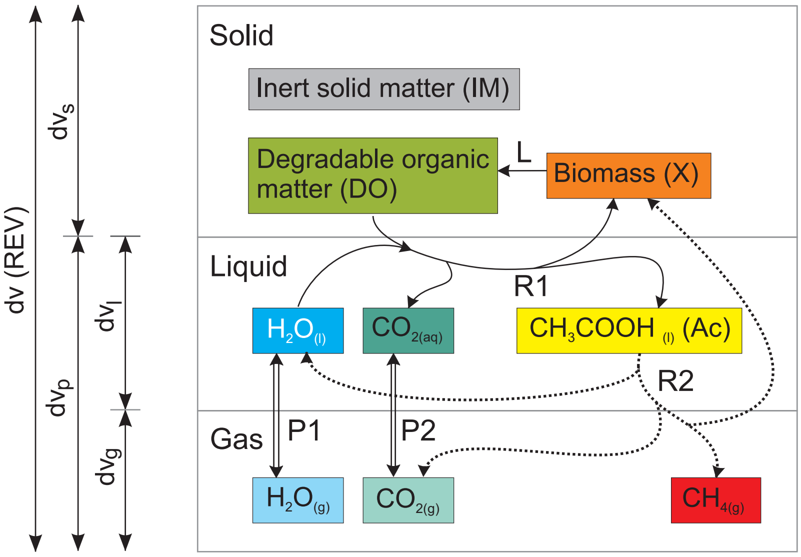

Figure 6.1: Overview of components, reactions and exchange processes.

Interactions of deformable porous media and fluids are counted among the multifield problems. In the proposed model, the macroscopic description within the Theory of Porous Media leads, together with the constitutive relations, to a set of nonlinear coupled differential equations. Several physical fields are coupled via conjoint state variables in a volume coupled formulation over the domain of a REV. A volume coupled problem may be distinguished from surface coupled problems in which the interactions are described at distinct interfaces. Examples in civil engineering are the analysis of aeroelasticity of bridges, Hübner [111], or discharge of silos, Leppert [141].
Different strategies exist to solve coupled problems. Weak and strong coupling or partitioned and simultaneous solution procedures are often distinghuised. The different approaches are for example discussed by Hübner [111] in an application on interface coupling.

The partitioned approach represents a staggered solution procedure, whereas in the simultaneous procedure the discretised equations are solved monolithically. Compared with partitioned solution procedures, a simultaneous solution may lead to better convergence properties in case of strong interactions between the fields, which motivates the application of this approach in this thesis.

6.1 Assembly of Final Balance Equations in Integral Form

The Principle of Virtual Work for the mixture is explained in equation (2.29) and rewritten here using equations (4.39) and (5.9)

$$\underbrace{\int_{V_0} \delta\mathbf{E} : (\mathbf{F}_s^{-1}(\tilde{\mathbf{T}}_e - \det\mathbf{F}_s \cdot (p_g + S_l \cdot (p_l - p_g) - p_{atm}) \cdot \mathbf{1}))\mathbf{F}_s^{-T})\, dV}_{\text{virtual internal work}} \tag{6.1}$$

$$= \underbrace{\int_{\Gamma_0} \delta\mathbf{u}\, \mathbf{t_0}\, dS}_{\text{work of surface pressures}}$$

$$+ \underbrace{\int_{V_0} \delta\mathbf{u}\, (\rho^{DO} + \rho^{IM} + \rho^{X} + \rho_l)\, \mathbf{g}\, dV}_{\text{work of volume loads (self}-\text{weight)}} ,$$

with the virtual Green strain

$$\delta\mathbf{E} = \frac{1}{2}\left(\mathbf{F}^T \mathrm{Grad}\, \delta\mathbf{u} + \mathrm{Grad}^{\,T} \delta\mathbf{u}\, \mathbf{F}\right) . \tag{6.2}$$

The solution of the Principle of Virtual Work requires the setting of boundary conditions, whereas their specification is optional in the balance equations (6.3) to (6.9).

Boundary conditions of Dirichlet type, Neumann type and Cauchy type may be considered in the simulation of structures. Different physical meanings are inherent, dependent on which governing equation is referred to.
Boundary conditions due to pressure forces, representing a Neumann type, are included in a weak form in a finite element formulation based on the Principle of Virtual Work and do not require special treatment. Dirichlet boundary conditions may prescribe displacements in a displacement-based formulation in order to describe fixed boundaries or displacement-controlled loading. Conditions of Cauchy type represent alignment of springs to describe flexible support at a boundary.

The detailed mass balance equations and the equation for conservation of energy are based on the general integral form derived in section 2.3.3, see (2.41). In the latter equation it is assumed that the whole control volume is occupied by a fluid phase. In a porous medium, only a part of the control volume is filled by the fluid phases depending on porosity and saturation. If a macroscopic, relative velocity related to the total surface area is used in the flux terms, the integration may be performed on the total domain. So, in the final formulation, the fluid velocities in the integral forms are replaced by the Darcy velocities $\mathbf{v}_{l,D}$ and $\mathbf{v}_{g,D}$. For definition of the Darcy velocity compare equations (4.7) and (4.8). Diffusive fluxes are implemented as well, but the investigation of their effects in separate analyses is not within the scope of this thesis.

Water The mass balance for $\mathrm{H_2O}$ includes storage terms and convective terms for both liquid and gas phase. Additionally, diffusive flux of vapour in the gas phase is considered. The partial density of water is expressed in terms of real density $\tilde{\rho}_l^{\mathrm{H_2O}}$, saturation S_l and porosity ϕ. The factors α_{R1}^{H2O} and α_{R1}^{H2O} represent the stoichiometric coefficient of $\mathrm{H_2O}$ in reactions R1 and R2. Coefficients of educts have got a negative sign. The quantities r_{R1}^{DO} and r_{R2}^{Ac} are the degradation rates of the main substrates in the reaction steps. In R1 degradable organic (DO) is the main substrate, whereas it is acetic acid (Ac) in R2. Fluxes resulting from boundary conditions are denoted by $q_{\mathrm{H_2O}}$ and the overall mass balance is given by

$$
\begin{array}{rcl}
\text{storage of water in liquid phase} & & \dfrac{d}{dt}\displaystyle\int_V S_l \phi \tilde{\rho}_l^{H_2O}\, dV \\
\text{storage of water in gas phase} & + & \dfrac{d}{dt}\displaystyle\int_V S_g \phi \tilde{\rho}_g^{H_2O}\, dV \\
\text{convective transport of water in liquid phase} & + & \displaystyle\int_S S_l \phi \tilde{\rho}_l^{H_2O} \mathbf{v}_{l,D} \mathbf{n}\, dS \\
\text{convective transport of vapour in gas phase} & + & \displaystyle\int_S S_g \phi \tilde{\rho}_g^{H_2O} \mathbf{v}_{g,D} \mathbf{n}\, dS \\
\text{diffusive transport in gas phase} & + & \displaystyle\int_S S_g \phi \tilde{\rho}_g^{H_2O} \mathbf{v}_g^{H_2O} \mathbf{n}\, dS \\
\text{sources and sinks from reactions} & = & \dfrac{d}{dt}\displaystyle\int_V \alpha_{R1}^{H_2O} r_{R1}^{DO} + \alpha_{R2}^{H_2O} r_{R2}^{Ac}\, dV \\
\text{other sources and sinks} & + & \dfrac{d}{dt}\displaystyle\int_V q^{H_2O}\, dV \; .
\end{array}
\tag{6.3}
$$

Mass Fraction of Carbon Dioxide in Gas Phase The structure of the balance equation for CO_2 is similar to that for water, whereas diffusion is considered both in the liquid and the gas phase. Sources in CO_2 are due to the production of carbon dioxide in reactions R1 and R2. With analogous notation the mass balance yields

$$
\begin{aligned}
\text{storage term CO}_2\text{ in liquid phase} \quad & \frac{d}{dt}\int_V S_l \phi \tilde{\rho}_l^{CO_2}\, dV \\
\text{storge term CO}_2\text{ in gas phase} \quad + & \frac{d}{dt}\int_V S_g \phi \tilde{\rho}_g^{CO_2}\, dV \\
\text{convective transport CO}_2\text{ in liquid phase} \quad + & \int_S S_l \phi \tilde{\rho}_l^{CO_2} \mathbf{v}_{l,D} \mathbf{n}\, dS \\
\text{convective transport CO}_2\text{ in gas phase} \quad + & \int_S S_g \phi \tilde{\rho}_g^{CO_2} \mathbf{v}_{g,D} \mathbf{n}\, dS \\
\text{diffusive transport in gas phase} \quad + & \int_S S_g \phi \tilde{\rho}_g^{CO_2} \mathbf{v}_g^{CO_2} \mathbf{n}\, dS \\
\text{diffusive transport in liquid phase} \quad + & \int_S S_l \phi \tilde{\rho}_l^{CO_2} \mathbf{v}_l^{CO_2} \mathbf{n}\, dS \\
\text{sources/sinks from reactions} \quad = & \frac{d}{dt}\int_V \alpha_{R1}^{CO_2} r_{R1}^{DO} + \alpha_{R2}^{CO_2} r_{R2}^{Ac}\, dV \\
\text{other sources and sinks} \quad + & \frac{d}{dt}\int_V q^{CO_2}\, dV\ .
\end{aligned}
\tag{6.4}
$$

Sources in CO_2 arise from the production of carbon dioxide in reactions R1 and R2.

Mass Fraction of Methane in Gas Phase Methane is considered to be a component of the gas phase only and connected to reaction R2, so that its mass balance is

$$
\begin{aligned}
\text{storage term CH}_4\text{ in gas phase} \quad & \frac{d}{dt}\int_V S_g \phi \tilde{\rho}_g^{CH_4}\, dV \\
\text{convective transport of CH}_4\text{ in gas phase} \quad + & \int_S S_g \phi \tilde{\rho}_g^{CH_4} \mathbf{v}_{g,D} \mathbf{n}\, dS \\
\text{diffusive transport in gas phase} \quad + & \int_S S_g \phi \tilde{\rho}_g^{CH_4} \mathbf{v}_g^{CH_4} \mathbf{n}\, dS \\
\text{sources and sinks from reactions} \quad = & \frac{d}{dt}\int_V \alpha_{R2}^{CH_4} r_{R2}^{Ac}\, dV \\
\text{other sources and sinks} \quad + & \frac{d}{dt}\int_V q^{CH_4}\, dV\ .
\end{aligned}
\tag{6.5}
$$

Acetic Acid Acetic acid is considered to exist only in the liquid state and connected both to reactions R1 and R2, so that the mass conservation is described by

$$
\begin{aligned}
\text{storage term CH}_3\text{COOH in liquid phase} \quad & \frac{d}{dt}\int_V S_l \phi \tilde{\rho}_l^{Ac}\, dV \\
\text{convective transport CH}_3\text{COOH in liquid phase} \quad +& \int_S S_l \phi \rho_l^{Ac} \mathbf{v}_{l,D} \mathbf{n}\, dS \\
\text{diffusive transport in liquid phase} \quad +& \int_S S_l \phi \rho_l^{Ac} \mathbf{v}_l^{Ac} \mathbf{n}\, dS \\
\text{sources and sinks from reactions} \quad =& \frac{d}{dt}\int_V \alpha_{R1}^{Ac} r_{R1}^{DO} + \alpha_{R2}^{Ac} r_{R2}^{Ac}\, dV \\
\text{other sources and sinks} \quad +& \frac{d}{dt} q_{Ac}\, dV \; .
\end{aligned}
\tag{6.6}
$$

Organic Matter Since organic matter is part of the solid phase only, no convective or diffusive flux terms occur in the mass balance. The rate of change in density of organic matter equals the amount degraded in steps R1 and the amount created from the decay of biomass in step L. Any sources and sinks from boundary conditions do not exist in the proposed approach as the solid phase is not considered in dissolved form. Hence, the mass balance yields

$$
\begin{aligned}
\text{storage term} \quad & \frac{d}{dt}\int_V \rho^{DO}\, dV \\
\text{sources and sinks from reactions} \quad =& \frac{d}{dt}\int_V \alpha_{R1}^{DO} r_{R1}^{DO} + \alpha_L^X r_L^X\, dV \; .
\end{aligned}
\tag{6.7}
$$

Biomass Similarly to balance of mass of organic matter, the conservation of biomass is formulated. Sources from steps R1 and R2 are considered as well as a sinks due to the lysis step L

$$
\begin{aligned}
\text{storage term} \quad & \frac{d}{dt}\int_V \rho^{X}\, dV \\
\text{sources from reactions} \quad =& \frac{d}{dt}\int_V \alpha_{R1}^{X} r_{R1}^{DO} + \alpha_{R2}^{X} r_{R2}^{Ac} + \alpha_L^X r_L^X\, dV \; .
\end{aligned}
\tag{6.8}
$$

Energy The balance of energy considers all phases with all components. The stored energy is dependent on temperature, density and heat capacity of the constituents. Convective and diffusive transport of the constituents are considered. Additionally, a term from thermal conduction is included. Sources and sinks in heat arise from the reactions

R1, R2 and P1 or from heat fluxes due to boundary conditions

$$
\begin{aligned}
\text{storage in solid phase} \quad & && \frac{d}{dt}\int_V \Big[\left(w_s^{IM} c_{p,s}^{IM} + w_s^{DO} c_{p,s}^{DO} + w_s^{X} c_{p,s}^{X}\right) \rho_s \Theta \\
\text{storage in liquid phase} \quad & + && \left(w_l^{\mathrm{H_2O}} c_{p,l}^{\mathrm{H_2O}} + w_l^{\mathrm{CO_2}} c_{p,l}^{\mathrm{CO_2}} + w_l^{\mathrm{Ac}} c_{p,l}^{\mathrm{Ac}}\right) \tilde{\rho}_l \phi S_l \Theta \\
\text{storage in gas phase} \quad & + && \left(w_g^{\mathrm{CO_2}} c_{p,g}^{\mathrm{CO_2}} + w_g^{\mathrm{CH_4}} c_{p,g}^{\mathrm{CH_4}} + w_g^{\mathrm{H_2O}} c_{p,g}^{\mathrm{H_2O}}\right) \tilde{\rho}_g \phi S_g \Theta \Big] \, dV \\
\text{conv. transport liquid} \quad & + && \int_S \left(w_l^{\mathrm{H_2O}} c_{p,l}^{\mathrm{H_2O}} + w_l^{\mathrm{CO_2}} c_{p,l}^{\mathrm{CO_2}} + w_l^{\mathrm{Ac}} c_{p,l}^{\mathrm{Ac}}\right) \tilde{\rho}_l \phi S_l \boldsymbol{\Theta} \mathbf{v}_s^l \mathbf{n} \, dS \\
\text{conv. transport gas} \quad & + && \int_S \left(w_g^{\mathrm{CO_2}} c_{p,g}^{\mathrm{CO_2}} + w_g^{\mathrm{CH_4}} c_{p,g}^{\mathrm{CH_4}} + w_g^{\mathrm{H_2O}} c_{p,g}^{\mathrm{H_2O}}\right) \tilde{\rho}_g \phi S_g \boldsymbol{\Theta} \mathbf{v}_s^g \mathbf{n} \, dS \\
\text{diff. transport liquid} \quad & + && \int_S \left(w_l^{\mathrm{CO_2}} c_{p,l}^{\mathrm{CO_2}} \mathbf{v}_l^{\mathrm{CO_2}} + w_l^{\mathrm{Ac}} c_{p,l}^{\mathrm{Ac}} \mathbf{v}_l^{\mathrm{Ac}}\right) \tilde{\rho}_l \phi S_l \boldsymbol{\Theta} \mathbf{n} \, dS \\
\text{diff. transport gas} \quad & + && \int_S \Big(w_g^{\mathrm{CO_2}} c_{p,g}^{\mathrm{CO_2}} \mathbf{v}_g^{\mathrm{CO_2}} + w_g^{\mathrm{CH_4}} c_{p,g}^{\mathrm{CH_4}} \mathbf{v}_g^{\mathrm{CH_4}} \\
& && + w_g^{\mathrm{H_2O}} c_{p,g}^{\mathrm{H_2O}} \mathbf{v}_l^{\mathrm{H_2O}}\Big) \tilde{\rho}_g \phi S_g \boldsymbol{\Theta} \mathbf{n} \, dS \\
\text{heat conduction} \quad & - && \frac{d}{dt}\int_V \lambda_s \mathrm{grad}\ \Theta \, dV \\
\text{source from reactions} \quad & = && \frac{d}{dt}\int_V \Delta H_{0,R1}^{R} r_{R1}^{DO} + \Delta H_{0,R2}^{R} r_{R2}^{Ac} \, dV \\
\text{sink from evaporation} \quad & + && \frac{d}{dt}\int_V \Delta H_{vap}^{P1} \, dV \; .
\end{aligned}
\tag{6.9}
$$

To enable the solution of the balance equations for mass and energy, boundary conditions are not mandatory, solely the setting of initial conditions is necessary. Boundary conditions of Dirichlet type may be used to set a particular value of a state variable. In the applications in chapter 7, Dirichlet conditions for pressure, saturation and temperature are used. Neumann conditions enforce a prescribed boundary flux which may in reality not occur dependent on the permeability of the material. Thus, they are not used herein. Analogously to the spring in solid mechanis, a Cauchy boundary condition for the equations of mass conservation of the fluid phases takes the internal solution of the analysed structure into account. Hence, both convective fluxes and heat fluxes across boundaries are described by means of Cauchy boundary conditions in most applications within this thesis. The formulation of convective flux of the liquid and the gas phase on boundaries Γ_l and Γ_g is formulated based on Darcy's law

$$
\mathbf{q}_l^{\Gamma_l} = -\frac{\tilde{\rho}_l k_{l,rel}}{\eta_l} \mathbf{K}(\mathrm{grad}\ p_l^{\Gamma} + \tilde{\rho}_l \mathbf{g}) \cdot \mathbf{n} \quad \text{and} \quad \mathbf{q}_g^{\Gamma_g} = -\frac{\tilde{\rho}_g k_{g,rel}}{\eta_g} \mathbf{K}(\mathrm{grad}\ p_g^{\Gamma} + \tilde{\rho}_g \mathbf{g}) \cdot \mathbf{n} \; . \tag{6.10}
$$

with the outward facing normal of the boundary $\mathbf{n}$. The pressure gradients across the boundary, grad p_l^Γ and grad p_g^Γ, are defined by

$$\operatorname{grad} p_\Gamma^l = \frac{p_{l,o} - p_{l,i}}{l} \quad \text{and} \quad \operatorname{grad} p_\Gamma^g = \frac{p_{g,o} - p_{g,i}}{l} \tag{6.11}$$

for a unit length $l = 1.0\,\text{m}$. The outer pressure $p_{\pi,o}$ is set a priori, whereas for the inner pressure $p_{\pi,i}$ the results of the simulation are used. The boundary flux may thus develop depending on the current state of the structure. The Cauchy boundary can be considered as a virtual boundary layer with prescribed properties. With respect to development of pressure inside the structure the term $\tilde{\rho}_\pi \cdot \mathbf{g}$ has to be considered. It is assumed that the capillary pressure is zero in the virtual boundary layer. Influx is distinguished from efflux so that an upwinding of density and mobilility is possible. The implementation of Cauchy boundaries can be interpreted as an extension of the analysed domain by ghost cells that describe the external state. Without any prescribed boundary conditions, the problem is simplified from an initial boundary value problem to an initial value problem. Then equations (6.3) to (6.9) describe the evolution of the state variables in time starting from a given initial state.

6.2 Iterative Solution and Linearisation

In this thesis, a combination of the Finite-Element method and the Box method is used for discretisation in space. The Backward Euler method is applied for discretisation in time, see also section 2.4. The resulting nonlinear, discrete equation system is solved by means of the Newton-Raphson method. The Newton-Raphson method is a numerical root finding algorithm, which is derived from a Taylor series expansion by keeping terms of first order only. Therefore, the balance equations are rewritten to obtain the structure of a root finding problem. A solution $\mathbf{z}$ is required to satisfy the equation $\mathbf{r}(\mathbf{z}) = 0$. The residual vector $\mathbf{r}(\mathbf{z})$ contains the balance equations evaluated at $\mathbf{z}$. The application of the Newton-Raphson procedure requires the linearisation of the residuum $\mathbf{r}$ with respect to the state variables $\mathbf{z}^T = [\mathbf{u}\ \mathbf{p}\ \mathbf{c}]$

$$\mathbf{r}(\mathbf{z})|_{n+1} + \left.\frac{\partial \mathbf{r}}{\partial \mathbf{u}}\right|_{n+1} d\mathbf{u} + \left.\frac{\partial \mathbf{r}}{\partial \mathbf{p}}\right|_{n+1} d\mathbf{p} + \left.\frac{\partial \mathbf{r}}{\partial \mathbf{c}}\right|_{n+1} d\mathbf{c} = \mathbf{0}\ . \tag{6.12}$$

This yields the *tangent matrix* or *Jacobian* $\mathbf{K_T}$. The submatrices of the equation system obtained by (6.12) are visualised by figure 6.2. The balance equations (6.6) to (6.9) are attributed to the degradation model. The vector $\mathbf{u}$ in (6.12) refers to the displacements of the solid skeleton for the case of plain strain, $d\mathbf{u}$ and $d\mathbf{w}$. The vector $\mathbf{p}$ represents the state variables of multiphase flow, and $\mathbf{c}$ summarises the state variables of chemical processes and degradation. Liquid pressure and gas saturation are chosen as state variables of multiphasic flow, which is known as *pressure-saturation formulation*. The different formulations

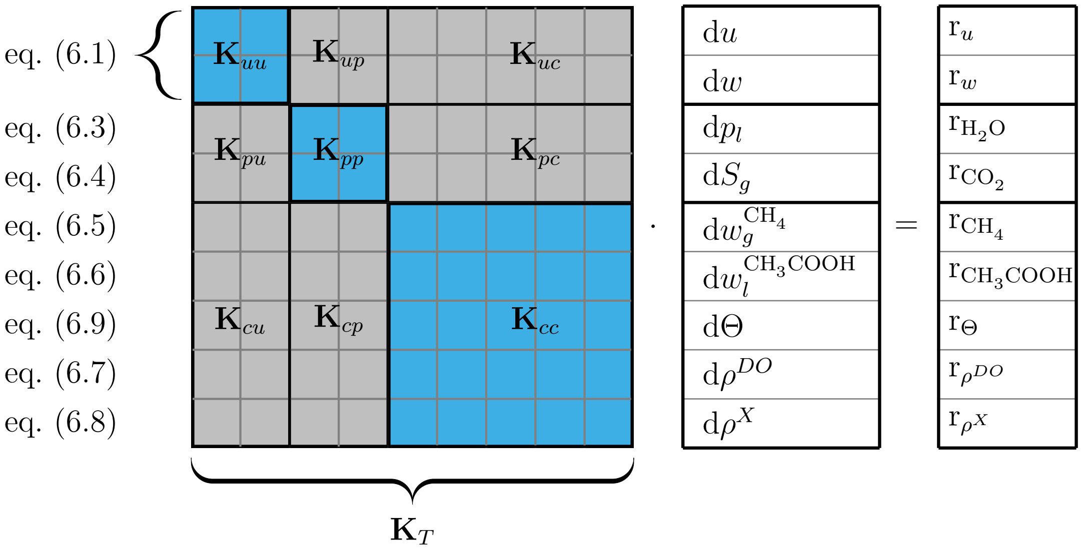

Figure 6.2: Schematic representation of the coupled system of equations on node level with the used primary unknowns. The balance equations, representing the residuals, are related to the rows of the system

are discussed by Helmig [103] and others. For the balance equations of degradation and heat generation, the mass fraction of methane in the gas phase, $w_g^{\mathrm{CH_4}}$, the mass fraction of acetic acid in the liquid phase w_l^{Ac}, the temperature Θ, the partial density of organic matter ρ_s^{DO} and the partial density of biomass ρ_s^{X} are chosen as state variables.

The matrices $\mathbf{K}_{uu}$, $\mathbf{K}_{up}$ and $\mathbf{K}_{uc}$ describe the derivation of the virtual work with respect to the nodal displacements $\mathbf{u}$ and the state variables $\mathbf{p}$ and $\mathbf{c}$ respectively. The internal virtual work is nonlinear with respect to both the kinematics and the material. With the chain rule, the linearisation of the internal virtual work with respect to $\mathbf{u}$ yields

$$\frac{\partial \delta W_{int}}{\partial \mathbf{u}} = \underbrace{\int_{V_0} \frac{\partial \delta \mathbf{E}}{\partial \mathbf{u}} : \mathbf{S}\, dV}_{K_{geom}} + \underbrace{\int_{V_0} \delta \mathbf{E} : \frac{\partial \mathbf{S}}{\partial \mathbf{u}}\, dV}_{K_{mat,u}} , \tag{6.13}$$

and the linearisation with respect to $\mathbf{p}$ and $\mathbf{c}$ leads to

$$\frac{\partial \delta W_{int}}{\partial \mathbf{p}} = \underbrace{\int_{V_0} \delta \mathbf{E} : \frac{\partial \mathbf{S}}{\partial \mathbf{p}}\, dV}_{K_{mat,p}} \quad \text{and} \quad \frac{\partial \delta W_{int}}{\partial \mathbf{c}} = \underbrace{\int_{V_0} \delta \mathbf{E} : \frac{\partial \mathbf{S}}{\partial \mathbf{c}}\, dV}_{K_{mat,c}} . \tag{6.14}$$

The first term K_{geom} in (6.13) emerges from the kinematical nonlinearity. The virtual strain $\delta\mathbf{E}$ depends not only on the virtual displacement field $\delta\mathbf{u}$ but also on the current deformation. This term is zero for linearisation with respect to $\mathbf{p}$ and $\mathbf{c}$ and vanishes for geometrically linear problems. The terms $K_{mat,u}$, $K_{mat,p}$ and $K_{mat,c}$ include the change of the stress state due to a change in $\mathbf{u}$, $\mathbf{p}$ and $\mathbf{c}$, under the presence of constant virtual displacements.

The matrix $\mathbf{K}_{up}$ contains the derivation of virtual work with respect to the state variables of multiphase transport and includes the influence of $K_{mat,p}$. Derivations with respect both to pressure and saturation occur due to the effective stress formulation. Furthermore, the external work of dead loads is coupled to saturation state and liquid density. The matrix $\mathbf{K}_{uc}$ describes dependencies of the virtual work on the state variables of the degradation model. Here the influence of organic and biomass density on creep rate is included. Additonally, external virtual work is affected by change in solid densities.

In (6.13) and (6.14) the linearisation of the second Piola-Kirchhoff stress $\mathbf{S} = \mathbf{F}^{-1}\tilde{\mathbf{T}}\mathbf{F}^{-T}$ with respect to $\mathbf{z}$ is required which yields

$$\frac{\partial \mathbf{S}}{\partial \mathbf{u}} d\mathbf{u} = \frac{\partial \mathbf{S}}{\partial \mathbf{F}_s} : \frac{\partial \tilde{\mathbf{F}}_{\mathbf{s}}}{\partial \mathbf{u}} \cdot d\mathbf{u} \ , \quad \frac{\partial \mathbf{S}}{\partial \mathbf{p}} d\mathbf{p} \ \text{ and } \ \frac{\partial \mathbf{S}}{\partial \mathbf{c}} d\mathbf{c} \ . \tag{6.15}$$

With equations (2.26) and (2.27) this finally leads to the requirement of consistent material operators $\tilde{\mathbf{T}}^s_{e},_{\mathbf{F}}$, $\tilde{\mathbf{T}}^s_{e},_{\mathbf{p}}$ and $\tilde{\mathbf{T}}^s_{e},_{\mathbf{c}}$ defined by

$$\tilde{\mathbf{T}}^s_{e},_{\mathbf{F}} = \frac{\partial \tilde{\mathbf{T}}^s_e}{\partial \mathbf{F}_s}, \ \tilde{\mathbf{T}}^s_{e},_{\mathbf{p}} = \frac{\partial \tilde{\mathbf{T}}_e}{\partial \mathbf{p}}, \ \text{and } \tilde{\mathbf{T}}^s_{e},_{\mathbf{c}} = \frac{\partial \tilde{\mathbf{T}}_e}{\partial \mathbf{c}} \ , \tag{6.16}$$

i.e. the linearisation of the effective Kirchhoff stress tensor w.r.t. to the state variables. Considering that the stress is split into the stresses of basic matrix and fibres, the total differential of the Kirchhoff stress with respect to $\mathbf{F}_s$ is

$$\frac{\partial \tilde{\mathbf{T}}^s_e}{\partial \mathbf{F}_s} \cdot d\mathbf{F}_s = n^B \frac{\partial \tilde{\mathbf{T}}^B}{\partial \mathbf{F}_s} \cdot d\mathbf{F}_s + n^F \frac{\partial \tilde{\mathbf{T}}^F}{\partial \mathbf{F}_s} \cdot d\mathbf{F}_s \ . \tag{6.17}$$

Analogously, the differentials with respect to $\mathbf{p}$ and $\mathbf{c}$ may be formulated.

The Kirchhoff stresses $\tilde{\mathbf{T}}^B$ and $\tilde{\mathbf{T}}^F$ are determined in a local iterative solution of the constitutive evolution equations. The local iteration of stresses is explained in detail by Krase [135] and Ebers-Ernst [58]. The constitutive equations for the material behaviour are discretised in time by means of the implicit Euler method. The *radial return* method is used to determine elastic and inelastic strain increments as well as stresses. The method maps an elastic predictor stress back to the yield surface in a corrector step so that the yield criterion is satisfied at the end of the timestep.

The equation system for the basic matrix is formed by the constitutive equations for elastic stress, strain balance, yield criterion and the definition of volumetric strain

$$\underbrace{\begin{bmatrix} \frac{\partial \mathbf{r}^B_{\tilde{T}}}{\partial \tilde{\mathbf{T}}^{B,n+1}} & \frac{\partial \mathbf{r}^B_{\tilde{T}}}{\partial \mathbf{A}^{B,n+1}_{in}} & \mathbf{0} & \mathbf{0} \\ \frac{\partial \mathbf{r}^B_{A}}{\partial \tilde{\mathbf{T}}^{B,n+1}} & \frac{\partial \mathbf{r}^B_{A}}{\partial \mathbf{A}^{B,n+1}_{in}} & \frac{\partial \mathbf{r}^B_{A}}{\partial \Delta\gamma^{B,n+1}_{pl}} & \frac{\partial \mathbf{r}^B_{A}}{\partial a^{B,n+1}_{v,in}} \\ \mathbf{0} & \frac{\partial r_{a^B_{v,in}}}{\partial \mathbf{A}^{B,n+1}_{in}} & 0 & \frac{\partial r_{a^B_{v,in}}}{\partial a^{B,n+1}_{v,in}} \\ \frac{\partial r^B_{f}}{\partial \tilde{\mathbf{T}}^{B,n+1}} & \mathbf{0} & 0 & \frac{\partial r^B_{f}}{\partial a^{B,n+1}_{v,in}} \end{bmatrix}}_{\mathbf{M}^B} \begin{bmatrix} d\tilde{\mathbf{T}}^{B,n+1} \\ d\mathbf{A}^{B,n+1}_{in} \\ d\Delta\gamma^{B,n+1}_{pl} \\ da^{B,n+1}_{v,in} \end{bmatrix} = \begin{bmatrix} -\mathbf{r}^B_{\tilde{T}} \\ -\mathbf{r}^B_{A} \\ -r_{a^B_{v,in}} \\ -r^B_{f} \end{bmatrix} \ . \tag{6.18}$$

The nonlinear equation system is solved for increments in Kirchhoff stress, Almansi strain, plastic multiplier and volumetric strain using the Newton-Raphson method. Similarly, the equation system for the fibres is given by the constitutive equations for elastic stress, strain balance and yield criterion. It yields

$$\underbrace{\begin{bmatrix} \frac{\partial \mathbf{r}^F_{\tilde{T}}}{\partial \tilde{\mathbf{T}}^{F,n+1}} & \frac{\partial \mathbf{r}^F_{\tilde{T}}}{\partial \mathbf{A}^{F,n+1}_{in}} & \mathbf{0} \\ \frac{\partial \mathbf{r}^F_{A}}{\partial \tilde{\mathbf{T}}^{F,n+1}} & \frac{\partial \mathbf{r}^F_{A}}{\partial \mathbf{A}^{F,n+1}_{in}} & \frac{\partial \mathbf{r}^F_{A}}{\partial \Delta\gamma^{F,n+1}_{pl}} \\ \frac{\partial r^F_{f}}{\partial \tilde{\mathbf{T}}^{F,n+1}} & \frac{\partial r^F_{f}}{\partial \mathbf{A}^{F,n+1}_{in}} & \mathbf{0} \end{bmatrix}}_{\mathbf{M}^F} \begin{bmatrix} d\tilde{\mathbf{T}}^{F,n+1} \\ d\mathbf{A}^{F,n+1}_{in} \\ d\Delta\gamma^{F,n+1}_{pl} \end{bmatrix} = \begin{bmatrix} -\mathbf{r}^F_{\tilde{T}} \\ -\mathbf{r}^F_{A} \\ -r^F_{f} \end{bmatrix} \tag{6.19}$$

and is solved for increments in Kirchhoff stress, Almansi strain and plastic multiplier.

The left hand sides M^B and M^F are used to determine the consistent material operator $\frac{\partial \tilde{\mathbf{T}}}{\partial \mathbf{F}}$ by

$$\mathbf{M}^B \begin{bmatrix} \frac{\partial \tilde{\mathbf{T}}^{B,n+1}}{\partial \mathbf{F}^{n+1}_S} \\ \frac{\partial \mathbf{A}^{B,n+1}_{in}}{\partial \mathbf{F}^{n+1}_S} \\ \frac{\partial \Delta\gamma^{B,n+1}_{pl}}{\partial \mathbf{F}^{n+1}_S} \\ \frac{\partial a^{B,n+1}_{v,in}}{\partial \mathbf{F}^{n+1}_S} \end{bmatrix} = \begin{bmatrix} \mathbf{0} \\ -\mathbf{r}^B_A \\ 0 \\ 0 \end{bmatrix} - \begin{bmatrix} \frac{\partial \mathbf{r}^B_{\tilde{T}}}{\partial \mathbf{F}^{n+1}_S} \\ \frac{\partial \mathbf{r}^B_{A}}{\partial \mathbf{F}^{n+1}_S} \\ \frac{\partial r_{a^B_{v,in}}}{\partial \mathbf{F}^{n+1}_S} \\ \frac{\partial r^B_{f}}{\partial \mathbf{F}^{n+1}_S} \end{bmatrix} \tag{6.20}$$

and for the fibres

$$\mathbf{M}^F \begin{bmatrix} \frac{\partial \tilde{\mathbf{T}}^{F,n+1}}{\partial \mathbf{F}^{n+1}_S} \\ \frac{\partial \mathbf{A}^{F,n+1}_{in}}{\partial \mathbf{F}^{n+1}_S} \\ \frac{\partial \Delta\gamma^{F,n+1}_{pl}}{\partial \mathbf{F}^{n+1}_S} \end{bmatrix} = \begin{bmatrix} \frac{-\partial \mathbf{r}^F_{\tilde{T}}}{\partial \mathbf{F}^{n+1}_S} \\ \frac{-\partial \mathbf{r}^F_{A}}{\partial \mathbf{F}^{n+1}_S} \\ \frac{-\partial r^F_{f}}{\partial \mathbf{F}^{n+1}_S} \end{bmatrix} \tag{6.21}$$

The operators $\frac{\partial \tilde{\mathbf{T}}}{\partial \mathbf{p}}$ and $\frac{\partial \tilde{\mathbf{T}}}{\partial \mathbf{c}}$ are derived analogously by replacing the partial derivatives with respect to $\mathbf{F}_s$ in (6.20) and (6.21) by the derivatives with respect to $\mathbf{p}$ and $\mathbf{c}$. It has to be noted that changes in the constitutive model of the basic matrix influence the stresses of the fibres, too, as the stress within the basic matrix determines the strength of fibres' bonding.

The matrix $\mathbf{K}_{pp}$ describes the twophasic flow. It considers the influence of gas saturation S_g and liquid pressure p_l on the balance of H_2O and CO_2. The matrix $\mathbf{K}_{cc}$ describes the local reaction processes and physical exchange processes. The matrices $\mathbf{K}_{pu}$ and $\mathbf{K}_{cu}$ contain the derivation of the balance equations (6.3) to (6.9) with respect to the displacements. Dependency on the deformation arises from the change in size of the control volume. Furthermore, effects from changing porosity and permeability are considered herein. The submatrices $\mathbf{K}_{pp}$, $\mathbf{K}_{pc}$, $\mathbf{K}_{cp}$ and $\mathbf{K}_{cc}$ form the subsystem for description of reactive transport and consider the influence of the corresponding seven state variables on the balance equations (6.3) to (6.9). For instance, temperature affects degradation rates and the viscosity of the fluid phases. A change in organic matter is related to the mass fractions of liquid and gaseous components due to the degradation products. The matrices $\mathbf{K}_{uu}$ and $\mathbf{K}_{up}$ are detemined analytically, whereas all other submatrices are obtained by numerical differentiation using a central difference scheme. The tangent matrix $\mathbf{K}_T$ is not symmetric, only the submatrix $\mathbf{K}_{uu}$ is symmetric.

6.3 Structure of the Algorithm

The structure of the algorithm is shown in figure 6.3. An important step is the computation of node values at the corner nodes of boxes which is explained by figure 6.4. After solution of the current interval and computation of depending node values, a check for non-physical solutions is implemented. Non-physical solutions are for example negative densities or volume fractions. They may occur if time step width is too large with respect to degradation rates. Similarly, negative fluid saturations or mass fractions of fluid components may occur if they are closed to their limits in combination with boundary fluxes.

```
Loop over all time increments, step ${}^{t+\Delta t}t={}^{t}t+\Delta t$
    Global Newton-Raphson iteration of balance equations, step j=j+1
        • Assemblage of load vector (right hand side)
        Loop over all elements
            • Stiffness submatrices $\mathbf{K}_{uu}$ and $\mathbf{K}_{up}$ (analytically)
            • Stiffness submatrices $\mathbf{K}_{uc}$, $\mathbf{K}_{pu}$, $\mathbf{K}_{pp}$, $\mathbf{K}_{pc}$, $\mathbf{K}_{cu}$, $\mathbf{K}_{cp}$, $\mathbf{K}_{cc}$ (numerically)
            Loop over all degrees of freedom
                residuum r
                perturbation of degree of freedoms by $+\delta^{DOF}$ and $-\delta^{DOF}$
                new node values (see fig. 6.4)
                new residuum at $+\delta^{DOF}$ and $-\delta^{DOF}$
                central difference
        • Assemblage of global stiffness matrix
        • Implementation of boundary conditions
        • Solution
        • Update displacements, u and v
        • Update $p_l$, $S_g$, $w_l^{CH3COOH}$, $w_g^{CH4}$, $\Theta$, $\rho^{DO}$, $\rho^{X}$
        • Check for non-physical values
        • Determine new nodal internal variables for constitutive model
          of transport and degradation (see fig. 6.4)
        • Update geometry, Update porosity and permeability (see
          equations (4.2) and (4.10)
        • Local Iteration of stresses of solid skeleton
            elastic predictor basic matrix
            corrector step basic matrix (Newton-Raphson iteration)
            elastic predictor step fibres
            corrector step fibres (Newton-Raphson iteration)
        • Check global convergence
        • Update solution for next time increment, or reset for new
          iteration with decreased time step width
```

Figure 6.3: Structure of the computational algorithm

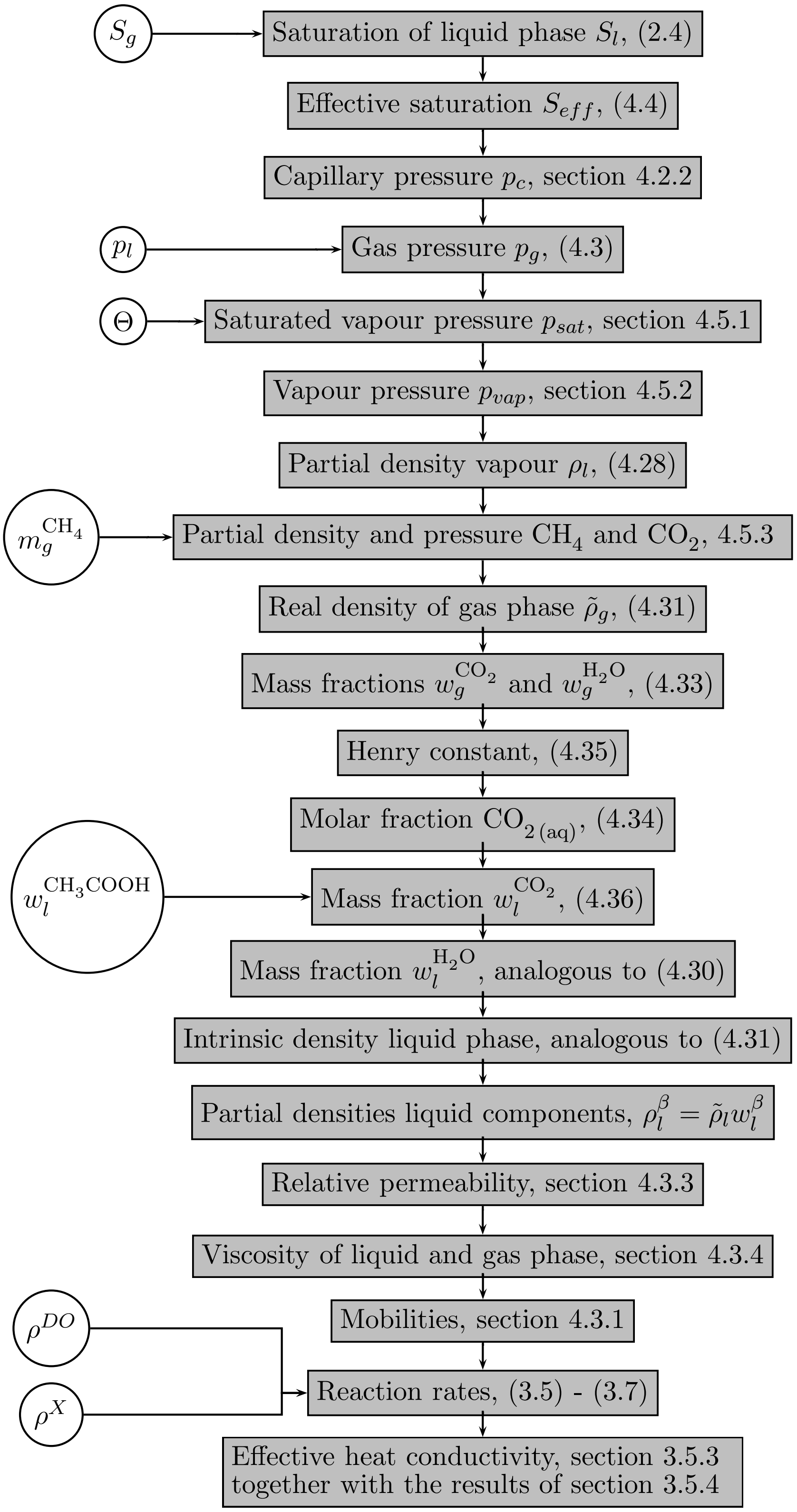

Figure 6.4: Flowchart of the determination of node values at corner nodes of boxes by the constitutive model. The primary variables are shown on the left when they enter the computational procedure the first time.

7 Analysis of Coupled Processes

The developed model is verified and validated against laboratory experiments. For assessment of coupled transport and deformation including transition from saturated to unsaturated conditions, a benchmark based on a drainage experiment of a sand column is used. Subsequently, a modelling challenge, which is organised for the *2nd Workshop on Hydro-Physico-Mechanics of Landfills*, enables validation of coupled transport, degradation and large deformations. Further examples show the scope of the model in its application on landfill structures considering also long term analyses. Finally, conclusions with respect to landfill monitoring are drawn.

7.1 Validation of Coupled Transport and Deformation with the ALERT Liakopoulos Benchmark

The interaction of multiphase flow and deformation is verified and validated using a benchmark organised by the European Network “ALERT Geomaterials” [120]. Major objective of the benchmark is to analyse the transition from saturated to unsaturated conditions within one mesh. The test is based on a laboratory experiment by Liakopoulos [143], who investigates the drainage of an initially saturated sand column by gravity. Liakopoulos analyses columns of different height and measures discharge rate and, by means of tensiometers, water pressure at certain time steps, fig. 7.1, left.

In the experiment, the column is first continuously saturated with water. Then, water inflow at the top is stopped and water can drain freely at the bottom. The benchmark refers to a column 1 m in height. Slightly different initial conditions are imposed compared to the laboratory test: First, hydrostatic water pressure is assumed; then, the water pressure at the bottom is set to atmospheric pressure simulating conditions for free drainage. Parameters and constitutive relations are given in [120] and listed in fig. 7.1. Liakopoulos does not determine the mechanical properties, therefore, for the benchmark case linear elasticity is assumed. A crucial point in the analysis is the transition from local saturated to unsaturated conditions. For a vanishing gas phase, $S_l = 1.0$, the corresponding mass balance equation degenerates to the equality $0 = 0$. Different approaches for describing the change in saturation state are discussed by Jommi and Vaunat [120] as well as Lewis and Schrefler [142]. With regard to the proposed model, the saturation of the gas phase is set to a value of $S_g = 1 \times 10^{-6}$. Only inert matter is considered, so that degradation processes do not occur. Phase transition processes or heat generation are not considered as well.

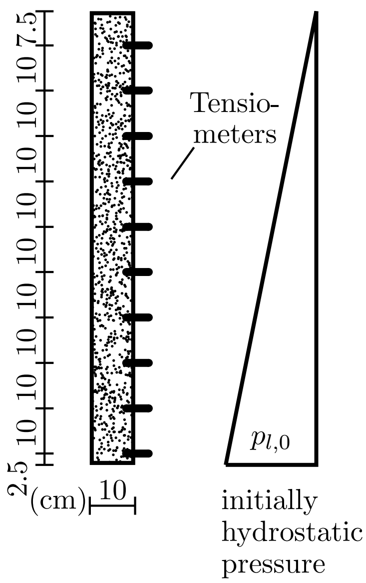

Porosity	$\phi = 0.29$
Solid grain density	$\tilde{\rho}_s = 2.000\,\mathrm{kg/m^3}$
Permeability	K=$4.51 \times 10^{-13}\,\mathrm{m^2}$
Relative perm. of water	$k_{wr} = 1 - 2.207(1 - S_l)^{1.0121}$ with S_l = degree of saturation
Relative perm. of air	$k_{ar} = (1 - S_e)^2(1 - S_e^{5/3})$ with $S_e = (S_l - 0.2)/0.8$
Retention curve	$S_l = 1.0 - 1.9722 \cdot 10^{-11} p_c^{2.4279}$ with p_c in (Pa)
Young's modulus	$E = 1.3\,\mathrm{MPa}$
Poisson's ratio	$\nu_P = 0.4$
Viscosity of water	$\mu^w = 1.0 \times 10^{-3}\,\mathrm{Pa \cdot s}$
Viscosity of air	$\mu^a = 1.8 \times 10^{-5}\,\mathrm{Pa \cdot s}$

Figure 7.1: Liakopoulos test and benchmark conditions

In the simulation, first the loading by self weight is applied stepwise. During loading and subsequent consolidation, the boundary at the bottom is impermeable. At the upper boundary, water pressure is set to atmospheric pressure and gas saturation is set to $S_g = 1 \times 10^{-6}$ allowing the outflux of water and maintaining saturated conditions. After completion of this pre-stage, the water pressure distribution is hydrostatic as in the benchmark case, compare figure 7.2, and the actual analysis starts. At time $t = 0$, water pressure at the bottom is set to atmospheric pressure and gas saturation is set to $S_g = 1 \times 10^{-6}$ allowing the drainage of water. Simultaneously, gas pressure is assumed to be atmospheric at the upper boundary and inflow of gas is enabled by a Cauchy boundary condition with $p_{g,o} = p_{atm}$.

Figure 7.2, 7.3 and 7.4 show isochrones of water pressure, capillary pressure and saturation respectively. Water pressure decreases with time and approaches steady-state conditions. The plot of saturation vs. height reveals that a front separating unsaturated from saturated condition proceeds downwards. Correspondingly, the capillary pressure develops. It is nearly zero in the saturated zone and is greater than zero in the unsaturated zone.

Since the problem is solved by numerous other researchers, see table 7.1, and as conditions are very well documented, the benchmark offers an excellent possibility for testing the proposed model. Own simulation results are compared with the results of the experiment and with the benchmark results reported by Jommi and Vaunat [120].

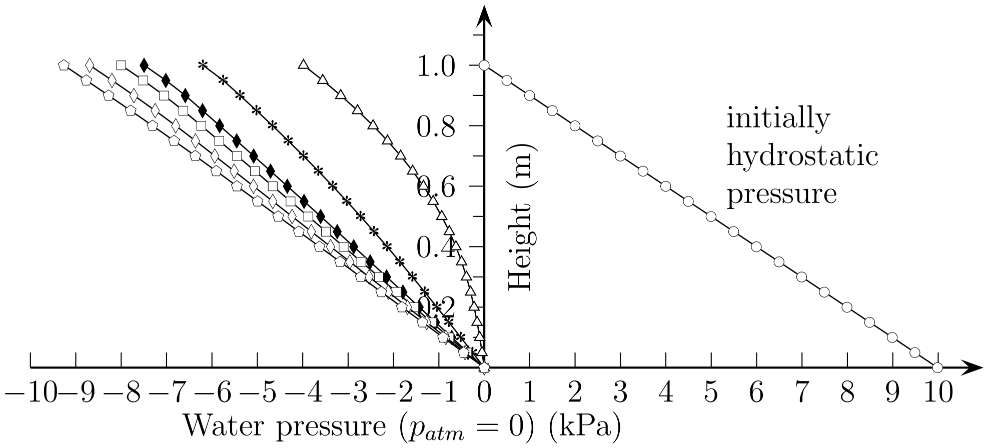

Figure 7.2: Water pressure isochrones (legend equiv. to figures 7.3 and 7.4)

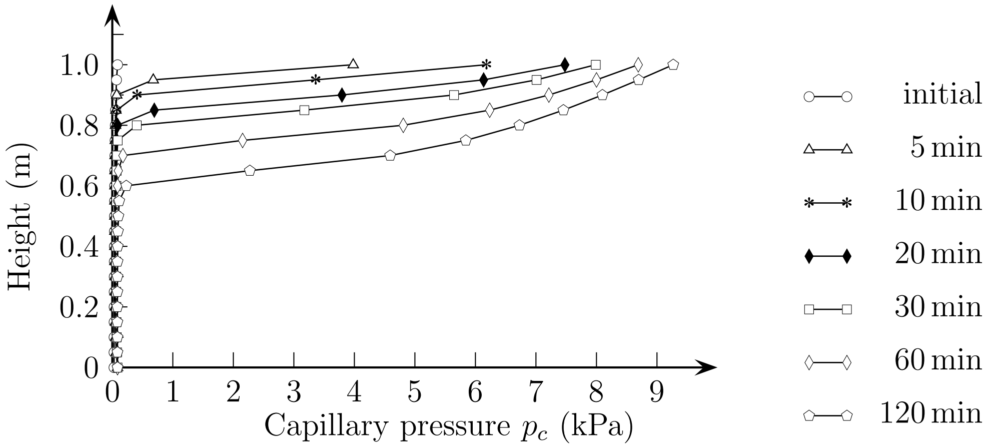

Figure 7.3: Isochrones of capillary pressure

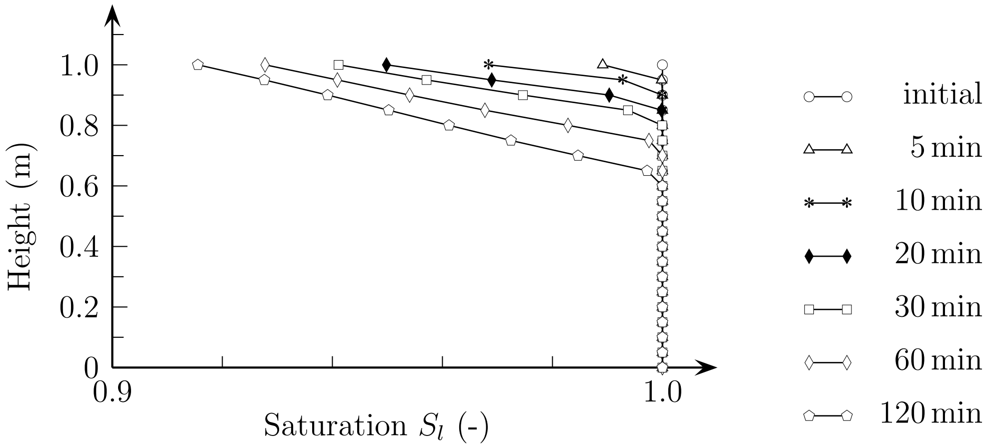

Figure 7.4: Isochrones of saturation

Water pressure isochrones after 30 min are compared in fig. 7.5. Pressure distribution is close to the results reported by Jommi and Vaunat [120] describing satisfactorily the experimental data.

In figure 7.7, left, gas pressure isochrones at t=30 min are compared showing that own simulation results agree well with the results obtained by the benchmark participants. A remarkable point of the curve pattern is the discontinuity in gas pressure where the local transition from saturated to unsaturated conditions occurs in the sample. This is obvious from the evolution of saturation as well, compare figure 7.6. The discontinuity is also present in the results by LCPC and UPC. Dangla et al. [45] confirm its occurence both numerically by analysis with a very fine mesh and analytically.

Table 7.1: Benchmark participants, explanation of abbreviations used in the graphs

EPFL	Ecole Polytechnique Fédérale de Lausanne
LCPC	Laboratoire Central des Ponts et Chaussées
LIEGE	Université de Liège
UPC	Universitat Polytècnica de Catalunya
UPD	Università degli Studi di Padova

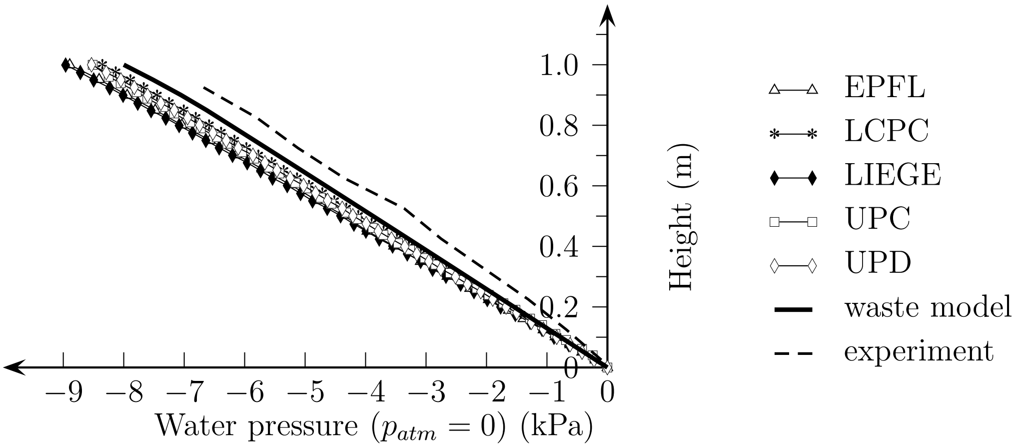

Figure 7.5: Comparison of own results with results from [120] and [143] - water pressure ($p_{atm} = 0$) at t=30 min

Figure 7.7 compares the evolution of displacement of the upper surface and shows only minor differences. The displacement rate is high in the beginning and then decreases. After 120 minutes, all numerical results nearly coincide. The displacement is affected by the effective stress formulation. At unsaturated conditions, the suction imposes additional compressive stress which is in this case relatively low due to the high saturations. The different curve pattern of the UPC results is due to an increase in net stress with time, combined with the applied linear elasticity law which is, of course, not realistic for soils. Deformation is small in this example, so that it may serve for validation within small strain kinematics.

From simulating the benchmark it is concluded that the developed model is able to correctly describe saturated and unsaturated conditions as well as local transition between the two states. The formulation of the effective stress using Bishop's approach is verified and validated for suctions up to 10 kPa and saturations of about $S_l = 0.9$.

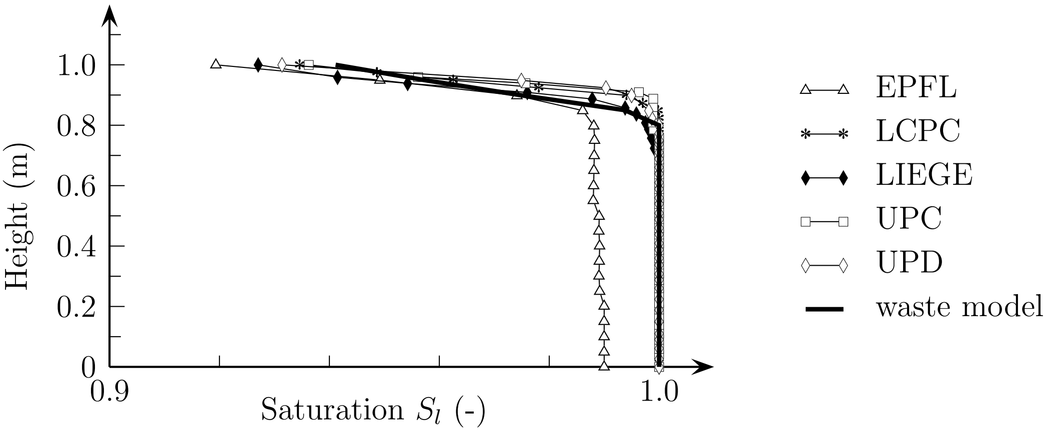

Figure 7.6: Comparison of own results with results from [120] - saturation at t=30 min

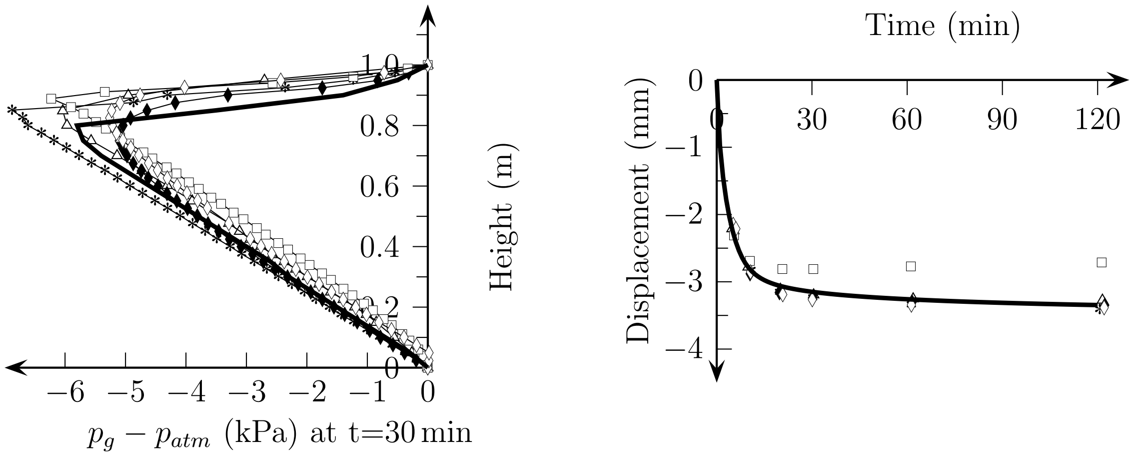

Figure 7.7: Comparison of own results with results from [120] - gas pressure (left) at t=30 min and top displacement (right)

7.2 Validation Based on Experiments with two Consolidating Anaerobic Reactors (CAR)

In this applicaton, two lysimeter experiments on waste samples are simulated. The tests are part of a modelling challenge made by the University of Southampton, Beaven et al. [16]. A description of the experimental setup together with data on waste composition and leachate chemistry during the first two months is provided. The participants of the challenge are asked to predict the future evolution of the experiments. The test series comprises originally four consolidating anaerobic reators of which two are referred to in the modelling challenge, herein denoted as CAR 1 and CAR 2. The complete experimental programme is described in detail by Ivanova [118]. The test is already referred to in section 3.4 to show the properties of the degradation model by a local analysis.

Each lysimeter consists of a perspex cylinder, 48 cm in diameter and 90 cm in height. A sample of 27 kg fresh waste is placed into the cylinder and covered both on top and on bottom by a geotextile and a gravel drainage layer. The composition of the used waste is shown in section 3.5.4 where intrinsic density and thermal conductivity are estimated for the selected material, table 3.10. The sample in CAR 1 is loaded by 150 kPa, the sample in CAR 2 by 50 kPa. Over the entire test duration of 919 days, settlements as well as volume and composition of gas and leachate are measured on a regular basis. By heating blankets, the lysimeters are kept at a temperature of $\Theta = 30\,^\circ\mathrm{C}$ during the test, which is confirmed by temperature measurements in the waste sample. Hence, the CARs are simulated under isothermal conditions.

Figure 7.8 shows the setup of a CAR and the boundary conditions used for the simulation. Displacements of the lateral boundaries are fixed in horizontal direction, whereas, displacements of the bottom are fixed in vertical direction. A Cauchy boundary condition at the upper boundary allows the flux of both liquid and gas over the upper sample surface. The permeability is set to a slightly lower value than that of the waste itself to allow for free drainage. The liquid pressure at the upper surface is assumed to equal the atmospheric pressure.

In the experiment, leachate is collected at the bottom and then recirculated, so that the reactor remains nearly saturated. In the simulation, the boundary at the bottom is set impermeable giving similar conditions. The fraction of the basic matrix is set to $n^B = 1.0$, as the compaction behaviour is here the governing mechanism of deformation. Parameters are chosen in correspondence to table 3.4. First, the behaviour of CAR 1 is simulated, whereas the parameters of the creep model are determined by fitting calculated to measured displacements. Measured cumulative gas volume is used to estimate the amount of degradable material. Due to sample size and experimental setup, homogeneous conditions may be presumed. Hence, an isotropic permeability is assumed. To consider the saturated state of the sample, the liquid saturation is set to $S_l = 0.99$ initially. As discussed in the previous section, a saturation of $S_l = 1.0$ is not possible with the presented approach as the mass balance of the gas phase would vanish. In that sense, the simulation of the CAR experiments is at the limits of the models' scope. For description of the slightly unsaturated conditions, the Brooks and Corey approximation of the data by Stoltz and Gourc [220] for fresh waste is used herein, see table 4.1 for $\rho_s = 0.54\,\mathrm{Mg/m^3}$. Due to the high saturation, the capillary pressure does not exceed the air entry pressure of 2.95 kPa considerably.

The initial sample height of 0.8 m corresponds to a sample volume of $\sim 0.145\,\mathrm{m^3}$ and a partial solid dry density of $\rho_s = 186.5\,\mathrm{kg/m^3}$. The loads are applied within a time period of 24 h in the simulations.

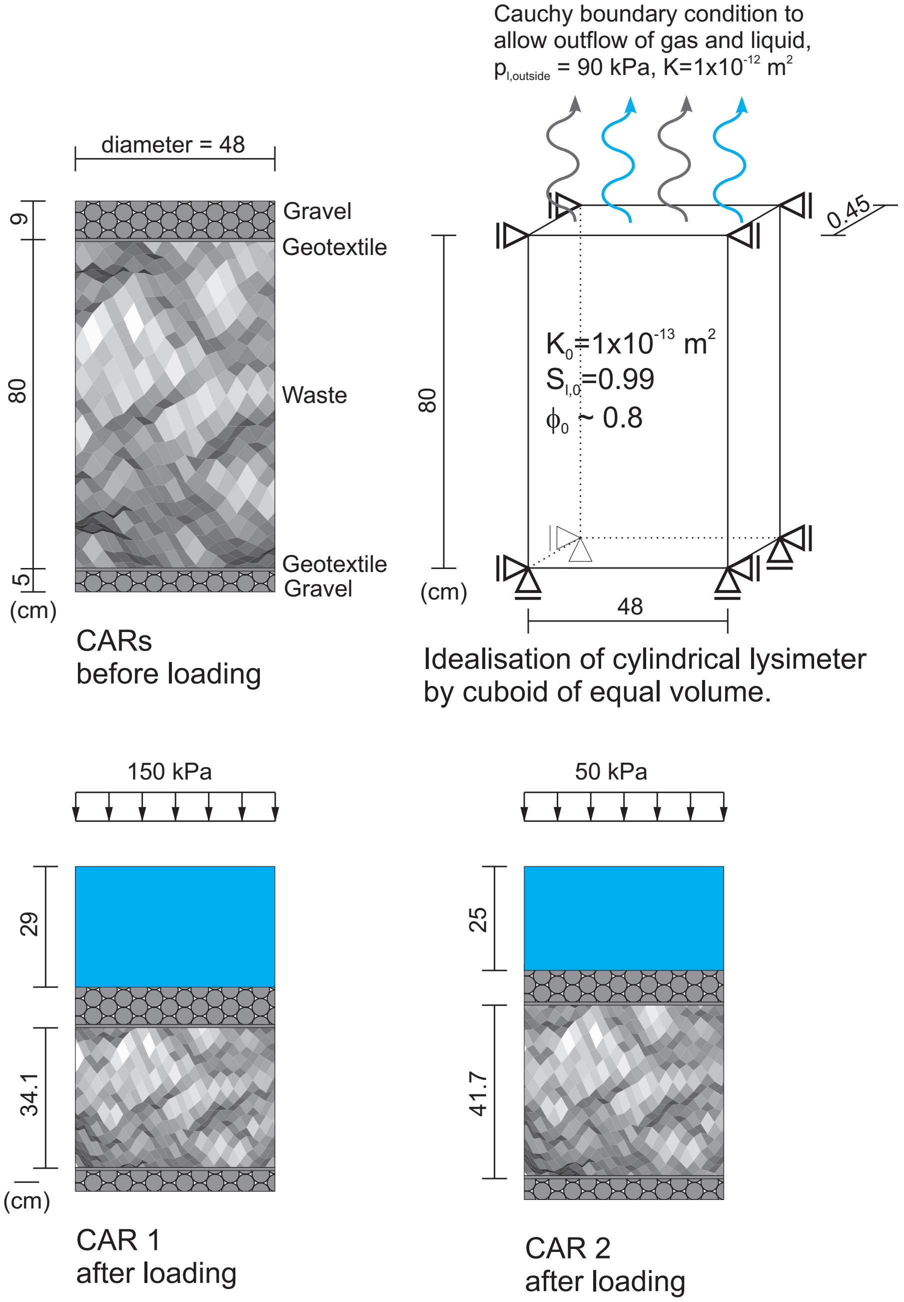

Figure 7.8: CAR lysimeter experiments. Setup for modelling with boundary conditions and waste heights after load application

7.2.1 Simulation of CAR 1

During the three-year test period, a cumulative gas volume of $\sim 8300\,\mathrm{l}$ is measured for CAR 1, see figure 7.9 (b) and (d). Assuming that the gas consists of methane and carbon dioxide only and that gas volume is determined at $\Theta = 303\,\mathrm{K}$ in the test, a partial density of organic matter of $\rho_s^{DO} = 51.31\,\mathrm{kg/m^3}$, corresponding to 7.44 kg organic matter, is chosen initially with respect to the gas yield of the degradation model. Figure 7.9 (b) and (d) compare the efflux of gas over the upper surface with the gas volume measured in the experiment. The final gas volumes are in good agreement assuming that the gas consists of methane and carbon dioxide only, fig. 7.9 (d). The total gas flux is slightly higher in the simulation if vapour is considered as well, fig. 7.9 (b). The gas production stops almost totally after 150 days in the simulation. The evolution of partial dry organic density confirms, that all organic matter is degraded until that time, see figures 7.10 (b) and 7.11. All figures of nodal values show results at a upper surface node representing the behaviour of the entire sample due to the homogeneous conditions.

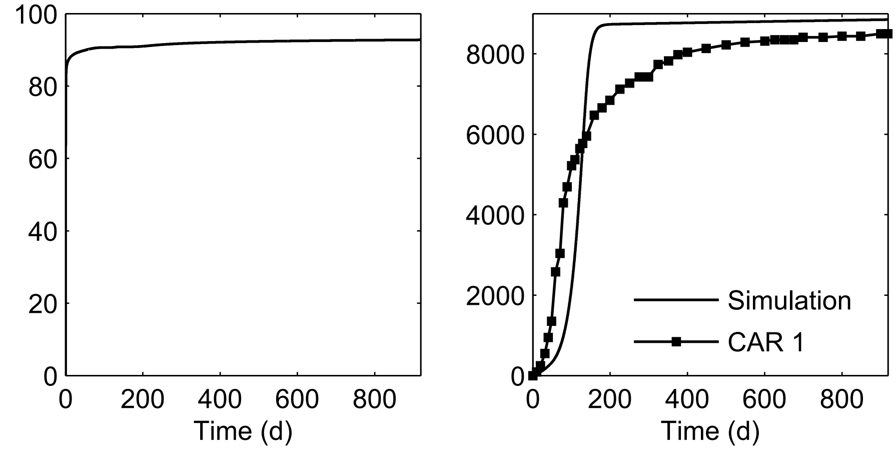

(a) Outflux liquid (l) (b) Outflux gas (l)

(c) Outflux distinguished by gas fractions (l) (d) Outflux original landfill gas (l)

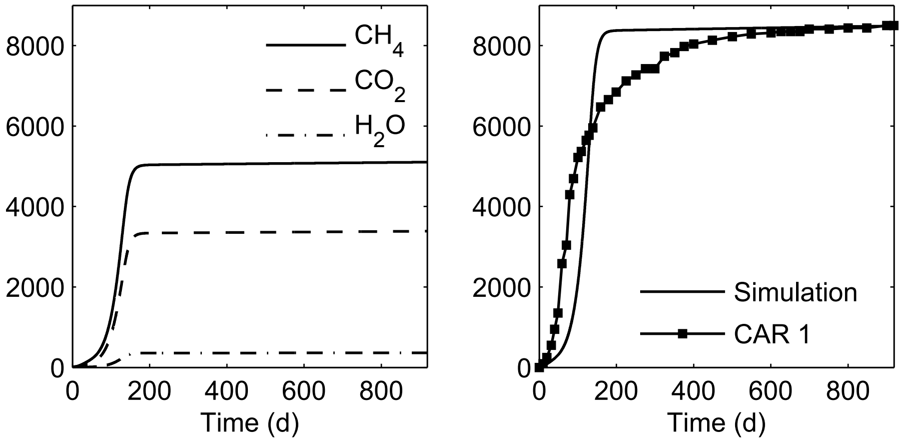

Figure 7.9: Results of simulation of CAR 1. Surface fluxes of liquid and gas. Gas fluxes compared with experimental data

Very low further gas production occurs only from the lysis of biomass observable in 7.11 (b) and its subsequent degradation. The comparison of simulated and measured gas volumes shows that the degradation rate is approximated very well during the first 100 days. Then, the gas production rate declines in the experiment, which is not captured by the model. The effect is also observed in the local analysis in section 3.4. In fact, the waste material consists of different fractions with respect to degradability. For instance, readily, moderately and hardly degradable material may be distinguished. A different degradation rate is to be assigned to each fraction. Thus, declining gas production rate can be explained by readily degradable material being degraded very quickly, whereas the lysimeter behaviour is governed later on by the decomposition of less degradable fractions. As only one type of organic matter is considered in the model, this effect cannot be described yet. An indirect consideration of degradability of different components may be realised by modifying the rate dependent on waste composition and degradation state. For instance, a relative digestibility is suggested by Lee and Fan [140] and applied in the model by McDougall [157].

Figure 7.9 (c) shows the gas flux separated into the components of the gas phase. After 919 d approx. 5110 l CH_4, 3390 l CO_2 and 360 l vapour have flowed over the upper boundary. In correspondance with the degradation model, volume fractions of 60 % CH_4 and 40 % CO_2 are obtained, which matches the experimental data very well.

Figure 7.9 (a) shows the efflux of liquid over the upper surface. Liquid volume is 79 l after the loading phase of 24 h, compare also figure 7.15 (b). As only the pore space is compressed, which is almost completely filled with liquid initially, an outflux of liquid corresponding to the compressed volume must occur. The theoretical flux for a displacement of 0.435 m is 79 l with which simulated results are in good agreement.

Fig. 7.10 (a) compares the evolution of solid density $\rho_{s,i}$ and porosity ϕ. As the two quantities are related by eq. (4.2), the curve patterns are symmetrical with respect to a horizontal axis. The solid density is first increased due to compaction from the initial value of 187 kg/m^3 to a value of 410 kg/m^3 after loading. The same density is obtained if the dry mass of 27 kg is related to the current volume after 0.435 m of settlements. The density is further increased due to compaction to a maximum value of almost 500 kg/m^3 after 70 d. With the beginning of degradation, compare figure 7.10 (b), the density decreases. In contrast, the porosity is first decreased due to compaction, then increased due to solid mass loss from degradation and again decreased due to compaction. Similarly, the solid density with respect to the undeformed configuration $\rho_{s,i,ref}$ reveals the solid mass loss due to degradation, cf. 7.10 (a).

(a) Total partial dry solid density

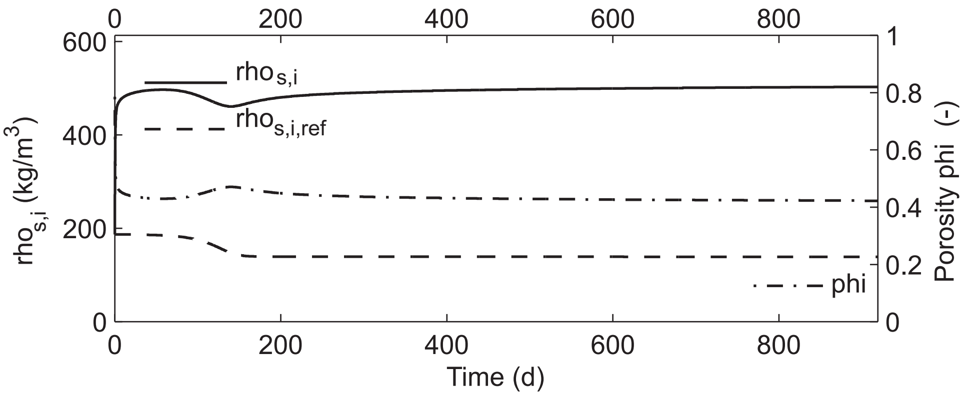

(b) Total partial dry reference density organic matter

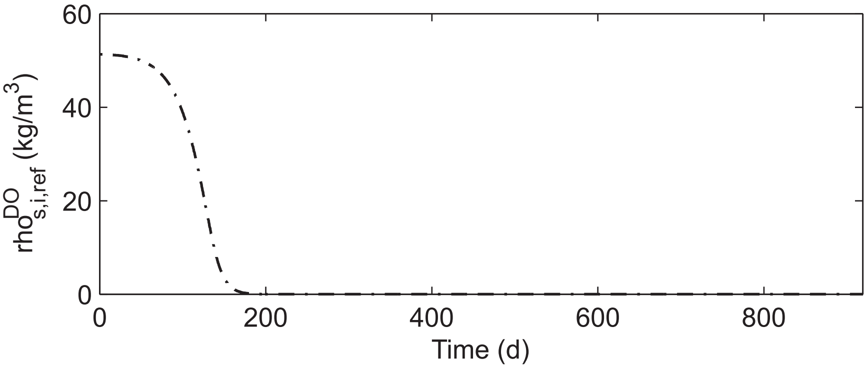

(c) Vertical surface displacement, linear time scale

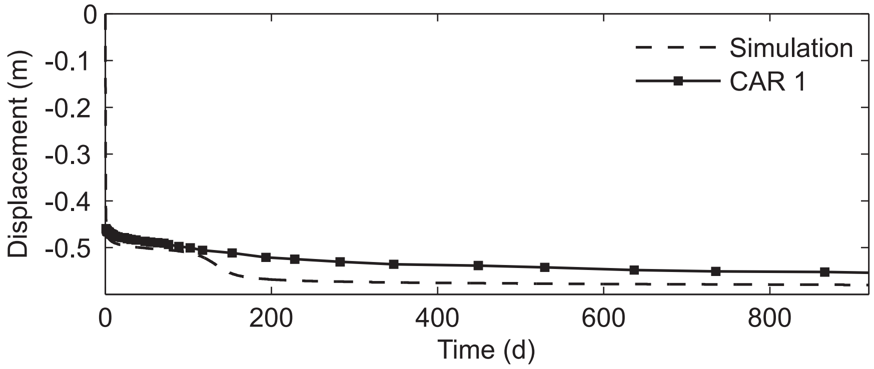

(d) Vertical surface displacement, logarithmic time scale

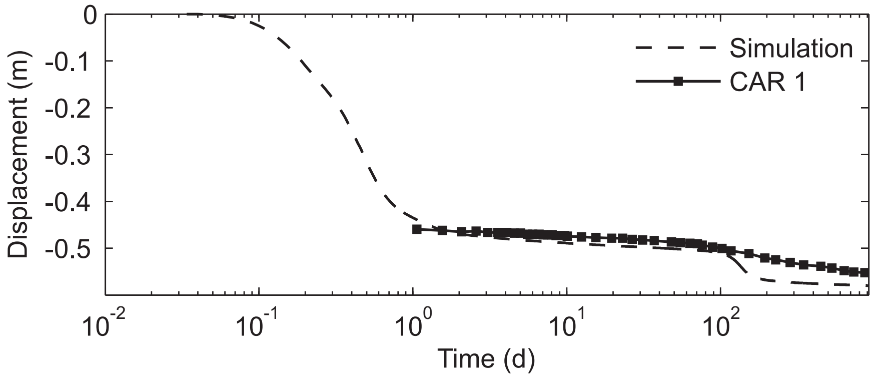

Figure 7.10: Results of simulation of CAR 1. Relation of density evolution and settlements, comparison with measured settlements

At the end of the simulation, the porosity is slightly greater than $\phi = 0.4$. Initial total porosity is estimated by Ivanova [118] to be $\phi = 0.4$ after loading which implies an intrinsic density of $\tilde{\rho}_s = 735\,\mathrm{kg/m^3}$ according to relation (4.2). This is an even lower value for the intrinsic density than assumed in the simulation and confirms that a density of $870\,\mathrm{kg/m^3}$ is within a realistic range for the analysed waste. The porosity is $\phi = 0.5$ in the simulation after loading. The total porosity at the end of the test is determined experimentally from moisture content and tests on drainable porosity to be $\phi = 0.31$, which is again lower than predicted in the simulation. Deviations in porosity are attributed to differences in estimation of $\tilde{\rho}_s$. A back calculation assuming that only the pore volume has been compressed and neglecting any degradation effects would give an initial porosity of $\phi = 0.78$ which is the same value as determined by the model for an intrinsic density of $870\,\mathrm{kg/m^3}$. In general, this reveals the difficulties in determining total porosity and intrinsic density for waste.

Fig. 7.10 (c) and (d) compare calculated displacements and measured settlements. The sample in CAR 1 is compressed by 0.459 m after 1 d which is described very well by the simulation. Within the first 100 d, simulation results and measurements are in good agreement as well. The settlement curve is nearly linear in a semi-logarithmic plot during that stage. After 100 d, an increase of settlement rate is observable which is for the test more obvious in log t scale. The acceleration is attributed to the influence of degradation. An increase in settlements is described by the model as well but with a higher rate than in the test. This corresponds to the gas prodcution curve which exhibits overestimated degradation rates after its inflexion point. Ivanova et al. [119] suppose half of the secondary settlement to be caused by biodegradation.

The parameter set for the compaction model obtained from the simulation of CAR 1 is given in table 7.2. The parameters a_{cr} and b_{cr} are chosen in correspondance with the values as given in figure 5.11. The initial density of $\rho_s = 186.5\,\mathrm{kg/m^3}$ is supposed to be the minimum density. Maximum density is supposed to equal the intrinsic density. The model may be applied straighforward in case that a higher intrinsic density is assumed, solely an adaptation of the parameters of the creep model is then necessary.

Table 7.2: Parameters of the compaction model for the simulation of the CARs

A_{cr}	$=$	$0.05\,\mathrm{h^{-1}}$	a_{cr}	$=$	0.5
n_{cr}	$=$	0.8	b_{cr}	$=$	8.0
p_{cr}	$=$	8.5	ρ_{min}	$=$	$186.5\,\mathrm{kg/m^3}$ = initial density
			ρ_{max}	$=$	$870\,\mathrm{kg/m^3} = \tilde{\rho}_s$

(a) Partial dry densities degradable organic matter

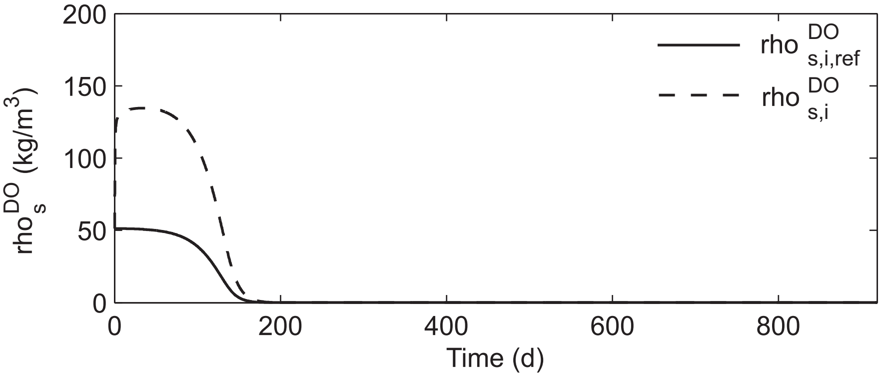

(b) Partial dry densities biomass

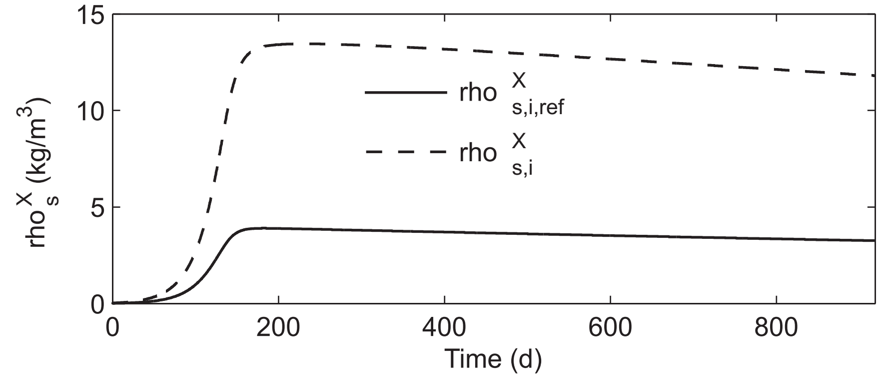

(c) Partial dry density inert material

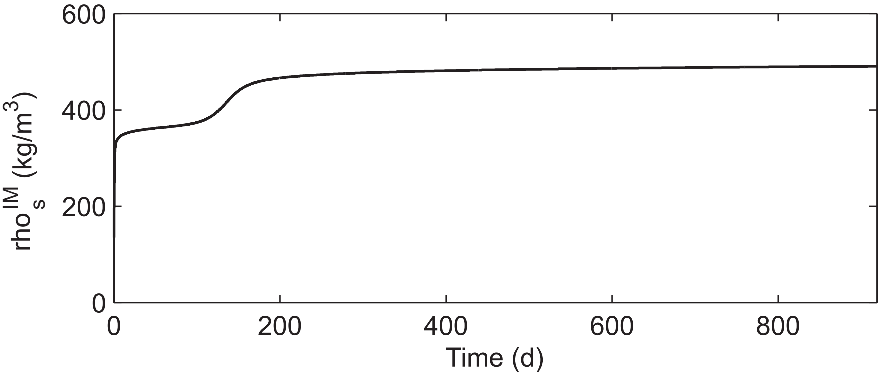

Figure 7.11: Results of the simulation of CAR 1. Comparison of densities of the solid components

The evolution of partial density of inert material figure 7.11 (c) reveals the pattern of the time-settlement curve as the inert material is not subject to biodegradation. Initially, the density ρ_s^{IM} is set to 135.2 kg/m^3 and increased up to $\sim$ 300 kg/m^3 due to initial compaction. A slow increase occurs during primary settlement followed by a further increase due to a higher settlement rate. Figure 7.12 (a) shows the development of liquid pressure which is at atmospheric pressure most times.

(a) Fluid pressures

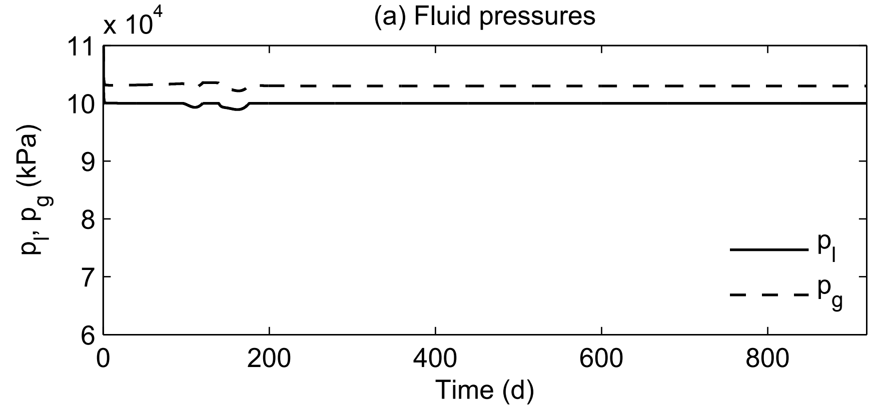

(b) Fluid saturations

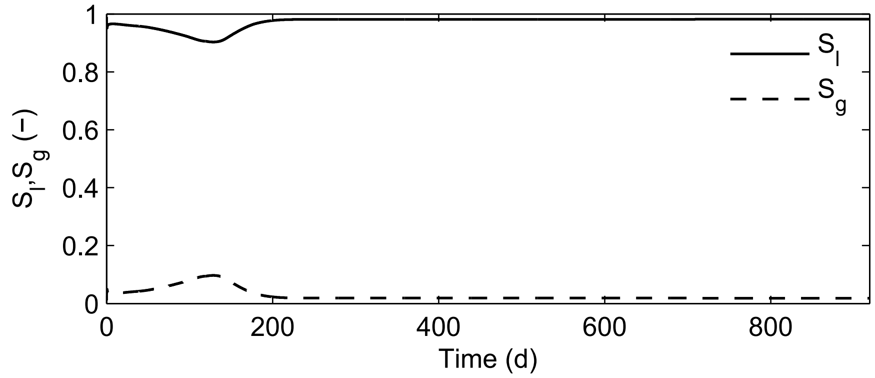

(c) Mass fractions of gas phase components

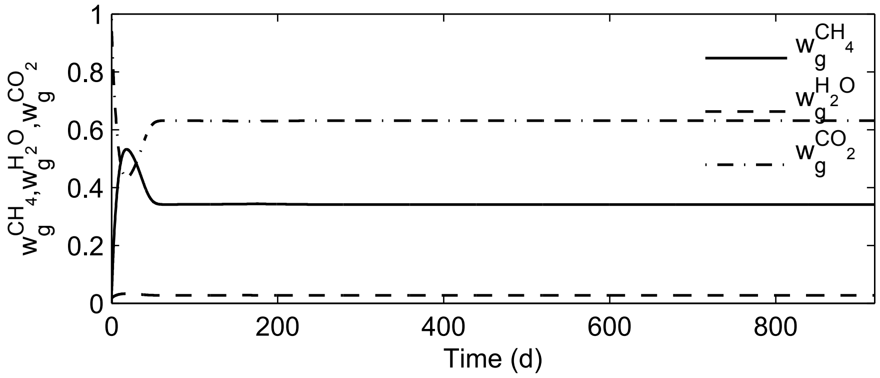

Figure 7.12: Results of simulation of CAR 1. Fluid pressures (a), saturations (b) and gas fractions (c) are shown

The gas pressure exceeds the liquid pressure by approx. 3 kPa due to the applied soil water retention curve. Liquid saturation in 7.12 (b) is close to full saturation most times. Within the first 150 d, a slight decrease in saturation occurs which is caused by the consumption of water during degradation. With further compaction, the deviation from the fully saturated state disappears. The phase of decreasing saturation and simultaneously increasing porosity is accompanied by slight fluctuations in pressure, cf. fig. 7.12 (a). Those fluctuations have not occured in the simulation without degradation shown in section 7.2.3. The mass fractions in the gas phase 7.12 (c) evolve according to the degradation model considering that first the initially present acetic acid is consumed in R2, compare also the change of the mass fraction of acetic acid in the liquid phase $w_l^{\mathrm{CH_3COOH}}$ in figure 7.13 (b).

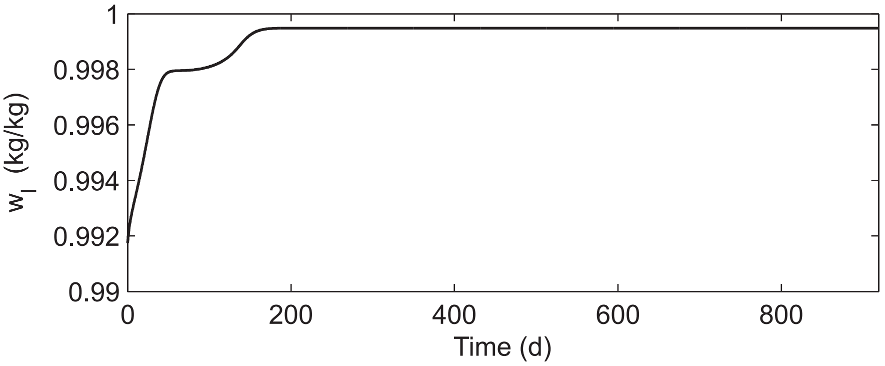
(a) Mass fraction H_2O in liquid phase

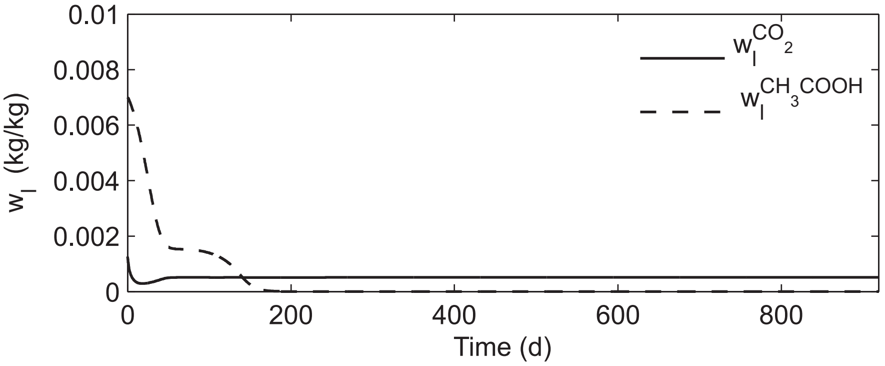
(b) Mass fractions CO_2 and acetic acid in liquid phase

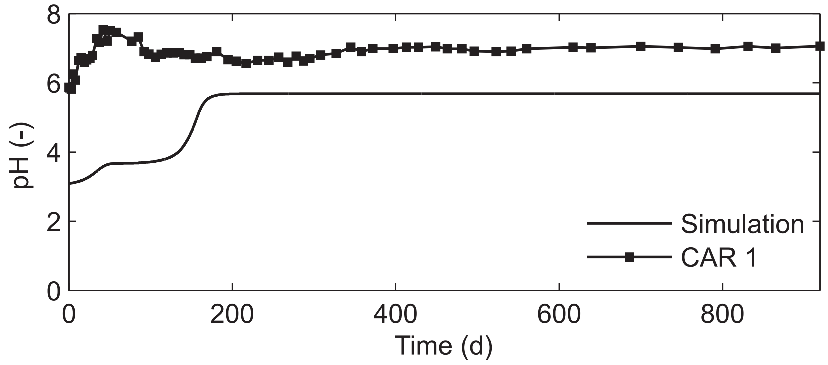
(c) Evolution of pH value

Figure 7.13: Results of simulation of CAR 1. Liquid fractions, (a) and (b), and pH evolution (c) are compared

The mass fractions of the liquid components are shown in figure 7.13 (a) and (b) together with the evolution of pH in (c). As the rate of reaction step R2 is higher than the rate of R1, the acetic acid which is produced in reaction step R1 does not accumulate. While the mass fraction of acetic acid, $w_l^{\mathrm{CH_3COOH}}$ or w_l^{Ac}, decreases, the fraction of H_2O in the liquid phase increases. The decrease of w_l^{Ac} is accompanied by an increase in pH up to pH = 6. The pH measured in the leachate remains nearly neutral after an initial increase up to pH = 8 at 100 d. This magnitude of pH cannot be described by the model as only acidic components are balanced. However, the analyses by Reichel and Haarstrick [197] show that a realistic description of pH remains difficult because of uncertainties according to the waste's buffer capacity, even when using a more detailed reaction scheme. Thus, the modelling of pH measured in waste leachate is an interesting aspect of future research.

Ivanova [118] supplements the lysimeter experiments by tests on the biochemical methane potential of the used waste material (BMP tests). The BMP tests indicate that $\sim 6.6\,\text{kg}$ organic matter are degraded anaerobically within the test period of 919 d. Partial densities in figure 7.14 are calculated from data on dry matter obtained in BMP tests and compared with the simulation results in figure 7.14. The data should be handled with care as it is obvious from the behaviour of CAR 2 that the reactors differ with respect to gas production, although the same material is used for sample preparation.

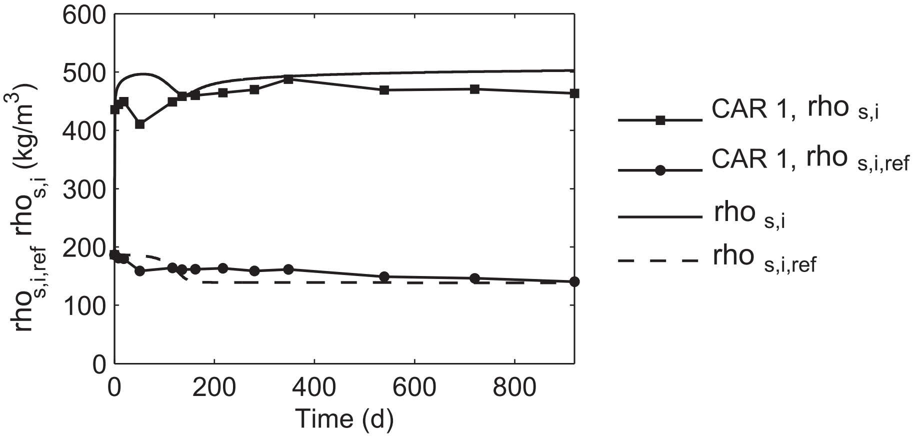

Figure 7.14: Results of simulation of CAR 1 (continuous lines). Comparison of solid densities with densities calculated from the results of BMP tests given in Ivanova [118] (lines with data points)

The zoom on the first 100 h in figure 7.15 confirms that any excess liquid pressure vanishes very quickly, see (a) and (b), and that the initial settlements are met well, (c). The short consolidation phase shows that the chosen hydraulic conductivity is high enough to enable quick drainage and that the reactor is described satisfactorily using one element.

The simulation of CAR 1 and the detailed presentation of results describing the waste mixture point out that several quantities have to be brought in line as caused by the complexity of the coupling.

(a) Liquid pressure

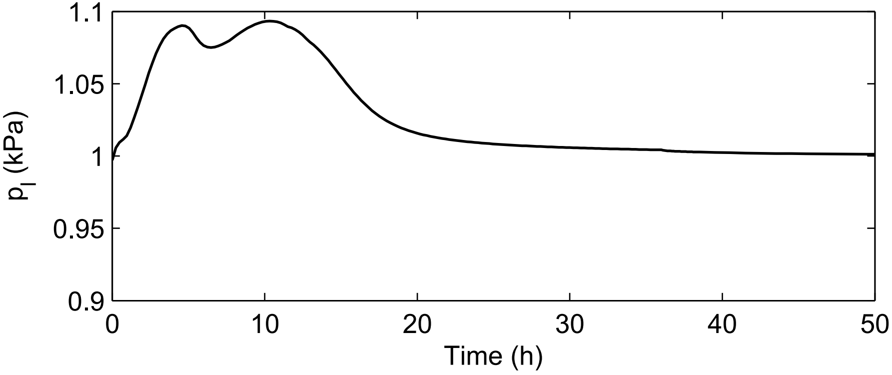

(b) Outflux liquid

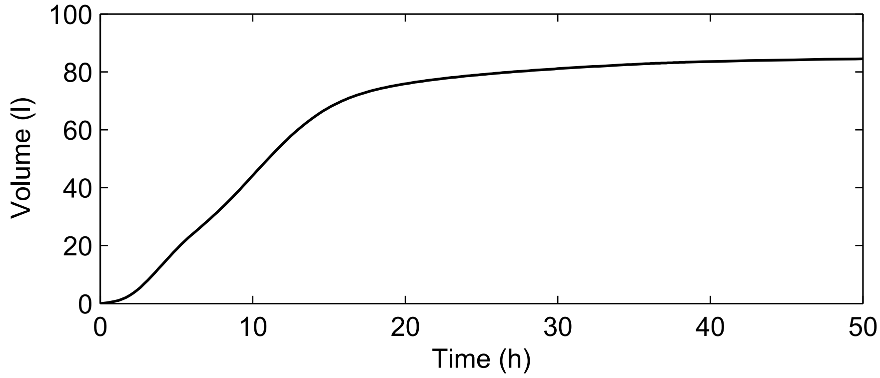

(c) Vertical surface displacement

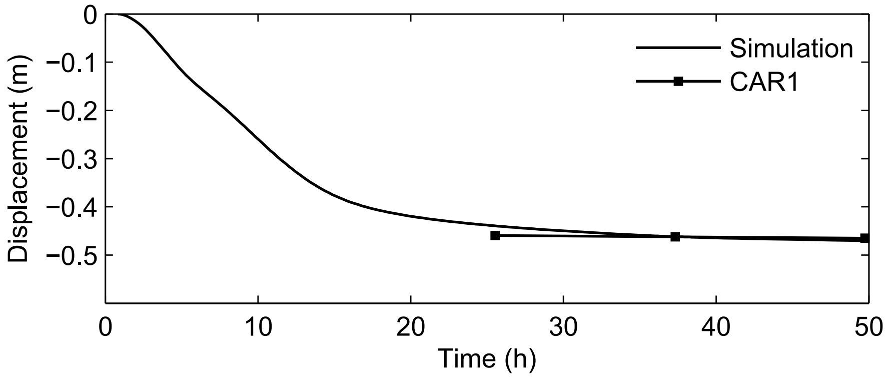

Figure 7.15: Results of simulation of CAR 1. Plots of liquid pressure (a), liquid surface flux (b) and surface displacements (c) during the first 100 h. The loading phase ends after 24 h in the simulation

7.2.2 Simulation of CAR 2

The parameter set from table 7.2 obtained in modelling the behaviour of CAR 1 is used for description of reactor CAR 2. The two tests are supposed to differ only by the applied load. Although the same waste material is used, figure 7.16 (b) and (d) show that less gas is produced in CAR 2. About 7000 l are measured after 919 d. This is met in the simulation by reducing the contained mass of organic matter from 7.44 kg to 6.09 kg. The reason for the different behaviour cannot be completely explained by Beaven [14]. It is likely that the variation in composition of the waste has caused the difference in gas production as environmental conditions are equal for both CARs due to experimental setup. Probably, more degradable matter or a higher fraction of readily degradable waste is contained in CAR 1. The evolution of the quantities investigated in the previous section is analogously in CAR 2. Thus, only gas volume and settlements are discussed here more in detail.

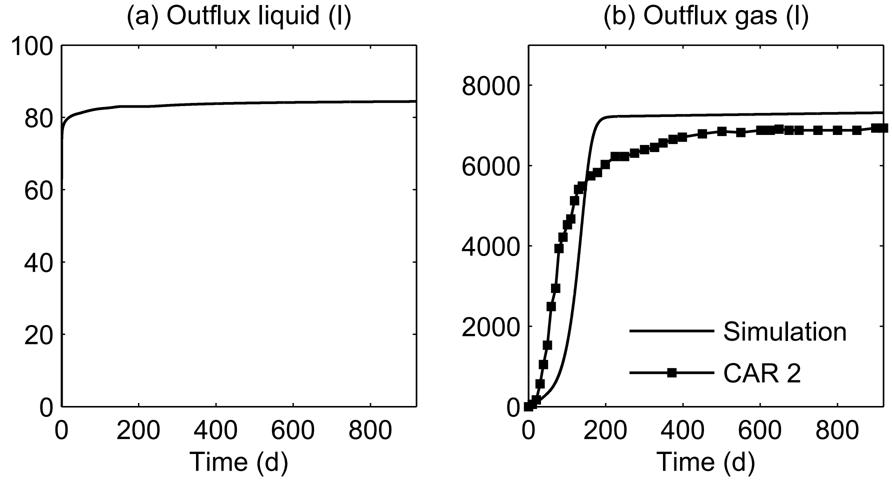

(a) Outflux liquid (l) (b) Outflux gas (l)

(c) Outflux distinguished by gas fractions (l) (d) Outflux original landfill gas (l)

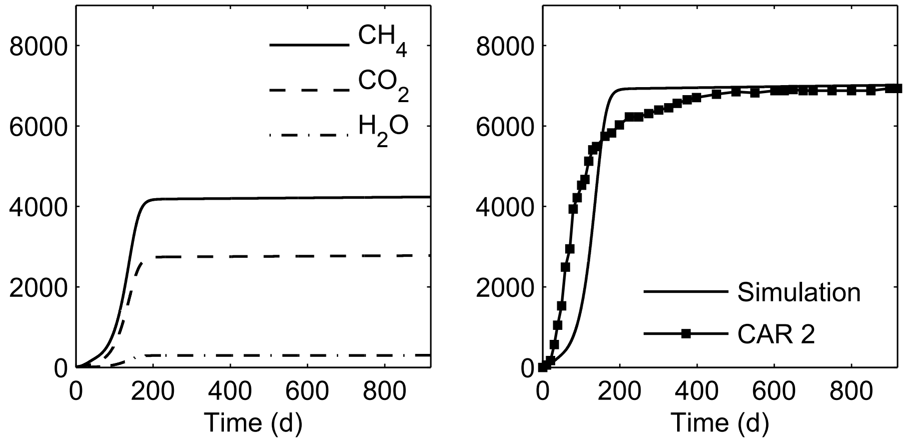

Figure 7.16: Results of simulation of CAR 1. Surface fluxes of liquid and gas. Gas fluxes are compared with experimental data

Due to the lower loading, the compaction of the sample in CAR 2 is less than in CAR 1. The initial settlement is $\sim 0.4\,\mathrm{m}$ which increases up to $\sim 0.5\,\mathrm{m}$ during stages of primary and secondary settlements, 7.17 (c) and (d). Less liquid flux occurs due to less compression of the sample, 7.16 (a). Evolution of gas fractions is analogous to CAR 1, figure 7.16 (c). As shown in the corresponding plot for CAR 1, figure 7.10, an increase of settlement rate after 100 d is observable on semilogarithmic scale in figure 7.17 (d). Again, this acceleration is attributed to solid mass loss from degradation and overestimated by the simulation. As in the simulation of CAR 1 the reason is the non-optimal approximation of degradation. Similar to the simulation of CAR 1, all organic matter is already decomposed after 200 d. Evolution of solid densities and porosity is also similar to CAR 2, the final porosity is around $\phi = 0.5$ in the simulation, compare 7.17 (a). In the tests porosity is determined to $\phi = 0.52$ after loading and $\phi = 0.31$ at the end of the experiments.

(a) Total partial dry solid density

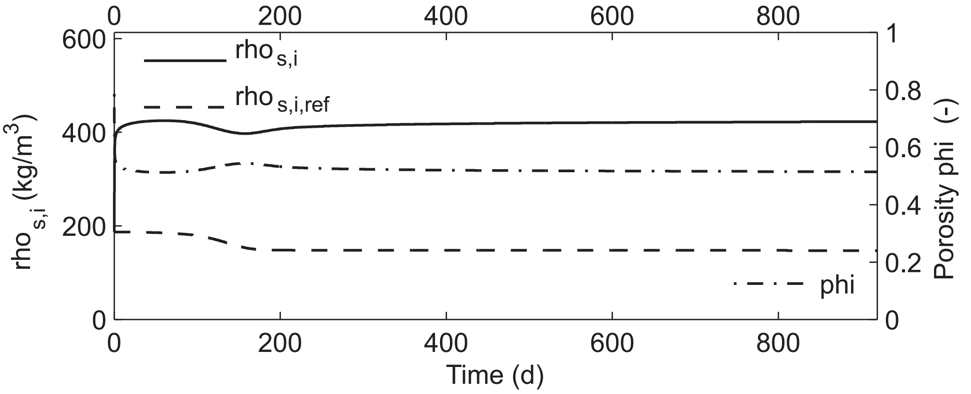

(b) Total partial dry reference density organic matter

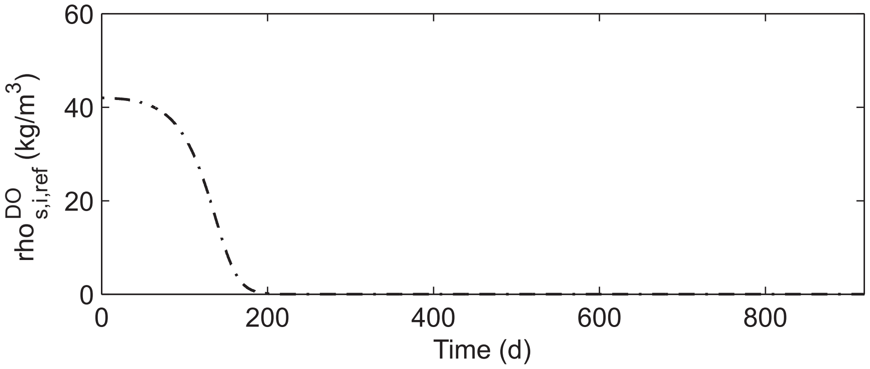

(c) Vertical surface displacement, linear time scale

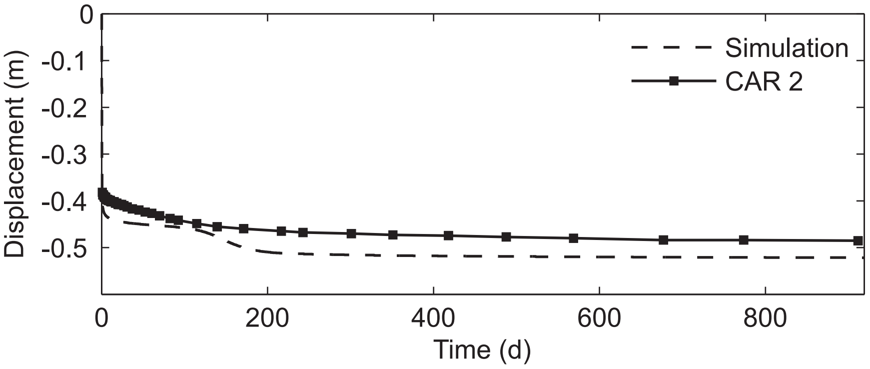

(d) Vertical surface displacement, logarithmic time scale

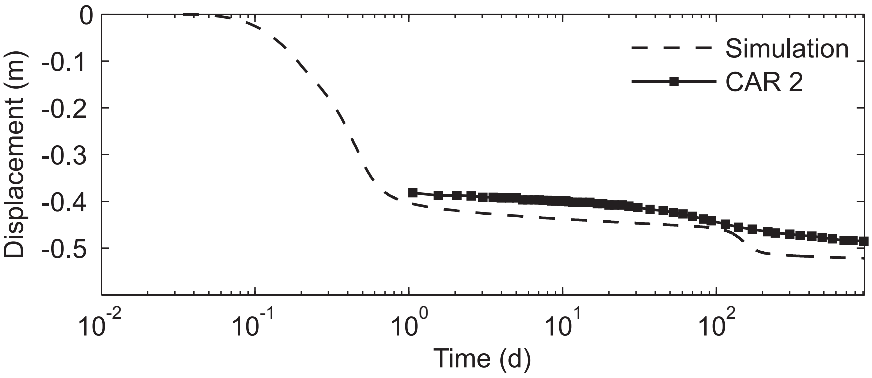

Figure 7.17: Results of simulation of CAR 1. Relation of density evolution and settlements. Comparison with measured settlements

7.2.3 Comparative Simulations without Degradation

Finally, the two experiments are simulated while degradation is disabled by assuming that the waste sample consists of inert matter only ($\Rightarrow \rho^{DO}_{s,0} = 0.0$, $\rho^{X}_{s,0} = 0.0$ and $\rho^{IM}_{s,0} = 186.5\,\mathrm{kg/m^3}$). In fact, a control reactor in which the sample is acidified in order to inhibit degradation is part of the test programme. Despite the special treatment, gas production starts after 280 days, proving the establishment of milieu conditions, which are appropriate for anaerobic degradation. Hence, the reactor is not used for validation in this thesis.

Figure 7.18 shows the evolution of solid densities. Due to the absence of decomposition, solid density is increased monotonically in both CARs. Slightly higher values are obtained at the end of the test compared to the previous simulations. Settlements are compared with the displacements obtained in sections 7.2.1 and 7.2.2. Figure 7.18, (b) and (c), show that no acceleration of settlement is observed in the simulation if degradation does not occur.

The simulations of the CARs show that the model is able to reproduce the different settlement mechanisms as described in figure 5.2 separately. Hence, the model is very flexible and considers instationary changes in the waste state automatically.

(a) Total partial dry solid density

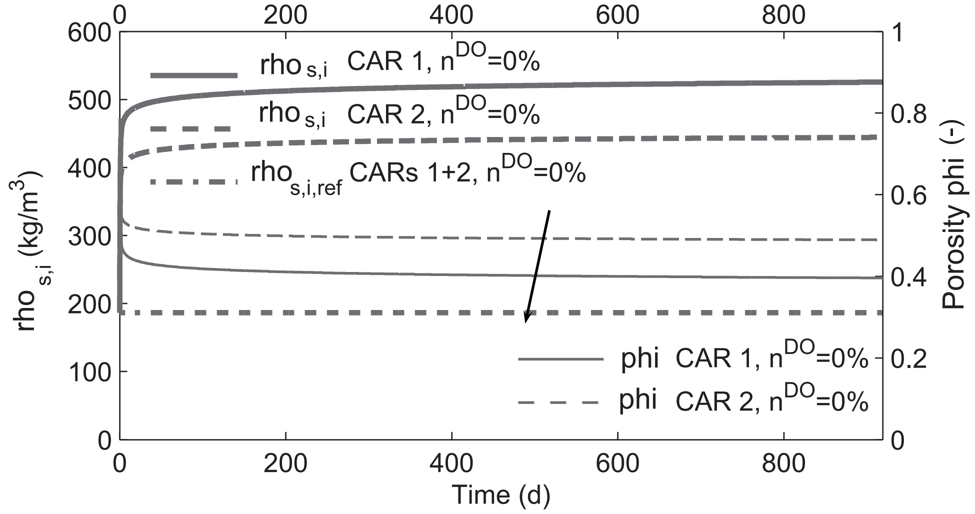

(b) Vertical surface displacement, linear time scale

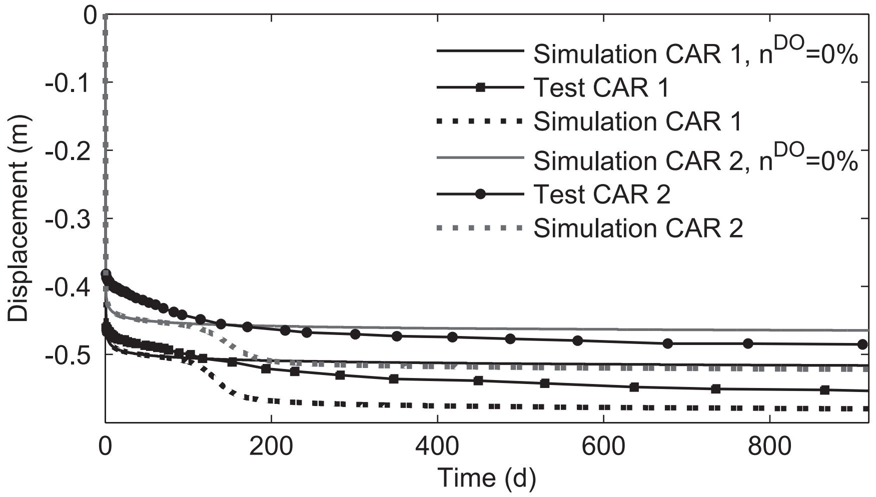

(c) Vertical surface displacement, logarithmic time scale

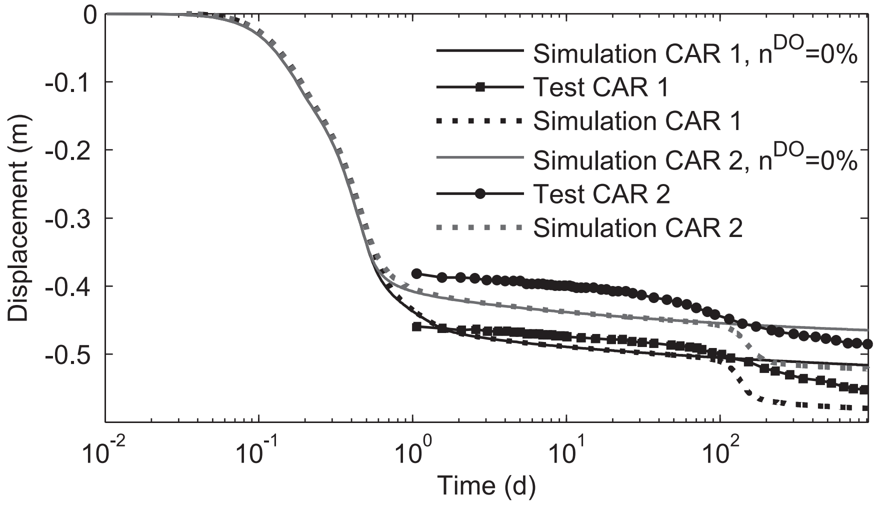

Figure 7.18: Results of simulation of CAR 1 and CAR 2. Comparison of results from sections 7.2.1 and 7.2.2 with results from simulation without degradation

7.3 Coupled Analyses of a Landfill Structure

The following examples show the capabilities and characteristics of the developed model in investigations of coupled processes in a landfill structure. The analysed landfill is 130 m wide at the base and 25 m high with a lateral slope inclination of 1:2. Exploiting symmetry, only half the cross section is considered. All analyses are performed for the case of plane strain. Figure 7.19 explains the setting of boundary conditions and table 7.3 lists a basic set of initial conditions and parameters. Some of them are modified throughout the particular examples which is described in the corresponding sections. The basic parameter set is selected with respect to the results of chapters 3, 4 and 5.

The maximum solid density $\tilde{\rho}_s$ is chosen based on the results from section 3.5.4 for the NMS waste. Initial spatial distribution over the landfill cross section is assumed to be homogeneous in the basic set. The initial porosity is determined from the solid bulk density by equation (4.2).

Parameters of elasticity and spontaneous plasticity are taken from section 5.2. The parameters of the creep model are listed in table 7.3. They are chosen different from the CAR experiments as the landfilled waste is much more dense than the waste samples used in the CAR experiments. Initial permeability is set to a relatively high value in the range of a sandy gravel assuming a ratio of 1:10 for vertical to horizontal permeability. The permeability of the bottom layer is by a factor of 1×10^5 less than the permeability of the waste in order to describe a mineral liner. Fibres' content is $n^F = 0.05$ in all analyses.

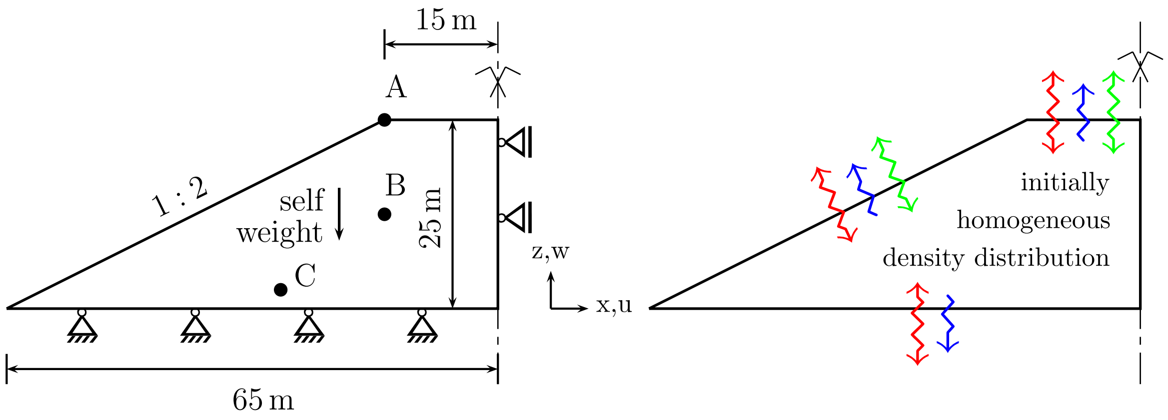

🟥 Cauchy boundary condition for heat flux
$\alpha_u = 0.05\,\mathrm{m}^2\cdot\mathrm{K/W},\ \Theta_o = 293\,\mathrm{K}$

🟦 Cauchy boundary condition for liquid flux
bottom: $K_h = K_v = 1\times10^{-16}\,\mathrm{m}^2,\ p_{l,o} = p_{atm}$
top and lateral: $K_h = 1\times10^{-10}\,\mathrm{m}^2, K_v = 1\times10^{-11}\,\mathrm{m}^2,\ p_{l,o} = p_{atm}$

🟩 Cauchy boundary condition for gas flux
top and lateral: $K_h = 1\times10^{-10}\,\mathrm{m}^2, K_v = 1\times10^{-11}\,\mathrm{m}^2,\ p_{g,o} = p_{atm}$

Figure 7.19: Boundary and initial conditions for analyses of a landfill structure

A relatively coarse structured mesh is used in order to reduce computational time. The governing physical fields are discretised by 10 elements in height and 23 elements in width. Due to the shape of the landfill, mesh width increases from top to bottom.

The following examples include long-term analyses over periods of up to almost 30 years. Nodes A, B and C in figure 7.19 are referred to when discussing the results of the simulations.

Table 7.3: Basic set of parameters and initial conditions for the analysed landfill structure

Initial conditions			
Saturation	$S_l = 0.65$	Organic matter	$\rho_s^{DO} = 100\,\mathrm{kg/m^3}$
Dry density	$\rho_s = 500\,\mathrm{kg/m^3}$	Inert matter	$\rho_s^{IM} = 400\,\mathrm{kg/m^3}$
K_h	$4.5 \times 10^{-11}\,\mathrm{m^2}$	Biomass	$\rho_s^{X} = 6 \times 10^{-2}\,\mathrm{kg/m^3}$
K_v	$4.5 \times 10^{-12}\,\mathrm{m^2}$	Acetic acid	$w_l^{Ac} = 1.0 \times 10^{-8}$
Liquid pressure	$p_l = p_{atm}$	Methane	$w_g^{\mathrm{CH_4}} = 2.5 \times 10^{-3}$
		Temperature	$\Theta = 303\,\mathrm{K}$
Parameters for creep model		**Parameters of degradation model**	
ρ_{min}	$500\,\mathrm{kg/m^3}$	Hydrolysis rate	$\mu_{max,R1} = 5 \times 10^{-7}\,\mathrm{s^{-1}}$
$\rho_{max} = \tilde{\rho}_S$	$1042\,\mathrm{kg/m^3}$	Methanog. rate	$\mu_{max,R2} = 4.6 \times 10^{-5}\,\mathrm{s^{-1}}$
A_{cr}	$9.22 \times 10^{-5}\,\mathrm{h^{-1}}$	Monod const. R1	$K_{s,R1} = 70\,\mathrm{kg/m^3}$
n_{cr}	0.939	Monod const. R2	$K_{s,R2} = 3\,\mathrm{kg/m^3}$
p_{cr}	10.11	Heat cond.	$\lambda_s = 1.5 \times 10^{-4}\,\mathrm{kW/(m \cdot K)}$
a_{cr}	0.5	f_w	set 1 in figure 3.10
b_{cr}	25.55	f_Θ	set 1 in table 3.3
		f_{pH}	set 4 in figure 3.9
Other parameters			
Atm. pressure	$p_{atm} = 1 \times 10^5\,\mathrm{kPa}$	Fibres content	$n^F = 0.05$
Res. gas satur.	$S_{g,res} = 0.01$		

7.3.1 Influence of Organic Matter Content on Settlements

The first model application focuses on the influence of varying initial organic matter content on settlements and degradation over a period of 27 years. To exclude any transient influence of temperature, the simulations are first performed under isothermal conditions at a temperature of $\Theta = 30\,^\circ\mathrm{C}$. For influences of temperature and liquid on the reactions rates of anaerobic biological degradation, the sets $f_{\Theta,set\,1}$ and $f_{\Theta,set\,2}$ from figure 3.6 are used. Also the influence of temperature on lysis is considered as plotted in figure 3.6.

Three cases are examined: case 1 considers a solid phase made up of inert material only and in cases 2 and 3, initial organic matter content is 20 % and 30 % respectively (in terms of solid dry mass organic matter per total solid dry mass). Initially, a homogeneous distribution of organic matter is assumed.

Figure 7.20 compares the time-settlement curve of the upper surface node A for the three cases. Initial settlement due to loading is 1.5 m, whereas settlement rate is high in the beginning and then decreases while solid density is increased, compare figure 7.22. The decrease in creep rate is due to the density dependent formulation of the compaction model as given by (5.23) and (5.26). The contour plots of solid density at different times in figure 7.23 show that compaction increases with depth due to the higher overburden pressure. Thus, the pattern of density distribution becomes very similar to that of the vertical stresses of the basic matrix, see figure 7.24 (c) and (d). After five years, surface settlement is 2.5 m or nearly 10 % of initial height while solid density has increased from 500 kg/m^3 to 550 kg/m^3. Until that point, the time-settlement curves of the three cases nearly coincide.

Subsequently, the settlement rate starts to increase in cases 2 and 3. According to the change in organic matter in node B shown in figure 7.21, it is obvious that this point is related to the point when conditions for degradation have improved. In fact, degradation starts from the very beginning of the simulation but the rate is low as implied by the assumed maximum rate of hydrolysis $\mu_{max,R1}$ and the initial biomass concentration. While biomass is growing, degradation rate is increased due to the application of Monod kinetics in the reaction model.

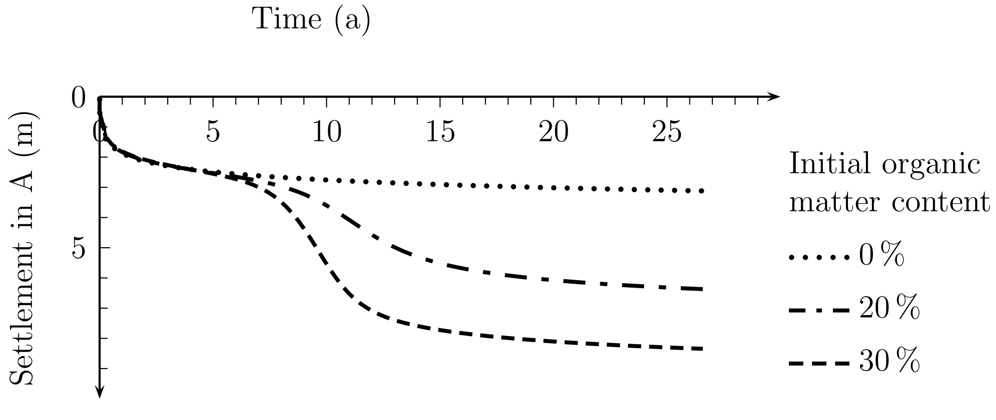

Figure 7.20: Time-settlement curves of node A for three cases with different initial organic matter content

Organic matter decomposition causes a solid mass loss, hence, total solid density starts to decrease as well. This triggers additional settlements as given by the formulation of the creep rate. The first inflexion point in the time-settlement curve nearly coincides with the point of maximum solid density. The evolution of solid density indicates that the rate of solid mass loss is higher than the settlement rate in the phase between five and ten years. Thus, the maximum in density is followed by a phase of interim loosening, whereas the magnitude of density does not drop below the initial density in this case.

While degradation diminishes after 10 years, total density increases again due to additional compaction. Settlement rate is lower at that time than in the initial compaction phase which is due to the continuous decay of biomass and due to decreased overburden pressure. The overall solid mass loss leads to a decrease in self weight, and thus the compressive vertical stresses in the basic matrix are reduced, see figure 7.24 (d) in comparison to 7.24 (c). Recalling the stress dependency of the compaction model, it is obvious that settlement rate is less than in the beginning of the simulation.

Degradation proceeds slightly faster in case 3 than in case 2 because of the initially higher density of organic matter in conjunction with the application of Monod kinetics. In the current model formulation, compaction causes an acceleration of decomposition. The density with respect to the current configuration is used in the Monod kinetics of hydrolysis step R1 but the Monod constant is not transformed and remains related to the reference configuration.

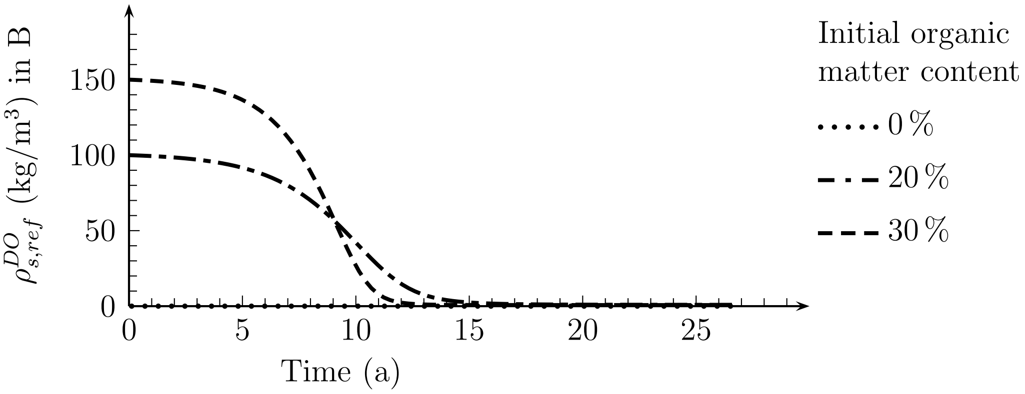

Figure 7.21: Evolution of organic matter content in B for three cases with different initial organic matter content

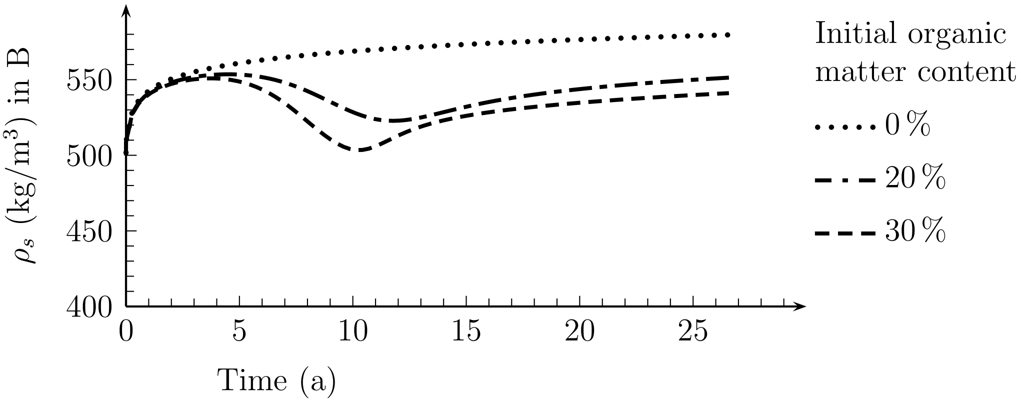

Figure 7.22: Evolution of total partial solid density in B for three cases with different organic matter content

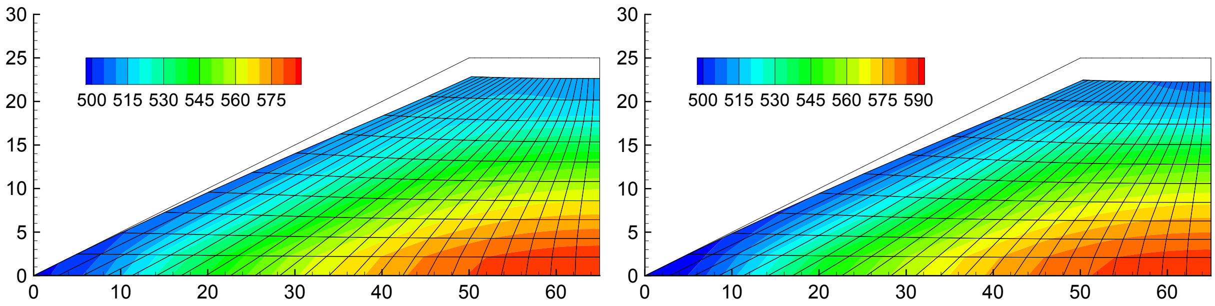

(a) ρ_s (kg/m^3) at $t = 2.2\,\mathrm{a}$ (b) ρ_s (kg/m^3) at $t = 4.9\,\mathrm{a}$

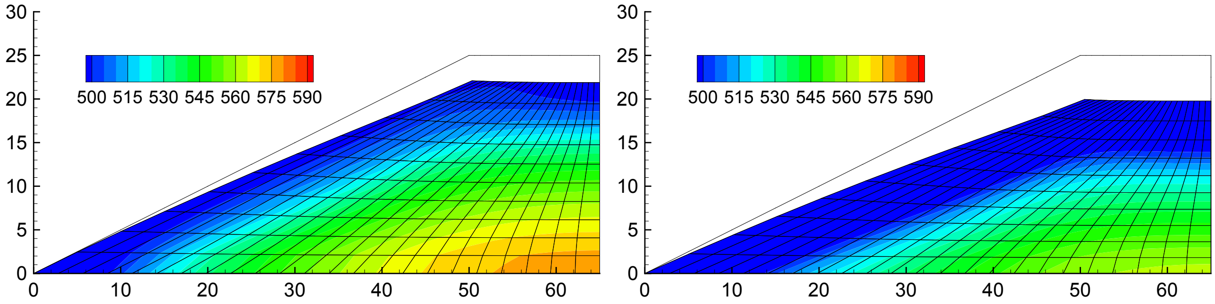

(c) ρ_s (kg/m^3) at $t = 7.7\,\mathrm{a}$ (d) ρ_s (kg/m^3) at $t = 13.2\,\mathrm{a}$

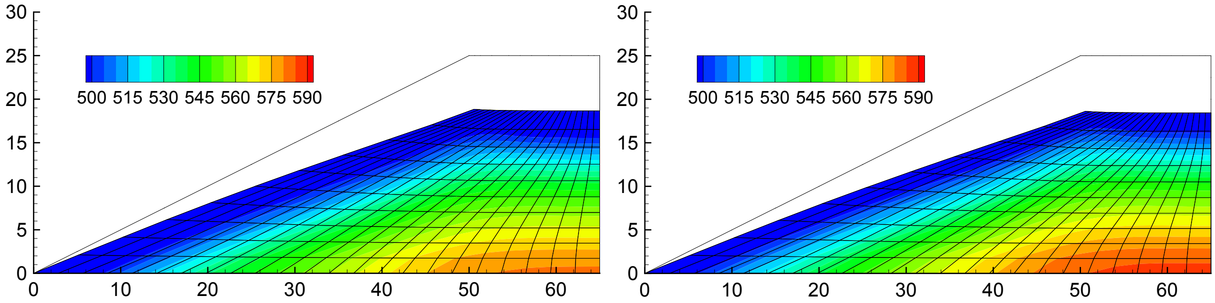

(e) ρ_s (kg/m^3) at $t = 21.4\,\mathrm{a}$ (f) ρ_s (kg/m^3) at $t = 26.9\,\mathrm{a}$

Figure 7.23: Contour plots of partial total solid dry density at different times for case 2, i.e. 20 % organic matter initally

To exclude this effect, the Monod constant may be related to the deformed configuration by the determinant of the deformation gradient. Alternatively, a further extension of the model could include a sorption step similar to Reichel and Haarstrick [197] so that organic matter is present in dissolved form. Monod kinetics may then be expressed in terms of concentrations and any density transformation is avoided.

Figure 7.21 shows that after 15 years almost all organic matter is degraded. The spatial variation of decompostion rate is very low due to the uniform environmental conditions as shown from the contour plots (a) and (b) in figure 7.25. Partly, organic matter is assimilated in the growth of biomass up to a maximum density of 4 kg/m^3 which then continuously decays, compare evolution of partial density of biomass in figure 7.26 (c). As degradation declines, the settlement rate declines as well.

The time-settlement curves prove that the higher the initial organic matter content is, the higher the final settlements are if all organic matter is decomposed. The same observations are for instance made by Wardwell and Nelson [238]. In case 1, settlements after 27 years are about 12 % of initial height whereas they are up to 26 % and 34 % in cases 2 and 3. As shown in section 5.1.3, such magnitudes are in the range of settlements observed on landfill sites.

Figure 7.24, (a) and (b), show horizontal stresses of the fibres at 2.2 years and at 27 years. Horizontal stresses concentrate in the center of the landfill. This can be explained by the lateral strain of the basic matrix which is constrained by the fibres. Close to the bottom, the fibre stresses decrease down to zero. The boundary is fixed horizontally, hence, no lateral strain is possible.

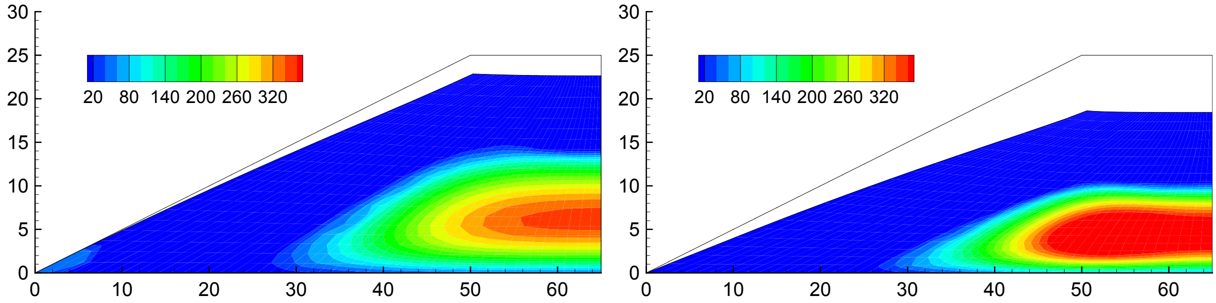

(a) σ^F_{xx} (kPa) at $t = 2.2\,\mathrm{a}$

(b) σ^F_{xx} (kPa) at $t = 26.9\,\mathrm{a}$

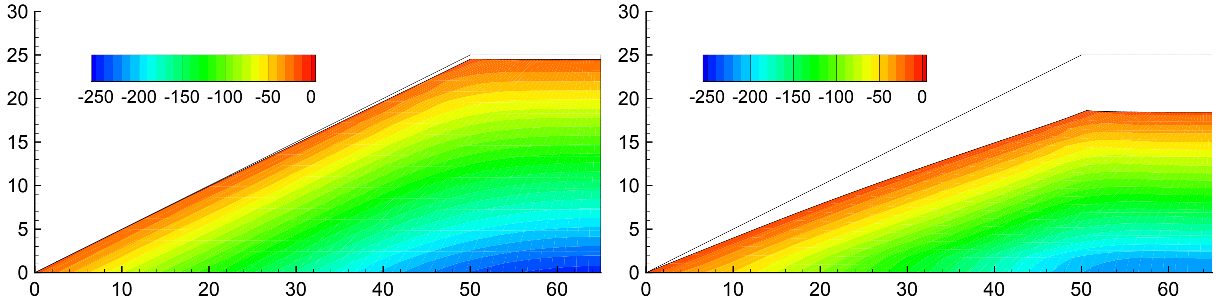

(c) σ^B_{zz} (kPa) at $t = 5\,\mathrm{h}$ (after loading)

(d) σ^B_{zz} (kPa) at $t = 26.9\,\mathrm{a}$

Figure 7.24: Vertical stresses of the basic matrix σ^B_{zz} and horizontal stresses of the fibres σ^F_{xx} at different times for case 2, i.e. 20 % organic matter initially

The pattern of porosity is directly linked to the density pattern, compare figures 7.23 and 7.25 (c) and (d). Especially in the outer layer, porosity increases due to degradation. In the center, porosity change is characterised by a decrease due to compaction, an increase from degradation and subsequent decrease from progressing compaction. In accordance with spatial density distribution, the porosity is about $\phi = 0.43$ after 27 years at the base and with $\phi = 0.52$ about 20 % greater in the surface layer.

The contour plots of solid density at different times in figure 7.23 reveal the density decrease and increase observed in figure 7.22. Thereby, the typical pattern of high compaction close to the landfill base and low compaction near to the surface is maintained over time. At the base, the dry density is about $\rho_s = 600\,\mathrm{kg/m^3}$ after 27 years. A greater or lower compaction can be described by adopting the parameters a_{cr} and b_{cr} or ρ_{max} which influence the infinite density in equation (5.26). For parameter determination, oedometric tests at different loadings are required.

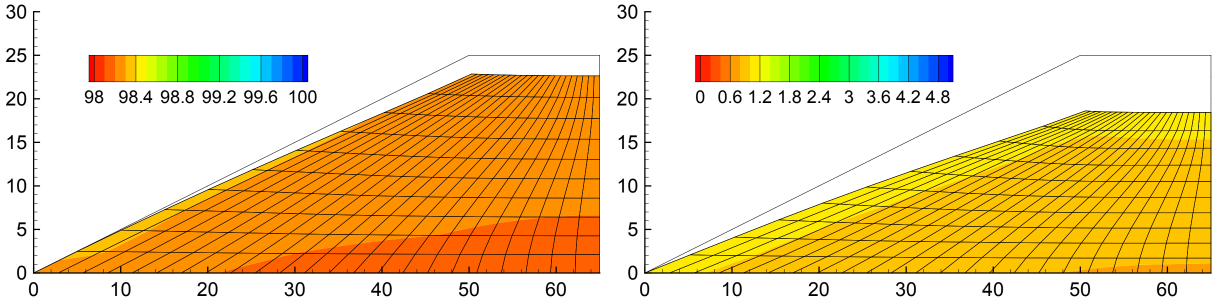

(a) $\rho_{s,ref}^{DO}$ (kg/m^3) at $t = 2.2\,$a (b) $\rho_{s,ref}^{DO}$ (kg/m^3) at $t = 26.9\,$a

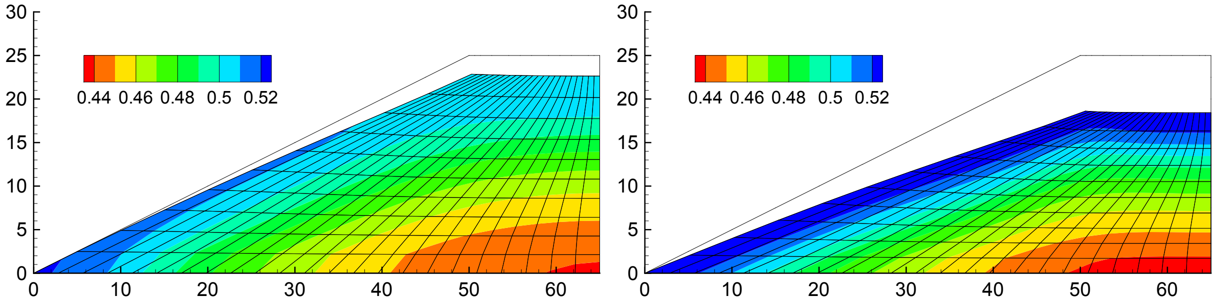

(c) ϕ (-) at $t = 2.2\,$a (d) ϕ (-) at $t = 26.9\,$a

Figure 7.25: Contour plots of organic matter and porosity at different times for case 2, i.e. 20 % organic matter initially

In figure 7.26 (b), different densities are plotted in one graph to show their relation. Contrary to total solid density, the density of inert matter increases monotonically. In figure 7.26 (a), the vertical displacement in A is shown in comparison with that in the inner nodes B and C. Settlement monotonically increases in all nodes. This confirms that the phases of density decrease may not be attributed to an uplift caused by excess pressure as for example observed by Ricken and Ustohalova [199].

In the long-term simulation, settlements seem to decline initially but are then suddenly increased due to degradation. If, for example, a surface liner system had been placed on top of the landfill, considerable damage would probably have been occured. The results prove the importance of site data on initial organic matter content for estimation of long-term settlements. Furthermore, they emphasise the demand for a realistic description of degradation processes. The proposed reaction model is very sensitive to biomass concentration which is, however, very difficult to measure both on site and in the lab. Practically, samples can be analysed with respect to a particular species of microorganisms but not with respect to an overall, total solid biomass.

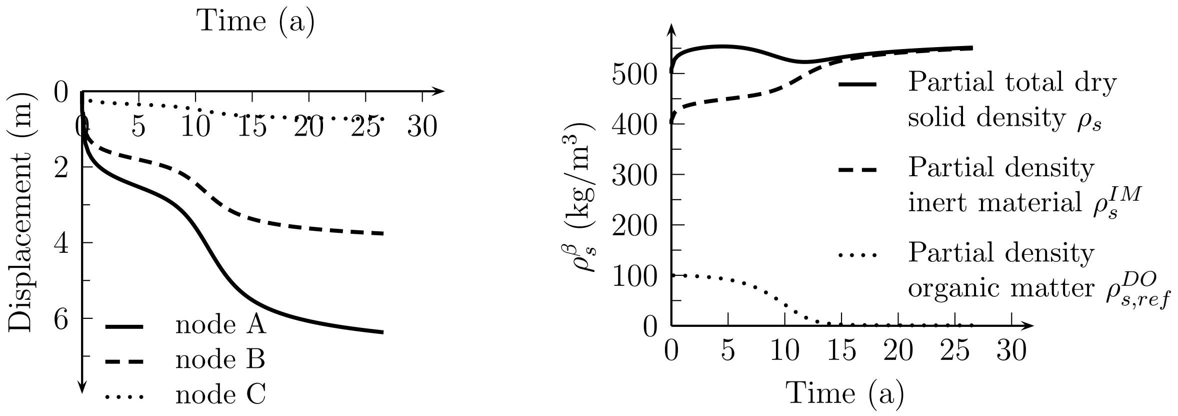

(a) Vertical displacement in A, B and C

(b) Comparison of densities in B

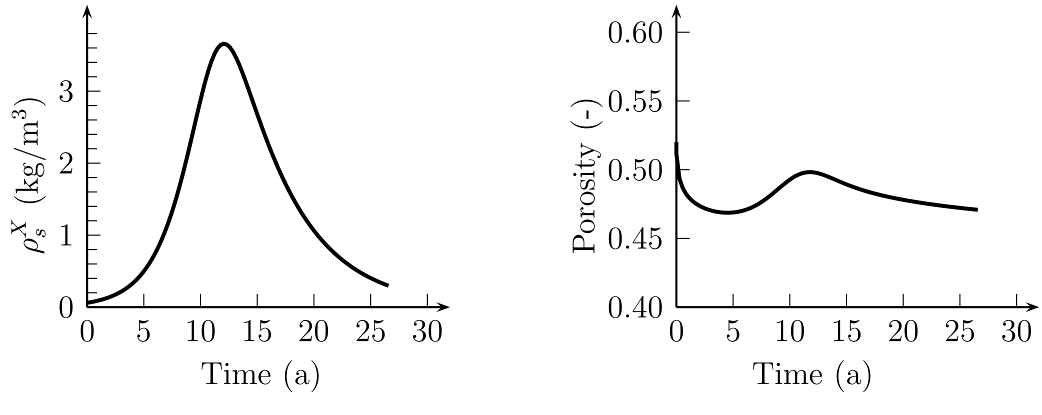

(c) Evolution of biomass in B

(d) Evolution of porosity in B

Figure 7.26: Comparison of displacements, densities and porosity for case 2, i.e. 20 % organic matter initially

Influence of Temperature on Degradation and Settlements Case 2 is additionally investigated in a non-isothermal analysis. Heat generation enthalpies are set according to section 3.5. The parameters of the degradation model are slightly modified considering the influence of transient temperature on degradation rates. Hydrolysis rate is increased up to $\mu_{max,R1} = 5.0 \times 10^{-6}\,\mathrm{s}^{-1}$ and for influence of moisture $f_{w,set1}$ is used. Two variants with different heat conductivity of the solid phase are compared. Conductivity is chosen to $\lambda_{s,1} = 0.15\,\mathrm{W/(m \cdot K)}$ in variant 1 and to $\lambda_{s,2} = 1.0\,\mathrm{W/(m \cdot K)}$ in variant 2.

Figure 7.27 shows the organic density in A and B. Due to the higher maximum reaction rate, degradation proceeds much faster initially than observed in the previous analyses. After 30 % of organic matter are decomposed, degradation stops almost completely as visible from the graphs in figure 7.27. From the evolution of temperature in A and B in figure 7.28, it is obvious that the stop of degradation is due to the quick temperature rise up to $\Theta = 80\,^{\circ}\mathrm{C}$ in B. At this temperature, the value of the temperature function becomes $f_{\Theta} \approx 0$. Temperature is high in the center and approaches the outer temperature of $\Theta = 20\,^{\circ}\mathrm{C}$ mainly because of thermal conduction, figures 7.29 (a) and (b). While heat is more and more transported to the outside, temperature slightly decreases to about 70 °C. Conditions for degradation improve again, compare also figure 3.6, and more organic matter is degraded as shown in figure 7.27. An equilibrium stage is reached and temperature is maintained at this level for about 15 years.

At the surface node A, degradation proceeds more uniformly due to the constantly lower temperature. Hence, no sudden stop of degradation is observed close to the surface.

Settlements differ mainly in the interim stage between 10 years and 20 years whereas the final compaction is similar to the isothermal analysis, see figure 7.30. Temperature rise is supposed to be overestimated by the model considering the temperature measurements on site by Mora Naranjo [170]. The overheating is a combined effect of maximum degradation rate, the function for temperature influence on degradation rates and the heat conductivity of the waste mixture.

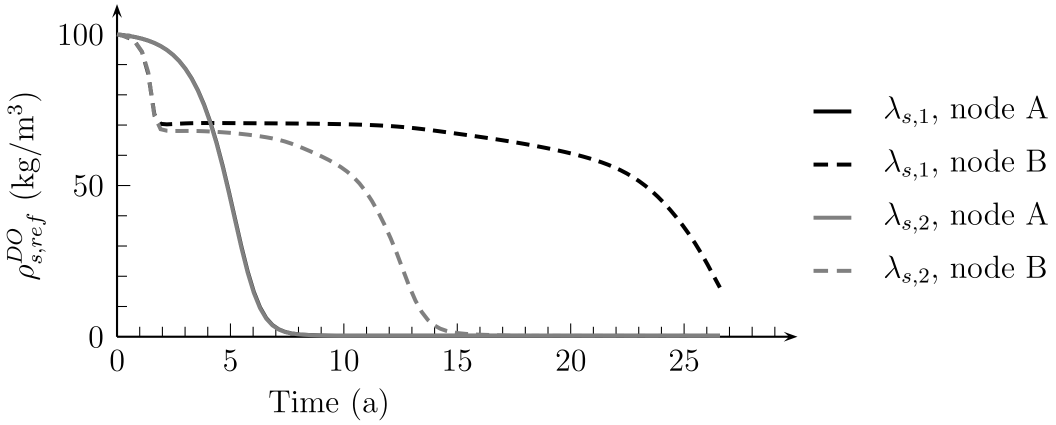

Figure 7.27: Partial density of organic matter at different nodes as influenced by heat generation. The density evolutions at node A coincide.

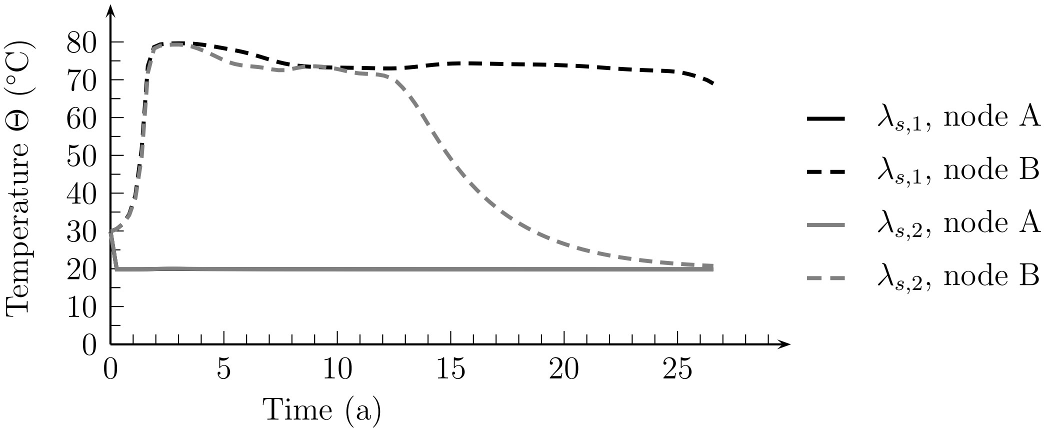

Figure 7.28: Temperature at different nodes for the two variants. The temperature evolutions at node A coincide.

The contour plots of temperature at different times in figure 7.29 show that increased heat is present over a broader area of the landfill for the material with lower heat conductivity. The example shows that the model may describe the temperature evolution in landfills but it is of high importance that reliable data on heat conductivity and degradation rates is available.

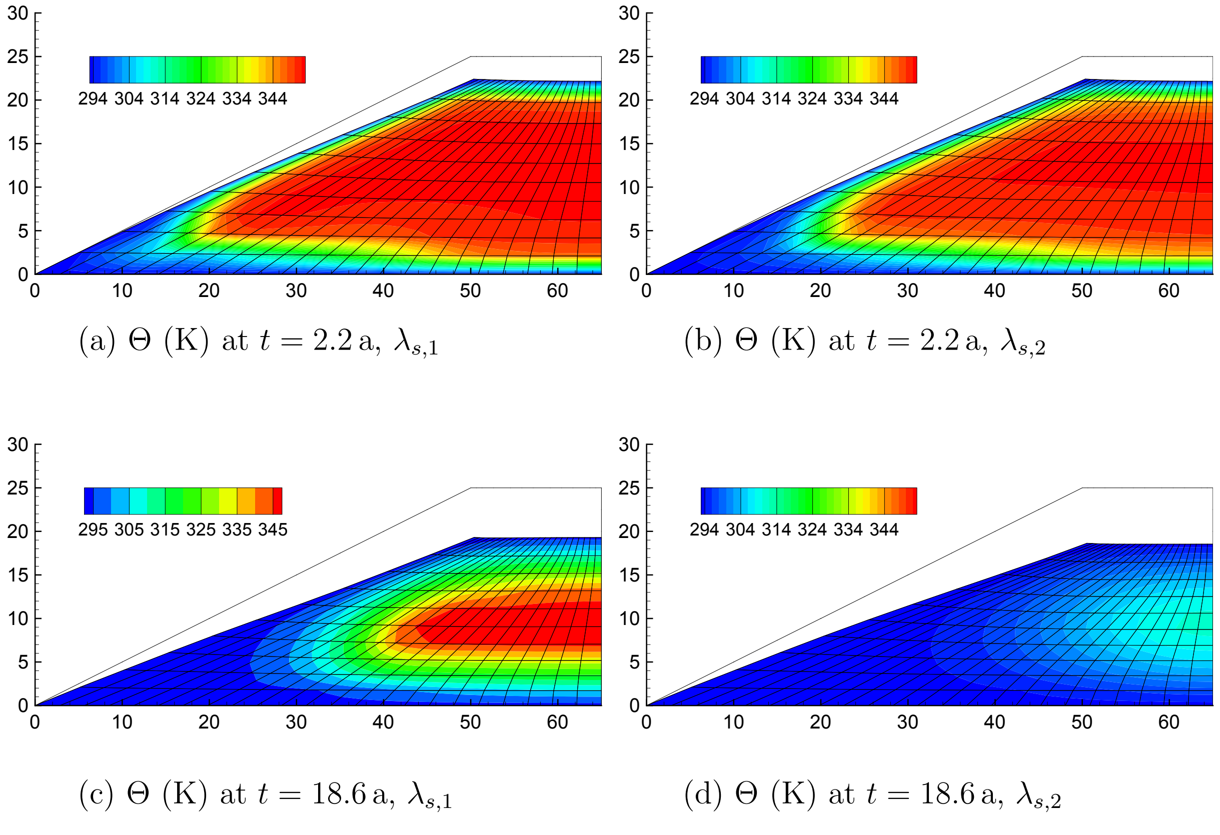

(a) Θ (K) at $t = 2.2\,\mathrm{a}$, $\lambda_{s,1}$

(b) Θ (K) at $t = 2.2\,\mathrm{a}$, $\lambda_{s,2}$

(c) Θ (K) at $t = 18.6\,\mathrm{a}$, $\lambda_{s,1}$

(d) Θ (K) at $t = 18.6\,\mathrm{a}$, $\lambda_{s,2}$

Figure 7.29: Contour plots of temperatures at different times for two solid heat conductivities, $\lambda_{s,1}$ and $\lambda_{s,2}$

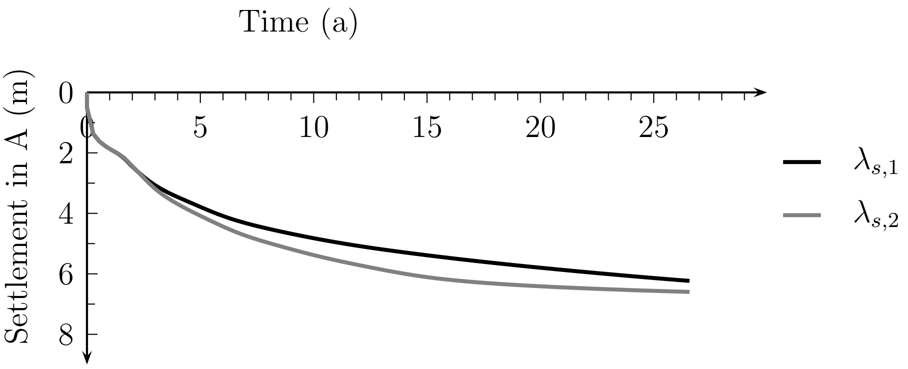

Figure 7.30: Time-settlement curves of node A for two different variants with $\lambda_{s,1}$ and $\lambda_{s,2}$

7.3.2 Simulation of a Gas Extraction System

Along with the anaerobic biological degradation of organic matter, landfill gas is produced. It is composed of carbon dioxide and methane mainly. The landfill gas can be collected and flared or, if possible, utilised in a gas engine to generate power. Simultaneously, harmful impacts on climate are reduced. A crucial point is usually the estimation of gas volume and its composition. If the fraction of the originary landfill gas is too low, the engine cannot be run effectively. Hence, tools for designing landfill gas extraction systems are of avail for landfill operators.

With the description of a horizontal gas collection system, this example shows a corresponding application of the proposed model. An inner Cauchy boundary condition is used to describe an active gas extraction. It is asssumed that the extraction pipe is placed exactly horizontally as shown in figure 7.31, whereas, in practice the pipes would be emplaced with a slight slope to separate condensate. The analysis is performed for an initial organic matter content of 20 %.

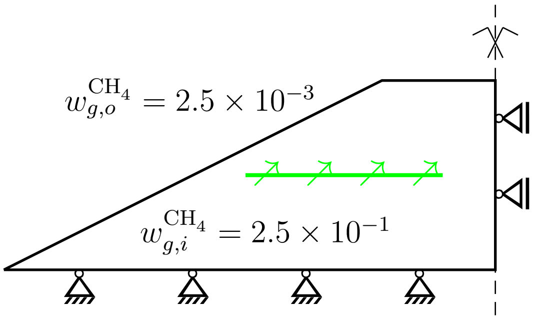

Description of a horizontal
gas extraction system
with an inner Cauchy boundary

$K_{h,o} = K_{v,o} = 1 \times 10^{-10}\,\mathrm{m}^2$

$p_{g,o,1} = p_{atm} - 50\,\mathrm{mbar}$

$p_{g,o,2} = p_{atm} - 20\,\mathrm{mbar}$

Figure 7.31: Description of a horizontal gas extraction system within the landfill

The gas phase of the developed model comprises only carbon dioxide, methane and vapour as components. To distinguish the air within the landfill from the outer air initially, the mass fraction of methane is set to a very low value of 2.5×10^{-3} outside the landfill whereas it is high within the landfill. The intended purpose is to have an indicator on whether air from outside is sucked into the landfill body. When operating an active gas extraction system this is ususally tried to avoide. The soaking of extraneous air might lead to aerobic conditions so that less methane is produced and the effectiveness of the engine is reduced. Hence, a low applied vacuum is usually chosen. It should, however, be of such magnitude that as less landfill gas as possible leaves the landfill body by diffuse emissions over the surface. In [180] a maximum suction of 200 mbar is given, whereas in [205] a suction of 50 mbar is used. Two cases with $p_{g,o,1} = 50\,\mathrm{mbar}$ and $p_{g,o,2} = 20\,\mathrm{mbar}$ are compared in the simulations. The permeability of the waste is $K_h = 1 \times 10^{-12}\,\mathrm{m}^2$ and $K_v = 1 \times 10^{-13}\,\mathrm{m}^2$ in this example. At $t = 2.2\,\mathrm{years} = t_E$ the extraction system is activated. The simulations are performed under isothermal conditions at $\Theta = 303\,\mathrm{K}$ to ensure uniform degradation. For case $p_{g,o,1}$ two variants are compared to analyse the influence of deformation on gas flow. Variant 1 assumes $\kappa_\phi = 1.0$ in (4.10), whereas variant 2 assumes $\kappa_\phi = 10.0$ implying a higher decrease in permeability in variant 2 due to compaction.

Figure 7.32 (a)-(d) show the spatial distribution of gas pressure for the two variants. At 0.5 h after activation of gas collection, the effect of gas extraction is already visible from the negative pressure close to the extraction pipe in figure 7.32 (a) and (b). The vacuum propagates faster for $\kappa_\phi = 1$ due to the higher permeability upon deformation. After 33 h a larger area of the landfill cross section is under negative pressure, compare figures 7.32, (c) and (d). In the center zone, the pressure is lower over a larger area in case of $\kappa_\phi = 1$.

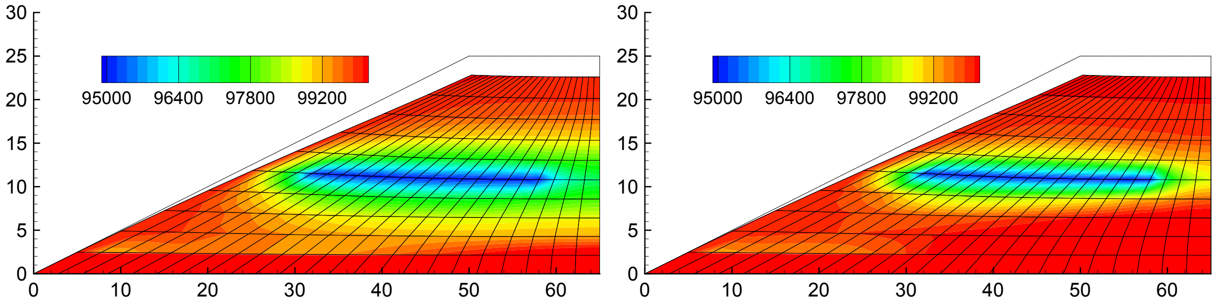

(a) p_g (Pa) at $t = t_E + 0.5\,\text{h},\ \kappa_\phi = 1.0$ (b) p_g (Pa) at $t = t_E + 0.5\,\text{h},\ \kappa_\phi = 10.0$

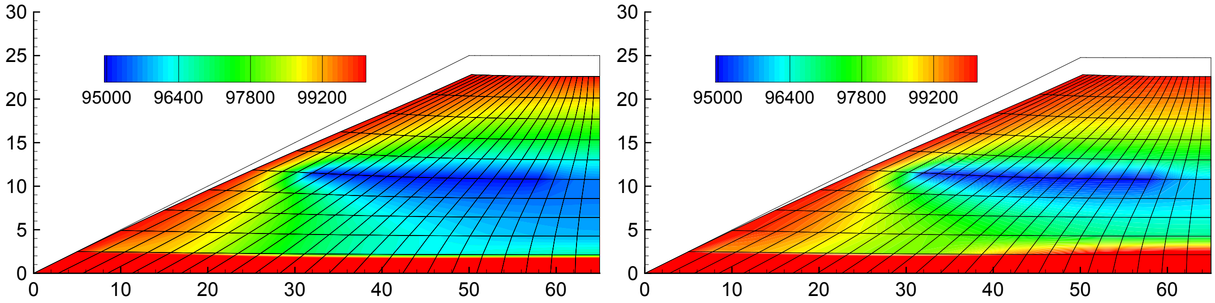

(c) p_g (Pa) at $t = t_E + 33\,\text{h},\ \kappa_\phi = 1.0$ (d) p_g (Pa) at $t = t_E + 33\,\text{h},\ \kappa_\phi = 10.0$

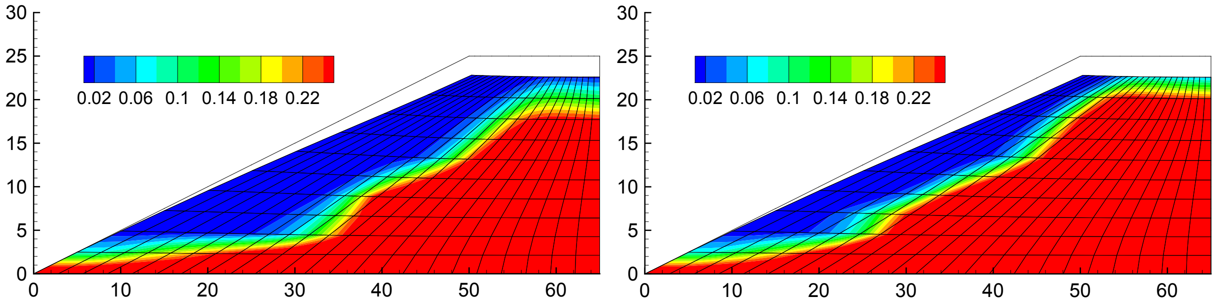

(e) $w_g^{\text{CH}_4}$ (-) at $t = t_E + 33\,\text{h},\ \kappa_\phi = 1.0$ (f) $w_g^{\text{CH}_4}$ (-) at $t = t_E + 33\,\text{h},\ \kappa_\phi = 10.0$

Figure 7.32: Contour plots of gas pressure and methane fraction at different times after initiation of gas extraction. Influence of deformation for $p_{g,o,1} = p_{atm} - 50\,\text{mbar}$ by comparing analyses with $\kappa_\phi = 1.0$ and $\kappa_\phi = 10.0$

The contour plots of methane fraction in figure 7.32 (e) and (f) show that air is sucked in from outside and that it has infiltrated deeper into the landfill for the case with higher permeability $\kappa_\phi = 1$ than for $\kappa_\phi = 10$ after 33 h. The figures also show that the extraneous air spreads faster in horizontal than in vertical direction due to the higher horizontal permeability.

Figure 7.33 compares the cumulative outflux of gas over the entire simulation period of 27 years for the analysed variants.

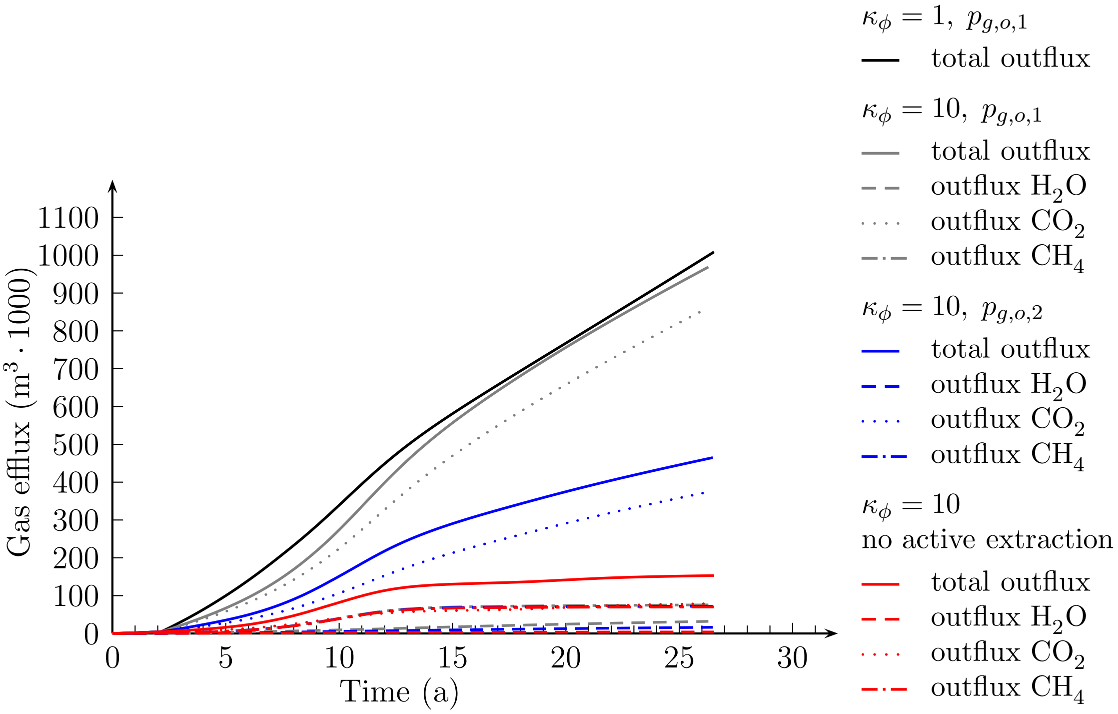

Figure 7.33: Comparison of efflux of gas. Gas volumes are determined for a temperature of $\Theta = 303$ K

For $p_{g,o,1}$ about 1×10^6 m^3 gas are extracted after 27 years. In MUV [180] extracted gas volumes up to 5.5×10^5 m^3 *per year* for the entire landfill are reported, so the results are within a realistic range. In case of $p_{g,o,2}$ the extracted volume is accordingly less.

In case of $p_{g,o,1}$ only less than 10 % of the collected gas is methane. The reason for not obtaining a ratio close to the typical ratio of 60 % to 40 % is the limited gas composition that can be described by the model. The extraction is switched on after 2.2 years. As shown in figures 7.32 (e) and (f) outer air is sucked in. This air has a low methane content and thus a high CO_2 content. The outer air affects the composition of the extracted gas volumes in the observed manner. This is proven by analysing case $p_{g,o,2}$. The extracted volume of methane is nearly the same, but the volume of CO_2 has considerably decreased, it is less than 50 % as in the case with 50 mbar of suction. A comparative analysis without an inner gas extraction system gives ratios of about 50 % of methane and 50 % of carbon dioxide. From the obtained gas production curve it is obvious that gas production is strongly related to degradation. Settlements ad degradation of organic matter proceed analogously to the first example in case of 20 % organic matter, see figures 7.20 and 7.21. It is concluded that in further extensions of the model additional gas components to describe ambient air, i.e. nitrogen and oxygen, may be included. Additionally, the degradation model may be supplemented by an aerobic pathway. Then, such an example can be described more realistically. Furthermore, the model could be applied to describe aerobic degradation from artifical aeration. The effect of deformation on hydraulic parameters is relatively low in this example, but nevertheless it is concluded that this influence has to be kept in long-term modelling of landfills, as the influence may vary as the cases arises. As porosity is related to density, also the change of permeability due to change in solid mass is considered, e.g. biofilm growth.

7.3.3 Modelling of an Infiltration Layer

Sufficient moisture content is essential to provide optimum conditions for biological activity. Therefore, on some landfill sites methods are applied which aim at enhancing moisture content to accelerate degradation. For example, collected leachate may be recirculated. The objective is to achieve a stable inert state of the disposed waste as soon as possible. This reduces monitoring effort and shortens landfill aftercare phase.

In the present example, a horizontal infiltration layer inside the landfill is described. Similarly to modelling the gas extraction system, a Cauchy boundary condition is set within the landfill. The liquid pressure outside the landfill $p_{l,o}$, which is needed for the Cauchy boundary condition, is set to a pressure of 150 mbar above atmospheric pressure. Depending on the inner landfill pressure, a pressure gradient evolves which induces a liquid flux into the waste. Like the Cauchy boundary condition for gas extraction, the boundary condition for infiltration is set at the boundaries of finite elements. This corresponds to the centers of a horizontal row of boxes.

The Cauchy boundary condition is again preferred here to a fixed flux by a Neumann condition, as it takes the inner, transient state into account. A fixed volume flux has to be set carefully with respect to porosity and permeability of the material, ensuring that the flux is physically possible.

The saturation outside the inner boundary is set to $S_{l,o} = 0.99$ so that mainly liquid flux, but also a very low gas flux is present. This avoids the problem of obtaining gas saturations which are too close to $S_g = 0.0$, compare the discussion of initial saturation when simulating the ALERT benchmark in section 7.1. The infiltration starts at $t = 2.2\,\text{years} = t_I$ and is deactivated after three weeks. The temperature of the infiltrating liquid is set to $\Theta_{l,o} = 293\,\text{K}$.

In total, five cases are investigated, their differences are shown by table 7.4. Case 1 is the basic case and discussed first. Organic matter content is 10 % in all cases.

Figure 7.35 (a) shows a contour plot of liquid saturation at 30 min after beginning of infiltration. The saturation is high at the bottom due to leachate that has percolated downwards in the 2.2 years before the infiltration and has not left the landfill body due to the low permeability of the mineral base liner.

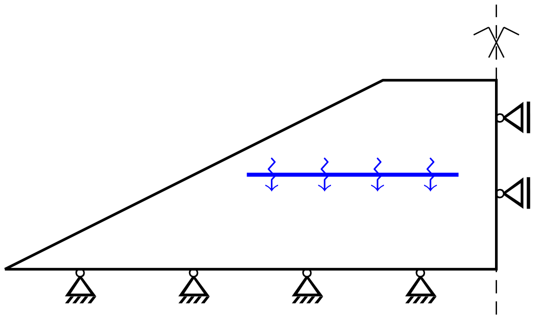

Modelling an infiltration layer
with an inner Cauchy boundary

$S_{l,o} = 0.99$

$K_{h,o} = K_{v,o} = 1 \times 10^{-10}\,\text{m}^2$

$\Theta_{l,o} = 293\,\text{K}$

$p_{l,o} = 1.15 \times 10^5\,\text{kPa}$

Figure 7.34: Description of a horizontal infiltration system within the landfill

Table 7.4: Analyed cases in infiltration example

	SWCC	κ_ϕ	$S_{l,0}$
Case 1	set 1	10.0	0.75
Case 2	set 1	1.0	0.75
Case 3	set 2	10.0	0.75
Case 4	set 1	10.0	0.25
Case 5	set 2	10.0	0.25

The SWCC sets refer to the data by Bente and McDougall [20] in table 4.1.

Furthermore, an area of high saturation has evolved around the infiltration layer. In the remainder zones of the landfill cross section, saturation is about $S_l = 0.7$, which is determined mainly by the water retention curve. After 20 d, saturation has remarkably increased up to almost full saturation in the landfill zone below the infiltration layer, fig. 7.35 (b). Correspondingly, liquid pressure evolves as shown in figures 7.35 (c) and (d). Pressure distribution below the infiltration layer is related to a waste column of about 10 m which is nearly saturated.

Figure 7.35 (e) shows the spatial distribution of temperature 30 min after infiltration is started. Right before infiltration, temperature has risen up to 80 °C in the landfill center. After liquid influx begins, the temperature decreases around the infiltration area because the inflowing liquid has a temperature of 293 K. After 20 d, 7.35 (f), a larger area with a temperature around 20 °C is present, whereas the temperature is higher in the landfill center.

The distribution of organic matter in figures 7.35 (g) and (h) indicates that under the influence of temperature best milieu conditions for degradation are created in a layer about 3 m away from the landfill surface in this example.

To show the immense effect of the water retention curve on the simulation results, in case 3 an SWCC that leads to a lower moisture retention capacity is used. Figure 7.36 compares saturations after 30 min and 20 d. Because of the lower moisture retention capacity, a higher amount of the initially stored liquid drains downwards and flows out of the landfill via the base liner, 7.36 (a) and (b). Thus, lowest saturation is about $S_l = 0.45$ whereas it is $S_l = 0.72$ in case 1. The increased loss in moisture is confirmed by cumulative water outflux vs. time in figure 7.37. In both cases, outflux rate decreases with time until infiltration starts. In case 1 an efflux of 40 m^3 is observed after 2.2 years whereas a volume of 100 m^3 is obtained in case 3. In a very short period after activation of infiltration the outflux increases. In case 1 a volume of 850 m^3 infiltrates into the landfill, in case 3 an influx of 560 m^3 is observed. The infiltrated liquid percolates downwards and leaves the landfill body with delay via the bottom liner and partly also the lateral boundary.

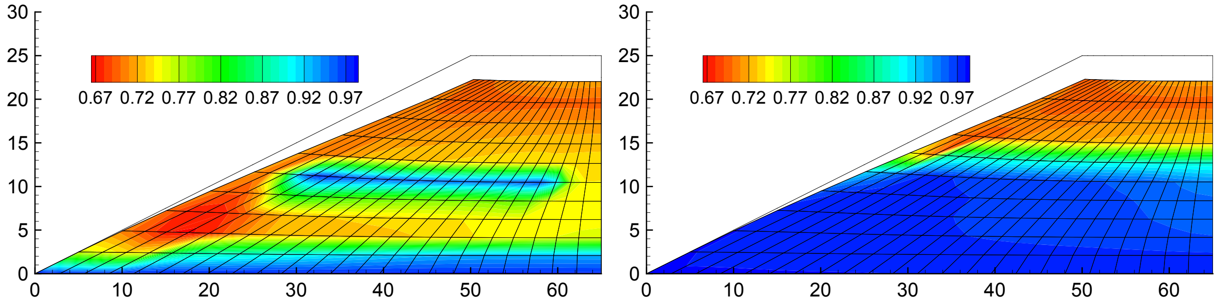

(a) S_l (-) at $t = t_I + 30\,\mathrm{min}$ (b) S_l (-) at $t = t_I + 20\,\mathrm{d}$

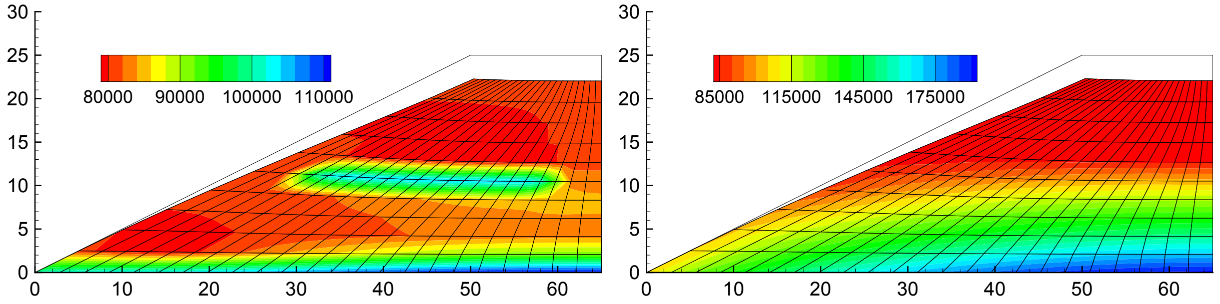

(c) p_l (kPa) at $t = t_I + 30\,\mathrm{min}$ (d) p_l (kPa) at $t = t_I + 20\,\mathrm{d}$

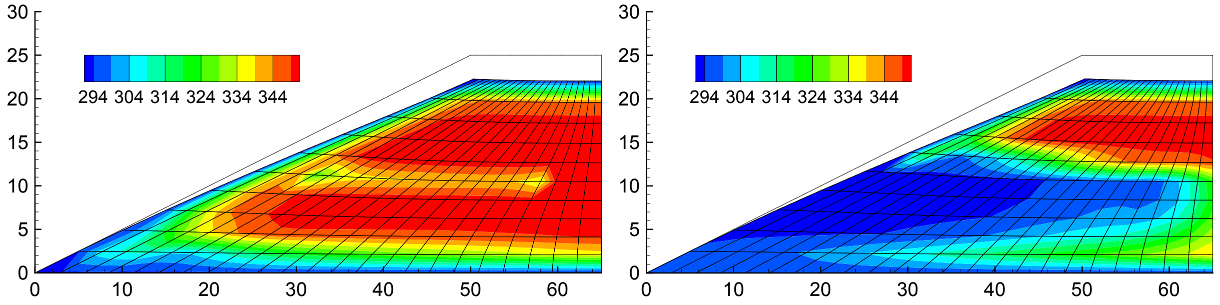

(e) Θ (K) at $t = t_I + 30\,\mathrm{min}$ (f) Θ (K) at $t = t_I + 20\,\mathrm{d}$

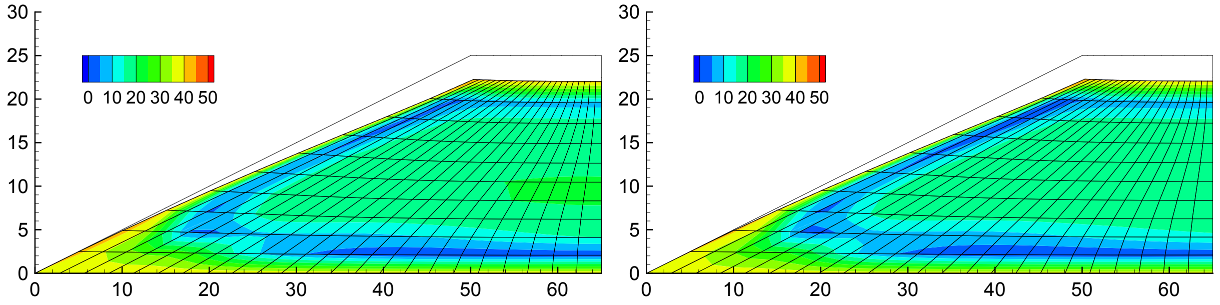

(g) $\rho^{DO}_{s,ref}$ (kg/m^3) at $t = t_I + 30\,\mathrm{min}$ (h) $\rho^{DO}_{s,ref}$ (kg/m^3) at $t = t_I + 20\,\mathrm{d}$

Figure 7.35: Comparison of different quantities for infiltration example. Contour plots at different times after activation of infiltration for case 1

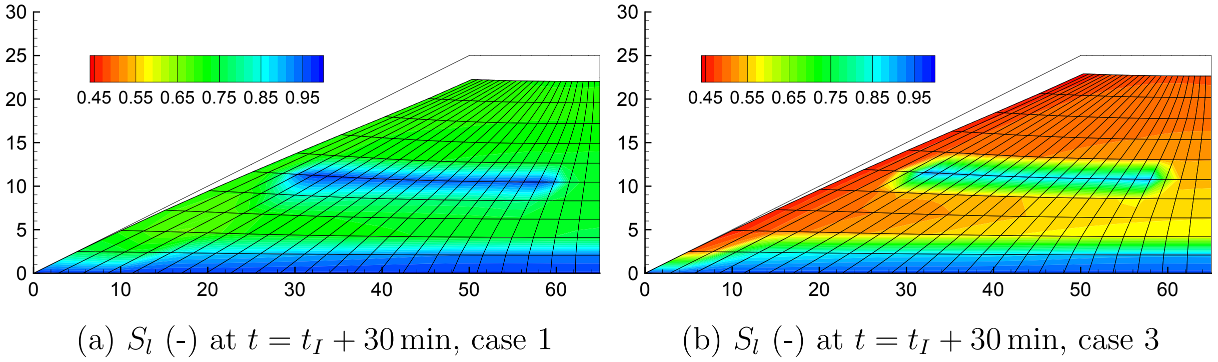

(a) S_l (-) at $t = t_I + 30\,\mathrm{min}$, case 1 (b) S_l (-) at $t = t_I + 30\,\mathrm{min}$, case 3

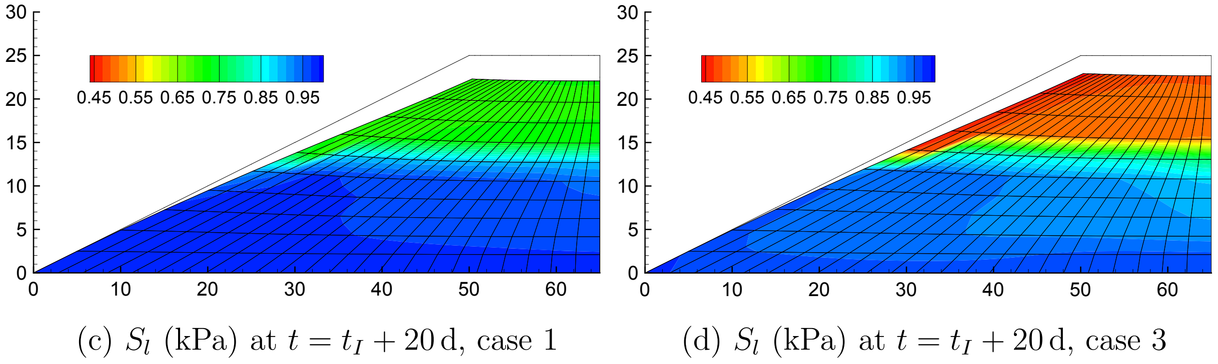

(c) S_l (kPa) at $t = t_I + 20\,\mathrm{d}$, case 1 (d) S_l (kPa) at $t = t_I + 20\,\mathrm{d}$, case 3

Figure 7.36: Comparison of saturation for two cases of SWCCs, case 1 and case 3

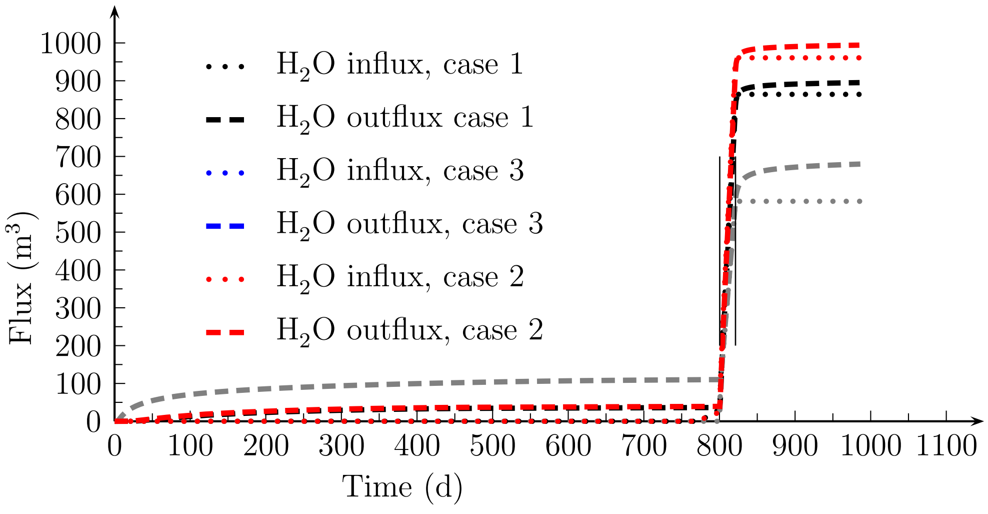

Figure 7.37: Comparison of outflux and influx of water over Cauchy boundaries for case 1, case 2, and case 3

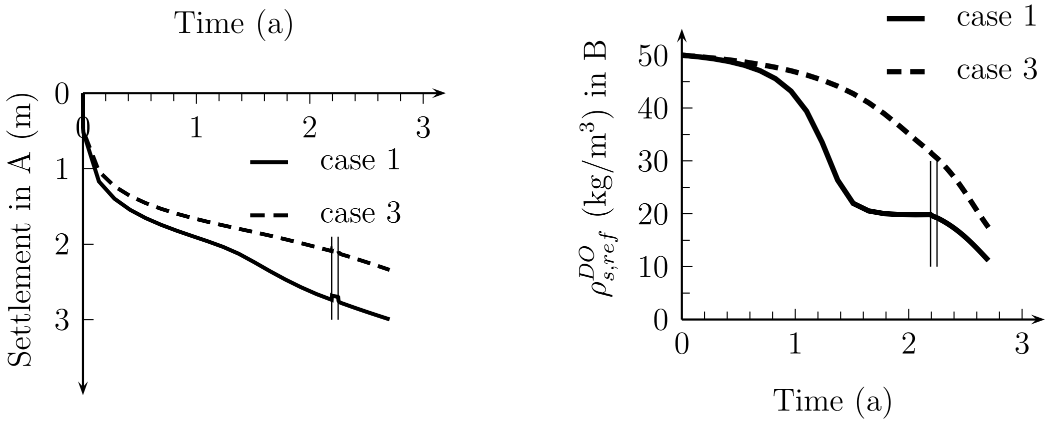

(a) Comparison of settlements

(b) Comparison of partial density of organic matter

Figure 7.38: Comparison of degradation and settlements in description of an infiltration system using two different SWCCs. In case 1 the SWCC implies a higher moisture retention capacity compared to case 3

Furthermore, the influence of deformation on permeability is investigated by comparing case 1 and case 2. In the beginning, almost no difference in ouflux is observable in figure 7.37. But more liquid is able to infiltrate the waste due to its higher permeability in case 2. The final relation between efflux and influx is equal in both cases.
Figure 7.38 shows the evolution of settlemens and density of organic matter for case 1 and case 3. The difference in settlements are influenced by different degradation rates and by the reduced moisture content which reduces the self-weight of the material. Degradation rate is higher in case 1 but then decreased due to temperature rise. While temperature is reduced, degradation rate increases again. In case 3 the heat generation rate and the rate with which heat is transported to the boundary are more attuned. So, the temperature rise and the sudden stop in degradation do not occur in the simulation. The uplift within the infiltration phase is attributed to pressure increase.

Case 4 and case 5 show the influence of moisture enhancement on degradation. First, the initial saturation is set to a low value of $S_l = 0.25$ describing relatively dry conditions. Like for case 1 and case 3, two moisture retention curves are compared. Figure 7.39 (a) shows that until beginning of infiltration the time-settlement curves are equal in case 4 and case 5. Any difference does not occur yet as in case 1 and case 3. Because of the initially very low moisture content the relative permeability of liquid is very low and, thus, nearly no liquid flows out of the landfill body. Due to the very low water content, the value of fw is nearly zero initially which inactivates degradation, see figure 7.39 (b). As infiltration starts, saturation at the inner node B increases rapidly up to almost full saturation, see figure 7.39 (c). Then, degradation is initiated due to increasing moisture. As in the previous non-isothermal examples, temperature rise limits degradation. Decomposition proceeds faster in case of higher moisture retention capacity of the waste in case 4 as less moisture drains downwards.

The application shows that the model may be applied to design infiltration systems, for example with respect to infiltration rate or distance of infiltration pipes. A prerequisite is, that sufficient data on moisture retention capacity of the waste and on permeability is available. If description of degradation is included, reaction rates have to be known. Special focus has to be laid on the influence functions for the effect of moisture content on biological activity.

Further analyses may provide an in-depths understanding of the overheating induced by the degradation in the simulations. It is assumed that degradation in reality proceeds more uniformly, for exact conclusions tests on site are necessary including temperature measurement. With respect to the active infiltration at landfills, site tests may also include distributed measurement of moisture content, see for example Clément et al. [40]. Within SFB 477, a project carried out at the Institut of Biochemical Engineering focuses on corresponding measurement techniques, Fischer [80].

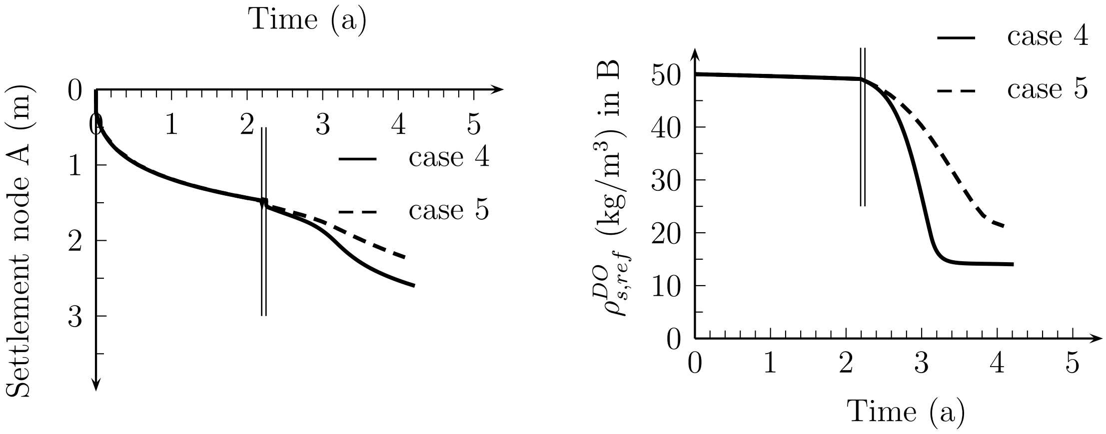

(a) Comparison of settlements

(b) Comparison of organic matter

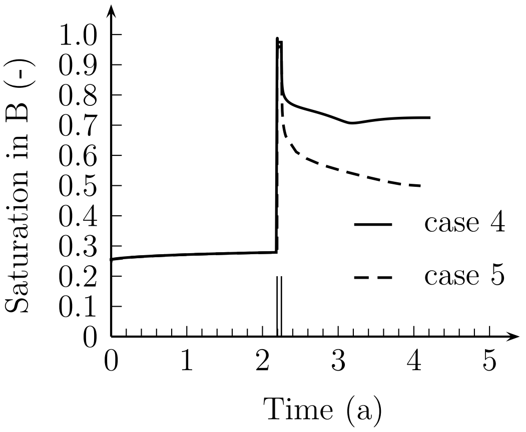

(c) Comparison of saturation

Figure 7.39: Comparison of settlement in A, organic matter and saturation in B for cases 4 and 5. The two thin lines mark the infiltration interval of 3 weeks

7.3.4 Landfill with Inhomogeneous Density Distribution

The last subsection shows two examples with an initially heterogeneous dry density distribution. Spatially varying densities are present on site due to fluctuations in the disposed waste material or due to different compaction impact in landfill infilling history. Furthermore, during landfill operation emplaced waste is sometimes moved to other parts of the landfill which may induce variations in density as well. For pratical applications

Inhomogeneous Organic Matter Content In the first example, density of organic matter is varied randomly in the range from 100 kg/m^3 to 120 kg/m^3, whereas an overall solid bulk density of 500 kg/m^3 is maintained. An isothermal analysis at $\Theta = 303\,\mathrm{K}$ (case 1) is compared with a non-isothermal variant (case 2). The temperature functions $f_{\Theta,\,set2}$ are used, which assume optimum conditions for hydrolysis around 293 K.
Figure 7.40 plots settlement and organic density vs. time. Degradation proceeds faster in the outer layer due to optimum temperatures. While organic matter is degraded quickly in node A, it is decomposed more slowly in node B, i.e. in the center, in the non-isothermal case. Degradation is deccelerated which influences settlement rate.

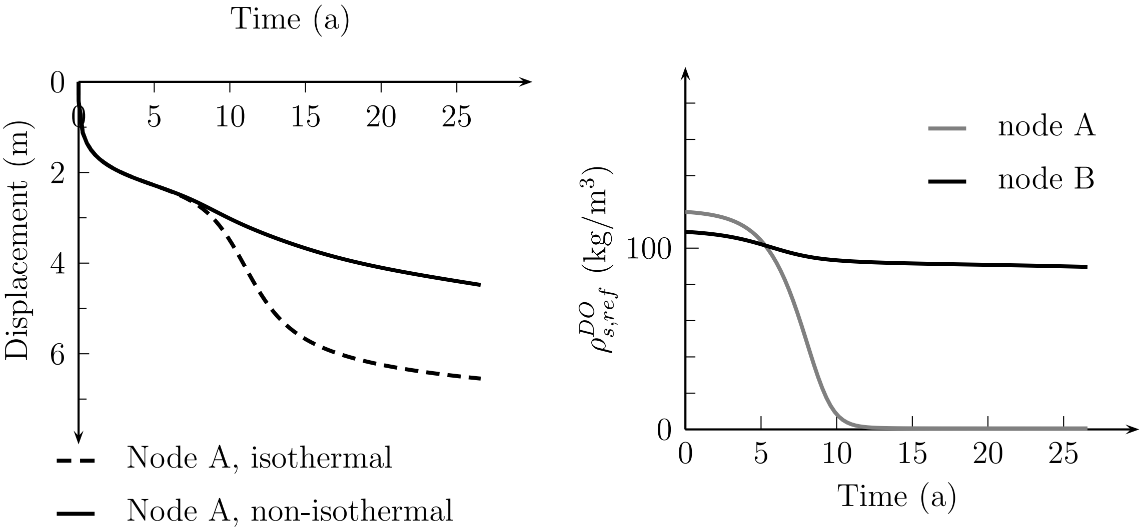

(a) Vertical displacement in node A
Comparison for case 1 and 2

(b) Partial density organic matter
in A and B for non-isothermal case

Figure 7.40: Influence of heat generation on degradation and settlements

Figure 7.41 (a) and (b) show the organic density w.r.t. the reference configuration after 2.2 years for the two cases. Spatial distributions are visibly equal. After 13.2 a (c) and (d) a relatively high fraction is decomposed in the isothermal case, on average 80 % of initial content. In the non-isothermal case, organic matter is hardly reduced until that time. Temperature distributions after 2.2 years and 13.2 years (e) and (f) show that the different behaviour is due to heat generation. As $\Theta = 303\,\mathrm{K} =$ const. in case 1 and $\Theta_o = 293\,\mathrm{K}$

in case 2 the densities $\rho_{s,ref}^{DO}$ at the landfill surface do not coincide. Temperature rises up to 52 °C, which is less than in the previous non-isothermal example. The reason is, that degradation stops already at lower temperatures due to the different parameter set for function f_Θ. The example confirms that maximum temperature in the waste is not only governed by the waste's heat conductivity but also by the applied temperature influence function f_Θ. Furthermore, the examples shows that the model is also applicable on landfills with a heterogeneous organic matter content. For practical applications, however, convergence properties should be improved by using finer meshes, for which a parallel code is supposed to be necessary.

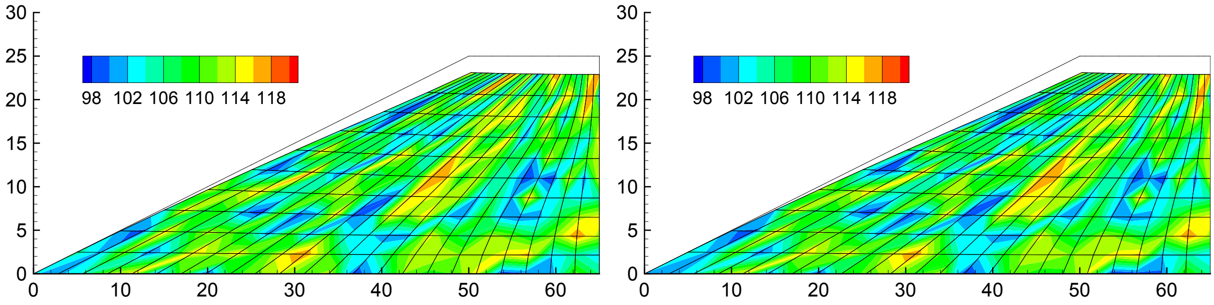

(a) $\rho_{s,ref}^{DO}$ (kg/m^3), isothermal, 2.2 a (b) $\rho_{s,ref}^{DO}$ (kg/m^3), non-isothermal, 2.2 a

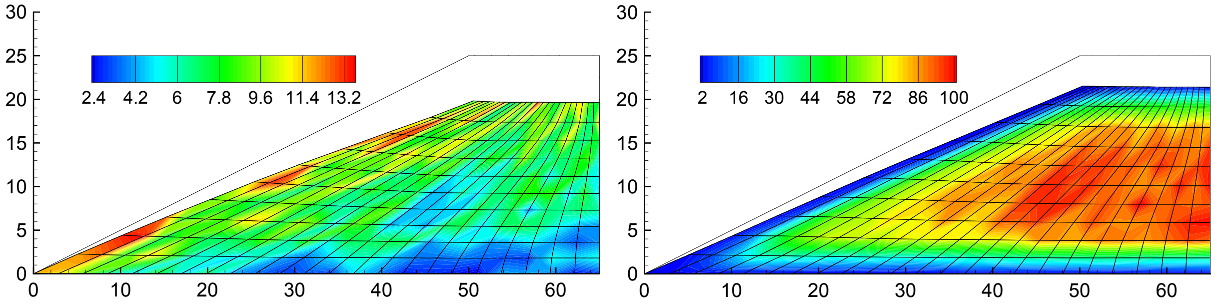

(c) $\rho_{s,ref}^{DO}$ (kg/m^3), isothermal, 13.2 a (d) $\rho_{s,ref}^{DO}$ (kg/m^3), non-isothermal, 13.2 a

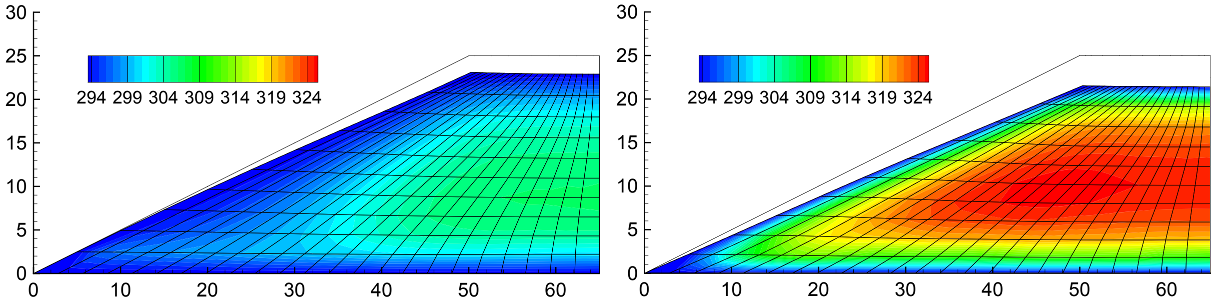

(e) Θ (K), non-isothermal 2.2 a (f) Θ (K), non-isothermal, 13.2 a

Figure 7.41: Comparison of organic matter content and temperature for isothermal and non-isothermal case at different times

Inhomogeneous Solid Density In the second example, the total solid density varies over the entire landfill cross section initially. Thereby, biomass ρ_s^X is varied between $10\,\mathrm{kg/m^3}$ and $20\,\mathrm{kg/m^3}$, organic matter ρ_s^{DO} varies from $100\,\mathrm{kg/m^3}$ to $140\,\mathrm{kg/m^3}$, and inert matter ρ_s^{IM} varies from $400\,\mathrm{kg/m^3}$ to $500\,\mathrm{kg/m^3}$. The density values are created using random numbers in the considered ranges. Degradation rates are low in this example to notice if and how the density variation is retained during the process of deformation. To increase settlement rate a higher maximum density of $\rho_{max} = 1200\,\mathrm{kg/m^3}$ is chosen in the compaction model.

Figure 7.42 (a) shows the initial variation of solid dry density. The contour plot of vertical stress in the basic matrix in (c) shows that the differences in density are counterbalanced in this case so that a quite uniform pattern of stress distribution is obtained in the beginning. After 27 years variations in stress are present caused by differences in density. Density variation after 27 years is shown in figure 7.42 (e). The initial pattern of variation has approached the typical pattern observable in the previous examples, e.g. figure 7.23. The density increases from top to bottom of the landfill. Local differences in settlements are obvious from the contour plot of inelastic Almansi strain in (g). The lower the local initial density, the higher the local deformation, compare figure 7.42 (b) and (h).

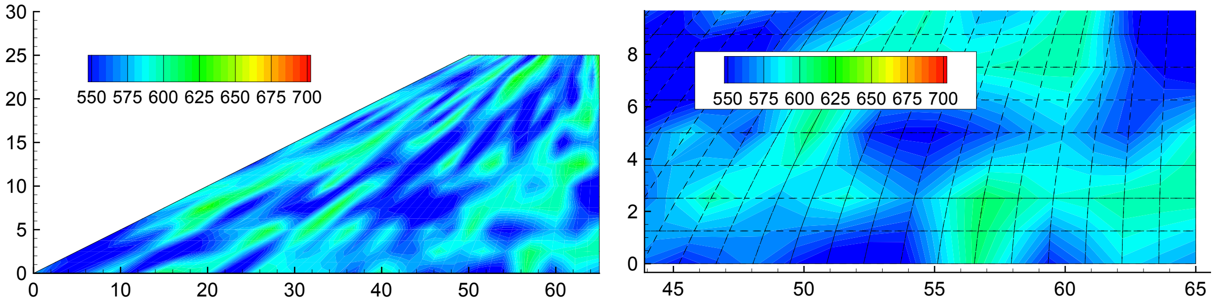

(a) ρ_s (kg/m^3), initially

(b) ρ_s (kg/m^3), initially, detail

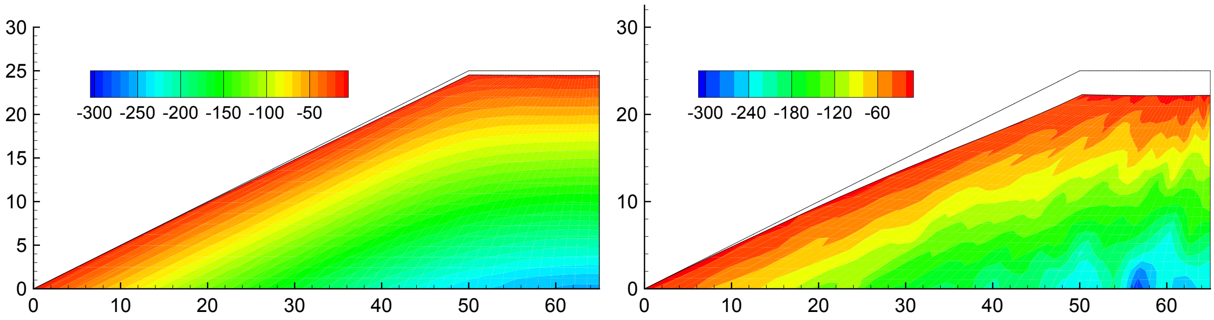

(c) σ^B_{zz} (kPa), after loading

(d) σ^B_{zz} (kPa) at $t = 27\,\mathrm{a}$

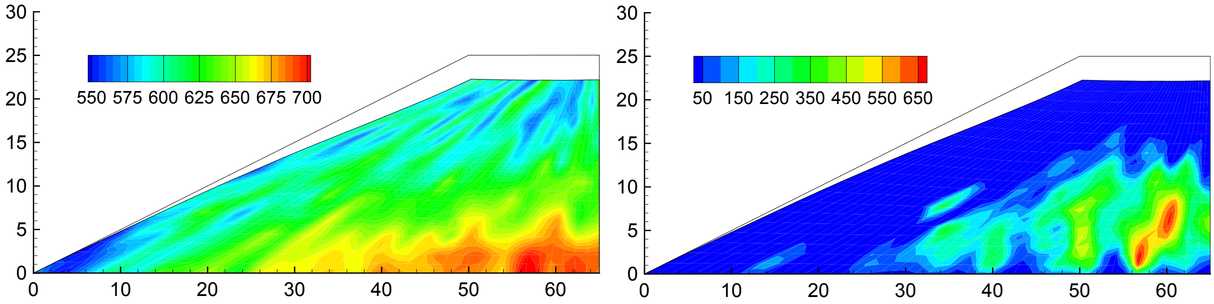

(e) ρ_s (kg/m^3) at $t = 27\,\mathrm{a}$

(f) σ^F_{xx} (kg/m^3) at $t = 27\,\mathrm{a}$

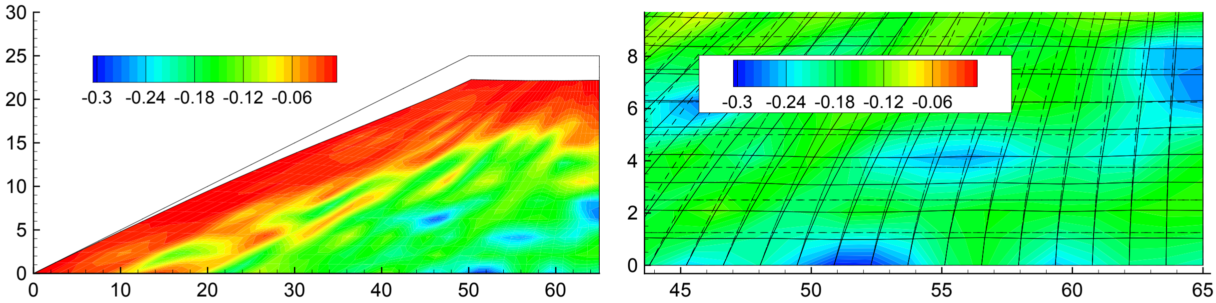

(g) $\mathrm{A}^B_{in,zz}$ (-) at $t = 27\,\mathrm{a}$

(h) $\mathrm{A}^B_{in,zz}$ (-) at $t = 27\,\mathrm{a}$, detail

Figure 7.42: Comparison of contour plots of density, stress and strain for initially heterogeneous dry solid bulk density

7.4 Discussion and Outlook

Landfill models of different levels of complexity have been developed so far. Some models consider the entire landfill as a control volume over which fluxes are balanced (sometimes termed *Black-Box models*). Other models resolve the landfill spatially by layers or elements. A trend to the latter type of models is observable and also the advantages of models that are able to describe the complex interactions in landfills are recognised, especially with respect to long-term prognoses. Advanced numerical landfill modelling has reached a broad acceptance in the international research community, which is shown by the number of responses to the HPM2 modelling challenge presented in [14]. There is, however, not the same level of acceptance of such models in engineering practice yet, although encouraging examples exist, e.g. the applications by Ricken et al. [200], Lopez et al. [146] and Martinez et al. [154]. A major cause is supposed to be the models' complexity that requires an extensive experimental effort to determine the increased number of input parameters.

Some parameters do not coincide with physical quantities that are determinable directly by laboratory experiments or usually measured on site. Thus, results of simulations are fitted against available monitoring data. The parameter set can be obtained by comparing simulations using different sets, or, more systematically, by methods like genetic algorithms and Monte Carlo simulations. Even if the fitting succeeds, it needs to be discussed if the obtained parameter set is unique, or if another parameter set could describe the experimental results similarly.

Regarding the proposed model, the simulations show that degradation processes govern landfill behaviour considerably. They influence composition of gas and leachate and have a significant effect on magnitude of settlements. The time-dependency of degradation is influenced by degradation rate. To describe, for example, a measured time-dependent gas production curve, biomass concentration, the kinetics' constants or the functions for influence of environmental conditions could be modified. The results may coincide in a short term but not if the milieu conditions of the landfill change in the long term. A quantity which is difficult to determine in particular is the biomass concentration. It is usually not possible to measure an overall biomass concentration in a waste sample or a leachate sample, which, however, would be essential for model validation, due to its high sensitivity to biomass concentration. Furthermore, experiments show that biological activity is very sensitive to heat generation, which requires determination of thermal conductivity of the waste or site measurements of temperature. If heat generation rate is higher than heat flux, the overheating of the landfill body may inhibit degradation totally. Further parameter studies are required to analyse this effect in detail. Hence, a comprehensive experimental programme that includes site measurements and laboratory tests is required to provide sufficient data for model validation.

The need of model validation against long-term site data is recognised by Elagroudy et al. [70] in a comparison of settlement models. The authors show that the different empirical models might diverge especially in the long term, although they all simulate the measured data in a short term sufficiently and similarly, compare figure 5.3. The authors find that slight variations in parameters may influence results considerably which is confirmed by own experiences. For gas generation models, analogous observations exist. Even quite simple models with a low number of parameters might differ considerably as shown by Scharff and Jacobs [209] who compare six models for estimating methane emissions of landfills and give recommendations on both model documentation and application. They emphasise that difficulties arise already from different waste categories used in specific countries and models. A common waste classification system, as discussed by Dixon and Jones [52] or Lamborn [138], would facilitate comparison of models. Scharff and Jacobs conclude that further validation using data of more landfills is necessary. Similarly, Thompson et al. [227] stress the fact that there is insufficient validation of methane generation models against recovery data. They compare methane generation estimates by six models with recovery rates from 35 Canadian landfills. Although the models' phenomenological approaches differ only slighty, the results differ considerably. Mean relative error is in the range between $-89\,\%$ and $+578\,\%$. Main conclusions are that site-specific data has to be used to enhance model accuracy and that further research on degradation rates is necessary.

In addition to comparison of modelling results with site data, model intercomparison using equal applications is considered being very important. New insights are given by challenges like the HPM2 challenge, Beaven et al. [16]. Currently, a new modelling challenge is organised with the aim of describing the behaviour of a landfill cell, Beaven [15]. Furthermore, it may be suggested to set up a benchmark in which parameters are more restricted, so that results of different models are better comparable. Then, the effects of different numerical and constitutive approaches are more easily detectable. Thereby, it is recommended to fix as many parameters as possbile a priori, at least for a basic benchmark case. In the HPM2 challenge, for instance, it was up to the modellers to estimate organic fractions and rates. A more restricted benchmark could define kinetic constants and initial values for organic matter content a priori.

Organised groups of model developers are excellent platforms for bringing together knowledge and experience on modelling. As such, the International Water Assosciation IWA has established several task groups, like the anaerobic digestion modelling taskgroup, the task group on mathematical modelling for design and operation of biological wastewater treatment, the IWAs specialist group on multiphase flow and transport in porous media or the task group on good modelling practice. Recently, the International Waste Working Group IWWG has set up a task group on Landfill Modelling LMTG, so that such an organised platform is now also available within the area of landfill modelling.

After validation of the proposed approach against site data, the model may be extended in different ways. Several options for model extension are summarised as follows:

- The modelling of active aeration of landfills to provide aerobic conditions may be included. To better describe such techniques, an aerobic degradation step may be implemented in the model. Then, the components of the gas phase have to be supplemented by oxygen and nitrogen.
- Based on experiments on moisture retention behaviour of waste the influence of compaction on the SWCC may be further analysed and included.
- An approach for considering the specific porosity structure in waste, including description of preferential flow, may be implemented.
- Analysis of waste within the view of unsaturated soil mechanics. The influence of suction on mechanical strength may be analysed and the use of classical geotechnical concepts in their application on municipal solid waste may be discussed.
- Systematical methods for developing a reduced degradation model may be applied. For instance, a modal analysis could be used as applied within the ILDM method (Intrinsic Low-Dimensional Manifolds in Composition Space, Maas and Pope [150]). Model reduction should be performed with respect to improvement of pH modelling.
- Methods for inverse modelling may be developed to conclude from site data on the state of the landfill.
- Landfills are constructed over considerably long periods of time, usually in the range of decades. If the construction process of a landfill shall be described by a model, it is necessary to describe the infilling process. Alternatively, sampling by drilling may provide the required data to set initial conditions.
- The model's scope may be modified and extended in accordance with quantities that are measured on site.

Table 7.5: Summary of monitoring regulation according to the German landfill act[1], Appendix 5

	Frequency	
Measurement	Operation	Aftercare
Meteorological data		
Precipitation	daily	
Temperature	daily	monthly mean
Wind data	daily	-
Evaporation	daily	
Emissions		
Leachate amount	daily	half-yearly
Leachate composition	quarterly	half-yearly
Collected gas amount	daily	weekly
Gas composition	monthly	half-yearly
Effectiveness gas extraction	half-yearly	
Odourous emissions	in case of odour nuisance	
Ground water		
Ground water level	half-yearly	
Composition	quarterly	half-yearly
Other site data		
Settlements	yearly	
Stability analyses	yearly	
Structure and composition of landfill body	yearly	-
Lining systems		
Deformation of base liner	yearly	
Sewer camera inspection	yearly	
Temperature in liner	site specific	
Control of surface liner	yearly	
Control of sealings	quarterly	

Recommendations on Landfill Monitoring The findings from model development and from the simulations are used in the following to give recommendations for landfill monitoring. In Germany, the monitoring of landfills is currently regularised by the new German landfill act[1]. Appendix 5 gives detailed instructions for operation of landfills, its documentation and landfill monitoring. For instance, a site diary with important landfill data must be kept. The delivered waste has to be classified, and location, date and way of emplacement have to be recorded. A waste cadastre is required with a maximum grid size of 2500 m^2 for heterogeneous waste. Yearly reports on landfill behaviour have to be prepared. Table 7.5 summarises the monitoring guidelines and shows that detailed regulations already exist. In addition to the regulatory demand by law, it is essential

---

[1] Verordnung zur Vereinfachung des Deponierechts, BGBl. 2009 I, S. 900., 27. April 2009

to take into account the monitoring measures that are currently performed by landfill operators. Furthermore, landfill site data is essential to validate the model on site scale as seen from the discussion in the first part of this section. Hence, the Institute for Structural Analysis has established contact with a German landfill operator. The landfill "Wittorferfeld" in Neumünster was chosen because of the very good available data basis. The landfill operator provided comprehensive and well documented data on

- landfill geometry,
- waste amounts,
- leachate collections system,
- gas collection system,
- analysis of slope stability, and
- settlements.

A very interesting point of the landfill act is the requirement of keeping a waste cadastre on site. The simulations reveal that the waste composition, especially organic matter content, influences deformation and emission behaviour considerably. So, cadastre data may improve accuracy of simulations and predictions. However, it is recognised that the practicability on site may be limited. The simulations also reveal the influence of temperature on biological activity as assumed in the corresponding influence functions. Even if those functions are known correctly, the heat conductivity of the overall waste mixture has to be known as well. Thus, for model validation, it may be recommended to measure temperature on site. In fact, temperature probes were installed by the operator of Wittorferfeld but had been destroyed in the early years of operation by a lightning stroke. Temperature data on the landfill base is, however, available from the yearly camera inspection of the sewers. Temperature measurements are also performed in the shafts for leachate collection.

In addition to site measurements, shown on the example of the landfill Wittorferfeld, laboratory tests should be performed if the proposed model is applied. Table 7.6 lists experiments that are considered to be very important and practically feasible.

If an estimation of settlement rates is desired, it is recommended to perform oedometric tests with the material at different loadings to determine the parameters of the creep model. Slope failures are usually not expected if the slope inclination is low and the drainage system is working suffciently. If landfill volume shall be exploited to a higher extent by steeper slopes for a short term tests to assess fibrous cohesion may be performed, so that the effect can bei incorporated into slope stability assessment. Steep slopes should be avoided in the long term due to the influence of degradation or precipitation on fibres' strength.

If landfill operators follow the demand by the landfill act, comprehensive data for model validation is available, whereas some additional laboratory experiments are required. It is

Table 7.6: Recommendations on basic supplementary laboratory tests in addition to monitoring on site

Field	Comments
Prognosis of settlements	
Oedometric tests	For different loadings. In long term tests the control of degradable matter before and after experiment may be included.
Tensile tests	If interimly steep slopes are to be constructed or if stability of steep slopes have to be proved.
Transport processes	
Hydraulic conductivity	For different densities close to proctor density.
Unsaturated hydraulic conductivity	Determination of SWCCs, if possible for different densities. Supplementation by outflow experiments.
Degradation processes	
Degradability	Organic matter content, waste classification into readily, moderately and hardly degradable
Kinetics	Lysimeter experiments for estimation of rates

recommended that tests performed for application of models are planned in cooperation with model developers or organisations like the LMTG of IWWG.

8 Summary

Disposal of municipal solid waste (MSW) remains an important part of waste management systems worldwide. Landfills that have been constructed throughout the last decades are still present and require considerably monitoring effort. Prognoses of landfill long-term behaviour are of avail for planning of monitoring programmes, for the estimation of aftercare duration and for a safe subsequent utilisation of a landfill site. In addition to site measurements, numerical models can increase the prognoses' reliability. Therefore, approaches are required that consider the complex interactions between deformation, degradation and transport processe. Within this work, a new model for simultaneous coupling of stress-deformation behaviour, transport processes and degradation, including heat generation and physical exchange processes, in municipal solid waste landfills is presented. Key aspects of the model are a joint continuum mechanical framework and a monolithic solution of the governing equations.

The Theory of Porous Media forms the continuum-mechanical framework for the model. Interactions are considered by coupling the governing physical fields over the domain of a representative elementary volume via selected state variables. The macroscopic approach avoids a discrete description of the waste's structure, which is usually unknown.

A simplified two-stage degradation model describes anaerobic, i.e. oxygen-free, biological processes. Heat generation from exothermic reactions is considered. The applied Monod kinetics include an instationary biomass concentration.

Transport of the leachate and the landfill gas are described by means of a generalised Darcy law. Both fluid phases consist of several components. The influence of deformation on the hydraulic properties porosity and permeability is considered. Since the data base on moisture retention properties is small, model development is supplemented by experimental work on the moisture retention properties of waste in cooperation with Edinburgh Napier University. Pressure plate tests using German MBT material show the difficulties in relating the soil water characteristic curve to any densification state. The results of the tests are used for parameter estimation in the simulations.

The model for stress-deformation behaviour treats MSW like a composite and considers in that way the reinforcing effect of fibrous particles. A novel creep model is presented which combines stress-dependency of creep rate with density-dependence. Via the solid dry bulk density, the creep rate is coupled to degradation which enables description of degradation-induced settlements. The concept of effective stress is included in the mechanical equilibrium and thus a separate description of separate settlement phenomena is enabled. For instance, pure consolidation may be separated from compaction induced by solid mass loss.

A combination of the Finite-Element method and the Box method is applied for spatial discretisation of the governing physical fields. The balance equations of the fluid phases are formulated in Eulerian description with respect to the movement of the solid phase. The approach represents an Arbitrary Lagrangian-Eulerian (ALE) method. For discretisation in time, the implicit Euler method is used. The nonlinear coupled system of equations is solved monolithically by means of the Newton-Raphson method.

The model is verified and validated against a benchmark for multiphase flow and a waste lysimeter experiment. Analyses of a landfill structure show the capabilities of the model in the estimation of long-term settlements, in the description of a gas extraction system and in modelling of an infiltration layer. Long-term analyses over periods of up to 30 years as well as heterogeneous density distributions are included.

The simulation results show that the developed model is able to describe a variety of coupled processes, if the model parameters are known. Laboratory experiments, especially on moisture retention properties and compaction behaviour are recommended to supplement site data. By having introduced the density as an indicator for compaction, implementation of the degradation dependence of mechanical properties can be considered straightforward. Also, a dependence on moisture content may be described.

The model represents a basis for the coupled description of landfills, from which constitutive approaches may be modified or extended. Further validation of the model using landfill site data is required.

Bibliography

[1] G. D. Aitchison. Relationship of moisture stress and effective stress functions in unsaturatedsoils. In *Proc. Conf. on Pore Pressure and Suction in Soils, Butterworths, London*, 1960.

[2] O. Alduchov and R. Eskridge. Improved magnus form approximation of saturation vapor pressure. *Journal of Applied Meteorology*, 35(4):601–609, 1996.

[3] H. Altenbach, J. Altenbach, and R. Rikards. *Einführung in die Mechanik der Laminat- und Sandwichtragwerke.* Deutscher Verlag für Grundstoffindustrie Stuttgart, 1996.

[4] I. Angelidaki, L. Ellegaard, and B. Ahring. A mathematical model for dynamic simulation of anaerobic digestion of complex substrates: focusing on ammonia inhibition. *Biotechnology and Bioengineering*, 42(2):159–166, 1993.

[5] G. Attenborough, R. Gregory, D. Hall, and L. McGoochan. Development of a landfill gas risk assessment model, GasSim. In *Proc. 25th Annual Landfill Gas Symposium. Solid Waste Association of North America, Monterey, CA, USA*, 2002.

[6] G. Attenborough, D. Hall, R. Gregory, and L. McGoochan. GasSim: Landfill gas risk assessment model. In *Proceedings Waste 2002*, pages 24–26, 2002.

[7] AWG. *30 Jahre Abfallwirtschaft, 70 Jahre Müllabfuhr, 1932-2002, Geschichte der Abfallwirtschaft im Landkreis Diepholz.* Abfall-Wirtschafts-Gesellschaft mbH (AWG), 2002.

[8] A. Bagherieh, N. Khalili, G. Habibagahi, and A. Ghahramani. Drying response and effective stress in a double porosity aggregated soil. *Engineering Geology*, 105(1-2): 44–50, 2009.

[9] M. Bai and J. Roegiers. Triple-porosity analysis of solute transport. *Journal of contaminant hydrology*, 28(3):247–266, 1997.

[10] K.-J. Bathe. *Finite-Elemente-Methoden.* Springer-Verlag, 1986.

[11] J. Bauer, K. Münnich, and K. Fricke. Influence of hydraulic conditions on mechanical waste properties. In *Proceedings 2nd International Workshop Hydro-Physico-Mechanics of Wastes, Southampton, UK*, 2007.

[12] J. Bauer, K. Münnich, and K. Fricke. Response of MBT residues in large scale triaxial compression tests. In *Proceedings Sardinia 2009, Twelth International Waste Management and Landfill Symposium, Italy*, 2009.

[13] R. P. Beaven. *The hydrogeological and geotechnical properties of household waste in relation to sustainable landfill.* PhD thesis, University of London, Department of Civil Engineering, Queen Mary and Westfield College, 2000.

[14] R. P. Beaven. Review of responses to a landfill modelling challenge. *Waste and Resource Management*, 161(4):155–166, 2008.

[15] R. P. Beaven. A challenge to modellers to predict the performance of a landfill cell. In *Proceedings Sardinia 2009, Twelfth International Waste Management and Landfill Symposium*, 2009.

[16] R. P. Beaven, L. K. Ivanova, and D. J. Richards. Setting a challenge to landfill modellers. *Waste and Resource Management*, 161(3):91–98, 2008.

[17] D. Bendz and V. Singh. Solute transport under steady and transient conditions in biodegraded municipal solid waste. *Water Resources Research*, 35(8):2333–2345, 1999.

[18] D. Bendz, V. Singh, H. Rosqvist, and L. Bengtsson. Kinematic wave model for water movement in municipal solid waste. *Water Resources Research*, 34(11):2963–2970, 1998.

[19] C. Benson, M. Barlaz, D. Lane, and J. Rawe. Practice review of five bioreactor/recirculation landfills. *Waste Management*, 27(1):13–29, 2007.

[20] S. Bente and J. McDougall. Pressure plate tests and tensiometer measurements for moisture retention behaviour of MBT waste, presentations at 1st Workshop for Measuring Moisture in Waste (MMW), 2nd-4th November, Braunschweig, 2009.

[21] S. Bente, V. Krase, U. Kowalsky, and D. Dinkler. Coupled simulation of MSW landfills. In *Proceedings Sardinia 2007, Eleventh International Waste Management and Landfill Symposium, Italy*, 2007.

[22] A. Berger and U. Krause. Investigations on the self-ignition of deposits containing combustibles. *Fire and Materials*, 32(4):231–248, 2008.

[23] J. Birkholzer, J. Rutqvist, E. Sonnenthal, and D. Barr. DECOVALEX-THMC task D: Long-term permeability/porosity changes in the EDZ and near field due to THM and THC processes in volcanic and crystalline-bentonite systems, Status report October 2005. Technical report, Lawrence Berkeley National Laboratory. Retrieved from: http://escholarship.org/uc/item/5g66807g, 2005.

[24] A. Bishop. The principle of effective stress. *Teknisk Ukeblad*, 106:859–863, 1959.

[25] A. Bjarngard and L. Edgers. Settlement of municipal solid waste landfills. In *Proceedings of the 13th Annual Madison Waste Conference*, pages 192–205. Madison: University of Wisconsin, 1990.

[26] D. E. Bleiker, G. Farquhar, and E. McBean. Landfill settlement and the impact on site capacity and refuse hydraulic conductivity. *Waste Management & Research*, 13 (6):533–554, 1995.

[27] G. Blight, J. Ball, and J. Blight. Moisture and suction in sanitary landfills in semiarid areas. *Journal of Environmental Engineering*, 118(6):865–877, 1992.

[28] J. Bluhm and R. de Boer. Effective stresses – a clarification. *Archive of Applied Mechanics*, 66:479–492, 1996.

[29] J. Bonet and R. Wood. *Nonlinear continuum mechanics for finite element analysis.* Cambridge University Press, 1997.

[30] R. M. Bowen. Compressible porous media models by use of the Theory of Mixtures. *International Journal of Engineering Science*, 20(6):697–735, 1982.

[31] R. H. Brooks and A. Corey. Properties of porous media affecting fluid flow. *Journal of the Irrigation and Drainage Division*, 92(IR2):61–88, 1966.

[32] A. Brovelli, F. Malaguerra, and D. Barry. Bioclogging in porous media: Model development and sensitivity to initial conditions. *Environmental Modelling & Software*, 24(5):611–626, 2009.

[33] M. Brusseau and P. Rao. Modeling solute transport in structured soils: A review. *Geoderma(Amsterdam)*, 46(1-3):169–192, 1990.

[34] N. Burdine. Relative permeability calculations from pore-size distribution data. *Petroleum Transactions AIME*, 198:71–78, 1953.

[35] W. Butz. Ansatz für die Schätzung der luftseitigen Deponieemissionen für das E-PRTR. Technical report, Umweltbundesamt Berlin, FG III 3.3, 2006.

[36] W. Butz. Ansatz für die Schätzung der luftseitigen Deponieemissionen für das E-PRTR, Ergänzung für Deponien, bei denen die letzte Ablagerung bereits lange zurückliegt. Technical report, Umweltbundesamt, FG III 3.3, 2007.

[37] CDM Executive Board. Revision of the approved baseline methodology AM0025. Technical report, UNFCCC/CCNUCC, 2006.

[38] T.-h. Chen and D. P. Chynoweth. Hydraulic conductivity of compacted municipal solid waste. *Bioresource Technology*, 51(2-3):205–212, 1995.

[39] Y. Chen, C. Zhou, and L. Jing. Modeling coupled THM processes of geological porous media with multiphase flow: Theory and validation against laboratory and field scale experiments. *Computers and Geotechnics*, 36(8):1309–1329, 2009.

[40] R. Clément, M. Descloitres, T. Günther, L. Oxarango, C. Morra, J.-P. Laurent, and J.-P. Gourc. Improvement of electrical resistivity tomography for leachate injection monitoring. *Waste Management*, 30(3):452–464, Mar. 2010.

[41] F. Collin, X. L. Li, J. P. Radu, and R. Charlier. Thermo-hydro-mechanical coupling in clay barriers. *Engineering Geology*, 64(2-3):179–193, 2002.

[42] A. Cooke, R. Rowe, and B. Rittmann. Modelling species fate and porous media effects for landfill leachate flow. *Canadian Geotechnical Journal*, 42(4):1116–1132, 2005.

[43] A. Corey. *Mechanics of immiscible fluids in porous media.* Water Resources Publications, LLC, 1994.

[44] J. Dach, M. Theisen, J. Jager, and M. Glesner. Ansätze zur Modellierung des Stoff- und Wärmetransports in Deponien mit Abfällen nach mechanisch-biologischer Abfallbehandlung (MBA). In *Universität Potsdam (Ed.), BMBF-Verbundvorhaben Mechanisch-biologische Behandlung von zu deponierenden Abfällen, Beiträge der 1. Tagung, 13./14. März 1996, Potsdam*, 1996.

[45] P. Dangla, O. Coussy, and R. Eymard. Contribution to the benchmark. in: Numerical benchmark on multiphase flow, Coordination report, ALERT programme 4: Thermo-hydro-mechanical coupling, 1997.

[46] J. D'Ans and E. Lax. *Taschenbuch für Chemiker und Physiker.* Springer, 1983.

[47] R. de Boer. *Trends in continuum mechanics of porous media.* Springer, 2005.

[48] M. De Velásquez, T. Orta, R. Cruz-Rivera, N. Rojas-Valencia, I. Monje-Ramirez, and J. Sánchez-Gómez. Determination of field capacity of municipal solid waste with surcharge simulation. *Waste Management & Research*, 21(2):137–144, 2003.

[49] A. Demetracopoulos, G. Korfiatis, E. Bourodimos, and E. Nawy. Unsaturated flow through solid waste landfills: Model and sensitivity analysis. *Water Resources Bulletin*, 22(4):601–609, 1986.

[50] E. Demirekler, R. Rowe, and K. Unlu. Modeling leachate production from municipal solid waste landfills. In *Proceedings Sardinia 1999, Seventh International Waste Management and Landfill Symposium, Italy.* CISA, 1999.

[51] D. Dinkler and H. Ahrens. *Finite-Element-Methoden Teil I.* Institut für Statik, TU Braunschweig, 2006.

[52] N. Dixon and D. R. V. Jones. Engineering properties of municipal solid waste. *Geotextiles and Geomembranes*, 23(3):205–233, 2005.

[53] J. Donea. *Arbitrary Lagrangian-Eulerian Finite Element Methods, in: Computational methods for transient analysis.* Elsevier, 1983.

[54] J. Donea, A. Huerta, J. Ponthot, and A. Rodriguez-Ferran. Arbitrary Lagrangian-Eulerian methods. *Encyclopedia of computational mechanics*, 1:1–25, 2004.

[55] E. Durmusoglu, M. Y. Corapcioglu, and K. Tuncay. Landfill settlement with decomposition and gas generation. *Journal of Environmental Engineering*, 131(9): 1311–1321, 2005.

[56] E. Durmusoglu, I. Sanchez, and M. Corapcioglu. Permeability and compression characteristics of municipal solid waste samples. *Environmental Geology*, 50(6): 773–786, Aug. 2006.

[57] W. Durner and H. Flühler. *Encyclopedia of Hydrological Sciences*, chapter 74: Soil hydraulic properties, pages 1103–1120. John Wiley & Sons, 2005.

[58] J. Ebers-Ernst. *Modellierung des Inelastischen Verformungsverhaltens von Siedlungsabfalldeponien.* PhD thesis, Institut für Statik, TU Braunschweig, 2001.

[59] T. Edil, V. Ranguette, and W. Wuellner. Settlement of municipal refuse. *ASTM Special Technical Publication 1070*, pages 225–239, 1990.

[60] W. Ehlers. A single-surface yield function for geomaterials. *Archive of Applied Mechanics*, 65:246–259, 1995.

[61] W. Ehlers, T. Graf, and M. Ammann. Deformation and localization analysis of partially saturated soil. *Computer Methods in Applied Mechanics and Engineering*, 193:2885–2910, 2004.

[62] H. Ehrig. Untersuchungen zur Gasproduktion aus Hausmüll. *Müll und Abfall*, 5: 173–183, 1986.

[63] G. Eipper. *Theorie und Numerik finiter elastischer Deformationen in fluidgesättigten porösen Festkörpern.* PhD thesis, Institut für Mechanik, Universität Stuttgart, 1998.

[64] M. El-Fadel and R. Khoury. Modeling settlement in msw landfills: a critical review. *Critical Reviews in Environmental Science and Technology*, 30(3):327–361, 2000.

[65] M. El-Fadel, A. Findikakis, and J. Leckie. A numerical model for methane production in managed sanitary landfills. *Waste Management & Research*, 7(1):31–42, 1989.

[66] M. El-Fadel, A. Findikakis, and J. Leckie. Numerical modelling of generation and transport of gas and heat in sanitary landfills II. model application. *Waste Management & Research*, 14(6):537–551, 1996.

[67] M. El-Fadel, A. Findikakis, and J. Leckie. Numerical modelling of generation and transport of gas and heat in landfills I. model formulation. *Waste management & research*, 14(5):483–504, 1996.

[68] M. El-Fadel, A. Findikakis, and J. Leckie. Gas simulation models for solid waste landfills. *Critical Reviews in Environmental Science and Technology*, 27(3):237–283, 1997.

[69] S. A. Elagroudy, M. H. Abdel-Razik, M. A. Warith, and F. H. Ghobrial. Waste settlement in bioreactor landfill models. *Waste Management*, 28:2366–2374, 2008.

[70] S. A. Elagroudy, M. A. Warith, and F. H. Ghobrial. *Solid Waste Settlement in Landfills/Bioreactor Landfills, in: Waste Management Research Trends.* Nova Science Pub Inc, 2008.

[71] EPA. EPA Ireland, Supporting Document for the Determination of Diffuse Methane Emissions from Landfill Sites, 2004.

[72] EPA. Landfill Gas Emissions model (LandGEM) version 3.02 user's guide. Technical report, U.S. Environmental Protection Agency (EPA), 2005.

[73] EPA. User's manual central America landfill gas model. Technical report, U.S. Environmental Protection Agency (EPA), 2007.

[74] EPA. User's manual Mexico landfill gas model. Technical report, U.S. Environmental Protection Agency (EPA), 2009.

[75] EPA. User's manual Ecuador landfill gas model. Technical report, U.S. Environmental Protection Agency (EPA), 2009.

[76] EPA. User's manual China landfill gas model. Technical report, U.S. Environmental Protection Agency (EPA), 2009.

[77] D. Fairbanks and C. Wilke. Diffusion coefficients in multicomponent gas mixtures. *Industrial & Engineering Chemistry*, 42(3):471–475, 1950.

[78] G. Farquhar and F. Rovers. Gas production during refuse decomposition. *Water, Air and Soil Pollution*, 2:483–495, 1973.

[79] P. Fillunger. Das Delesse'sche Gesetz. *Monatshefte für Mathematik*, 42(1):87–96, 1935.

[80] N. Fischer. Electrical resistivity measurements in MBT waste, presentation at the 1st workshop for measuring moisture in waste (MMW), 2nd-4th November, Braunschweig, 2009.

[81] B. Francois and L. Laloui. ACMEG-TS: A constitutive model for unsaturated soils under non-isothermal conditions. *International Journal for Numerical and Analytical Methods in Geomechanics*, 32:1955–1988, 2008.

[82] B. Francois, L. Laloui, and C. Laurent. Thermo-hydro-mechanical simulation of ATLAS in situ large scale test in Boom clay. *Computers and Geotechnics*, 36(4): 626–640, 2009.

[83] D. Fredlund and N. Morgenstern. Stress state variables for unsaturated soils. *Journal of the Geotechnical Engineering Division*, 103(5):447–466, 1977.

[84] D. G. Fredlund. *Soil Mechanics for Unsaturated Soils.* John Wiley & Sons, Inc., 1993.

[85] A. L. Garcia de Cortazar and I. T. Monzon. MODUELO 2: A new version of an integrated simulation model for municipal solid waste landfills. *Environmental Modelling & Software*, 22(1):59–72, 2007.

[86] A. L. Garcia de Cortazar, J. H. Lantaron, O. M. Fernandez, I. T. Monzon, and M. F. Lamia. Modelling for environmental assessment of municipal solid waste landfills (Part 1: Hydrology). *Waste Management & Research*, 20(2):198–210, 2002.

[87] A. L. Garcia de Cortazar, J. H. Lantaron, O. M. Fernandez, I. T. Monzon, and M. F. Lamia. Modelling for environmental assessment of municipal solid waste landfills (Part II: Biodegradation). *Waste Management & Research*, 20(6):514–528, 2002.

[88] H. Gavala, I. Angelidaki, and B. Ahring. Kinetics and modeling of anaerobic digestion process. *Advances in Biochemical Engineering Biotechnology*, 81:57–94, 2003.

[89] B. Gharabaghi, M. Singh, C. Inkratas, I. Fleming, and E. McBean. Comparison of slope stability in two Brazilian municipal landfills. *Waste Management*, 28(9): 1509–1517, 2008.

[90] S. Gholamifard, R. Eymard, and C. Duquennoi. Modeling anaerobic bioreactor landfills in methanogenic phase: Long term and short term behaviors. *Water Research*, 42(20):5061–5071, 2008.

[91] T. Graf. *Multiphasic flow processes in deformable porous media under consideration of fluid phase transitions.* PhD thesis, Universität Stuttgart, Institut für Mechanik, 2008.

[92] W. Gray and B. A. Schrefler. Analysis of the solid stress tensor in multiphase porous media. *International Journal for Numerical and Analytical Methods in Geomechanics*, 31:541–581, 2007.

[93] GTZ. Fachliche Leitlinien Abfallwirtschaft. Technical report, Deutsche Gesellschaft für Technische Zusammenarbeit (GTZ) GmbH, 2003.

[94] GTZ website. http://www.gtz.de/de/themen/3943.htm, access on 19.10.2009, 2009.

[95] A. Haarstrick, D. C. Hempel, L. Ostermann, H. Ahrens, and D. Dinkler. Modelling of the biodegradation of organic matter in municipal landfills. *Waste Management & Research*, 19(4):320–331, 2001.

[96] A. Haarstrick, N. Mora-Naranjo, J. Meima, and D. C. Hempel. Modeling anaerobic degradation in municipal landfills. *Environmental Engineering Science*, 21(4):471–484, 2004.

[97] M. Hamdan. Single-phase flow through porous channels a review of flow models and channel entry conditions. *Applied Mathematics and Computation*, 62(2-3):203–222, 1994.

[98] H. Hamelers. Modeling composting kinetics: A review of approaches. *Reviews in Environmental Science and Biotechnology*, 3(4):331–342, 2004.

[99] J. Hanel. *Modell zur Analyse von gekoppelten Transport- und Stoffabbauprozessen in Deponien.* PhD thesis, Institut für Statik, TU Braunschweig, 2001.

[100] M. Hashemi, H. I. Kavak, T. T. Tsotsis, and M. Sahimi. Computer simulation of gas generation and transport in landfills–I: quasi-steady-state condition. *Chemical Engineering Science*, 57(13):2475–2501, 2002.

[101] P. Haupt. *Continuum Mechanics and Theory of Materials.* Springer, 1999.

[102] H. Heinke, A. Haarstrick, and D. Hempel. Studies on physico-chemical and biochemical properties of municipal solid wastes. In *Proceedings Sardinia 2005, 10th International Waste Management and Landfill Symposium, Italy.* CISA, 2005.

[103] R. Helmig. *Multiphase Flow and Transport Processes in the Subsurface: A contribution to the modeling of hydrosystems.* Springer-Verlag, 1997.

[104] C. H. Hettiarachchi, J. N. Meegoda, J. Tavantzis, and P. Hettiaratchi. Numerical model to predict settlements coupled with landfill gas pressure in bioreactor landfills. *Journal of Hazardous Materials*, 139(3):514–522, 2007.

[105] K.-U. Heyer. Deponienachsorge und kein Ende? *Müll und Abfall*, 42:1, 2010.

[106] J. Hoeks. Significance of biogas production in waste tips. *Waste Management & Research*, 1(1):323–335, 1983.

[107] G. Holzapfel. *Nonlinear Solid Mechanics.* John Wiley & Sons, Ltd., Chichester, 2000.

[108] D. Hosser, M. Dehne, H. Ahrens, and J. Kindlein. Modelling simplification of landfill processes by using methods of reliability theory. *Waste Management & Research*, 21(2):119–126, 2003.

[109] R. Huber and R. Helmig. Multiphase flow in heterogeneous porous media: A classical finite element method versus an implicit pressure-explicit saturation-based mixed finite element - finite volume approach. *International Journal for Numerical Methods in Fluids*, 29:899–920, 1999.

[110] R. Huber and R. Helmig. Node-centered finite volume discretizations for the numerical simulation of multiphase flow in heterogeneous porous media. *Computational Geosciences*, 4(2):141–164, Sept. 2000.

[111] B. Hübner. *Simultane Analyse von Bauwerk-Wind-Wechselwirkungen.* PhD thesis, Institut für Statik, TU Braunschweig, 2003.

[112] A. P. Hudson. *Evaluation of the vertical and horizontal hydraulic conductivities of household wastes.* PhD thesis, School of Civil Engineering and the Environment, 2007.

[113] K. Hutter, L. Laloui, and L. Vulliet. Thermodynamically based mixture models of saturated and unsaturated soils. *International Journal for Numerical and Analytical Methods in Geomechanics*, 4(4):295–338, 1999.

[114] IPCC. Revised 1996 IPCC guidelines for national greenhouse gas inventories: Workbook. Technical report, IPCC, 1996.

[115] IPCC. Revised 1996 IPCC guidelines for national greenhouse gas inventories: Reference manual. Technical report, IPCC, 1996.

[116] IPCC. IPCC good practice guidance and uncertainty management in national greenhouse gas inventories. Technical report, IPCC, 2000.

[117] J. Islam and N. Singhal. A one-dimensional reactive multi-component landfill leachate transport model. *Environmental Modelling & Software*, 17(6):531–543, 2002.

[118] L. Ivanova. *Quantification of Factors Affecting Rate and Magnitude of Secondary Settlement of Landfills.* PhD thesis, School of Civil Engineering and the Environment, University of Southampton, 2007.

[119] L. Ivanova, D. Richards, and D. Smallman. The long-term settlement of landfill waste. *Waste and Resource Management*, 161(3):121–133, 2008.

[120] C. Jommi and J. Vaunat. A numerical benchmark on multiphase flow - coordination report. Technical report, ALERT Geomaterials, Group 4, Thermo-Hydro-Mechanical Coupling, 1997.

[121] M. Kaviany. *Principles of Heat Transfer in Porous Media.* Springer-Verlag, 1995.

[122] Y. K. Kazimoglu. *Moisture retention and conductivity properties of waste refuse: a laboratory study.* PhD thesis, Napier University Edinburgh, School of the Built Environment, 2007.

[123] N. Khalili and M. Kabbaz. A unique relationship for chi for the determination of the shear strength of unsaturated soils. *Geotechnique*, 48(5):681–687, 1998.

[124] R. Khanbilvardi, S. Ahmed, and P. Gleason. Flow investigation for landfill leachate (FILL). *Journal of environmental engineering*, 121(1):45–57, 1995.

[125] J. Kindlein, D. Dinkler, H. Ahrens, and A. Haarstrick. Modelling reactive transport processes in landfills, change of hydraulics due to degradation and biofilm growth. In *Proceedings Sardinia 2005, Tenth International Waste Mangement and Landfill Symposium, Italy*. CISA, 2005.

[126] J. Kindlein, D. Dinkler, and H. Ahrens. Numerical modelling of multiphase flow and transport processes in landfills. *Waste Management & Research*, 24(4):376–387, 2006.

[127] P. Kjeldsen, M. A. Barlaz, A. P. Rooker, A. Baun, A. Ledin, and T. H. Christensen. Present and long-term composition of MSW landfill leachate: A review. *Critical Reviews in Environmental Science and Technology*, 32(4):297–336, 2002.

[128] C. Kleinstreuer and T. Poweigha. Dynamic simulator for anaerobic digestion processes. *Biotechnology and Bioengineering*, 24(9):1941–1951, 1982.

[129] R. Kockel. *Scherfestigkeit von Mischabfall im Hinblick auf die Standsicherheit von Deponien*. PhD thesis, Ruhr-Universität Bochum, 1995.

[130] R. M. Koerner and T. Y. Soong. Assessment of ten landfill failure using 2-D and 3-D stability analysis procedures. In *Proceedings Österreichische Geotechniktagung, Wien*, 1999.

[131] R. M. Koerner and T. Y. Soong. Leachate in landfills: the stability issues. *Geotextiles and Geomembranes*, 18(5):293–309, Oct. 2000.

[132] F. Kölsch. *Der Einfluss der Faserbestandteile auf die Scherfestigkeit von Siedlungsabfall*. PhD thesis, Leichtweiß-Institut für Wasserbau, TU Braunschweig, 1996.

[133] F. Kölsch. Nachträgliche Standsicherheitsuntersuchung - Bandung und Ihlenberg. In Witt and Katzenbach, editors, *2. Symposium Umweltgeotechnik, Freiberg*, 2005.

[134] G. P. Korfiatis, A. C. Demetracopoulos, E. L. Bourodimos, and E. G. Nawy. Moisture transport in a solid waste column. *Journal of Environmental Engineering*, 110: 780–796, 1984.

[135] V. Krase. *Stability of Municipal Solid Waste Landfills*. PhD thesis, Institut für Statik, TU Braunschweig, 2008.

[136] V. Krase, S. Bente, U. Kowalsky, and D. Dinkler. Modelling the stress-deformation behaviour of municipal solid waste. *Géotechnique*, 60:1 – 11, 2010. doi: 10.1680/geot.2010.60.00.1.

[137] L. Laloui, F. Collin, and V. De Gennaro (Ed.). Lecture notes of ALERT 2009 graduate school, in European Journal of Environmental and Civil Engineering, 13(7-8), 2009.

[138] J. Lamborn. Characterisation of municipal solid waste composition into model inputs. In *Proceedings Third International Workshop Hydro-Physico-Mechanics of Landfills*, 2009.

[139] D. Lee and T. Donaldson. Dynamic simulation model for anaerobic digestion of cellulose. In *Proceedings Sixth Symposium on Biotechnology for Fuels and Chemicals, Gatlinburg, Tennesse*. CONF-840509-4, Oak Ridge National Lab., TN (USA), 1984.

[140] Y.-H. Lee and L. T. Fan. Kinetic studies of enzymatic hydrolysis of insoluble cellulose: Analysis of the initial rates. *Biotechnology and Bioengineering*, 24:2383–2406, 1982.

[141] C. Leppert. *Mehrphasenmodell für granulare Medien zur numerischen Untersuchung des Phasenübergangs bei der Entleerung von Silos*. PhD thesis, Institut für Statik, TU Braunschweig, 2007.

[142] R. Lewis and B. A. Schrefler. *The Finite Element Method in the Static and Dynamic Deformation and Consolidation of Porous Media*. John Wiley & Sons, Ltd., 1998.

[143] A. C. Liakopoulos. *Transient Flow Through Unsaturated Porous Media*. PhD thesis, University of California, 1965.

[144] C.-N. Liu, R.-H. Chen, and K.-S. Chen. Unsaturated consolidation theory for the prediction of long-term municipal solid waste landfill settlement. *Waste Management & Research*, 24:80–91, 2006.

[145] A. Lobo, A. Lopez, N. Cobo, and I. Tejero. Simulation of municipal solid waste reactors using MODUELO. *Waste and Resource Management*, 161(3):99–104, 2008.

[146] A. Lopez, N. Cobo, M. Cuartas, and A. Lobo. Estimating the future emissions of an old landfill by simulation. In *Proceedings Sardinia 2009, Twelfth International Waste Management and Landfill Symposium*, 2009.

[147] N. Lu and W. Likos. *Unsaturated soil mechanics*. John Wiley and Sons Inc., 2004.

[148] J. Lüke. *Entwicklung und Anwendung eines Stoffgesetzes für Siedlungsabfälle*. PhD thesis, RWTH Aachen, Geotechnik in Forschung und Praxis, WBI-Print 11, Verlag Glückauf Essen, 2002.

[149] G. Lyberatos and I. Skiadas. Modelling of anaerobic digestion - a review. *Global Nest: the International Journal*, 1:63–76, 1999.

[150] U. Maas and S. Pope. Simplifying chemical kinetics: Intrinsic low-dimensional manifolds in composition space. *Combustion and Flame*, 88(3-4):239–264, 1992.

[151] S. Machado, M. Carvalho, and O. Vilar. Constitutive model for municipal solid waste. *Journal of Geotechnical and Geoenvironmental Engineering*, 128:940–951, 2002.

[152] S. Machado, O. Vilar, and M. Carvalho. Constitutive model for long term municipal solid waste mechanical behavior. *Computers and Geotechnics*, 35(5):775–790, 2008.

[153] G. Magnus. Versuche über die Spannkräfte des Wasserdampfes. *Ann. Phys. Chem.*, 61:225–242, 1844.

[154] A. Martinez, G. Simoes, A. Cortazar, R. Padilla, C. Catapreta, and V. Morais. Water balance of an experimental landfill using moduelo. In *Proceedings Sardinia 2009, Twelfth International Waste Management and Landfill Symposium*, 2009.

[155] I. Mason. Mathematical modelling of the composting process: A review. *Waste Management*, 26(1):3–21, 2006.

[156] P. McCreanor and D. Reinhart. Mathematical modeling of leachate routing in a leachate recirculating landfill. *Water Research*, 34(4):1285–1295, 2000.

[157] J. McDougall. A hydro–bio–mechanical model for settlement and other behaviour in landfilled waste. *Computers and Geotechnics*, 34:229–246, 2007.

[158] J. McDougall and J. Hay. Hydro-bio-mechanical modelling of landfilled waste: formulation and testing. In *International Workshop "Hydro-Physico-Mechanics of Landfills" LIRIGM Grenoble University France 21-22 March*, 2005.

[159] J. McDougall, R. Sarsby, and N. Hill. A numerical investigation of landfill hydraulics using variably saturated flow theory. *Geotechnique*, 46(2):329–341, 1996.

[160] J. McDougall, R. Sarsby, and N. Hill. Discussion - a numerical investigation of landfill hydraulics using variably saturated flow theory. *Geotechnique*, 48:143–144, 1998.

[161] J. McDougall, I. Pyrah, and S. Yuen. Extended phase relations and load effects in MSW. *Waste Management*, 24:251–157, 2004.

[162] J. Meima, N. M. Naranjo, and A. Haarstrick. Sensitivity analysis and literature review of parameters controlling local biodegradation processes in municipal solid waste landfills. *Waste Management*, 28(5):904–918, 2008.

[163] S. M. Merry, W. U. Fritz, M. Budhu, and K. Jesionek. Effect of gas on pore pressures in wet landfills. *Journal of Geotechnical and Geoenvironmental Engineering.*, 132 (5):553–561, 2006.

[164] P. A. Miller and N. L. Clesceri. *Wastes Sites as Biological Reactors.* Lewis Publishers, 2003.

[165] R. Millington and J. Quirk. Permeability of porous solids. *Transactions of the Faraday Society*, 57:1200–1207, 1960.

[166] J. Mitchell and J. Santamarina. Biological considerations in geotechnical engineering. *Journal of Geotechnical and Geoenvironmental Engineering*, 131(10):1222–1233, October 2005.

[167] MMW. Minutes of 1st workshop for measuring moisture in waste (MMW), 2nd-4th November, Braunschweig, 2009.

[168] J. Monod. The growth of bacterial cultures. *Annu. Rev. Microbiol.*, 3:371–394, 1949.

[169] N. Mora-Naranjo, J. A. Meima, A. Haarstrick, and D. C. Hempel. Modelling and experimental investigation of environmental influences on the acetate and methane formation in solid waste. *Waste Management*, 24(8):763–773, 2004.

[170] N. F. Mora Naranjo. *Analyse und Modellierung anaerober Abbauprozesse in Deponien.* PhD thesis, Gemeinsame Naturwissenschaftliche Fakultät der Technischen Universität Carolo-Wilhelmina zu Braunschweig, 2004.

[171] C. E. Mortimer. *Chemie, Das Basiswissen der Chemie.* Georg Thieme Verlag Stuttgart, New York, 1987.

[172] Y. Mualem. A new model for predicting the hydraulic conductivity of unsaturated porous media. *Water Resources Research*, 12:513–522, 1976.

[173] K. Mudrack and S. Kunst. *Biologie der Abwasserreinigung.* Spektrum Akademischer Verlag Heidelberg, Berlin, 1985.

[174] I. Münch. *Ein geometrisch und materiell nichtlineares Cosserat-Modell - Theorie, Numerik und Anwendungsmöglichkeiten.* PhD thesis, Fakultät für Bauingenieur-, Geo- und Umweltwissenschaften, Universität Karlsruhe, 2007.

[175] K. Münnich, J. Bauer, and K. Fricke. Investigation on relationship between vertical and horizontal permeabilities of MBT wastes. In *Proceedings Sardinia 2005, Tenth International Waste Management and Landfill Symposium,Italy*, 2005.

[176] K. Münnich, J. Bauer, and K. Fricke. Laboratory tests to determine water balance parameters of MBT material. In *Proceedings 3rd International Workshop Hydro-Physico-Mechanics of Landfills, Braunschweig, Germany*, 2009.

[177] K. Münnich, J. Bauer, and K. Fricke. Einfluss des Einbauwassergehaltes auf das Langzeitverhalten von MBA-Deponien. In *Deponietechnik 2010. Hamburger Berichte 35, Technische Universität Hamburg-Harburg*, 2010.

[178] R. Murphy and E. Garwell. Infiltration rates through landfill liners. Technical report, University of South Florida, 1998.

[179] W. Murphy and P. Gilbert. Settlement and cover subsidence of hazardous waste landfills. Technical report, US EPA, 1985.

[180] MUV. Ministerium für Umwelt und Verkehr Baden-Württemberg, Deponigas, Beschleunigung der Abbauprozesse, Methanoxidationsfilter. Reihe Abfall, Heft 77, 2004.

[181] G. A. Narsilio, O. Buzzi, S. Fityus, T. S. Yun, and D. W. Smith. Upscaling of Navier-Stokes equations in porous media: Theoretical, numerical and experimental approach. *Computers and Geotechnics*, 36:1200–1206, 2009.

[182] D. Nayagum, J. White, T. Rees-White, D. Holmes, and K. Zardava. Numerical modelling of the flow dynamics of air and leachate through waste material under vertical drainage and forced-air flow. In *Proceedings Third Workshop Hydro-Physico-Mechanics of Landfills, Braunschweig*, 2009.

[183] J. Noble and A. Arnold. Experimental and mathematical modeling of moisture transport in landfills. *Chemical Engineering Communications*, 100(1):95–111, 1991.

[184] M. Nuth and L. Laloui. Effective stress concept in unsaturated soils: Clarification and validation of a unified framework. *International Journal for Numerical and Analytical Methods in Geomechanics*, 32(7):771–801, 2008.

[185] Y. Ogor and M. Guerbois. Comparison of landfill methane emission models: a case study. In *Proceedings Sardinia 2005, Tenth International Waste Management and Landfill Symposium, Italy*, 2005.

[186] C. Oldenburg, S. Borglin, and T. Hazen. Multiphase modeling of flow, transport, and biodegradation in a mesoscale landfill bioreactor. Technical report, Lawrence Berkeley National Laboratory, Earth Sciences Division, 2002.

[187] C. M. Oldenburg. T2LBM version 1.0: Landfill bioreactor model for TOUGH2. Technical report, Earth Sciences Division, Lawrence Berkeley National Laboratory, University of California, 2001.

[188] H. Oonk and H. Woelders. Dutch research programme on sustainable landfilling - focus on hydrology. In *Proceedings 2nd International Workshop Hydro-Physico-Mechanics of Wastes, Southampton*, 2007.

[189] H. Oumeraci. *Hydromechanik, (Lecture Notes on Hydromechanics).* Leichtweiß-Institut für Wasserbau, Abt. Hydromechanik und Küsteningenieurwesen, TU Braunschweig, 1999.

[190] I. S. Oweis. Estimate of landfill settlements due to mechanical and decompositional processes. *Journal of Geotechnical and Geoenvironmental Enginnering*, 132(5):644–650, May 2006.

[191] A. Papafotiou, R. Helmig, J. Schaap, P. Lehmann, A. Kaestner, H. Flühler, I. Neuweiler, R. Hassanein, B. Ahrenholz, J. Tölke, A. Peters, and W. Durner. From the pore scale to the lab scale: 3-D lab experiment and numerical simulation of drainage in heterogeneous porous media. *Advances in Water Resources*, 31: 1253–1268, 2008.

[192] H. Parisch. *Festkörper-Kontinuumsmechanik: Von den Grundgleichungen zur Lösung mit Finiten Elementen.* Vieweg+ Teubner Verlag, 2003.

[193] H. Park and S. Lee. Long-term settlement behaviour of MSW landfills with various fill ages. *Waste Management & Research*, 20:259–268, 2002.

[194] W. Powrie, R. Beaven, and A. P. Hudson. Factors affecting the hydraulic conductivity of waste. In *Proceedings First Workshop on Hydro-Physico-Mechanics of Landfills, Grenoble*, 2005.

[195] W. Powrie, D. Richards, and K. Velkushanova. Mechanisms of settlement in biodegradable wastes. In *Proceedings Third International Workshop Hydro-Physico-Mechanics of Landfills, Braunschweig*, 2009.

[196] T. Reichel. *Modelle für die Beschreibung des Emissionsverhaltens von Siedlungsabfällen.* PhD thesis, Institut für Bioverfahrenstechnik, TU Braunschweig, 2008.

[197] T. Reichel and A. Haarstrick. Modelling decomposition of MSW using genetic algorithms. *Waste and Resource Management*, 161(3):113–120, 2008.

[198] T. Ricken and R. de Boer. Multiphase flow in a capillary porous medium. *Computational Materials Science*, 28:704–713, 2003.

[199] T. Ricken and V. Ustohalova. Modeling of thermal mass transfer in porous media with applications to organic phase transition in landfills. *Computational Materials Science*, 32:498–508, 2005.

[200] T. Ricken, M. Robeck, and R. Widmann. A 3D-finite element simulation of biological conversion processes in landfills using a multiphase model based on the theory of porous media. In *Proceedings Sardinia 2009, Twelfth International Waste Management and Landfill Symposium, Italy*, 2009.

[201] H. Rosqvist and G. Destouni. Solute transport through preferential pathways in municipal solid waste. *Journal of contaminant hydrology*, 46(1-2):39–60, 2000.

[202] C.-C. Rossow. Introduction to numerical methods in aerodynamics. Lecture Notes, Institute for Fluid Mechanics, TU Braunschweig, 2005.

[203] B. Rotter, D. Barry, J. Gerhard, and J. Small. Parameter and process significance in mechanistic modeling of cellulose hydrolysis. *Bioresource Technology*, 99(13): 5738–5748, 2008.

[204] B. Rüth, B. Lennartz, and P. Kahle. Water regime of mechanical-biological pretreated waste materials under fast-growing trees. *Waste Management & Research*, 25:408–416, 2007.

[205] Rytec. GmbH, Deponiegas in der Stilllegungs- und Nachsorgephase am Beispiel der Deponie Dreieich-Buchschlag, 2005.

[206] R. Sanchez, M. Hashemi, T. T. Tsotsis, and M. Sahimi. Computer simulation of gas generation and transport in landfills. II: Dynamic conditions. *Chemical Engineering Science*, 61(14):4750–4761, July 2006.

[207] R. Sanchez, T. T. Tsotsis, and M. Sahimi. Computer simulation of gas generation and transport in landfills. III: Development of landfills' optimal model. *Chemical Engineering Science*, 62(22):6378–6390, Nov. 2007.

[208] T. Schanz. Mechanik teilgesättigter Böden, Abschlussbericht zur DFG Forschergruppe, 2008.

[209] H. Scharff and J. Jacobs. Applying guidance for methane emission estimation for landfills. *Waste Management*, 26(4):417–429, 2006.

[210] B. Schrefler, L. Simoni, E. Turska, and X. Zhan. Zur Berechnung von ungesättigten Konsolidationsproblemen. *Bauingenieur*, 68:375–384, 1993.

[211] B. A. Schrefler. Multiphase flow in deforming porous material. *International Journal for Numerical Methods in Engineering*, 60:27–50, 2004.

[212] P. R. Schroeder, T. S. Dozier, P. A. Zappi, B. M. McEnroe, J. W. Sjostrom, and R. L. Peyton. The hydrologic evaluation of landfill performance (HELP) model. Engineering documentation for version 3. Technical report, Environmental Laboratory, U.S. Army Corps of Engineers, Waterways Experiment Station, Vicksburg, MS 39180-6199, 1994.

[213] C. Shackelford and M. Glade. Analytical mass leaching model for contaminated soil and soil stabilized waste. *Ground Water*, 35(2):233–242, 1997.

[214] L. Shen and Z. Chen. Critical review of the impact of tortuosity on diffusion. *Chemical Engineering Science*, 62(14):3748–3755, 2007.

[215] H. Siegrist, D. Vogt, J. Garcia-Heras, and W. Gujer. Mathematical model for meso- and thermophilic anaerobic sewage sludge digestion. *Environmental Science & Technology*, 36(5):1113–1123, 2002.

[216] G. Sigel. Abfall und Energie, Vortrag anlässlich der 14. Abfalltagung des LANU in Neumünster, am 27.11.2003, 2003.

[217] M. K. Singh, J. S. Sharma, and I. R. Fleming. A design chart for estimation of horizontal displacement in municipal landfills. *Waste Management*, 29(5):1577–1587, 2009.

[218] A. W. Skempton. Effective stress in soils, concrete and rocks. In *Proc. Conf. on Pore Pressure and Suction in Soils, Butterworths, London*, pages 4–16, 1960.

[219] B. Staley, M. Barlaz, and F. de los Reyes. Evaluation of factors affecting the initiation of methanogenesis in solid waste. In *Proceedings, Global Waste Management Symposium, September 7-10, Colorado, USA*, 2008.

[220] G. Stoltz and J.-P. Gourc. Influence of compressibility of domestic waste on fluid permeability. In *Proceedings Sardinia 2007, Eleventh International Waste Management and Landfill Symposium, Italy*, 2007.

[221] W. Straub and D. Lynch. Models of landfill leaching: moisture flow and inorganic strength. *Journal of the Environmental Engineering Division*, 108(2):231–250, 1982.

[222] W. Straub and D. Lynch. Models of landfill leaching: Organic strength. *Journal of the Environmental Engineering Division*, 108(2):251–268, April 1982.

[223] W. Sutherland. The viscosity of gases and molecular force. *Philosophical Magazine Series 5*, 36(223):507–531, 1893.

[224] O. Tabasaran. Überlegungen zum Problem Deponiegas. *Müll und Abfall*, 8:204–210, 1976.

[225] O. Tabasaran and G. Rettenberger. Grundlagen zur Planung von Entgasungsanlagen, Müll-Handburch, Band 4, Nr. 4547. Technical report, Erich Schmidt Verlag, 1987.

[226] O. Tetens. Über einige meteorologische Begriffe. *Zeitschrift für Geophysik*, 6:297–309, 1930.

[227] S. Thompson, J. Sawyer, R. Bonam, and J. Valdivia. Building a better methane generation model: Validating models with methane recovery rates from 35 Canadian landfills. *Waste Management*, 29(7):2085–2091, 2009.

[228] F. Tong, L. Jing, and R. W. Zimmerman. An effective thermal conductivity model of geological porous media for coupled thermo-hydro-mechanical systems with multiphase flow. *International Journal of Rock Mechanics and Mining Sciences*, 46(8): 1358–1369, 2009.

[229] UBA. Ansatz für die Schätzung der luftseitigen Deponieemissionen für den ersten Berichtszeitraum. Technical report, Umweltbundesamt Berlin, 2002.

[230] UBA. Umwelt-Kernindikatiorensystem, Ablagerungsquoten der Hauptabfallströme, 2009. http://www.umweltbundesamt-umwelt-deutschland.de/umweltdaten/public/theme.do?nodeIdent=2896, access on 16.10.2009.

[231] M. Uguccioni and C. Zeiss. Comparison of two approaches to modeling moisture movement through municipal solid waste. *Journal of Environmental Systems*, 25 (1):41–63, 1997.

[232] V. Ustohalova. *Process oriented modeling of the long-term behavior impact of landfills in closure care and post closure care - decompositions and transport processes.* PhD thesis, Department of Building Sciences, University of Duisburg-Essen, 2005.

[233] V. Ustohalova, T. Ricken, and R. Widmann. Estimation of landfill emission lifespan using process oriented modeling. *Waste Management*, 26(4):442–450, 2006.

[234] M. van Genuchten. A closed-form equation for predicting the hydraulic conductivity of unsaturated soils. *Soil Science Society of America Journal*, 44(5):892–898, 1980.

[235] V. Vavilin, V. Vasiliev, A. Ponomarev, and S. Rytow. Simulation model methane as a tool for effective biogas production during anaerobic conversion of complex organic matter. *Bioresource technology*, 48(1):1–8, 1994.

[236] P. Von Wolffersdorff. Verformungsprognosen für stützkonstruktionen. In *Veröffentlichungen des Institutes für Bodenmechanik und Felsmechanik der Universität Fridericiana in Karlsruhe.* Heft 141, 1997.

[237] D. Wall and C. Zeiss. Municipal landfill biodegradation and settlement. *Journal of environmental engineering*, 121:214–223, 1995.

[238] R. Wardwell and J. Nelson. Settlement of sludge landfills with fiber decomposition. In *Proc. 10th International Conference on Soil Mechanics and Foundation Engineering, Stockholm*, volume 2, pages 397–401, 1981.

[239] A. Warrick. *Soil physics companion.* CRC Press, 2002.

[240] G. Watson, W. Powrie, and A. Blades. An investigation into the effects of degradation on waste structure. In *Proceedings Sardinia 2007, Eleventh International Waste Management and Landfill Symposium, Italy*, 2007.

[241] B. Weber. *Minimierung von Emissionen der Deponie.* PhD thesis, Institut für Siedlungswasserwirtschaft und Abfalltechnik der Universität Hannover, 1990.

[242] J. White, J. Robinson, and Q. Ren. Modelling the biochemical degradation of solid waste in landfills. *Waste Management*, 24(3):227–240, 2004.

[243] J. K. White, Q. Ren, and J. P. Robinson. A framework to contain a spatially distributed model of the degradation of solid waste in landfills. *Waste Management & Research*, 21:330–345, 2003.

[244] C. Wilke and P. Chang. Correlation of diffusion coefficients in dilute solutions. *American Insitute of Chemical Engineers Journal*, 1(2):264–270, 1955.

[245] N. Yesiller, J. L. Hanson, and W.-L. Liu. Heat generation in municipal solid waste landfills. *Journal of Geotechnical and Geoenvironmental Engineering*, 131(11):1330–1344, 2005.

[246] A. Young and D. Davies. Applications of computer modelling to landfill processes - summary. Technical Report CWM 039B/92, Summary of DoE Report Number CWM 039A/92, Department of the Environment, 1992.

[247] L. Yu, F. Batlle, J. Carrera, and A. Lloret. Gas flow to a vertical gas extraction well in deformable MSW landfills. *Journal of Hazardous Materials*, 168(2-3):1404–1416, Sept. 2009.

[248] D. P. Zeccos. *Evaluation of Static and Dynamic Properties of Municipal Solid Waste.* PhD thesis, University of California, Berkeley, 2005.

[249] C. Zhang, M. Schmidt, G. Staupendahl, and U. Heemann. Entwicklung eines Stoffansatzes zur Beschreibung des Kompaktionsverhaltens von Salzgrus. Technical report, GSF-Forschungszentrum für Umwelt und Gesundheit, Institut für Tieflagerung, 1993.

Berichte aus dem Institut für Statik ab 2003

Nr.	2003-96	B. HÜBNER: Simultane Analyse von Bauwerk-Wind-Wechselwirkungen
Nr.	2003-97	J. GEISTEFELDT: Stochastische Finite-Element-Methoden mit Anwendung auf aeroelastische Tragsysteme
Nr.	2003-98	O. KNOKE: Beulwiderstände zusammengesetzter Zylinder-Kegel-Schalen
Nr.	2005-99	A. KÖLKE: Modellierung und Diskretisierung bewegter Diskontinuitäten in randgekoppelten Mehrfeldsystemen
Nr.	2006-100	D. DINKLER (Hrsg.): Institut für Statik, Lehre und Forschung, 1996-2006
Nr.	2006-101	A. VEHRE: Ein Reduktionsverfahren für Fluid-Struktur-Wechselwirkung mit Finiten Raum-Zeit-Elementen
Nr.	2006-102	M. LÖHR: Analyse aeroelastischer Systeme mit Spektralen Stochastischen Finite-Element-Methoden
Nr.	2006-103	L. ASCHENBRENNER: Mehrkomponenten-Modell zur Beschreibung des Deformationsverhaltens von Asphalt
Nr.	2006-104	T. ZÜMENDORF: Ein gradientenabhängiges Modell für Schädigung bei viskoplastischem Materialverhalten
Nr.	2007-105	C. LEPPERT: Mehrphasenmodell für granulare Medien zur numerischen Untersuchung des Phasenübergangs bei der Entleerung von Silos
Nr.	2007-106	V. KRASE: Stability of Municipal Solid Waste Landfills
Nr.	2007-107	J. PONTOW: Imperfektionsempfindlichkeit und Grenzlasten von Schalentragwerken
Nr.	2009-108	M. BECKMANN: Ein gradientenabhängiges Modell für anisotrope Schädigung von Beton unter Berücksichtigung von Porendruck
Nr.	2010-109	P. SUN: Fluid-Struktur-Wechselwirkung mit aktiver Schwingungskontrolle durch piezoelektrische Materialien
Nr.	2010-110	J. VELDE: 3D Nonlocal Damage Modeling for Steel Structures under Earthquake Loading
Nr.	2010-111	K. SCHUSTER: 3D Nonlocal Damage Modeling for Steel Structures under Earthquake Loading

Sonderdrucke

Phänomenologische Modelle für Werkstoffe des Bauwesens.
Hermann Ahrens zum 60. Geburtstag (1998).
Herausgeber: D. Dinkler, U. Kowalsky.

Baustatik-Baupraxis 8.
Berichte der Fachtagung am 21. und 22. März 2002 in Braunschweig.
Herausgeber: D. Dinkler.

Institut für Statik, Technische Universität Braunschweig
Beethovenstraße 51, 38106 Braunschweig, Deutschland
Telefon +49 (0)531 / 391-3667, Telefax +49 (0)531 / 391-8116
E-Mail statik@tu-bs.de, Homepage http://www.statik.tu-bs.de